



UNIVERSITÀ
DEGLI STUDI
FIRENZE

**DOTTORATO DI RICERCA IN
FISICA E ASTRONOMIA**

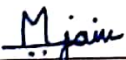
CICLO XXXIII

COORDINATORE Prof. Raffaello D'Alessandro

**Development of a new apparatus for precision gravity measurements
with atom interferometry**

Settore Scientifico Disciplinare FIS/03


Dottorando
Dott. Manan Jain


(firma)

Tutore
Prof. Guglielmo Maria Tino


(firma)

Coordiatore
Prof. Raffaello D'Alessandro


(firma)

Anni 2017/2020

ABSTRACT

The computational work in this doctoral thesis describes the virtual realization of an atom interferometry based gravity gradiometer aiming at an accurate determination of the Newtonian gravitational constant G . The experimental design and interferometric scheme is different from all the measurements published so far. This virtual realization aims on the cancellation of ambient gravity gradients from their exact - conjugate fictitiously generated gravity gradients from our scheme, therefore resulting in a relative accuracy of 10^{-6} using only 10^4 atoms in each cloud. Precise simulations are developed meticulously incorporating all the aspects of interferometric scheme with well - characterized tungsten source masses measuring the phases accumulated by the atomic clouds traversing the path resulting from Mach - Zehnder gravimetric sequence in the presence and absence of the aluminium platform supporting the new configuration of source masses. One other possible source mass design made out of copper (assuming the geometrical configuration analogous to the aluminium platform) is also considered, so as to complete a comparative study of phase acquisition due to different designs of source masses arising from different total gravitational potentials and material densities. These precise simulations also target at achieving the phase noise minimization for the interferometric signal in presence of gravity, as a result to completely eliminate the presence of systematic errors. The simulation in this thesis incorporates a presence of a finite - sized solenoidal coil affecting only second half of the upper interferometer resulting in the opening of ellipse, henceforth the systematic errors which are faced while performing the elliptic fit will be completely eliminated. The gravity gradiometer as per the new design in the thesis is currently being built for the measurement runs of continuous data acquisition to be possible. The phase noise minimization condition for the modified experimental scheme has been performed and is reported in this thesis. Lastly, the gravity gradient cancellation for both the two source mass designs with a relative uncertainty of 0.1%, 0.5% and 1.0% have been performed and is reported in this thesis.

ACKNOWLEDGEMENTS

On the very outset of this thesis, firstly I would like to extend my sincere and heartfelt thanks towards my doctoral supervisor Prof. Guglielmo Tino and my research mentor Dr. Gabriele Rosi. I am indebted to Prof. Tino for his constant support, encouragement and guidance. I consider myself very fortunate that I had opportunity to work with Dr. Rosi. I am thankful to Prof. Tino for giving me this opportunity because this opportunity was everything. It is indeed a privilege that Prof. Tino and Dr. Rosi had faith in me despite I made several trivial errors during my doctoral research. Personally, I have never witnessed a young person like my research mentor during my years here who is extremely clever, helpful and considerate even when I made mistakes seeing on which any professor or an advisor could lose his/her faith. I am happy to declare that in these three years, I not only became a better researcher but also a person with a good level of patience and consideration.

I thank my sister for being a hard taskmaster believing in my capability and helping me bring the best out of me to write the best thesis possible. I thank my parents and aunt for raising a stubborn and impulsive child like me and helping me achieve the best version of myself, both as an aspiring physicist and as a good-natured person.

I am very thankful to all my mentors and seniors in physics who gave me their valuable time for meaningful and stimulating discussions, namely - Raman Sehgal, Sushil Sharma, Pulkit Rai, Giulio D'Amico, Kanhaiya Pandey. It was pure luck that I had an opportunity to learn from a scientist like Raman Sehgal who taught me Python from scratch, eventually yielding the results stated in this thesis in a record time. From the first day of my Master degree till now, I have admired a senior like Pulkit Rai whose knowledge in physics and many aspects of life are exemplary and flawless, with his consistent encouragement towards me to sit back and relax only after the results are perfected. Learning from him was a great honour because he is a person who constantly smiles no matter how harsh circumstances and challenges he is facing. It was very nice of Dr. Sushil Sharma who spent his valuable time encouraging me to give an informal talk about my doctoral work and discuss physics in front of his colleagues. The feedback from him and his colleagues increased my confidence while delivering a talk or a seminar, which marks as a stepping stone for making a good academic career. I remember when I was in first year of my PhD candidature, I have seen Giulio D'Amico working tirelessly in lab with great motivation, I don't have enough words to truly express my gratitude towards him. I was fortunate enough to have stimulating discussions of cold atoms with him. He helped me by answering my scientific queries even after he left the lab despite his busy schedule, which was an important checkpoint in my doctoral candidature. This important checkpoint played a vital role in helping me secure a postdoctoral position. Lastly, in my life, the first person who taught to get my hands on the experimental apparatus in cold atom lab was Dr. Kanhaiya Pandey. I hope to meet Dr. Pandey again if I become capable enough to discuss physics or cold atom experiments with a skilful and brilliant person like him.

The days of my doctoral degree were the most challenging days of my lifetime, as it truly was a roller-coaster ride. Being present in a sophisticated laboratory for two years working on computer helped me progress in the direction of being an independent researcher. All this led

to unlocking my potential to do best research possible that I never could have accomplished without guidance and comments from my PhD supervisor and my research mentor. My life became less stressful when I found people here in whom I found good friends, all of whose presence was of great significance. I am thankful to these people in Florence who treated me so well providing me moral support in fantastic ways by conducting reunions, house parties, playing indoor/outdoor games and travel explorations. The names of all these people are: Harshal, Shweta, Avishek, Maitreyee, Murtaza, Shamaila, Nihar, Deepti, Gunjan, Atif, Tassadaq, Prasanna, Akande, Prosenjit, Pjeter, Lorenzo, Alessandro, Francesco, Giulio, Leonardo, Enlong.

I would like to thank all Indian people close to my heart. Names of these precious people who all equally believed that I could pursue this endeavour and produce fruitful results are: Abhinit Parelkar, Aditya Khandekar, Ajinkya Bhavsar, Amir Ahemad, Ankit Jain, Arun Yadav, Avinash Rajendran, Awani Saraf, Ian Fonseca, Mustafa Bohra, Narendra Rathod, Nishchal Dwivedi, Prasad Damale, Pratik Bhanuse Pulkit Rai, Rajeshwari Shekar, Rhushabh Jagalpure, Rishi Jain, Sahil Upadhyaya, Taha Ahmed, Zeeshan Siddiqui.

Contents

1	Introduction	5
1.1	Light interferometry and Atom interferometry	5
1.2	Atom interferometers as inertial sensors	7
1.3	Measuring G with atom interferometry	8
1.4	Motivations and Objectives	9
1.5	Thesis Outline	12
2	Atom Interferometry: Theoretical Background	15
2.1	Atom - light field interaction	15
2.1.1	Two - level atom interacting with travelling waves: Rabi oscillations	15
2.1.2	Raman Transitions	23
2.1.3	Phase Shift Calculation: Mach - Zehnder Raman Atom Interferometer	28
2.2	Applications of Atom Interferometry	30
2.2.1	Embarking with new ideas from research in Atom In- terferometry	31
3	Experimental Sequence	35
3.1	Outline of the new experimental scheme	35
3.1.1	<i>Step - I</i> : Phase Noise Minimization	35
3.1.2	<i>Step - II</i> : Gravity Gradient Cancellation	39
4	Magnetic Fields: Phase Noise Minimization and 2D - MOT	43
4.1	Introduction to Phase Noise Minimization	43
4.2	Understanding of the <i>jitter</i> due to an applied magnetic field	45
4.3	B-pulse coil Activation	45
4.4	Monte Carlo simulation to calculate the difference in phase between the two clouds (in absence of classical trajectories of atoms)	47

4.4.1	Phase variation with respect to change in physical parameters	48
4.5	Interferometric phase as a function of time - dependent atomic trajectories	50
4.6	Precise optimization position and relative sensitivity estimation	53
4.7	Monte Carlo simulation for phase difference calculation between the two clouds (accounting classical trajectories of atoms)	53
4.7.1	Optimized and Unoptimized phases for different atomic populations	54
4.8	Magnetic field equations of finite continuous solenoid: Bias and B-pulse coils	62
4.9	Phases obtained due to the sole effect of bias coil	63
4.10	Monte Carlo simulation of the gradiometric sequence	63
4.10.1	Monte Carlo simulation for the relative phase calculation in the complete experimental sequence for the case of two atomic clouds	65
4.11	Results from Monte Carlo simulation	69
4.11.1	All variable behaviours associated with 3D scenario	69
4.11.2	Comments about graphs	76
4.11.3	Peak-to-peak variations	76
4.12	Stability of fixed parameters	76
4.12.1	Baseline stability	76
4.12.2	Phase sensitivity due to variation in bias coil current	77
4.12.3	Phase sensitivity due to variation in B-pulse coil current	78
4.12.4	Phase sensitivity due to z_m	79
4.13	Designing new anti-helmholtz coil system	79
4.13.1	2D-MOT coil system with rectangular arrangement: Mathematical Analysis	80
4.13.2	2D-MOT coil system - Calculation and Simulation: Coil parameters, magnetic field and magnetic field gradients	83
4.14	Conclusions and Outlook	87
5	Source Masses: Design, Calculation and Simulation	89
5.1	Source Mass Design: Geometrical Configuration - I	89
5.1.1	Z - Coordinates	89
5.1.2	X and Y - Coordinates	91
5.1.3	Gravitational Potentials and Accelerations	93
5.1.4	Determination of radius of tungsten source mass cylindrical disks	104
5.2	Source Mass Design: Geometrical Configuration - II	105

5.3	Precise estimation of initial $\pi/2$ -pulse	109
5.4	Linearity of gravitational acceleration	111
5.5	Simulation and Calculation: Phases due to fictitious gravity gradient	113
5.5.1	Single - atom gradient calculation (Geometrical Configuration- I)	115
5.5.2	Single - atom gradient calculation (Geometrical Configuration- II)	116
5.6	Residual Phases: Achieving the relative accuracy of 10^{-6} . . .	116
5.6.1	Results: Configuration - I	116
5.6.2	Results: Configuration - II	119
5.6.3	Comments about graphs	135
5.6.4	Peak-to-peak variations	135
5.7	Conclusions and Outlook	137
6	Conclusions	139
6.1	Results	139
6.2	Future Prospects	140
A	Magnetic Fields: Exact solution	155
B	List of Codes	161
C	List of Publications	197
C.1	Publications in International Journals	197
C.2	Conference Proceedings	197

Development of a New Apparatus for Precision Gravity Measurements with
Atom Interferometry

Chapter 1

Introduction

The work that we present in this thesis lays a computational foundation of a vertical fountain Atom Interferometer (AI) which can be used to perform high - precision measurements of Newtonian Gravitational Constant G through atom interferometry. This apparatus will be also useful for performing high sensitivity gravitational tests and realizing measurements of earth's gravitational acceleration (atom gravimetry) and the gravity gradients (atom gradiometry). This thesis completes two major targets; to minimize the phase noise in the interferometric signal and to cancel the gravity gradients.

In this first Chapter, we introduce the subject and motivate the topic of atom interferometry. We start with analogy between light and atom interferometers and end stating briefly how G is measured using MAGIA apparatus with description of thesis organization.

1.1 Light interferometry and Atom interferometry

An Atom Interferometer (AI) exploits the wave nature of matter resulting in the phenomenon of interference between two or more matter wavefronts. The data occurring from interference yields information about the atoms and related parameters of interest (for example, gravitational acceleration, Newtonian gravitational constant, gravity gradients, etc.). In this regard, an atom interferometer becomes conceptually analogous to a standard light interferometer, subject to following key differences:

- *Roles between matter and light are exchanged:* Considering a light interferometer, a coherent beam of light splits and follows two different optical trajectories; the trajectories of these two light beams are

steered using material components (i.e., glass beam-splitters, mirrors, gratings, etc.). Just after the light beams interfere, their intensity display an interference pattern as a function of the relative optical path length. Whereas, in an AI, the mirrors and beam-splitters (optical components) are realized with laser pulses. These light pulses are produced by two counterpropagating vertical laser beams. Manipulating laser frequency detuning and photon momenta, these light pulses can behave analogous to mirrors and beam-splitters as it happens in light interferometer. The production of these mirror and beam-splitter laser pulses is detailed in Section 2.1.1.

- *In an AI, the probe particles are affected by gravity:* Atoms being massive particles possess a high sensitivity towards earth's gravitational field and other environmental conditions (like inertial effects and accelerations). The interference of atoms caused due to an AI contains information about variation of earth's gravitational acceleration. This is so because an atom experiences slightly different gravitational acceleration at different altitudes, leading to existence of a non-zero gravity gradient.

It is well-known as it has been demonstrated in a large variety of experiments that light and matter particles both possess a dual nature and behave in similar ways, depending on the experimental configuration, either as quantum particles (photons - massive particles) or as waves (light waves - matter waves). AI is indeed a classic experimental example of wave - particle duality. This wave - particle duality is explained by an AI as follows: Consider a two - level atom with a well - defined ground state and a first excited state, freely moving in a certain direction. When the atom with this internal state structure is irradiated by a light pulse coupling the two internal energy levels, its original wavefunction splits spatially into two wavefunctions each having equal amplitudes. The idea is that after interrogation, the atom is in a superposition of the two internal states, but with different momenta. The two internal states will have equal amplitude only if the atom is irradiated by a $\pi/2$ -pulse. These two parts of the wavefunction traverse different trajectories experiencing different local forces and acquiring different momentum states. When these two wavefunctions are recombined using light pulses, an interference pattern is generated such that the internal state population becomes a function of the relative phase accumulated on the two different atomic trajectories.

As stated earlier, atoms being massive particles with a high sensitivity to environmental conditions (like inertial effects and accelerations), pose as a good probe for examining fundamental tests like UFF (Universality of Free

Fall) in the field of gravitational physics [1, 2, 3, 4, 5, 6]. Atoms being intrinsically sensitive results in access to increased degrees of freedom with several possibilities to manipulate them. Furthermore, AI sensitivity depends essentially on two features: free evolution time and momentum transfer. Stimulated Raman transitions are used to obtain a considerably large momentum transfer. In a recent work [7], Mach-Zehnder interferometers with momentum separation of up to $141\hbar k$ and gradiometers of up to $82\hbar k$ have been demonstrated.

1.2 Atom interferometers as inertial sensors

The choice of neutral atoms to perform interferometry as a probe for revealing quantum behaviours arose from the first matter-wave interferometer which was realized in 1947 by Enrico Fermi [8], the experiment used slow neutrons being diffracted (via Bragg diffraction) by crystal planes with different chemical compositions, resulting in the measurement of the relative sign of the neutron scattering length from different nuclei samples. Some years later the first matter-wave interferometry experiment on electrons was performed using a Mach-Zehnder interferometric scheme arranged with crystals of few hundreds of atomic layers as mirrors [9, 10, 11]. As time passed, it became clear at one point that the electrically neutral atoms (neutral matter) were a good choice to perform atom interferometry measurements with a scope of building high sensitivity devices for acceleration detection due to reasons like: possibilities of producing very cold samples by laser cooling and other techniques, manipulating atoms with laser fields thus easily realizing beam splitters and mirrors, a good control of the atomic velocities and therefore the interrogation times. Moreover, for scientists working in the field of interferometry, atoms were preferred over neutrons for one main reason that neutrons are difficult to produce in the laboratories. Taking this reason into the account, several research groups around the world started to realize AI experiments [12, 13, 14, 15].

Till the date, the field of atom interferometry has gained recognition via different experiments across the globe carrying out precise measurements of: Newtonian Gravitational Constant [16, 17, 18, 19, 20, 21, 22, 23, 24, 25, 26, 27, 28], h/m [29], h/m_u [30], h/m_{Cs} [31], h/m_{Na} [32], atomic polarizability [33, 34], gravity acceleration [35, 36, 37], curvature [38, 39], Earth's gravity gradient [40] and gravity gradient sensitivity [41], fine - structure constant [42, 43] and rotations [44, 45, 46, 47]. Another example is the use of AIs for testing the Einstein Equivalence Principle [48, 49]. Different experiments have attempted to determine the values of many fundamental

constants precisely for geophysical applications and metrological interests [16, 17, 19, 20, 21, 22, 23, 24, 30, 50, 51]. Accelerometers based on the concept of atom interferometry are employed for many practical applications including metrology, geodesy, geophysics [52], engineering prospecting and inertial navigation [53, 54]. Ongoing studies show that the space environment will allow to take full advantage of the potential sensitivity of atom interferometers [55, 56, 57]. In past, two new interferometer schemes based on multi-photon transitions have been developed and demonstrated [58]. About more than a decade ago, one of the research works [59] quote about general relativity tests at unprecedented precision level. From a technological aspect, designing different transportable apparatus [52, 60, 61] requires noteworthy efforts to compactify systems of optics and electronics side-by-side developing robust laser locks [62].

A precise determination of the acceleration due to gravity g and of its gradient have important applications in several scientific domains. Geophysics and metrology pose as two common examples, but also more practical applications can be found in exploratory initiatives for underground resources (oil, water, etc.). In this context, transportable devices are engineered and assembled for mapping Earth mass anomalies, for monitoring behavior in volcanoes and also to measure gravitational changes before the happening of earthquakes. Nowadays, atomic gravimeters are available as commercial products.

1.3 Measuring G with atom interferometry

The acronym MAGIA stands for Measurement of G by Atom Interferometry. This state-of-the-art experimental apparatus (Figure 1.1) had its destiny to precisely measure the Newtonian gravitational constant G . The experiment fulfilled its destiny in 2014 [16]. In the following years, the apparatus realized several other gravitational measurements [35, 38, 48, 66]. However, in order to understand the particular design of the MAGIA setup, we shall briefly describe the principle of the G determination stating the reason for its relevance.

Among many fundamental constants, this fundamental quantity G is known with the highest relative uncertainty. The last CODATA recommended value is:

$$G = 6.67384(80) \times 10^{-11} m^3 K g^{-1} s^{-2} \quad (1.1)$$

holding a relative uncertainty of 1.2×10^{-4} . The particular nature of the gravitational force poses several difficulties in the experimental determination of

the constant G . Since gravitational force is long - ranged and extremely weak, it exercises control over large neutral masses, henceforth leading to big systematic effects in laboratory experiments. Due to this reason, all the classical determinations of G which lay their foundations as macroscopic suspended masses, i.e. torsion pendulums, or free-falling corner cubes incur from inevitable systematics which become strenuous to characterize. Whereas, atom interferometry provides an alternative method for high - precision measurement of G with a completely different systematic budget from the classical experiments and it can be used to validate one of the previous inconsistent measurements thus reducing the relative uncertainty on G .

In the MAGIA experiment [18, 19], G is determined from the measurement of the differential acceleration experienced by two samples of cold ^{87}Rb atoms when in presence of a well characterized set of tungsten source masses. Repeating the measurement for two different source masses arrangements, namely CLOSE and FAR, the interferometric phase imprinted on atoms contains solely the effect of the masses along with simultaneous elimination of the phase contribution from gravitational field of earth. Having an accurate knowledge of the source mass distribution, the value of G can be measured with a high precision. With a relative uncertainty of 150 parts per million, the value of G measured from MAGIA experiment is:

$$G = 6.67191(99) \times 10^{-11} m^3 Kg^{-1} s^{-2} \quad (1.2)$$

1.4 Motivations and Objectives

In this thesis, we computationally implement a new design highlighting two crucial steps - the first step is to minimize the phase noise in the gradiometer signal, and, the second step is to build a new configuration of source masses [63], thereby pushing the relative accuracy beyond 10^{-4} . This combination of phase noise minimization in the interferometric signal along with an implementation of new design of source masses will pave the way towards a precise determination of G using laser-cooled atoms and quantum interferometry to probe gravity.

Primary objective with motivation: The motivation and approach behind phase noise minimization is explained as follows. During the Mach - Zehnder interferometric sequence, two spatially separated atomic clouds are launched using moving optical molasses technique along the fountain axis, exhibiting a free fall motion. Subsequently, they are simultaneously interrogated by the same Raman beams [16, 17, 35, 48]. As a consequence, the retroreflecting

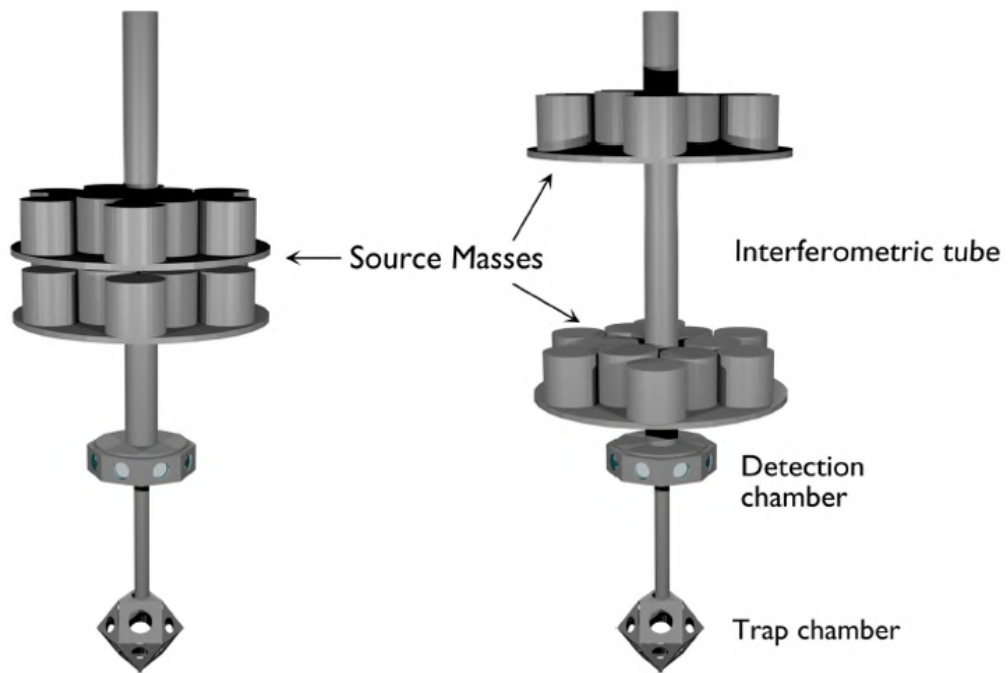


Figure 1.1: Overview of the MAGIA with source masses working in two different geometrical configurations: CLOSE (left) and FAR (right), used for the double differential measurement of G . Cold atomic clouds of ^{87}Rb are prepared in the trap chamber (at the bottom of the setup) in a 3D-MOT (three - dimensional magneto - optical trap). Two cold atomic cloud samples of ^{87}Rb are launched vertically inside the interferometric tube using moving optical molasses technique. When the clouds are in the vicinity of their respective apogees, their vertical acceleration is measured using pulse sequences of a Mach - Zehnder atom interferometer. This measurement is conducted in both CLOSE and FAR geometrical configurations of the source masses.

mirror vibrations impact both the upper and lower clouds (behaving as simultaneous upper and lower interferometers) resulting in a correlation among their interferometric signals. Lissajous figures (representing interferometric fringes) are obtained [17] and the phase difference is extracted by fitting point distribution with an ellipse. In fact, the two fringes can be described with independent amplitudes and the vertical offsets, and with a relative phase difference (Φ). Furthermore, due to the presence of systematic errors in the method of elliptic fitting, the small differential phases (Φ) were not accurately fitted with the ellipse fitting method [17, 20], so, it is convenient to add an external and well-controlled relative phase shift in order to have a differential phase of about $\pi/2$. This differential phase requirement was derived from a simulation performed previously [17], where the noise level and the ellipse angle were varied for the noise - produced effects on the estimated value of Φ , also a bias depending on both the noise and the ellipse angle itself; in particular, is minimum for $\Phi \approx \pi/2$ was found [17, 20]. Whereas, in the case when systematic effects are independent of k_{eff} , for each measurement the *k-reversal procedure* [64] can be applied.

Secondary objective with motivation: Gravity gradients present a vital obstacle in high-precision measurements using atom interferometry. Controlling their effects to the required stability and accuracy imposes very compelling requirements on the relative positioning of freely falling atomic clouds, as in the case of precise tests of Einstein's equivalence principle. The crucial simulations presented in this thesis are developed meticulously incorporating all the aspects of interferometric scheme with dense, cylindrical - shaped tungsten source masses, measuring the phases accumulated by the atomic clouds traversing the path resulting from Mach - Zehnder gravimetric sequence in the presence and absence of the aluminium platform constituting as first new configuration of source masses. The second new configuration marks a torus - shaped block created from a consecutive stacking of 43 torus - shaped copper rings, inflicting phases on the atomic clouds traversing Mach - Zehnder trajectory. This second configuration assumes the geometrical configuration analogous to the aluminium platform of the first configuration. This crucial research is conducted so as to complete a comparative study of phase acquisition due to these two different designs of source masses arising from different total gravitational potentials and distinct material densities. The second source mass configuration is carved out of copper because it is a material which is pure, homogeneous and less expensive, and in our case it assumes simpler geometry as compared to the tungsten cylindrical blocks from the first configuration. In simple words, all this is done so as to witness the impact of gravitational potentials created from different materials (possessing different densities and geometries) on the cloud of cold ^{87}Rb atoms.

Now we explain the motivation behind gravity gradient cancellation. When we cancel the gravity gradient with a recently discovered technique [65], the ellipse (a Lissajous figure representing a plot of relative upper versus relative lower populations of the atoms in the two clouds) degenerates into a line marking a zero phase shift. Our scheme of phase noise minimization which employs a finite-sized solenoidal coil will affect only the second half of the upper interferometer (upper cloud). Due to this, the ellipse can be completely opened. Henceforth, the systematic errors which are faced while performing the elliptic fit will be vanished. Also, as per the standard gradiometric scheme, it is technically challenging to produce a pair of ultra-cold samples and routinely place them with a minimized spatial resolution [16, 17, 20]. The new procedure [65, 66] simulates the effect of a gravity gradient on the atomic trajectories in the sense that it is able to generate a *fictitious* gravity gradient. In our simulations, we applied this technique [65] to two simultaneous interferometers positioned along the vertical direction to computationally simulate this effect for measuring local gravity gradients, void of requirement of the precise knowledge of relative position between the atomic clouds [66].

1.5 Thesis Outline

The experiment to be performed in near future is described in this thesis taking into account all theoretical aspects, but mainly from a computational point of view for experimental physicists. Firstly, from a complete theoretical introduction on the basic tools for improving the gradiometric signal in the experimental sequence to the theory and formalisms for Raman transitions are presented in Chapters 1 and 2 respectively. Chapter 2 ends with applications in this emerging field of atom interferometry. An overview of the terms contributing to the phase shift, useful for systematic studies, is reported at the end.

Chapter 3 explains the modified experimental sequence for the virtual realization of this new experiment in a clear way, presenting an account of the mathematical description underlying the basic idea of the scheme.

Chapter 4 presents itself as a complete study of the phase noise minimization in the interferometric signals (in the presence of gravity) with successful results. In addition to this, the last section of Chapter 4 also describes a workable design (with related calculations specifying physical parameters) of two - dimensional magneto - optical trap compatible with the new design of the experiment presented in this thesis.

Chapter 5 contains a detailed description of the two new designs of source

masses and phase calculations including compensation of ambient gravity gradients underlying results stating a relative accuracy of 10^{-6} , which is achieved while cancelling the real gravity gradient with a *fictitious* gravity gradient [66], all of which is reported here.

The thesis ends summarizing the results obtained, and, the future scope for the experiment in Chapter 6. Lastly, all the important simulations which produced the results are documented in the thesis, provided as Appendices.

Chapter 2

Atom Interferometry: Theoretical Background

In this Chapter, we shall describe theoretical formalisms useful to introduce Atom interferometry. In the beginning, we shall illustrate a simple case of a two-level atomic system irradiated by a monochromatic photon source. In our next step, stimulated Raman transitions will be introduced with an outlook of multi-level atomic configuration interacting with two counter-propagating light beams. Experimental parameters and variables, that will be used in this thesis, are introduced in order to make the reading easier and more directly comprehensible. The main physical phenomena that can induce a phase shift in the interferometer signal are separately considered and analytical expressions for the different phase terms are derived wherever necessary.

2.1 Atom - light field interaction

2.1.1 Two - level atom interacting with travelling waves: Rabi oscillations

Let us consider a simple two - level atomic system with ground and excited states marked as $|g\rangle$ and $|e\rangle$ respectively, with their corresponding energy eigenvalues as $\hbar\omega_g$ and $\hbar\omega_e$. In this mathematical treatment, we will omit spontaneous emission, because here the first excited state $|e\rangle$ is stable enough during the pulse sequence is between the magnetically insensitive hyperfine energy levels $|F = 1, m_F = 0\rangle$ and $|F = 2, m_F = 0\rangle$ in ^{87}Rb . Energy levels $|g\rangle$ and $|e\rangle$ are coupled by an incoming electromagnetic field of frequency ω with a corresponding wavevector \vec{k} .

In the rotating - wave approximation, the Hamiltonian is given by:

$$\mathcal{H} = \frac{\hat{p}^2}{2m} + \hbar\omega_e|e\rangle\langle e| + \hbar\omega_g|g\rangle\langle g| + \hbar\Omega e^{i(\vec{k}\cdot\vec{r}-\omega t)}|e\rangle\langle g| + \hbar\Omega^* e^{-i(\vec{k}\cdot\vec{r}-\omega t)}|g\rangle\langle e| \quad (2.1)$$

The above Hamiltonian equation consists of three crucial elements: kinetic energy of the atom, in which the momentum operator \hat{p} acts upon momentum part of the relevant state, diagonal matrix element Hamiltonian - $\mathcal{H}_D = \hbar\omega_e|e\rangle\langle e| + \hbar\omega_g|g\rangle\langle g|$, and lastly, the off - diagonal matrix element Hamiltonian - $\mathcal{H}_{\Omega\Omega^*} = \hbar\Omega e^{i(\vec{k}\cdot\vec{r}-\omega t)}|e\rangle\langle g| + \hbar\Omega^* e^{-i(\vec{k}\cdot\vec{r}-\omega t)}|g\rangle\langle e|$. This implies:

$$\mathcal{H} = \frac{\hat{p}^2}{2m} + \mathcal{H}_D + \mathcal{H}_{\Omega\Omega^*} \quad (2.2)$$

Here, Ω is referred to as *Rabi frequency*. Rabi Frequency is a measure of atomic population fluctuation between $|g\rangle$ and $|e\rangle$ states, therefore coupling the ground and first excited states. Mathematically, Rabi frequency is expressed as:

$$\Omega_{|g\rangle\rightarrow|e\rangle} = \frac{\vec{d}_{|g\rangle\rightarrow|e\rangle}\cdot\vec{E}_0}{\hbar} \quad (2.3)$$

where $\vec{d}_{|g\rangle\rightarrow|e\rangle}$ is the transition dipole moment for the transition: $|g\rangle \rightarrow |e\rangle$, whereas $\vec{E}_0 = \hat{\epsilon}E_0$ marks the amplitude of electric field vector from the incoming monochromatic electromagnetic radiation. The reason which explains the existence of a complex conjugate of Rabi frequency in the fourth term of equation 2.1 is that the polarization ϵ can be complex. For example - in the case of a circularly polarized light, or, the electric field amplitude vector for the case of plane wave is complex itself: $\vec{E}_0 = |\vec{E}_0|e^{i\phi}$. This argument clarifies the meaningful existence of Ω^* in the Hamiltonian for a simple two - level atomic system illuminated by an incident monochromatic light.

Considering light travelling as a stream of photons, when atoms are illuminated by the first $\pi/2$ - pulse, atoms receive a momentum kick from the photon and they go from the ground state to an excited state. Basically, the atom is now in the superposition of these two states, equivalent to understanding that the atom has two different trajectories spanned by two momentum states. After half - time of the interferometric sequence, a combination of a π and a $\pi/2$ - pulse steers back the two different paths of atom for it to reach a definite state. To be more clear and precise, we will explore the scenario of a simple two-level scheme considering light as a bunch of photons, which will take us towards the path of realizing mirrors and beam splitters using laser pulses as done in atom interferometers.

Since we are using the picture of photons interacting with atom [29], the atomic states are labelled in the momentum basis by spanning into the corresponding tensor products in Hilbert spaces:

$$|g, \vec{p}_g\rangle = |g\rangle \otimes |\vec{p}_g\rangle$$

and,

$$|e, \vec{p}_e\rangle = |e\rangle \otimes |\vec{p}_e\rangle$$

Under the momentum basis, the spatial dependence arises via the translational operator:

$$e^{\pm i\vec{k}\cdot\vec{r}}|\vec{p}\rangle = |\vec{p} \pm \hbar\vec{k}\rangle \quad (2.4)$$

The above quantum state transformation expresses the well - known result: Absorption of a photon with a wavevector \vec{k} changes the atomic momentum by $\hbar\vec{k}$. The light field couples the quantum momentum states $|g, \vec{p}_g\rangle$ and $|e, \vec{p}_e + \hbar\vec{k}\rangle$.

For the sake of convenience, we employ the transformations $|\tilde{g}\rangle = e^{-i\omega_g t}|g\rangle$ and $|\tilde{e}\rangle = e^{-i\omega_e t}|e\rangle$ inside Hamiltonian terms of equation 2.2 as follows:

$$\mathcal{H}_{\Omega^*} = \hbar[\Omega e^{i(\vec{k}\cdot\vec{r}-\phi(t))}|\tilde{e}\rangle\langle\tilde{g}| + \Omega^* e^{-i(\vec{k}\cdot\vec{r}-\phi(t))}|\tilde{g}\rangle\langle\tilde{e}|] \quad (2.5)$$

$$\mathcal{H}_D = \hbar[\omega_e|\tilde{e}\rangle\langle\tilde{e}| + \omega_g|\tilde{g}\rangle\langle\tilde{g}|] \quad (2.6)$$

with $\phi(t) = \delta t$ and $\delta = \omega - \omega_e + \omega_g$. Here, δ is known as *detuning* of irradiated monochromatic light source. Hence, the total Hamiltonian becomes:

$$\mathcal{H} = \frac{\hat{p}^2}{2m} + \hbar[\Omega e^{i(\vec{k}\cdot\vec{r}-\phi(t))}|\tilde{e}\rangle\langle\tilde{g}| + \Omega^* e^{-i(\vec{k}\cdot\vec{r}-\phi(t))}|\tilde{g}\rangle\langle\tilde{e}|] + \hbar[\omega_e|\tilde{e}\rangle\langle\tilde{e}| + \omega_g|\tilde{g}\rangle\langle\tilde{g}|] \quad (2.7)$$

The term $\frac{\hat{p}^2}{2m}$ responsible for being an external degree of freedom and the phase $\phi(t)$ depending on both the laser frequency and on the internal energy of the atoms play an important role in the phase shift calculation of an atom interferometer.

The time evolution of a time - dependent quantum state $|\psi(t)\rangle$ can be expressed in terms of time - dependent coefficients $a_{|g,\vec{p}\rangle}(t)$ and $a_{|e,\vec{p}+\hbar\vec{k}\rangle}(t)$:

$$|\psi(t)\rangle = a_{|e,\vec{p}+\hbar\vec{k}\rangle}(t)|\tilde{e}, \vec{p} + \hbar\vec{k}\rangle e^{\frac{-i|\vec{p}+\hbar\vec{k}|^2 t}{2m\hbar}} + a_{|g,\vec{p}\rangle}(t)|\tilde{g}, \vec{p}\rangle e^{\frac{-i|\vec{p}|^2 t}{2m\hbar}} \quad (2.8)$$

These time - dependent coefficients can be calculated by solving Schroedinger's equation:

$$i\hbar \frac{d|\psi(t)\rangle}{dt} = \mathcal{H}|\psi(t)\rangle \quad (2.9)$$

In the limit where $\phi(t)$ is constant during the pulse, the probability of finding an atom in state $|e\rangle$ after an interaction time τ is then given by:

$$|a_{|e, \vec{p} + \hbar \vec{k}\rangle}(t)|^2 = \frac{1}{2}(1 - \cos \Omega\tau) \quad (2.10)$$

The atom undergoes the well - known Rabi oscillations between the two states $|g\rangle$ and $|e\rangle$. Two configurations relevant for atom interferometry in the particular case where $a_g(t_0) = 1$ and $a_e(t_0) = 0$ result in:

- *Case - I*: $\pi/2$ -pulse: $\Omega\tau = \pi/2$

$$|\psi(t)\rangle = \frac{1}{\sqrt{2}}[|g, \vec{p}\rangle - i|e, \vec{p} + \hbar \vec{k}\rangle e^{-i\phi(t)}] \quad (2.11)$$

- *Case - II*: π -pulse: $\Omega\tau = \pi$

$$|\psi(t)\rangle = -i|e, \vec{p} + \hbar \vec{k}\rangle \quad (2.12)$$

From *case - I*, when the atom is interrogated with a $\pi/2$ -pulse, the photon (carrying momentum $\hbar \vec{k}$) from this $\pi/2$ -pulse spans the atom into a coherent superposition with equal wave packet amplitudes, resulting in the formation of two different internal energy states. The wavepackets are separated by an atomic recoil velocity $v_r = \hbar|k|/m$. This implies that $\pi/2$ -pulse plays the role which beam splitter does in the classical optical interferometry. Similarly, from *case - II*, we can conclude that if the π -pulse is applied to a superposition state, the resulting atomic wavefunction is still a superposition state, but with swapped momentum states, resulting in a *mirror-like* behavior. Note that when the atom is in the ground state $|g\rangle$ a π -pulse corresponds to an absorption of an incoming photon with energy $\hbar\omega_L$ and to the acquisition of a momentum $+\hbar k_L$, but when the atom is initially in the state $|e\rangle$, a stimulated emission occurs so a photon with energy $\hbar\omega_L$ is emitted copropagating with the laser light and the atomic momentum changes by $-\hbar k_L$. Hence, the condition $\Omega\tau = \pi$ results in behavior of π -pulse analogous to the role of mirrors in the classical optical interferometry. Experimentally, this is done by selecting the coupling parameters resulting in the conditions: $\Omega\tau = \pi/2$ and $\Omega\tau = \pi$.

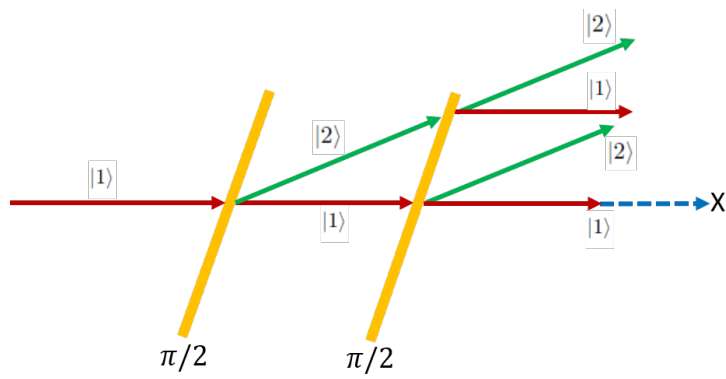


Figure 2.1: Action of $\pi/2$ - pulses on states $|1\rangle$ and $|2\rangle$.

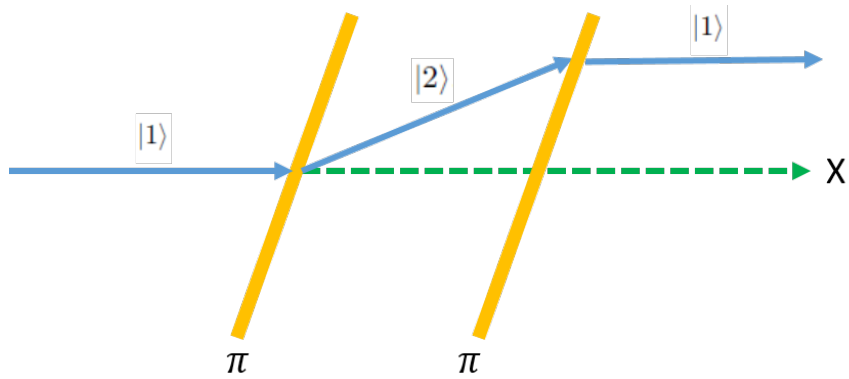


Figure 2.2: Action of π - pulses on states $|1\rangle$ and $|2\rangle$.

Let $a_1(t)$ and $a_2(t)$ be the amplitude probabilities of detecting the atom in the corresponding state at a time t . Let us now split in two terms, one due to the interaction with the electric field and another one related with the free evolution of the atomic wavefunction, hence the amplitudes in equation 2.8 and the Hamiltonian with rotating - wave approximation modify as:

$$a_1(t) = a_{|e, \vec{p} + \hbar \vec{k}\rangle}(t) e^{\frac{-i|\vec{p} + \hbar \vec{k}|^2 t}{2m\hbar}} = c_1(t) e^{-i\omega_b t} \quad (2.13)$$

$$a_2(t) = a_{|g, \vec{p}\rangle}(t) e^{\frac{-i|\vec{p}|^2 t}{2m\hbar}} = c_2(t) e^{-i\omega_a t} \quad (2.14)$$

$$\mathcal{H} = \frac{|\vec{p}|^2}{2m} + \hbar\omega_a |g, \vec{p}\rangle \langle g, \vec{p}| + \hbar\omega_b |e, \vec{p} + \hbar \vec{k}\rangle \langle e, \vec{p} + \hbar \vec{k}| - \vec{d} \cdot \vec{E}_L \quad (2.15)$$

where ω_a and ω_b are the frequencies of the ground and excited states respectively. Also, d is an electric dipole operator and E_L is the electric field vector of the incoming coherent monochromatic laser field expressed as: $E_L = E_0 \cos(k_L \cdot \vec{r} - \Omega_L t + \phi_L)$. In the rotating wave approximation [67], one gets the following differential equations for the coefficients:

$$i\dot{c}_1(t) = \frac{\Omega}{2} e^{i(\Delta t - \phi_L)} c_2(t) \quad (2.16)$$

$$i\dot{c}_2(t) = \frac{\Omega^*}{2} e^{-i(\Delta t + \phi_L)} c_1(t) \quad (2.17)$$

Introducing generalized Rabi frequency Ω_G as:

$$\Omega_G = \sqrt{\Delta^2 + \Omega^2} \quad (2.18)$$

The exact solution for these time - dependent coefficients are reduced as follows:

$$c_1(t) = e^{i\Delta t/2} \left[c_1(0) \cos\left(\frac{\Omega_G t}{2}\right) - ic_1(0) \frac{\Delta}{\Omega_G} \sin\left(\frac{\Omega_G t}{2}\right) - ic_2(0) \frac{\Omega}{\Omega_G} e^{-i\phi_L} \sin\left(\frac{\Omega_G t}{2}\right) \right] \quad (2.19)$$

$$c_2(t) = \frac{1}{e^{i\Delta t/2}} \left[-ic_1(0)e^{i\phi_L} \frac{\Omega}{\Omega_G} \sin\left(\frac{\Omega_G t}{2}\right) + c_2(0) \cos\left(\frac{\Omega_G t}{2}\right) + ic_2(0) \frac{\Delta}{\Omega_G} \sin\left(\frac{\Omega_G t}{2}\right) \right] \quad (2.20)$$

By performing a measurement of the atomic state as a function of the interaction time τ one would find that the probability of finding the atom in the states $|1\rangle$ and $|2\rangle$ periodically oscillates at frequency Ω_G :

$$P_1(\tau) = \left(\frac{\Omega \cos(\Omega_G \tau / 2)}{\Omega_G} \right)^2 \quad (2.21)$$

and

$$P_2(\tau) = \left(\frac{\Omega \sin(\Omega_G \tau / 2)}{\Omega_G} \right)^2 \quad (2.22)$$

Incorporating the scenario of an exact resonance ($\Delta = 0$), the time-dependent coefficients further simplify as:

$$c_1(t) = c_1(0) \cos(\Omega t / 2) - ic_2(0)e^{-i\phi_L} \sin(\Omega t / 2) \quad (2.23)$$

and

$$c_2(t) = c_2(0) \cos(\Omega t / 2) - ic_1(0)e^{i\phi_L} \sin(\Omega t / 2) \quad (2.24)$$

In such conditions, if a light pulse of temporal length τ is sent on an atom initially in the state $|1\rangle$ its final state at the end of the interaction becomes:

$$|\psi(\tau)\rangle = \cos\left(\frac{\Omega\tau}{2}\right) |1\rangle + e^{i(\phi_L - \frac{\pi}{2})} \sin\left(\frac{\Omega\tau}{2}\right) |2\rangle \quad (2.25)$$

All relevant and useful information arising from $|\psi(\tau)\rangle$ is listed in Table 2.1.

Temporal evolution can be described using the two eigenstates $|g, \vec{p}\rangle$ and $|e, \vec{p} + \hbar\vec{k}\rangle$ with corresponding energy levels as:

$$|1\rangle = |g, \vec{p}\rangle \rightarrow E_1 = \hbar\omega_a + \frac{|\vec{p}|^2}{2m} = \hbar\omega_1$$

$$|2\rangle = |e, \vec{p} + \hbar\vec{k}\rangle \rightarrow E_2 = \hbar\omega_b + \frac{|\vec{p} + \hbar\vec{k}|^2}{2m} = \hbar\omega_2$$

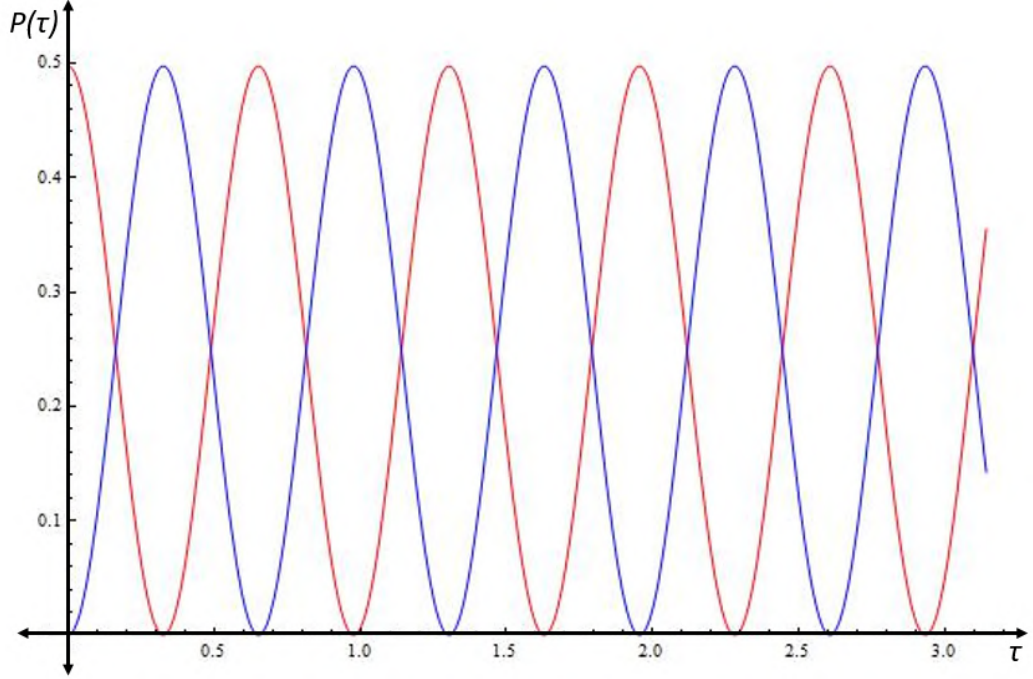


Figure 2.3: Calculated probabilities $P(\tau)$ of detecting a rubidium atom in either state $|1\rangle$ (red) or $|2\rangle$ (blue) after an interaction with a light field for a time τ , with $\Delta = 6.834$ GHz and $\Omega = 6.8$ GHz.

Pulse Type	τ	$ \psi(\tau)\rangle$	$P_1(\tau)$	$P_2(\tau)$
π	π/Ω	$e^{i(\phi_L - \frac{\pi}{2})} 2\rangle$	$(\frac{\Omega \cos(\Omega_G \pi/2\Omega)}{\Omega_G})^2$	$(\frac{\Omega \sin(\Omega_G \pi/2\Omega)}{\Omega_G})^2$
$\pi/2$	$\pi/2\Omega$	$\frac{1}{\sqrt{2}}(1\rangle + e^{i(\phi_L - \frac{\pi}{2})} 2\rangle)$	$(\frac{\Omega \cos(\Omega_G \pi/4\Omega)}{\Omega_G})^2$	$(\frac{\Omega \sin(\Omega_G \pi/4\Omega)}{\Omega_G})^2$

Table 2.1: Pulse types with their respective temporal lengths τ and population probabilities $P(\tau)$ (also see Figure 2.3). Here, $P_1(\tau)$ $P_2(\tau)$ denote population probabilities of detecting an atom in states $|1\rangle$ (red) and $|2\rangle$ respectively. Also, it is clearly visible here how π and $\pi/2$ pulses behave like mirror and beam-splitter respectively.

which implies definition of laser detuning Δ and resonant ω_0 frequencies:

$$\omega_0 = \omega_b - \omega_a = \omega_{ab} - \frac{\vec{p} \cdot \vec{k}}{m} + \frac{\hbar |\vec{k}|^2}{2m} \quad (2.26)$$

$$\Delta = \omega_L - \omega_0 = \omega_L - \left(\omega_{ab} + \frac{\vec{p} \cdot \vec{k}}{m} + \frac{\hbar |\vec{k}|^2}{2m} \right) \quad (2.27)$$

clearly showing the *Doppler effect* and the recoil terms.

2.1.2 Raman Transitions

Let us consider a three - level system with two ground state hyperfine levels $|1\rangle$ and $|2\rangle$ being coupled via a virtual intermediate state $|i\rangle$ by two lasers of angular frequencies ω_1 and ω_2 with their corresponding wavevectors as \vec{k}_1 and \vec{k}_2 .

A Raman transition with two counter-propagating laser beams of frequencies ω_1 and ω_2 is shown in Figure 2.4. Ignoring the effects from Doppler shift, the resonance condition responsible for driving a coherent Raman transition between states $|1\rangle$ and $|2\rangle$ is: $\hbar(\omega_1 - \omega_2) = E_2 - E_1$. These Raman laser beams travelling in opposite directions change the atom's momentum during the transition. The absorption of photon of a wavevector k_2 and the stimulated emission of one in the opposite direction $\vec{k}_2 \approx -\vec{k}_1$ resulting in atom experiencing two recoil kicks in the same direction. Hence, as presented in Figure 2.4, the Raman transition couples $|1, \vec{p}\rangle$ and $|2, \vec{p} + 2\hbar\vec{k}\rangle$ so that an atom in Raman interferometric scheme has a wavefunction of the form: $\psi = A|1, \vec{p}\rangle + B|2, \vec{p} + 2\hbar\vec{k}\rangle$. The Raman resonance condition ($\hbar(\omega_2 - \omega_1) = E_2 - E_1$) is sensitive to atom's velocity for counter-propagating beams providing the basis for the Raman cooling of atoms. For interferometry this velocity sensitivity is a complicating factor and we shall assume that the Raman pulses are sufficiently short: $1/\tau_{pulse} \approx \Delta v/\lambda$ ($\Delta v =$ velocity selection range width, $\tau_{pulse} =$ pulse duration, $\lambda =$ laser wavelength) to drive transitions over the whole range of velocity components along the laser beam.

Two - photon Raman transitions on a multi - level atom

Taking into account a multi-level atomic system with two well-defined energy levels, $|g\rangle$ and $|e\rangle$ (for example, the two magnetically insensitive hyperfine levels of rubidium ground state), and a virtual intermediate state $|i\rangle$. The

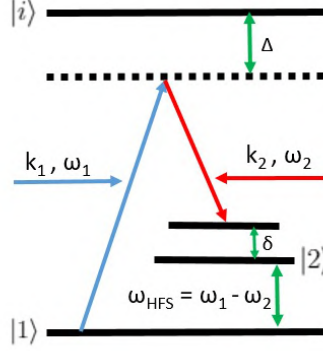


Figure 2.4: Energy levels and laser frequencies used for Raman transition.

Internal states	Energy
$ 1\rangle$	$E_1 = \hbar\omega_g + \frac{ \vec{p} ^2}{2m} = \hbar\omega_1$
$ 2\rangle$	$E_2 = \hbar\omega_e + \frac{ \vec{p} + \hbar(\vec{k}_{R1} - \vec{k}_{R2}) ^2}{2m} = \hbar\omega_2$
$ i0\rangle$	$E_{i0} = \hbar\omega_i + \frac{ \vec{p} + \hbar\vec{k}_{R1} ^2}{2m} = \hbar\omega_{i0}$
$ i2\rangle$	$E_{i2} = \hbar\omega_i + \frac{ \vec{p} + \hbar\vec{k}_{R2} ^2}{2m} = \hbar\omega_{i2}$
$ i1\rangle$	$E_{i1} = \hbar\omega_i + \frac{ \vec{p} + \hbar(2\vec{k}_{R1} - \vec{k}_{R2}) ^2}{2m} = \hbar\omega_{i1}$

Table 2.2: Calculated energy magnitudes of all the internal states for a Raman transition coupling the two ground state hyperfine levels $|1\rangle$ and $|2\rangle$.

state $|i\rangle$ represents an intermediate and a virtual state obtained as a summation over all the hyperfine levels. Electric field vectors of the two participating counter-propagating light beams in a two-photon Raman transition are:

$$\vec{E}_{R1}(\vec{r}, t) = \hat{E}_{R1,0} \cos[\vec{k}_{R1} \cdot \vec{r} - \omega_{R1}t + \phi_{R1}] \quad (2.28)$$

and

$$\vec{E}_{R2}(\vec{r}, t) = \hat{E}_{R2,0} \cos[\vec{k}_{R2} \cdot \vec{r} - \omega_{R2}t + \phi_{R2}] \quad (2.29)$$

with ω_{R1} and ω_{R2} simultaneously been acted upon the same atom.

The Hamiltonian for the described system in the electric-dipole approximation is:

$$\mathcal{H} = \sum_s \hbar\omega_s |s\rangle \langle s| - \vec{d} \cdot (\vec{E}_{R1} + \vec{E}_{R2}), \forall s = \{1, 2, i0, i2, i1\} \quad (2.30)$$

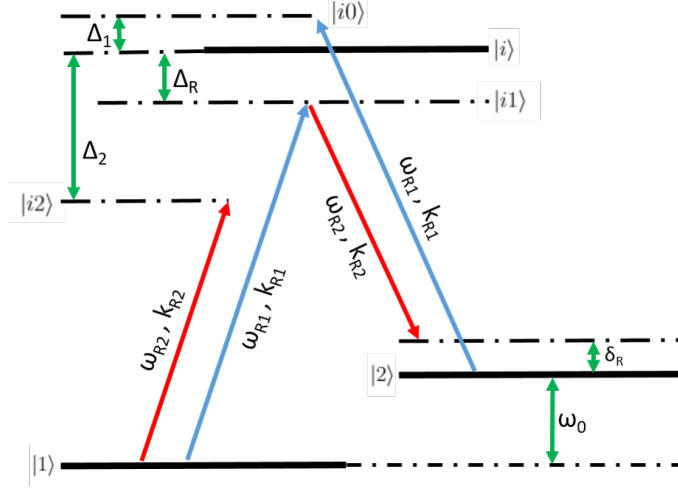


Figure 2.5: Frequency diagram of a Raman transition coupling the two ground state hyperfine levels $|1\rangle$ and $|2\rangle$ with a small detuning δ_R taking all the possible virtual intermediate states (also see Table 2.2) - $|i\rangle$, $|i0\rangle$ and $|i1\rangle$. The common detuning of the two monochromatic and coherent light fields from the direct transition is Δ_R .

which will be applied on the atomic wavefunction:

$$|\psi(t)\rangle = \sum_s c_s(t) e^{-i\omega_s t} |s\rangle \quad (2.31)$$

As per Figure 2.5:

$$\Delta_1 \text{ (detuning of light field } E_{R1}) = |2\rangle \rightarrow |i0\rangle$$

$$\Delta_2 \text{ (detuning of light field } E_{R2}) = |1\rangle \rightarrow |i2\rangle$$

$$\Delta_R \text{ (common detuning from the excited level } |i1\rangle) = |1\rangle, |2\rangle \rightarrow |i1\rangle$$

Defining the Rabi frequency induced by the laser l ($l = 1, 2$) between the states $|m\rangle$ ($m = 1, 2$) and $|n\rangle$ ($n = i0, i1, i2$) as:

$$\Omega_{mnl} = \frac{\langle n | -\vec{d} \cdot \vec{E} | m \rangle}{\hbar} \quad (2.32)$$

The time - dependent coefficients derived in the previous section are re-derived in the scenario of two - photon Raman transition under the rotating - wave approximation:

$$i\dot{c}_1(t) = c_{i0}(t) \frac{\Omega_{1i01}^*}{2} e^{i(\Delta_R t - \phi_{R1})} + c_{i2}(t) \frac{\Omega_{1i22}^*}{2} e^{i(\Delta_2 t - \phi_{R2})} \quad (2.33)$$

$$i\dot{c}_2(t) = c_{i0}(t) \frac{\Omega_{2i02}^*}{2} e^{i(\Delta_R t - \delta_R t - \phi_{R2})} + c_{i1}(t) \frac{\Omega_{1i22}^*}{2} e^{i(\Delta_2 t - \phi_{R2})} \quad (2.34)$$

$$i\dot{c}_{i0}(t) = c_1(t) \frac{\Omega_{1i01}^*}{2} e^{i(-\Delta_R t + \phi_{R1})} + c_2(t) \frac{\Omega_{2i02}^*}{2} e^{i(-\Delta_R t + \delta_R(t) + \phi_{R2})} \quad (2.35)$$

$$i\dot{c}_{i1}(t) = c_2(t) \frac{\Omega_{2i11}^*}{2} e^{i(-\Delta_1 t + \phi_{R1})} \quad (2.36)$$

$$i\dot{c}_{i2}(t) = c_1(t) \frac{\Omega_{1i22}^*}{2} e^{i(-\Delta_2 t + \phi_{R2})} \quad (2.37)$$

The three excited levels can be adiabatically eliminated [68] by integrating the three equations and taking out of the integrals the slowly varying terms, resulting in:

$$i\dot{c}_1(t) = c_1(t) \left[\frac{|\Omega_{1i01}|^2}{4\Delta_R} + \frac{|\Omega_{1i22}|^2}{4\Delta_2} \right] + c_2(t) \left[\frac{\Omega_{1i01}^* \Omega_{2i02}}{4(\Delta_R - \delta_R)} e^{-i(\phi_{R1} - \phi_{R2} - \delta_R(t))} \right] \quad (2.38)$$

$$i\dot{c}_2(t) = c_1(t) \left[\frac{\Omega_{2i02}^* \Omega_{1i01}}{4\Delta_R} e^{i(\phi_{R1} - \phi_{R2} - \delta_R t)} \right] + c_2(t) \left[\frac{|\Omega_{2i02}|^2}{4(\Delta_R - \delta_R)} + \frac{|\Omega_{2i11}|^2}{4\Delta_1} \right] \quad (2.39)$$

Let us now simplify the equations by defining the frequency light shifts of the two states, their sum and difference:

$$\Omega^{AC} = \Omega_2^{AC} + \Omega_1^{AC} \quad (2.40)$$

$$\delta^{AC} = \Omega_2^{AC} - \Omega_1^{AC} \quad (2.41)$$

where:

$$\Omega_1^{AC} = \left[\frac{|\Omega_{1i01}|^2}{4\Delta_R} + \frac{|\Omega_{1i22}|^2}{4\Delta_2} \right] \quad (2.42)$$

$$\Omega_2^{AC} = \left[\frac{|\Omega_{2i02}|^2}{4(\Delta_R - \delta_R)} + \frac{|\Omega_{2i11}|^2}{4\Delta_1} \right] \quad (2.43)$$

Introducing more effective physical parameters with respect to two - photon Raman transition:

$$\omega_{\text{eff}} = \omega_{R1} - \omega_{R2} \quad (2.44)$$

$$\vec{k}_{\text{eff}} = \vec{k}_{R1} - \vec{k}_{R2} = \frac{\vec{k}_{R1}}{|\vec{k}_{R1}|} (|\vec{k}_{R1}| + |\vec{k}_{R2}|) \quad (2.45)$$

$$\phi_{\text{eff}} = \phi_{R1} - \phi_{R2} \quad (2.46)$$

$$\Omega_{\text{eff}} = \frac{\Omega_{1i01}\Omega_{2i02}}{2\Delta_R} \quad (2.47)$$

$$\Omega_{G,\text{eff}} = \sqrt{\Omega_{\text{eff}}^2 + (\delta_R - \delta^{AC})^2} \quad (2.48)$$

Considering $\delta_R \ll \Delta_R$, then one has:

$$i\dot{c}_1(t) = c_1(t)\Omega_1^{AC} + c_2(t)\frac{\Omega_{\text{eff}}^*}{2}e^{-i(\phi_{\text{eff}} - \delta_R(t))} \quad (2.49)$$

$$i\dot{c}_2(t) = c_1(t)\frac{\Omega_{\text{eff}}^*}{2}e^{i(\phi_{\text{eff}} - \delta_R(t))} + c_2(t)\Omega_2^{AC} \quad (2.50)$$

In order to remove time - dependency in the off - diagonal terms, we rotate the coefficients in a way:

$$c_1(t) = s_1(t)e^{it\frac{(\delta_R - \Omega^{AC})}{2}} \quad (2.51)$$

$$c_2(t) = s_2(t)e^{-it\frac{(\delta_R + \Omega^{AC})}{2}} \quad (2.52)$$

resulting in:

$$i\dot{s}_1(t) = \frac{1}{2} \left[s_1(t)(\delta_R - \delta^{AC}) + s_2(t)\Omega_{\text{eff}}e^{-i\phi_{\text{eff}}} \right]$$

and

$$i\dot{s}_2(t) = \frac{1}{2} \left[-s_2(t)(\delta_R - \delta^{AC}) + s_1(t)\Omega_{\text{eff}}e^{i\phi_{\text{eff}}} \right]$$

Solving the above system of time - dependent differential equations gives the following general expression for the non - rotated terms of the atomic

wavefunction:

$$s_1(t) = \left\{ c_1(0) \left[\cos\left(\frac{\Omega_{G,\text{eff}}t}{2}\right) - ic_1(0) \frac{\delta_R - \delta^{AC}}{\Omega_{G,\text{eff}}} \sin\left(\frac{\Omega_{G,\text{eff}}t}{2}\right) \right] + c_2(0)e^{-i\phi_{\text{eff}}} \left[-i \frac{\Omega_{\text{eff}}}{\Omega_{G,\text{eff}}} \sin\left(\frac{\Omega_{G,\text{eff}}t}{2}\right) \right] \right\} \quad (2.53)$$

and

$$s_2(t) = \left\{ c_1(0)e^{i\phi_{\text{eff}}} \left[-i \frac{\Omega_{\text{eff}}}{\Omega_{G,\text{eff}}} \sin\left(\frac{\Omega_{G,\text{eff}}t}{2}\right) \right] + c_2(0) \left[\cos\left(\frac{\Omega_{G,\text{eff}}t}{2}\right) + ic_2(0) \frac{\delta_R - \delta^{AC}}{\Omega_{G,\text{eff}}} \sin\left(\frac{\Omega_{G,\text{eff}}t}{2}\right) \right] \right\} \quad (2.54)$$

Considering a laser pulse having a temporal length τ , phase shifts and the momenta transferred resulting from the transitions are:

Momentum state transitions	Acquired phase magnitudes
$ g, \vec{p}\rangle \rightarrow g, \vec{p}\rangle$	$(\tau/2)(\delta_R - \Omega^{AC})$
$ g, \vec{p}\rangle \rightarrow e, \vec{p} + \hbar\vec{k}\rangle$	$\phi_{eff} - \frac{\pi}{2} + (\tau/2)(-\delta_R - \Omega^{AC})$
$ e, \vec{p} + \hbar\vec{k}\rangle \rightarrow g, \vec{p}\rangle$	$-\phi_{eff} - \frac{\pi}{2} + (\tau/2)(\delta_R - \Omega^{AC})$
$ e, \vec{p} + \hbar\vec{k}\rangle \rightarrow e, \vec{p} + \hbar\vec{k}\rangle$	$(\tau/2)(-\delta_R - \Omega^{AC})$

2.1.3 Phase Shift Calculation: Mach - Zehnder Raman Atom Interferometer

In this Section, we study a complete interferometric sequence (Figure 2.6) with Raman pulses to evaluate the phase shifts imprinted on the atom's wavefunction as it traverses its path in time $2T$. This interferometric sequence is equivalent to a set of two consecutive identical Ramsey sequences ($\tau - \tau$), that results in a non - destructive interference of atoms.

Using the results (from previous section) of the phases acquired during different momentum transfers, the total phases across two paths acquired due to the π and $\pi/2$ laser pulses (labelled with an effective wavevector k_{eff}) with temporal lengths respectively being 2τ and τ are:

Path - I (Figure 2.6): $|g, \vec{p}\rangle \rightarrow |g, \vec{p}\rangle \rightarrow |e, \vec{p} + \hbar\vec{k}_{\text{eff}}\rangle \rightarrow |g, \vec{p}\rangle$:

$$\begin{aligned} \phi_{\text{Path-I}} = & (\tau/2)(\delta_R - \Omega^{AC}) + \phi_{\text{eff}}^{T-\tau} - \frac{\pi}{2} + (2\tau/2)(-\delta_R - \Omega^{AC}) \\ & - \phi_{\text{eff}}^{2T-\tau} - \frac{\pi}{2} + (\tau/2)(\delta_R - \Omega^{AC}) \end{aligned} \quad (2.55)$$

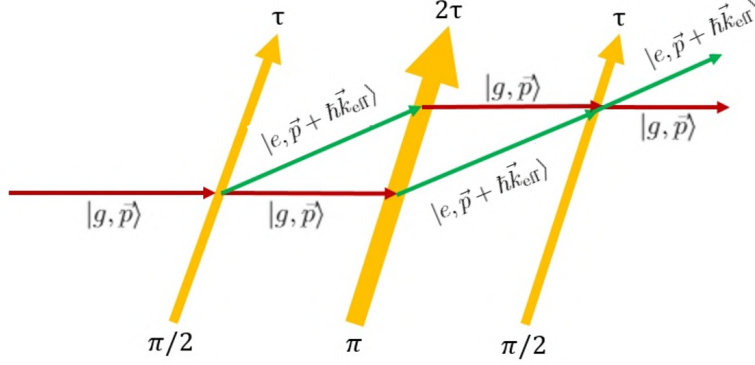


Figure 2.6: Schematic of a Mach - Zehnder atom interferometer.

Path - II (Figure 2.6): $|g, \vec{p}\rangle \rightarrow |e, \vec{p} + \hbar \vec{k}_{\text{eff}}\rangle \rightarrow |g, \vec{p}\rangle \rightarrow |g, \vec{p}\rangle$:

$$\begin{aligned} \phi_{\text{Path-II}} = \phi_{\text{eff}}^0 - \frac{\pi}{2} + (\tau/2)(-\delta_R - \Omega^{AC}) - \phi_{\text{eff}}^{T-\tau} - \frac{\pi}{2} \\ + (2\tau/2)(\delta_R - \Omega^{AC}) + (\tau/2)(\delta_R - \Omega^{AC}) \end{aligned} \quad (2.56)$$

Complete phase difference in Mach - Zehnder interferometric scheme is:

$$\Delta\phi = \phi_{\text{eff}}^{2T-\tau} - 2\phi_{\text{eff}}^{T-\tau} + \phi_{\text{eff}}^0 + \delta_R\tau \quad (2.57)$$

The above equation represents the complete phase difference for a spatially localized wavepacket, that wavepacket itself being a coherent sum over momentum states. This is so because it is clear in equation 2.57 that the resulting phase shift is independent of momentum. Moreover, $\Delta\phi$ can be varied by any accelerated motion of the atom relative to the wavefronts of the Raman beams or by any relative variation between the atomic frequency and the Raman frequency difference.

Gravity Gradiometer: Freely - falling Raman Atom Interferometer

Considering acceleration due to gravity uniform in our experimental region, we can write:

$$v_z(t) = v_z(0) - gt \quad (2.58)$$

If we consider two atomic samples in free fall, simultaneously interrogated by the same electromagnetic pulses, we can obtain a gradiometer, i.e. an apparatus which is able to measure the difference in gravitational acceleration

between two points. In this case, the difference of the phase shifts of the two simultaneous interferometers, depends from the relative gravitational acceleration difference felt by the couple of atomic clouds. Considering two different atomic clouds separated by a baseline with initial conditions: $z(0) = 0$ and $v(0) = v_0$, we can write phase shifts in the basis of time and momentum transfers as follows:

$$\phi(|g, \vec{p}\rangle \rightarrow |g, \vec{p}\rangle, 0) = 0 \quad (2.59)$$

$$\phi(|g, \vec{p}\rangle \rightarrow |e, \vec{p} + \hbar\vec{k}\rangle, T) = k_{\text{eff}}(v_0T - gT^2/2) \quad (2.60)$$

$$\phi(|e, \vec{p} + \hbar\vec{k}\rangle \rightarrow |g, \vec{p}\rangle, T) = k_{\text{eff}}(v_0T - gT^2/2 + \hbar k_{\text{eff}}T/m) \quad (2.61)$$

$$\phi(|e, \vec{p} + \hbar\vec{k}\rangle \rightarrow |e, \vec{p} + \hbar\vec{k}\rangle, 2T) = k_{\text{eff}}(2v_0T - 2gT^2 + \hbar k_{\text{eff}}T/m) \quad (2.62)$$

Complete phase shift becomes:

$$\Delta\phi_g = -k_{\text{eff}}gT^2 \quad (2.63)$$

In common atom gravimeters the acceleration is not directly determined from the measured phase shift, but determining the frequency ramp that exactly compensates the Doppler shift induced by gravity during the free fall.

2.2 Applications of Atom Interferometry

Atom Interferometry presents a colossal potential in high precision measurements in the contexts of both pure and engineering sciences. The major areas of potential applications are internal and gravitational measurements and related effects, tests of fundamental principles in physics, experimental verifications for atoms in quantum regimes and revealing the unknown properties of atoms at ultracold temperatures.

It is interesting to note that for nearly every optical phenomena lying in a classical regime, there exists an analogue at atomic scale. In atom interferometry, the experiments depict spatial separation of an atomic wavefunction, which wavefunctions after interference contain the information about the properties of atoms. In case if an ensemble of atoms are moving along the gravity axis, then the resulting interference pattern will reveal the information about atoms under the influence of gravity, henceforth containing the information about gravitational acceleration of earth [35, 69].

2.2.1 Embarking with new ideas from research in Atom Interferometry

In this Section, we will discuss the following aspects briefly so as to establish the recent research results indicating a scope of new research ideas in this emerging field of atom interferometry:

- Quantum violation of Weak - Equivalence Principle
- Measuring the gravitational acceleration with precision matter - wave velocimetry
- Macroscopic coherence in the measurement of Newtonian Gravitational constant

Quantum violation of Weak - Equivalence Principle

Einstein's weak equivalence principle states that in all inertial frames of reference, the inertial and gravitational masses are equivalent. Experimentally, this can be tested by preparing atomic samples with different states, and then allowing them to fall freely under the gravitational influence. We shall describe the motivation for physics behind the violation of weak equivalence principle at a quantum scale.

Starting with the effective mass of photon [70], we have:

$$M_{eff} = \frac{h\nu}{c^2} = \frac{h}{c\lambda}$$

From Newtonian mechanics, the uncertainty in acceleration due to gravity is:

$$\Delta a_g = \frac{GM_{eff}}{r_{eff}^2} = \frac{Gh}{c\lambda r_{eff}^2}$$

and the corresponding uncertainty change in position is:

$$\Delta x_g = \Delta a_g t_{eff}^2 = \frac{Gh}{c\lambda} \times \frac{t_{eff}^2}{r_{eff}^2} = \frac{Gh}{\lambda c^3}$$

This gives rise to the equation of generalized uncertainty principle:

$$\Delta x = \frac{h}{\Delta p} + \frac{Gh\Delta p}{c^3\lambda}$$

The second term in this generalized form of uncertainty principle becomes very crucial when the length scales are very small or are of the order of

Planck's length. This generalized uncertainty principle has been rigorously incorporated by Brukner and Zych [71] to define the inertial and gravitational mass - energy operators:

$$\hat{M}_\alpha = m_\alpha \hat{I} + \frac{\hat{H}_\alpha}{c^2}, \forall \alpha \in \{i, g\}$$

In the above equation, the subscript labels i and g denote inertial and gravitational mass - energy operators respectively. Performing a simple product between the two operators \hat{M}_g and \hat{M}_i^{-1} yields:

$$\hat{M}_g \hat{M}_i^{-1} = m_g m_i \hat{I} + \frac{m_g \hat{H}_i^{-1}}{c^2} + \frac{m_i \hat{H}_g}{c^2} + \mathcal{O}\left(\frac{1}{c^4}\right)$$

which is clearly unequal to unity, henceforth violating weak equivalence principle at a quantum scale along with an indication of off - diagonal terms present in this equation. These off - diagonal terms are:

$$\hat{M}_g \hat{M}_i^{-1} = \left(m_g \hat{I} + \frac{\hat{H}_g}{c^2} \right) \left(m_i \hat{I} + \frac{\hat{H}_i^{-1}}{c^2} \right)$$

Hitherto, for quantum Weak Equivalence Principle violation, the centre - of - motion acceleration becomes:

$$a = \hat{M}_g \hat{M}_i^{-1} g$$

In 2015, a free - fall experiment of ultracold atomic samples using a combination of large momentum transfer atom interferometer operating under Mach - Zehnder interferometric scheme and gravity gradiometer was implemented [72], which resulted in gravimeter sensitivity of 4×10^{-8} for ^{88}Sr atoms. There is a scope of creating optically separated states using large momentum transfer atom interferometer as WEP violation will increase with the energy difference between internal levels, which makes it advantageous to be used for the states with an energy gap greater than the hyperfine splitting. Also, In different research groups, atom-based tests of the Einstein's equivalence principle are flourishing [3, 4, 5, 6, 48].

Measuring the gravitational acceleration with precision matter - wave velocimetry

Recently, a new method [35] was demonstrated in our laboratory (experimental apparatus detailed in [38, 73]) to perform an interferometric measurement for g without any need for a vibration isolation system or post-corrections

based on seismometer data monitoring the residual accelerations at the sensor head with cold rubidium atoms, and was compared with a measurement done in our laboratory in 2012 [74]. The motivation behind performing this experiment comes from the vibration noise of the measurement platform (which remains undistinguished from the relevant acceleration signal) arising as one of the crucial limitation [75] of an atomic gravimeter. In this measurement of acceleration due to gravity, two successive Ramsey interferometric sequences were used to explore the velocity variation of freely falling cold rubidium atom samples.

Our instrument has a fractional stability of 9×10^{-6} at 1 s of integration time, which is one order of magnitude better than a standard Mach-Zehnder interferometer (operated without any vibration isolation or applied post-correction). The short term stability of the instrument is limited by both the interrogation and the free - fall times.

The long term stability and accuracy depend on the velocity variations introduced by the light shift during the preparation phase. The free-fall time and the interrogation time are both strictly related to the temperature of the atomic sample. These freely falling cold atomic cloud samples are prepared in a narrow velocity distribution [76, 77]. Therefore, ultracold atom sources become highly beneficial for several reasons: they increase the efficiency of the velocity selection process (down to the pK regime) while preserving high atom numbers; allowing longer free evolution times; providing atomic samples with larger coherence lengths that can be probed in longer interferometers with limited loss of contrast.

This method shows very interesting perspectives for being further developed towards state-of-the-art performance and beyond.

Macroscopic coherence in measurement of Newtonian Gravitational constant

When an interferometer is operated in a gravitational field, it is in an accelerated frame. A quantity which is independent of a frame of reference is important - this is second partial derivative of the gravitational potential, or, the space-time curvature. A particle's wavefunction acquires a phase shift due to curvature. Theorizing is one thing, but measuring such delicate effect is quite another. In a beautiful experiment, Kasevich's group measured the tidal force - a measure of spacetime curvature, on the wavefunction of an individual particles inside an atom interferometer. This experiment was inspired by the experiment performed at Department of Physics and Astronomy, University of Florence [48] where differential effect of curvature on two separated atom interferometers was measured.

Tidal force was generated by movable external source masses. With this, the effect of Earth's gravity is eliminated by comparing the interference fringes of the interferometer with the ones of another interferometer located about 30 cm from the source masses. To confirm this, they varied the separation d between the interferometer arms and showed that the signal from curvature is proportional to d^2 . This experiment was performed in a 10 m high fountain- the height corresponding to a free fall time of about 2.8 s, enough to perform interferometry. Momentum of about one hundred photons separated the spatial components of each individual atom's wavefunction by ≈ 30 cm. While one of these two partial wavefunctions formed the *sensor* interferometer, the other formed the *reference* interferometer.

The differential acceleration was measured to a staggering precision of 0.6 nm/s^2 with sensitivity $5 \times 10^{-9} \text{ m/s}^2/\sqrt{\text{Hz}}$. The curvature generated by the source masses (84 kg lead) was about 1 radian phase shift. Experimental demonstration of effect of curvature on the wavefunction of individual particles, conclusively established coherence over a macroscopic scale.

These remarkable advances have paved the way of the usage of atom interferometry in the future detection of gravitational waves.

Chapter 3

Experimental Sequence

3.1 Outline of the new experimental scheme

The complete experimental scheme highlights two major steps - phase noise minimization in the interferometric signal in the presence of gravity and cancellation of ambient gravity gradients with implementation of a novel design of source masses.

As shown in Figure 3.1, the two cold atomic cloud samples are trapped and cooled in a magneto-optical trap (MOT) and sequentially launched towards the interferometric region after they are prepared in $|F = 1, m_F = 0\rangle$ and $|F = 2, m_F = 0\rangle$ states (following dipole - allowed transition: $5S_{1/2} \rightarrow 6P_{3/2}$ with $\lambda = 421.5$ nm) using juggling mechanism. The first step to minimize the phase noise in the gravimetric signal is achieved by adding an external-well-controlled relative phase shift in order to produce a differential phase of $\pi/2$, therefore satisfying the required condition [17] for phase noise minimization, i.e., $\Delta\phi \approx \pi/2$.

A measurement of the local gravity gradient is performed by Raman interferometry. The gravitational perturbation on the atomic trajectories produced by a well-known set of source masses can be accurately modelled. In previous works [16, 17, 20, 48], the Raman gradiometer was used to determine G performing a further differential measurement between the gradiometric signals in two different source mass configurations, namely CLOSE and FAR. A new approach to building a new design for the high precision measurements of atom interferometry is described in Section 3.1.2.

3.1.1 *Step - I: Phase Noise Minimization*

Consider an atomic fountain tube (Figure 3.1) consisting of a pair of thermal clouds sequentially launched from a three - dimensional magneto - optical

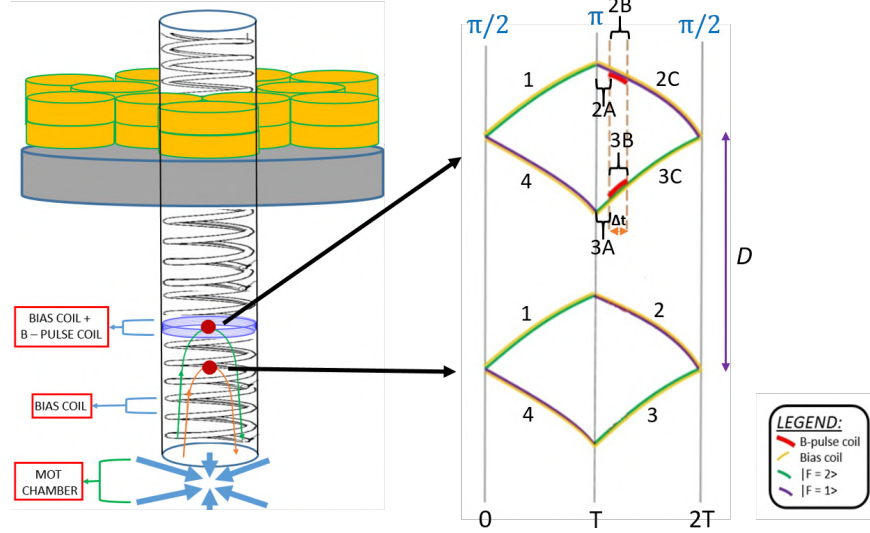


Figure 3.1: LEFT: Overview of the experimental apparatus, RIGHT: Schematic of the modified Mach - Zehnder interferometric sequence for phase noise minimization with arm labelled in accordance with equations 3.1, 3.2 and 3.3.

trap. This sequential launching is achieved by standard moving optical molasses technique along with a simultaneous interrogation by a sequence of three counter - propagating Raman pulses, forming a traditional Mach - Zehnder interferometric sequence.

Now we will describe the modification to be done in the experimental sequence to fulfill our objective. Firstly, a finite - solenoidal coil is wrapped along the altitude axis of the hollow cylindrical design of the interferometric tube covering complete altitude in a helical trend. This coil generates a bias magnetic field which helps in defining quantization axis for the individual atoms inside the atomic cloud samples. This bias magnetic field remains switched ON throughout the complete experimental session. Secondly, during the second-half time period of the interferometric scheme, i.e., from T to $2T$, an extra finite - solenoidal coil other than the bias coil should produce another magnetic field from a very small time - window $\Delta t \in [4 \text{ ms}, 10 \text{ ms}]$. For this to be implemented, an extra finite - solenoidal coil of much smaller size than the bias coil is wound around the tube in the vicinity of the apogee point of the upper atomic thermal cloud sample. In this thesis, we will refer to the magnetic field coil producing bias magnetic field throughout the complete experimental session as *bias coil* and the extra finite - solenoidal

coil remaining active for a very small time - window $\Delta t \in [4 \text{ ms}, 10 \text{ ms}]$, as *B-pulse coil*. The B-pulse coil has to be positioned precisely in a way that the centre of mass of the upper thermal atomic cloud sample must coincide with the centre of the B-pulse coil which lies at the midway of the helix. We have to note that for this implementation to have an outcome of triumph, it is necessary that the flow of current inside both the coils is in the same direction and both the atomic cloud samples are prepared in magnetically-insensitive hyperfine states, so that there must be no phase contribution during interferometric sequence from the first-order Zeeman effect (because in first-order Zeeman shifts, the hyperfine energy level difference is directly proportional to the azimuthal quantum number of that magnetically-sensitive hyperfine state). Thanks to the second-order Zeeman shift, because in this case, the energy difference between the hyperfine levels is proportional to the square of the magnetic field and is independent of the magnetic azimuthal quantum number. When one applies this scheme of phase - noise minimization in a traditional Mach - Zehnder gravimetric sequence, the modified sequence becomes as shown in Figure 3.1 (right).

Let T_P be the B-pulse time duration, \bar{T}_{AP} is the average time at which the upper atomic thermal cloud attains its point of apogee, T be the half-time of the experimental sequence and B_{bias} be the bias magnetic field that remains activated till the end of the experimental sequence.

An atomic cloud experiences splitting of its wavefunction due to an illumination from a pair of laser beams from opposite directions serving as a $\pi/2$ -pulse. This one wavefunction (of our atomic cloud) which is now in superposition of two states having equal amplitudes which are allowed to evolve spatially for half - time T of the experimental sequence. After half - time T , the two split wavefunctions are irradiated by π -pulse, resulting in steering of trajectories of matter waves accompanied by a mirror exchange of two different momentum states. After π -pulse is applied at time T , the two arms begin to freely evolve again from time T to $\bar{T}_{AP} - T_P/2$. Till now, from time 0 to $\bar{T}_{AP} - T_P/2$, the interferometer arms are only affected by the presence of bias coil magnetic field B_{bias} . Now, from $\bar{T}_{AP} - T_P/2$ to $\bar{T}_{AP} + T_P/2$, the arms are perturbed by the resultant magnetic field modulus B_T (produced from bias and B-pulse coils) for a short time window $\Delta t \in [4 \text{ ms}, 10 \text{ ms}]$. Finally, in the time left, from $\bar{T}_{AP} + T_P/2$ to $2T$, the arms of the upper interferometer are only affected by the magnetic field of the bias coil. Simultaneously, in the same timeline, the lower atomic thermal cloud sample only experiences the effects of bias coil. The phases acquired (due to second-order Zeeman effect) across every arm (arms marked in right - side of Figure 3.1) of both

interferometers is calculated as follows:

$$\Delta\phi = \phi_{UP} - \phi_{LOW} = 2\pi\alpha \left(\oint B_T^2|_{UP} dT - \oint B_T^2|_{DW} dT \right) \quad (3.1)$$

where ϕ_{UP} is the upper atom - interferometer and ϕ_{LOW} is the lower atom - interferometer running in the time circuit from $t = 0$ to $t = 2T$. ϕ_{UP} and ϕ_{DW} are expressed as:

$$\phi_{UP} = (\phi_1^{UP} + \phi_{2A}^{UP} + \phi_{2B}^{UP} + \phi_{2C}^{UP}) - (\phi_{3A}^{UP} + \phi_{3B}^{UP} + \phi_{3C}^{UP} + \phi_4^{UP}) \quad (3.2)$$

$$\phi_{LOW} = (\phi_1^{LOW} + \phi_2^{LOW}) - (\phi_3^{LOW} + \phi_4^{LOW}) \quad (3.3)$$

Phase acquired in each arm is expressed by breaking down the contour integral of equation 3.1 into different time domains:

$$\begin{aligned} \phi_1^{UP} &= \pi\alpha \int_{0|F=1}^T B_{bias}^2 dT \\ \phi_{2A}^{UP} &= -\pi\alpha \int_{T|F=2}^{\bar{T}_{AP}-T_P/2} B_{bias}^2 dT \\ \phi_{2B}^{UP} &= -\pi\alpha \int_{\bar{T}_{AP}-T_P/2|F=2}^{\bar{T}_{AP}+T_P/2} B_T^2 dT \\ \phi_{2C}^{UP} &= -\pi\alpha \int_{\bar{T}_{AP}+T_P/2|F=2}^{2T} B_{bias}^2 dT \\ \phi_{3A}^{UP} &= \pi\alpha \int_{T|F=1}^{\bar{T}_{AP}-T_P/2} B_{bias}^2 dT \\ \phi_{3B}^{UP} &= \pi\alpha \int_{\bar{T}_{AP}-T_P/2|F=1}^{\bar{T}_{AP}+T_P/2} B_T^2 dT \\ \phi_{3C}^{UP} &= \pi\alpha \int_{\bar{T}_{AP}+T_P/2|F=1}^{2T} B_{bias}^2 dT \\ \phi_4^{UP} &= -\pi\alpha \int_{0|F=2}^T B_{bias}^2 dT \end{aligned}$$

Experimentally, the lower interferometer will also experience some leakage of the resultant magnetic field B_T from the upper interferometer for $\Delta t \in$

[4 ms, 10 ms], but this leakage is negligible as the length of the B-pulse coil along the fountain axis is 23 cm. Henceforth, the lower atomic cloud does not experience a significant amount of jitter from this resultant magnetic field leakage as the baseline between the two atomic clouds is 23 cm, but, in our simulation we have accounted this leakage (from the upper interferometer) in order to have a realistic model of the our apparatus yielding as precise results as possible. Therefore, the phases acquired in each arm of the lower interferometer from timeline 0 to $2T$ are written as follows:

$$\begin{aligned}\phi_1^{LOW} &= \pi\alpha \int_{0|F=1\rangle}^T B_{bias}^2 dT \\ \phi_2^{LOW} &= -\pi\alpha \int_{T|F=2\rangle}^{2T} B_{bias}^2 dT \\ \phi_3^{LOW} &= \pi\alpha \int_{T|F=1\rangle}^{2T} B_{bias}^2 dT \\ \phi_4^{LOW} &= -\pi\alpha \int_{T|F=2\rangle}^{2T} B_{bias}^2 dT\end{aligned}$$

3.1.2 Step - II: Gravity Gradient Cancellation

As shown in Figure 3.2, sixteen stacked cylindrical disks of sintered tungsten forming two concentric hexagonal enclosures supported by torus - shaped aluminium platform serves as a new design of source masses, capable of generating linear gravitational acceleration profiles. There is another useful design presented in this thesis which accounts as another configuration of source masses prepared using copper (with different geometrical arrangement) also being capable of producing linear profiles of acceleration due to gravity. Both of these configurations are explained in detail in Chapter 5. In the earlier works [16, 17, 20], the double differential measurement between the phases in the FAR and CLOSE configurations led to an estimate in the value of universal gravitational constant G [16], whereas the FAR and CLOSE configurations in our new design are defined as the whole system of source masses with platform being away from the ground and lying close to the ground respectively.

In this thesis, performing a virtual realization incorporating new designs of source masses was one of the important tasks, leading to production of real gravity gradients then compensated with a high precision. The geometry of source masses plays a vital role in producing the resultant gravitational potential which becomes a contributing factor for the phase evolving from the

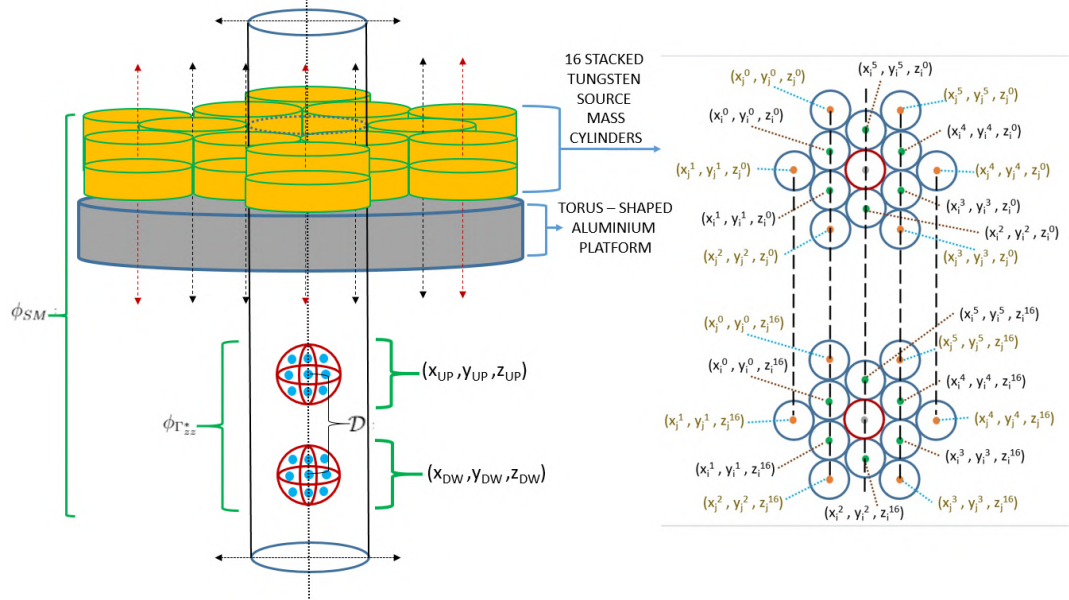


Figure 3.2: LEFT: Two atomic clouds separated by a vertical-separation distance \mathcal{D} producing phases from fictitious gravity gradient $\phi_{\Gamma_{zz}^*}$, with the phases ϕ_{SM} arising from the geometrical arrangement of source masses and the total gravitational potential of one of the new designs of the source masses, RIGHT: Geometric arrangement of source masses with labelled coordinates, the labelled coordinates are calculated in Chapter 5.

ambient gravity gradient. Generalized coordinates of every element in this configuration of source masses are calculated and then reported in Chapter 5. Here, we have performed series of simulations so as to cancel the real gravity gradient from fictitiously produced gravity gradient. The resulting negligible difference between the phase produced by the novel designs of source masses and the phase produced due to the action of fictitious gravity gradient is labelled as *residual phase* (and denoted as ϕ_R) in this thesis. This fictitious gravity gradient is measured by the interferometric phase, which is produced by slightly changing the wavelength of the second laser pulse (which happens to be π -pulse as per our pulse sequence).

The event-timeline of the experimental scheme with some limited ongoing mathematics behind the phase production is now described as follows. Here, we only describe the event-timeline considering the first configuration (tungsten source masses with aluminium platform) because it has a geometry complicated as compared to the other source mass design of interest (torus-shaped copper block).

From starting time of the experimental sequence, i.e., at $t = 0$ to the ending time, i.e., at $t = 2T$, the source masses with and without platform follow the same equations of trajectory as the atomic clouds. Now, at this point we are looking at the phases produced due to the design of the source masses, which come from the gravitational potential generated by the novel system of source masses. Mathematically speaking, total gravitational potential experienced by single atoms due to two hexagonal concentric rings $i = 0$ and $i = 1$ in one gravimeter with absence of platform is:

$$U(x-x_i, y-y_i, z-z_i) = U(x-x_0, y-y_0, z-z_0) + U(x-x_1, y-y_1, z-z_1) \quad (3.4)$$

such that:

$$U(x-x_0, y-y_0, z-z_0) = \sum_{n=1}^{16} \sum_{k=0}^5 U(x-x_0^k, y-y_0^k, z-z_0^n) \quad (3.5)$$

and,

$$U(x-x_1, y-y_1, z-z_1) = \sum_{n=1}^{16} \sum_{k=0}^5 U(x-x_1^k, y-y_1^k, z-z_1^n) \quad (3.6)$$

where the labels $i = 0$ and $i = 1$ respectively indicate one complete inner and outer hexagonal contour created due to arrangement of cylindrical tungsten source masses, k labels the hexagonal arrangement formed by cylindrical source masses and n labels a tower of source mass cylinders stacked one above the other, 16 in total. Also, we know that the phases are dependent on the gravitational potential of the whole system of source masses, implying:

$$\begin{aligned} \phi_{SM} = & \frac{m_{Rb}}{\hbar} \oint U_{UP}(x-x_i, y-y_i, z-z_i) dt \\ & - \frac{m_{Rb}}{\hbar} \oint U_{DW}(x-x_i, y-y_i, z-z_i) dt \end{aligned} \quad (3.7)$$

where ϕ_{SM} is the phase imprinted on atoms from the effect of gravitational potential of the source masses from time $t = 0$ and $t = 2T$. In the above equation, U_{UP} and U_{DW} are gravitational potentials experienced by the upper and lower atomic cloud trajectories from one single atom - interferometer. And, both U_{UP} and U_{DW} take their mathematical representations from equation 3.4. To include the geometry of the platform, the gravitational potential of the torus - shaped platform U_P is also included:

$$\begin{aligned} \phi_{SM} = & \frac{m_{Rb}}{\hbar} \oint U_{UP}^{TOT}(x-x_i, y-y_i, z-z_i) dt \\ & - \frac{m_{Rb}}{\hbar} \oint U_{DW}^{TOT}(x-x_i, y-y_i, z-z_i) dt \end{aligned} \quad (3.8)$$

where,

$$U^{TOT} = U + U_P \quad (3.9)$$

In the same timeline, from $t = 0$ to $t = 2T$, phases resulting due to the fictitious gravity gradient are produced at $t = T$, by manipulating two - photon wavevector of π -pulse. These phases are proportional to the distance which marks the difference between centre of masses of both the clouds separated vertically inside the gravity gradiometer by a finite distance. Basically, the phase gradient over the fixed baseline d between the centre of mass coordinates of the two clouds can be written as a function of phase (single - valued phase, not a Monte Carlo) of two individual atoms located at the centre of the clouds as:

$$\nabla\phi = \frac{\phi_{SM}(x_{UP}^{CM}, y_{UP}^{CM}, z_{UP}^{CM}) - \phi_{SM}(x_{DW}^{CM}, y_{DW}^{CM}, z_{DW}^{CM})}{d} \quad (3.10)$$

Now, remembering the fact that there is an ensemble of atoms forming a thermal cloud, with each atom exhibiting its motion along each axis, resulting in calibration of baseline as:

$$\mathcal{D} = (z_{UP} - z_{DW}) + (v_z^{UP} - v_z^{DW})T \quad (3.11)$$

At $t = T$, the phases due to fictitious gravity gradient are produced from:

$$\phi_{\Gamma_{zz}^*} = \mathcal{D}\nabla\phi \quad (3.12)$$

Cancellation of gravity gradients marks from the occurrence of residual phase at $t = 2T$:

$$\phi_R = \phi_{SM} - \phi_{\Gamma_{zz}^*} \quad (3.13)$$

In Chapter 5, we report a precise compensation of gravity gradients with a relative accuracy of 10^{-6} , with the Monte Carlo simulation for this virtual realization being provided in the Appendix of this thesis.

Chapter 4

Magnetic Fields: Phase Noise Minimization and 2D - MOT

4.1 Introduction to Phase Noise Minimization

Now we know that an extra finite - solenoidal coil with a magnetic field (value different than the magnitude of the bias field) has to be applied only on the second part of the atom interferometer. This will acquire the desired magnitude of phase shift. As a consequence, it will split the energy levels due to the second - order Zeeman effect (which is explained in the next section). Speaking in the simplest way, the phase difference in the experimental sequence is given as:

$$\Delta\phi = \phi_1 - \phi_2 \tag{4.1}$$

where ϕ_1 and ϕ_2 are the two phases produced by the two identical cold atomic cloud samples (separated by a vertical distance d) having states placed in magnetically - insensitive hyperfine states for our case of chosen wavelength: $\lambda = 421.5$ nm marking a dipole-allowed transition $5S_{1/2} \rightarrow 6P_{3/2}$ of ^{87}Rb . These two atomic clouds are located at two different positions across the fountain axis of the atomic fountain tower. In order to reduce the sensitivity to external and uncontrolled magnetic fields, the two interferometers are operated on atoms in the magnetically - insensitive $m_F = 0$ state. Now, using the fact that this solenoidal coil generates a magnetic field for a finite length, we can write these phases ϕ_1 and ϕ_2 for two different positions of these two clouds z_1 and z_2 as follows:

$$\phi_1 = 2\pi\alpha B_z'^2(z_1)\Delta t \tag{4.2}$$

$$\phi_2 = 2\pi\alpha B'_z{}^2(z_2)\Delta t \quad (4.3)$$

where:

$$B'_z(z_1) = \frac{\mu_0 n I}{2} \left[\frac{(z_1 + L/2)}{\sqrt{(z_1 + L/2)^2 + R^2}} - \frac{(z_1 - L/2)}{\sqrt{(z_1 - L/2)^2 + R^2}} \right] \quad (4.4)$$

$$B'_z(z_1) = \frac{\mu_0 n I \mathcal{B}_{z_1}}{2}$$

and,

$$B'_z(z_2) = \frac{\mu_0 n I}{2} \left[\frac{(z_2 + L/2 - d)}{\sqrt{(z_2 + L/2 - d)^2 + R^2}} - \frac{(z_2 - L/2 - d)}{\sqrt{(z_2 - L/2 - d)^2 + R^2}} \right] \quad (4.5)$$

$$B'_z(z_2) = \frac{\mu_0 n I \mathcal{B}_{z_2}}{2}$$

which gives:

$$\Delta\phi(z_1, z_2) = \frac{2\pi\alpha\mu_0^2 n^2 I^2 \Delta t}{4} [\mathcal{B}_{z_1}^2(z_1) - \mathcal{B}_{z_2}^2(z_2)] \quad (4.6)$$

Here in equations 4.4 and 4.5, for this moment we have assumed simplified algebraic expressions of magnetic fields only along the axis of gravity. But in our simulations, we have incorporated a much more mathematically complicated expression possessing non-zero X, Y and Z magnetic field components (Section 4.8). This incorporates the dynamics of atoms in three-dimensions.

As per previously done research [17], the required phase noise minimization for an interferometric signal in the presence of gravity yields a condition, which is: $\Delta\phi \approx \pi/2$. For example, if we calculate the other relevant parameters by fixing $\Delta\phi \approx \pi/2$ and $\Delta t = 5$ ms, then the above equation reduces to:

$$\Delta\phi = \kappa_{\pi/2}(\Delta\mathcal{B}(z_1, z_2)) \quad (4.7)$$

where $\kappa_{\pi/2} = \frac{2\pi\alpha\mu_0^2 n^2 I^2 \Delta t}{4} \approx 0.42$, which is calculated using the values of current, number of turns and Δt as 24 mA, 1000 and 5 ms respectively.

The selection and calculation of all the relevant physical parameters is reported in the later sections of this thesis. These experimentally applicable magnitude of these physical parameters for high precision measurements like the one stated in this thesis is shown assuming a true mathematical form of magnetic field given in Section 4.8. Here $\Delta\mathcal{B}(z_1, z_2) = (\mathcal{B}_{z_1}^2(z_1) - \mathcal{B}_{z_2}^2(z_2))$ and $\alpha = 575.15$ Hz/G² is the constant arising from the second order Zeeman effect. The relative phase $\Delta\phi$ in the above equation corresponds to a hyperfine level splitting into magnetically-insensitive sublevels, for example: $|F = 1, m_F = 0\rangle$ and $|F = 2, m_F = 0\rangle$.

4.2 Understanding of the *jitter* due to an applied magnetic field

Now, with all this knowledge, our objective is to apply a magnetic field pulse when the atomic cloud is at its apogee and its velocity at this point is very close to zero. Thanks to the second order Zeeman effect so that a total phase change of $\pi/2$ can be acquired after Zeeman splitting. This *jitter* occurring due to shine of magnetic field pulse results in spatial and time inhomogeneities. Time inhomogeneity can be controlled by using a good current generator. However, if the magnetic field is not constant and is exhibiting a spatial variability, that implies that one out of two clouds which experienced jittering in a certain localized zone, may interfere with another cloud which is either launched prior or will be launched after this cloud at its apogee, as explained in Figure 4.1.

4.3 B-pulse coil Activation

A magnetic field B removes the degeneracy among m_F energy sublevels. The first order Zeeman shift is:

$$\Delta E_{Z,I} = \mu_B g_J m_F |\mathbf{B}| \quad (4.8)$$

For those atoms the first non - zero term is the effect to the second order in the field:

$$\Delta E_{Z,II} = \frac{h\nu_{ab}}{4} \left(\frac{\mu_B g_J |\mathbf{B}|}{2A} \right)^2 = h a_{Z,II} |\mathbf{B}|^2 \quad (4.9)$$

with a negative sign for $|F = 2\rangle$ and a positive one for $|F = 1\rangle$, therefore yielding an energy shift $2\Delta E_{Z,II}$ to the hyperfine splitting between the two $m_F = 0$ states. Turning a magnetic field on, uniform in the region around the ensemble of atoms (forming an atomic cloud) during the second half of the interferometer sequence the atomic resonance varies with the external magnetic field while the reference oscillator maintains the same frequency. This yields an accumulated phase shift [17] expressed as follows:

$$\Delta\phi_{Z,II} = 2\pi \int_T^{2T} a_{Z,II} |\mathbf{B}(\mathbf{t})|^2 dt \quad (4.10)$$

where the sensitivity to magnetic fields for such atoms is expressed by a constant arising due to second - order Zeeman effect: $a_{Z,II} = 575.15 \text{ Hz/G}^2$.

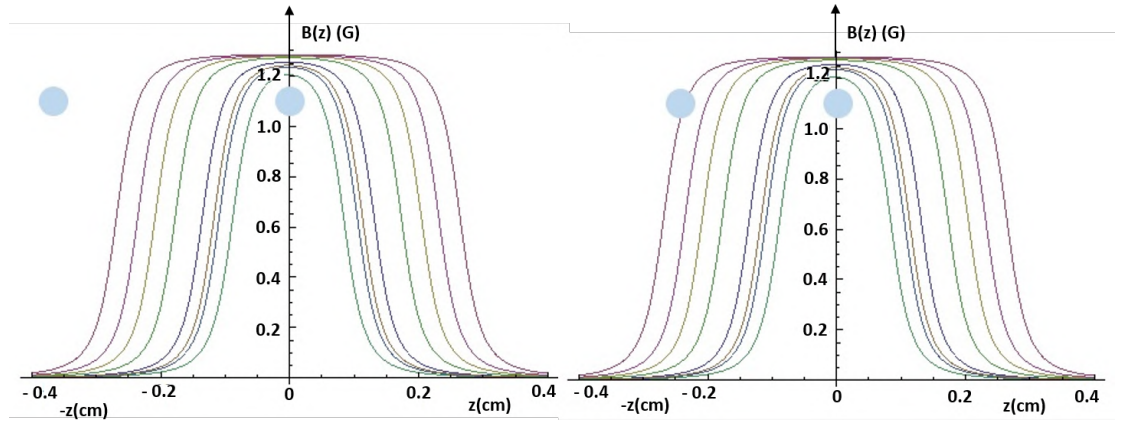


Figure 4.1: Artistic approach to explain the *jitter*: A plot of magnetic field for a finite length solenoid along z-axis versus change in position on Z-axis. Here, the pale blue circles denote atomic clouds, the blue circle at Y-axis is the one of two clouds, whereas the blue circle at left is the cloud in the higher region (These are separated by the fact that positions of both the clouds differ by a vertical separation distance $d = 23$ cm). In these two plots, we have considered the two magnetically - insensitive hyperfine states to be $|F = 1, m_F = 0\rangle$ and $|F = 2, m_F = 0\rangle$. In the plot at left, the magnetic field is only applied to one cloud in the state $|F = 1, m_F = 0\rangle$, and this magnetic field does not interfere with other cloud in $|F = 2, m_F = 0\rangle$ state, this is the scenario of *independent jittering*, which has to be achieved. In the plot at the right, the applied magnetic field from the coil starts to interfere with the cloud in the state $|F = 2, m_F = 0\rangle$, with this all the measurements will contain errors due to leakage of the other magnetic field, this is the scenario of *relative jittering*.

Here, magnetic field is indirectly time - dependent: $B(t) = B(x(t), y(t), z(t))$, where $x(t)$, $y(t)$ and $z(t)$ denote the motions of atoms (forming atomic cloud samples) along X, Y and Z axes respectively.

4.4 Monte Carlo simulation to calculate the difference in phase between the two clouds (in absence of classical trajectories of atoms)

First, a calculation was needed to be done to determine the correct value of current and the correct value of length which was to be used for introducing this extra finite - solenoidal coil around the interferometric tube. To proceed with this, we calculate derivatives in equation 4.6 partially with respect to variables z_1 (Z-coordinate of the upper atomic cloud) and z_2 (Z-coordinate of the lower atomic cloud). Thus, we define a new function:

$$\chi(z_1, z_2, L) = \sqrt{\left(\frac{\partial(\Delta\phi(z_1, z_2))}{\partial z_1}\right)^2 + \left(\frac{\partial(\Delta\phi(z_1, z_2))}{\partial z_2}\right)^2} \quad (4.11)$$

where L is the predictable length range of this new coil which ranges from 0.10 m to 0.60 m. After plotting of this function (as shown in Figure 4.2), the minimum from the resulting plot was found out to be at 0.266 m. Hence, the value of length of the B - pulse coil to be used in the experiment is approximately 26.6 cm for the B - pulse coil activation time of 5 ms. We say here that this is an approximated value because we are disregarding the three - dimensional motion of atoms at the moment.

The value of current was found using simple calculation as follows: For the time(Δt) of 5 ms with a condition of $\Delta\phi \approx \pi/2$ and using the estimated length (in the absence of classical trajectories of atoms) now which is 26.6 cm, we determined the difference $\Delta\mathcal{B}(z_1, z_2)$ at $z_1 = 0$ and $z_2 = 0$, resulting in $\Delta\mathcal{B}(z_1 = 0, z_2 = 0) = 3.75$. Then using this value in equation 4.6, the current was found out to be ≈ 24 mA. This is the value of the current when the positions of the atoms inside the cloud are fixed, not possessing any variation in their physical parameters like positions and velocities. For a more realistic situation (like in our experimental sequence), non - zero values of standard deviations are considered for the variations in position and velocities for the cold atomic cloud samples in next sections of this thesis.

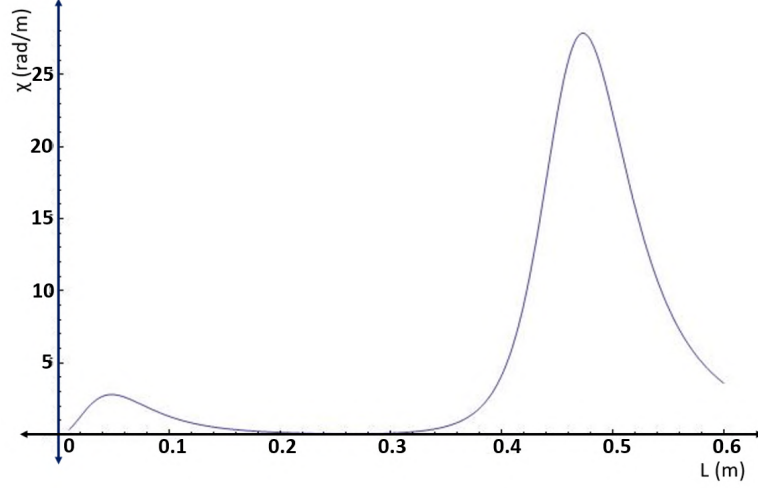


Figure 4.2: χ versus L : L is the range of predictable length values of the coil used. The coil lengths were considered ranging from 1 cm to 60 cm. The lowest point is the minima between the two clear peaks in the graph. The minima yields the magnitude of 26.6 cm (excluding classical trajectories of atoms), with the corresponding value of χ as 3.82 rad/m on Y-axis.

4.4.1 Phase variation with respect to change in physical parameters

After finding the correct magnitude of current for the coil analytically, a Monte Carlo simulation was carried out for the difference in phase ($\Delta\phi$) between the two clouds in the states $|F = 1, m_F = 0\rangle$ and $|F = 2, m_F = 0\rangle$, to be equal to $\pi/2$. Ten thousand random values of z_1 and z_2 (in the range of -0.025 m to 0.025 m) were generated using a normal distribution function with the values for standard deviation varying from 0.005 to 0.010, incrementing with a magnitude of 0.001. The standard deviation in our system is a representation of the atomic cloud width. The resulting values of $\Delta\phi$ were stored in a representation of two-dimensional square mesh with (0,0) as point of origin and vertices of this square grid being (0.002,0.002), (0.002,-0.002), (-0.002,0.002) and (-0.002,-0.002), spanning over 25 points in total. Hence, for each particular value of standard deviation, 25 values of $\Delta\phi$ (in the vicinity of $\pi/2$) were obtained. A 3D-plot concerning this scenario was generated as shown in Figure 4.3.

Using equations 4.6 and 4.7, different values of current for B - pulse coil are calculated for permissible time window: $\Delta t \in [5, 10]$ ms. Furthermore,

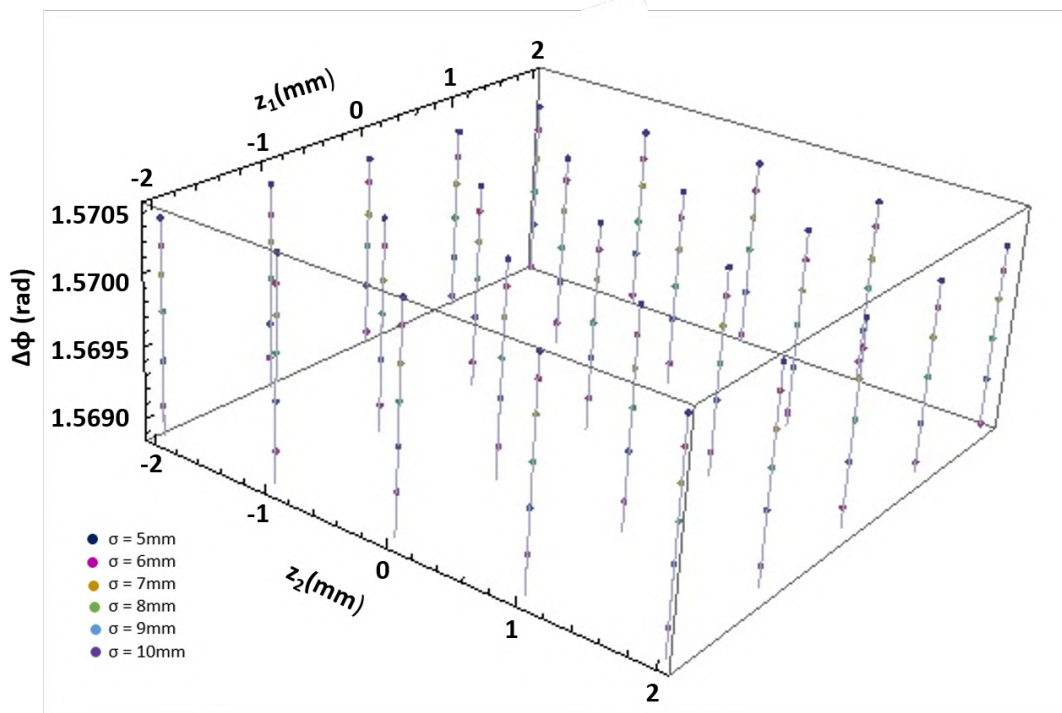


Figure 4.3: 3D-plot showing variation in the value of $\Delta\phi$ in the vicinity of $\pi/2$, with 25 vertices of square lattice in the XY-plane. According to this plot, the maximum and minimum values of $\Delta\phi$ are 1.5705 and 1.5690 respectively. This gives a phase variation of 1.5 mrad in this complete square mesh of 25 coordinates (when both the atomic clouds serve as fixed points).

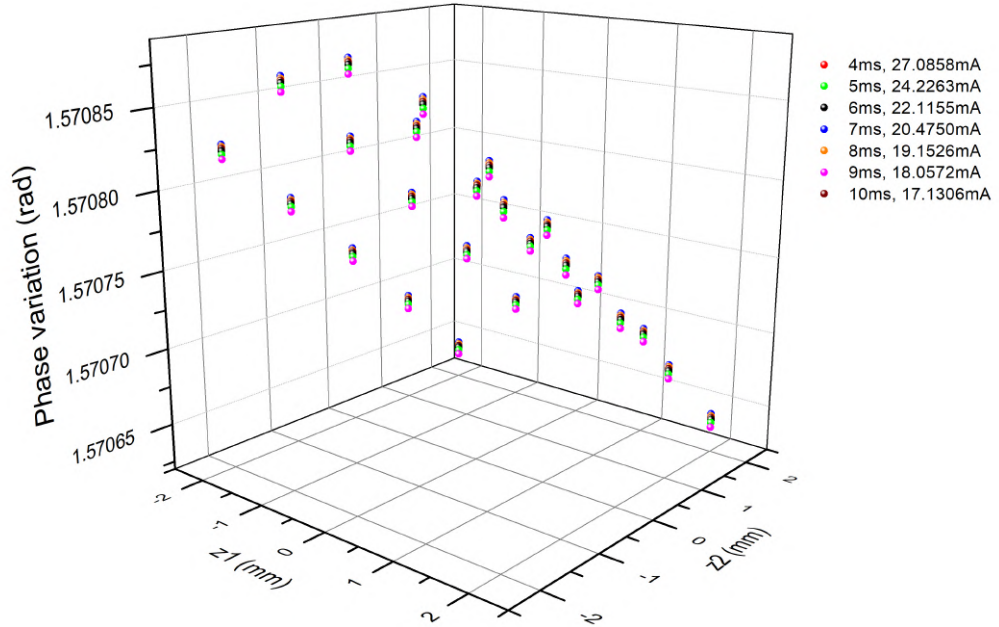


Figure 4.4: 3D-plot displaying a variation in the value of $\Delta\phi$ in the vicinity of $\pi/2$, with 25 vertices of square lattice in the XY-plane, for each different value of current though B - pulse coil paired with its corresponding value of Δt . This 3D-plot is NOT created from a Monte Carlo simulation as it is a case of two individual atoms acting as a fixed points along the fountain axis inside the gravity gradiometer.

using $z_1 \in [-2, 2]$ mm and $z_2 \in [-2, 2]$ mm, the phase variations for different time windows and corresponding current values are plotted in Figure 4.4.

4.5 Interferometric phase as a function of time - dependent atomic trajectories

The equations of motion for a particle in a parabolic trajectory with kicks induced from the laser pulses were written (in the format of piecewise functions) in our simulations for time domains 0 to T and T to $2T$ as explained below.

Let z_0 and z_1 be the coordinates of the two individual atoms (along foun-

Development of a New Apparatus for Precision Gravity Measurements with Atom Interferometry

z1 mm	z2 mm	Phase		Phase		Phase		Phase		Phase	
		rad	rad	rad	rad	rad	rad	rad	rad	rad	rad
		4ms, 27.0858mA	5ms, 24.2263mA	6ms, 22.1155mA	7ms, 20.4750mA	8ms, 19.1526mA	9ms, 18.0572mA	10ms, 17.1306mA			
0	0	1.57079	1.5708	1.5708	1.5708	1.5708	1.5708	1.5708	1.57079	1.5708	
0	-1	1.57084	1.57084	1.57084	1.57085	1.57085	1.57085	1.57084	1.57084	1.57084	
0	-2	1.57088	1.57088	1.57089	1.57089	1.57089	1.57089	1.57088	1.57088	1.57089	
0	1	1.57075	1.57075	1.57075	1.57076	1.57076	1.57075	1.57075	1.57075	1.57075	
0	2	1.5707	1.5707	1.5707	1.57071	1.57071	1.5707	1.5707	1.5707	1.57071	
-1	0	1.57078	1.57078	1.57078	1.57079	1.57079	1.57079	1.57078	1.57078	1.57078	
-1	-1	1.57082	1.57083	1.57083	1.57083	1.57083	1.57083	1.57082	1.57083	1.57083	
-1	-2	1.57086	1.57087	1.57087	1.57087	1.57087	1.57086	1.57086	1.57087	1.57087	
-1	1	1.57073	1.57073	1.57074	1.57074	1.57074	1.57074	1.57073	1.57074	1.57074	
-1	2	1.57068	1.57069	1.57069	1.57069	1.57069	1.57068	1.57068	1.57069	1.57069	
-2	0	1.57073	1.57074	1.57074	1.57074	1.57074	1.57073	1.57074	1.57074	1.57074	
-2	-1	1.57078	1.57078	1.57078	1.57079	1.57079	1.57078	1.57078	1.57078	1.57078	
-2	-2	1.57082	1.57082	1.57082	1.57083	1.57083	1.57082	1.57082	1.57082	1.57082	
-2	1	1.57069	1.57069	1.57069	1.57069	1.57069	1.57069	1.57069	1.57069	1.57069	
-2	2	1.57064	1.57064	1.57064	1.57065	1.57065	1.57064	1.57064	1.57064	1.57064	
1	0	1.57078	1.57078	1.57078	1.57079	1.57079	1.57078	1.57078	1.57078	1.57078	
1	-1	1.57082	1.57083	1.57083	1.57083	1.57083	1.57082	1.57083	1.57083	1.57083	
1	-2	1.57086	1.57087	1.57087	1.57087	1.57087	1.57086	1.57086	1.57087	1.57087	
1	1	1.57073	1.57073	1.57074	1.57074	1.57074	1.57073	1.57074	1.57074	1.57074	
1	2	1.57068	1.57069	1.57069	1.57069	1.57069	1.57068	1.57068	1.57069	1.57069	
2	0	1.57073	1.57074	1.57074	1.57074	1.57074	1.57073	1.57074	1.57074	1.57074	
2	-1	1.57078	1.57078	1.57078	1.57079	1.57079	1.57078	1.57078	1.57078	1.57078	
2	-2	1.57082	1.57082	1.57082	1.57083	1.57083	1.57082	1.57082	1.57082	1.57082	
2	1	1.57069	1.57069	1.57069	1.57069	1.57069	1.57069	1.57069	1.57069	1.57069	
2	2	1.57064	1.57064	1.57064	1.57065	1.57065	1.57064	1.57064	1.57064	1.57064	

Figure 4.5: Same results (here in a tabular form) from Figure 4.4 explicitly showing every phase value at all the 25 points created from permutations of z_1 and z_2 spanned as a square lattice. From this table, it is clear that the maximum variation in $\Delta\phi$ across a square lattice for the stated combinations of currents and time windows is 250 μrad .

tain height) at the starting point. Simplified equations for the displacement vectors representing trajectories of each arm of Mach-Zehnder interferometer are listed in the format of piecewise functions as follows:

ARM - 1 in Figure 3.1:

$$\vec{z}_1(t) = z_{UP}\hat{k} + \left(v_r t + v_z^0 t - \frac{gt^2}{2} \right) \hat{k}, \forall t \in [0, T] \quad (4.12)$$

ARM - 2 in Figure 3.1:

$$\vec{z}_1(t) = \left(\frac{-g(t-T)^2}{2} - \frac{gT^2}{2} + (t-T)(v_z^0 - gT) + T(v_r + v_z^0) + z_{UP} \right) \hat{k}, \forall t \in [T, 2T] \quad (4.13)$$

ARM - 4 in Figure 3.1:

$$\vec{z}_2(t) = \left(z_{UP} + v_z^0 t - \frac{gt^2}{2} \right) \hat{k}, \forall t \in [0, T] \quad (4.14)$$

ARM - 3 in Figure 3.1:

$$\vec{z}_2(t) = \left(\frac{-g(t-T)^2}{2} - \frac{gT^2}{2} + (t-T)(v_z^0 + v_r - gT) + v_z^0 T + z_{UP} \right) \hat{k}, \forall t \in [T, 2T]$$

(4.15)

Similarly, for another Mach - Zehnder interferometer with a non - zero and a finite separation distance (baseline), the displacement vectors representing trajectories of each arm are listed as follows:

ARM - 1 in Figure 3.1:

$$\vec{z}_1(t) = z_{DW}\hat{k} + \left(v_r t + v_z^0 t - \frac{gt^2}{2} \right) \hat{k}, \forall t \in [0, T] \quad (4.16)$$

ARM - 2 in Figure 3.1:

$$\vec{z}_1(t) = \left(\frac{-g(t-T)^2}{2} - \frac{gT^2}{2} + (t-T)(v_z^0 - gT) + T(v_r + v_z^0) + z_{DW} \right) \hat{k}, \forall t \in [T, 2T] \quad (4.17)$$

ARM - 4 in Figure 3.1:

$$\vec{z}_2(t) = \left(z_{DW} + v_z^0 t - \frac{gt^2}{2} \right) \hat{k}, \forall t \in [0, T] \quad (4.18)$$

ARM - 3 in Figure 3.1:

$$\vec{z}_2(t) = \left(\frac{-g(t-T)^2}{2} - \frac{gT^2}{2} + (t-T)(v_z^0 + v_r - gT) + v_z^0 T + z_{DW} \right) \hat{k}, \forall t \in [T, 2T] \quad (4.19)$$

For accounting the kicks from the laser pulses in our system, the recoil velocity v_r of the rubidium atom was used, which is:

$$v_r = \frac{\hbar k}{m} \quad (4.20)$$

where m is the mass of a rubidium atom, k is the two - photon wavevector calculated for $\lambda = 421.5$ nm and \hbar is the reduced Planck's constant.

Using above equations, the modulus of the magnetic field in the complete system was expressed as a function of time, for it to be used to calculate the total phases of both Mach - Zehnder interferometers:

$$\begin{aligned} \phi_c = & - \int_{0|F=2\rangle}^T \frac{2\pi\alpha}{2} B^2(t) dt + \int_{T|F=1\rangle}^{2T} \frac{2\pi\alpha}{2} B^2(t) dt \\ & - \int_{T|F=2\rangle}^{2T} \frac{2\pi\alpha}{2} B^2(t) dt + \int_{0|F=1\rangle}^T \frac{2\pi\alpha}{2} B^2(t) dt \end{aligned} \quad (4.21)$$

such that:

$$\phi_c(t) = \phi_c(B(x(t), y(t), z(t))) = 2\pi\alpha \oint B^2(x(t), y(t), z(t)) dt \quad (4.22)$$

Here, the integrals associated with state $|F = 2\rangle$ are taken to be negative and the integrals associated with $|F = 1\rangle$ are taken to be positive, therefore yielding an energy shift of $2\Delta E_{Z,II}$ to the hyperfine splitting between the two $m_F = 0$ states [17, 20].

4.6 Precise optimization position and relative sensitivity estimation

In order to optimize the position of the gradiometer with respect to the dimensions and address of the B-pulse coil, we extract the Z-coordinate value of the cold atomic cloud at the local maximum. So, we use equation 4.22 only for the B-pulse coil (or equivalently applying equation 3.1 only for the B-pulse coil) to find the precise optimization position z_m , resulting in $z_m = -4.64$ mm when $I_{B-pulse} = 19$ mA and $L_{B-pulse} = 23$ cm. Note that $L_{B-pulse} = 23$ cm is chosen here because now we have accounted the equations describing atomic trajectories in three-dimensions.

Relative sensitivity \mathcal{S} is mathematically defined as:

$$\mathcal{S} = 1 - \frac{\phi_C}{\phi_C^O}$$

where ϕ_C and ϕ_C^O are gradiometric phases due to only B-pulse coil excluding and including z_m respectively. Relative sensitivities of the gradiometric phase with respect to the gradiometer position and to the baseline value respectively are shown in Figures 4.6 and 4.7.

4.7 Monte Carlo simulation for phase difference calculation between the two clouds (accounting classical trajectories of atoms)

Fixing some parameters and applying variations to one - dimensional dynamic variables of the atomic clouds to minimize the phase noise was done in the simulation. The purpose of this step was to study how these dynamic variables affect the stability of our phase values with respect to the variation in these variables representing positions, velocities, standard deviations in

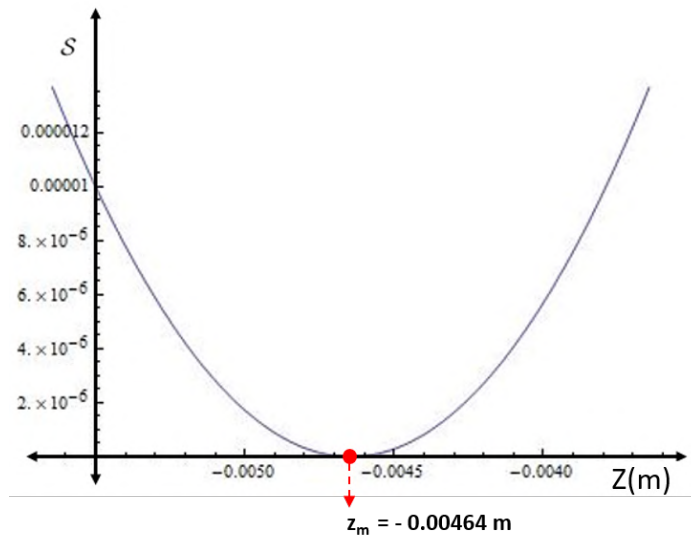


Figure 4.6: Relative sensitivity of the gradiometric phase with respect to the gradiometer position. Here, the intercept on the X-axis marks the value $z_m = -0.00464$ m with Z-coordinate being varied between $(z_m - 1)$ mm and $(z_m + 1)$ mm.

positions and velocities of the two atomic cloud species. All the parameters used in the Monte Carlo simulation for two atomic clouds traversing along the fountain axis are listed in Table 4.1.

4.7.1 Optimized and Unoptimized phases for different atomic populations

The plots marking the phase stabilities due to all the five variables associated only with the axis of launch (or free-fall) - z_{00} , z_{11} , σ_z , v_z and σ_{v_z} are shown in Figures 4.8 - 4.12. This 1D - simulation was carried out for two different population magnitudes of atoms inside each atomic cloud. The atomic populations chosen were 1000 and 10000. This is done as a sake of a double - cross check and verification between the plots in these two populations which differ by a factor of 10, and, the plot comparison of these five variables with the actual three - dimensional scenario. The actual 3D scenario employs the exact formulation of magnetic fields for the case of a finite - solenoidal coil, hence containing the elliptic functions of first, second and third kinds (Section 4.8), whereas the one - dimensional scenario which considers only the motion of two atomic clouds traversing their motion along

Parameters	Fixed values and Variations
Length	4 m (fixed value for bias coil)
Length	23 cm (fixed value for B-pulse coil)
Current	9.9 mA (fixed value for bias coil)
Current	19 mA (fixed value for B-pulse coil)
Time	4 ms (B-pulse duration)
Baseline	23 cm
Atomic Population	10^3 and 10^4 (per cloud)
Offset	1.735 m (Gradiometer position)
A_T	222.11 ms (Average apogee time)
A_D	241.862 mm (Average apogee distance)
z_m	-4.6 mm (Optimization position of gradiometer)
z_{11}	$\{z_{11} - 0.2, z_{11} - 0.1, z_{11}, z_{11} + 0.1, z_{11} + 0.2\}$ mm
z_{00}	$\{z_{00} - 0.2, z_{00} - 0.1, z_{00}, z_{00} + 0.1, z_{00} + 0.2\}$ mm
σ_z	$\{2.8, 2.9, 3.0, 3.1, 3.2\}$ mm
v_z	$\{v_0 - 0.2, v_0 - 0.1, v_0, v_0 + 0.1, v_0 + 0.2\}$ mm/s
σ_{v_z}	$\{2.8, 2.9, 3.0, 3.1, 3.2\}$ mm/s

Table 4.1: Complete list of parameters used in simulation to minimize the phase noise in interferometric signal. Particularly in this simulation, the atomic motion across XY-plane is disregarded.

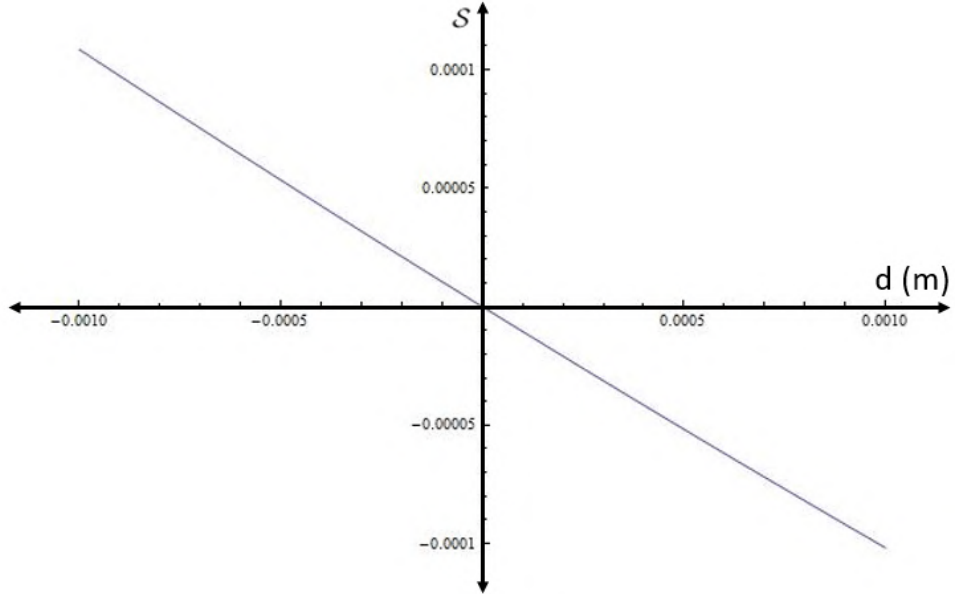


Figure 4.7: Relative sensitivity of the gradiometric phase with respect to the baseline value.

fountain axis, uses a quite simpler algebraic expression (equations 4.4 and 4.5) to compute magnetic fields. Furthermore, the optimization position (z_m) of the gradiometer with respect to the short / B – pulse coil is included in both 1D and 3D cases, in order to generate *OPTIMIZED* (including z_m) and *UNOPTIMIZED* (excluding z_m) phase magnitudes for variation in all the five parameters.

Looking at all the plots (Figures 4.8 - 4.12), we conclude that these plots do not display any clear trends. It is clear that the variation in atomic population does not result in any trend formation. Hence we arrive at an understanding that all these plots (Figures 4.8 - 4.12) represent random fluctuations in $\Delta\phi$ rather than being a part of systematic variation. With this understanding, we can say that if one carries out infinitely many simulations, by taking infinite number of variations in cloud variables (across the X - axis), one will be able to observe that the phase values should average, thereby converging to one specific value.

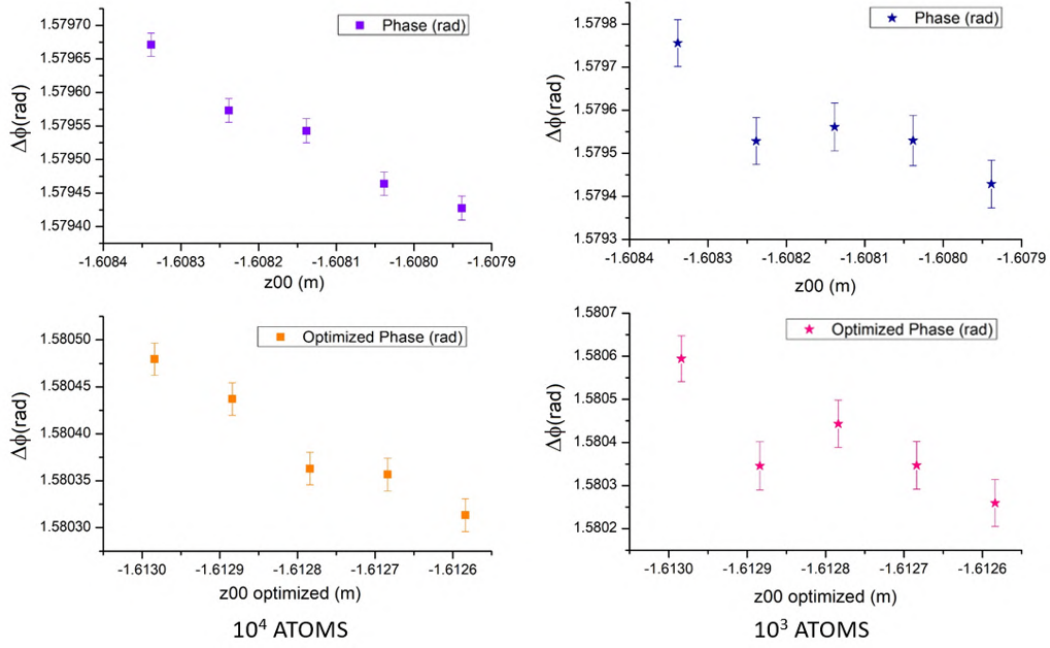


Figure 4.8: Visualizing *UNOPTIMIZED* (two upper graphs) and *OPTIMIZED* phases (two lower graphs): Phase variation for two different atomic populations with respect to the upper cloud position variable z_{00} with and without taking into account the optimization of the gradiometer position with respect to the B-pulse coil z_m . In the upper two graphs (*UNOPTIMIZED* phases), we observe a maximum phase fluctuation of $500 \mu\text{rad}/\text{mm}$ and $680 \mu\text{rad}/\text{mm}$ for 10^4 and 10^3 atoms respectively. Similarly, in the lower two graphs (*OPTIMIZED* phases), we observe a maximum phase fluctuation of $330 \mu\text{rad}/\text{mm}$ and $660 \mu\text{rad}/\text{mm}$ for 10^4 and 10^3 atoms respectively.

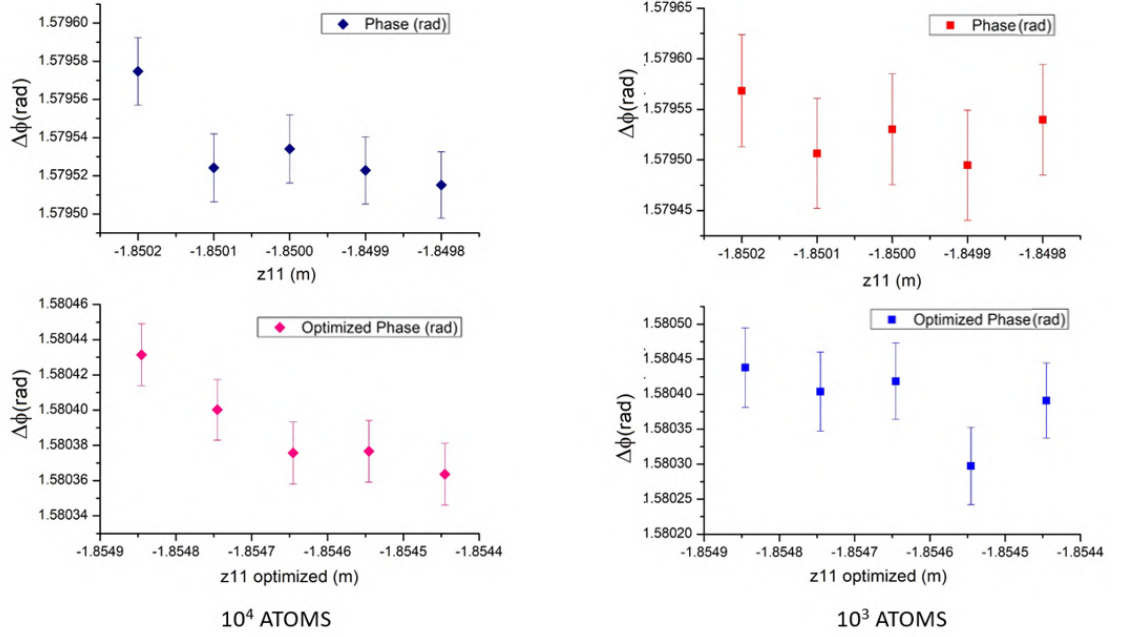


Figure 4.9: Visualizing *UNOPTIMIZED* and *OPTIMIZED* phases: Phase variation for two different atomic populations with respect to the lower cloud position variable z_{11} with and without taking into account the optimization of the gradiometer position with respect to the B-pulse coil z_m . In the upper two graphs (*UNOPTIMIZED* phases), we observe a maximum phase fluctuation of $140 \mu\text{rad}/\text{mm}$ and $160 \mu\text{rad}/\text{mm}$ for 10^4 and 10^3 atoms respectively. Similarly, in the lower two graphs (*OPTIMIZED* phases), we observe a maximum phase fluctuation of $138 \mu\text{rad}/\text{mm}$ and $310 \mu\text{rad}/\text{mm}$ for 10^4 and 10^3 atoms respectively.

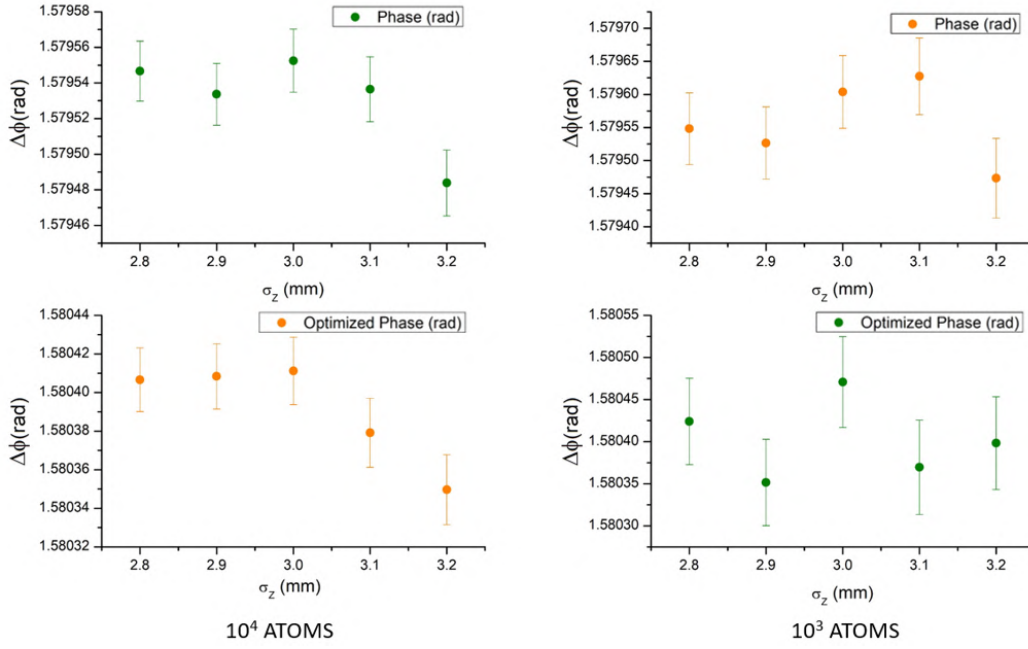


Figure 4.10: Visualizing *UNOPTIMIZED* and *OPTIMIZED* phases: Phase variation for two different atomic populations with respect to the atomic cloud width variable σ_z with and without taking into account the optimization of the gradiometer position with respect to the B-pulse coil z_m . In the upper two graphs (*UNOPTIMIZED* phases), we observe a maximum phase fluctuation of $140 \mu\text{rad/mm}$ and $350 \mu\text{rad/mm}$ for 10^4 and 10^3 atoms respectively. Similarly, in the lower two graphs (*OPTIMIZED* phases), we observe a maximum phase fluctuation of $130 \mu\text{rad/mm}$ and $250 \mu\text{rad/mm}$ for 10^4 and 10^3 atoms respectively.

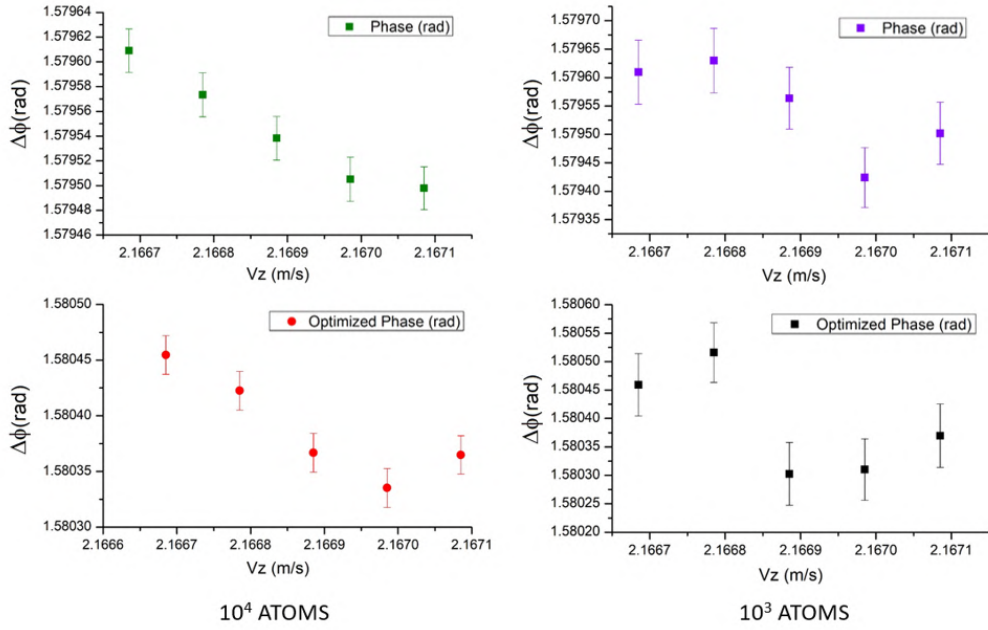


Figure 4.11: Visualizing *UNOPTIMIZED* and *OPTIMIZED* phases: Phase variation for two different atomic populations with respect to the atomic cloud velocity variable v_z with and without taking into account the optimization of the gradiometer position with respect to the B-pulse coil z_m . In the upper two graphs (*UNOPTIMIZED* phases), we observe a maximum phase fluctuation of $220 \mu\text{rad}/\text{mm}/\text{s}$ and $450 \mu\text{rad}/\text{mm}/\text{s}$ for 10^4 and 10^3 atoms respectively. Similarly, in the lower two graphs (*OPTIMIZED* phases), we observe a maximum phase fluctuation of $250 \mu\text{rad}/\text{mm}/\text{s}$ and $500 \mu\text{rad}/\text{mm}/\text{s}$ for 10^4 and 10^3 atoms respectively.

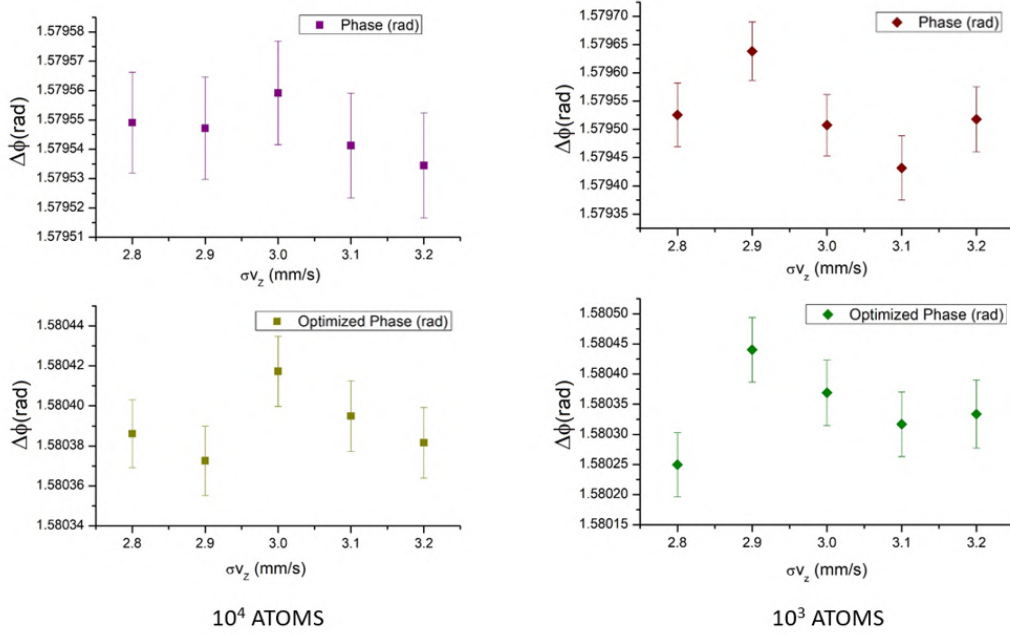


Figure 4.12: Visualizing *UNOPTIMIZED* and *OPTIMIZED* phases: Phase variation for two different atomic populations with respect to the standard deviation in atomic cloud velocity variable σ_{v_z} with and without taking into account the optimization of the gradiometer position with respect to the B-pulse coil z_m . In the upper two graphs (*UNOPTIMIZED* phases), we observe a maximum phase fluctuation of $50 \mu\text{rad}/\text{mm}/\text{s}$ and $400 \mu\text{rad}/\text{mm}/\text{s}$ for 10^4 and 10^3 atoms respectively. Similarly, in the lower two graphs (*OPTIMIZED* phases), we observe a maximum phase fluctuation of $90 \mu\text{rad}/\text{mm}/\text{s}$ and $360 \mu\text{rad}/\text{mm}/\text{s}$ for 10^4 and 10^3 atoms respectively.

4.8 Magnetic field equations of finite continuous solenoid: Bias and B-pulse coils

In our simulation, we treated bias and B-pulse coils as finite continuous solenoids [78] wrapped around the atomic fountain tower with the currents flowing through both the coils in the same direction. A finite continuous solenoid has its structure created by a sheet of conductive material with current uniformly distributed across the cylindrical surface of the solenoid unlike cascading of discrete coils. In Appendix A of the thesis, we have provided the generalized solution for the case when bias and B-pulse coils are treated as finite solenoidal coils by readapting the mathematical formulation implemented earlier [79]. The equations [78] used in our simulation to minimize the phase noise in the interferometric signal (complete simulation code provided in Appendix B) are written below in cylindrical coordinate system (ρ, ϕ, z) as follows:

$$A_\phi = \chi \left[\eta k \left(\frac{k^2 + h^2 - k^2 h^2}{k^2 h^2} \mathcal{K}(k^2) - \frac{1}{k^2} \mathcal{E}(k^2) + \frac{h^2 - 1}{h^2} \mathcal{E}_\pi(h^2, k^2) \right) \right]_{\eta_-}^{\eta_+} \quad (4.23)$$

where

$$\begin{aligned} \chi &= \frac{\mu_0 I}{4\pi l} \sqrt{\frac{R}{\rho}} \\ \eta_\pm &= z \pm \frac{l}{2} \\ h &= \frac{2\sqrt{R\rho}}{R + \rho} \\ k_\pm &= 2\sqrt{\frac{R\rho}{(R + \rho)^2 + \eta_\pm^2}} \end{aligned}$$

where A_ϕ is the vector potential and \mathcal{K} , \mathcal{E} and \mathcal{E}_π are elliptic integrals of first, second and third kinds respectively. Now, using the relationship between magnetic field density and vector potential ($\vec{B} = \nabla \times \vec{A}$), the radial and axial components can be expressed in cylindrical coordinate system as:

$$B_\rho = \frac{\mu_0 I}{2\pi l} \sqrt{\frac{R}{\rho}} \left[\frac{k^2 - 2}{k} \mathcal{K}(k^2) + \frac{2}{k} \mathcal{E}(k^2) \right]_{\eta_-}^{\eta_+} \quad (4.24)$$

$$B_z = \frac{\mu_0 I}{4\pi l \sqrt{R\rho}} \left[\eta k \left(\mathcal{K}(k^2) + \frac{R - \rho}{R + \rho} \mathcal{E}_\pi(h^2, k^2) \right) \right]_{\eta_-}^{\eta_+} \quad (4.25)$$

Physical parameters: Bias coil (for 4 m tower)	Magnitudes
Coil altitude	4 m
Number of turns per metre/ altitude	1000
Coil current chosen	10 mA
Coil activation time	440 ms
Chosen internal diameter for 4 m tower	35 mm

Table 4.2: Technical information used for the bias coil in all the simulations.

4.9 Phases obtained due to the sole effect of bias coil

The purpose of the bias coil is to define a quantization axis for the atoms in the cold atomic cloud samples. This bias magnetic field coil [79] remains switched ON throughout the complete experimental sequence. The experimental sequence terminates at 440 ms. The simulation results for the cases of single - atom gravity gradiometric sequences inside fountain tube of 4 m tall length is shown in Figure 4.13. Technical information for bias coil used in the simulations is listed in Table 4.2.

4.10 Monte Carlo simulation of the gradiometric sequence

Using the exact expressions of magnetic fields [78], a test code (in python) was written and executed where the phases in each arm were calculated using Simpson's numerical integration method with 1100 equal parts in each arm of both interferometers so as to keep good precision intact in the resulting magnitude of the total gradiometric phase. Increasing number of parts for Simpson's method more than 1000 - 1200 does not change the result significantly, and it increases the computation time. First, this simulation was written and executed for two single - atom Mach - Zehnder interferometers (forming a gravity gradiometer, experimental sequence depicted in Figure 4.14) with separation distance of 23 cm, results for this scenario are shown in the Figure 4.15. Simulation variables being set for this particular test simulation are mentioned in Table 4.3.

Then this simulation was modified for 1000 atoms so as to produce the result for the gradiometric phases for the two atomic clouds spanned in magnetically - insensitive hyperfine states inside the 4 m tall atomic fountain tower. The results for extending this simulation to the case of atomic cloud

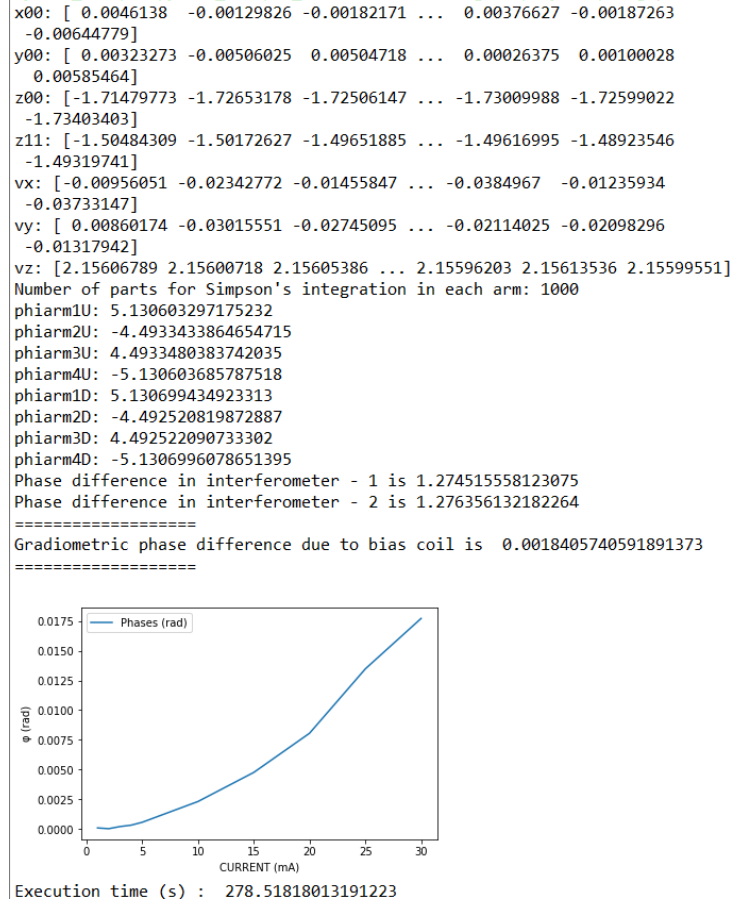


Figure 4.13: Visual of the output at the the python console for phase calculation solely due to the effect of bias coil for the scenario of two single-atom Mach - Zehnder interferometers forming a gravity gradiometer (example of 4 m tower): x_{00} and y_{00} indicate the positions of the atoms inside the cold cloud samples across the XY-plane with a standard deviation of 5 mm, z_{00} and z_{11} indicate the vertical positions of the two clouds with an inter-separation distance of 23 cm. In this example, the gradiometric phase is 1.84 mrad for the two clouds with width of 5 mm located at vertical positions of -1.50 m and -1.73 m below the midway (point of origin) of the atomic fountain tower. Code evaluation time is ≈ 5 minutes on INTEL-i5 processor. Relevant parameters used in the simulation are stated in Table 4.2. Lastly, the graph shown the variation in gradiometric phase due to different values of current applied through the bias coil at fixed points, i.e., for $z_{00} = -1.73$ m and $z_{11} = -1.50$ m. And, this graph matches exactly with the specific value reported in the simulation = 1.84 mrad (Y-axis) at 6.5 mA (X-axis).

Physical parameters: B - pulse coil	Magnitudes
Coil altitude	26.6 cm
Number of turns per metre / altitude	1000
Coil current range (including atomic trajectories)	22.50 mA - 23.75 mA (9 ms) 31.75 mA - 33 mA (5 ms)
Magnetic field modulus generated ($\Delta t = 9$ ms)	290 mG - 330 mG
Magnetic field modulus generated ($\Delta t = 5$ ms)	400 mG - 440 mG
Coil activation time(s) chosen (Δt)	5 ms, 9 ms
Coil activation time window (Δt)	4 ms - 10 ms

Table 4.3: Parameters and their respective magnitudes set in a test simulation (see Figure 4.15) where two - single atom Mach - Zehnder interferometers experience the resultant magnetic field of both bias and B-pulse coils. These physical parameters are compatible with an atomic fountain tube standing 4 m tall.

are reported in the next section.

4.10.1 Monte Carlo simulation for the relative phase calculation in the complete experimental sequence for the case of two atomic clouds

Employing appropriate loop structures with invoking parallelization, the program was modified such that it will produce new random values every time it runs, therefore obeying Maxwell - Boltzmann distribution spanned inside thermal cold atomic cloud samples. So, for one atom in each interferometer with some random position defined according to the values of standard deviations, the program evaluates the relative phase of the two interferometers producing results in the vicinity of $\pi/2$, as shown in Figure 4.15, following the trajectories as defined in Figure 4.14. So, if we choose to run the loop of this program 1000 times, it gives the result for 1000 atoms. This program indexes the atoms with atom number from 0 to 999, for the case of 1000 atoms. Calculation of phase of each iteration is automatically stored in a .txt file in the same folder where the windows batch file was saved and executed using Anaconda Powershell Prompt. This combination of using a windows batch file and Anaconda Powershell Prompt (called *parallelization*) contributed in the optimization of the computation time by a factor of eight.

The variables arising from the cylindrical coordinate system, namely: r , σ_r , v_r and σ_{v_r} , reveal the collective information about the atomic motion spanned across the XY-plane, such that: $r = \sqrt{x^2 + y^2}$, $\sigma_r = \sqrt{\sigma_x^2 + \sigma_y^2}$,

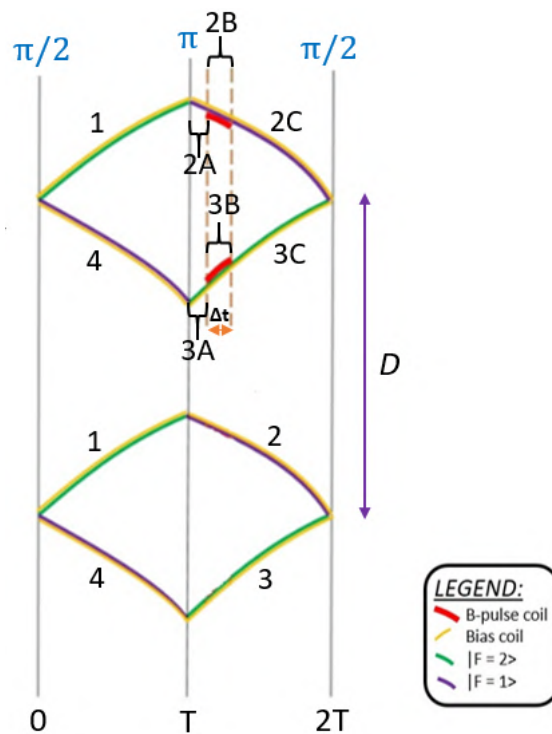


Figure 4.14: Gradiometric sequence (along-with B-pulse coil): Sketch of two parallel Mach-Zehnder interferometers separated by D experiencing magnetic fields from bias and B-pulse coils, where the two parallel brown-colored dotted lines indicate the B-pulse coil is switched ON for time range Δt (4 ms - 10 ms) in the second part of only one interferometer. Here, T is the evolution time for the atomic clouds, it also marks the half time of the experimental sequence. This experimental sequence terminates at the time $2T$, which is 440 ms.

Experimental parameters	Fixed magnitudes
Number of atoms in each cloud	1000
Fountain tube internal diameter	35 mm
Length (bias coil)	4 m
Length (B-pulse coil)	23 cm
Current (bias coil)	9.9 mA
Current (B-pulse coil)	19 mA
Time chosen	4 ms
Experimental sequence total time	440 ms
B - pulse coil activation permissible time window	4 ms - 10 ms
Bias coil activation time ($2T$)	440 ms
Baseline	0.23 m
Calculated offset	1.735 m
A_T	222.11 ms
A_D	241.862 mm
v_0	216.688511 mm/s
g	9.80491 m/s ²
z_m	-4.6 mm
Recoil velocity of rubidium atom (v_r)	≈ 22 mm/s

Table 4.4: Fixed experimental parameters used in three - dimensional simulation for obtaining the phase - noise minimization condition.

Variables	Variations
r	{0.0, 0.5, 1.0, 1.5, 2.0} mm
z_{DW}	{ $z_{11} - 0.2, z_{11} - 0.1, z_{11}, z_{11} + 0.1, z_{11} + 0.2$ } mm
z_{UP}	{ $z_{00} - 0.2, z_{00} - 0.1, z_{00}, z_{00} + 0.1, z_{00} + 0.2$ } mm
σ_r	{2.6, 2.8, 3.0, 3.2, 3.4} mm
σ_z	{2.8, 2.9, 3.0, 3.1, 3.2} mm
v_r	{0.0, 0.5, 1.0, 1.5, 2.0} mm/s
v_z	{ $v_0 - 0.2, v_0 - 0.1, v_0, v_0 + 0.1, v_0 + 0.2$ } mm/s
σ_{v_r}	{14, 17, 20, 23, 26} mm/s
σ_{v_z}	{2.8, 2.9, 3.0, 3.1, 3.2} mm/s

Table 4.5: Nine variables governing the motion of atomic cloud and their respective variations. These variations are set in the simulation producing $\Delta\phi \approx \pi/2$.

$$v_r = \sqrt{v_x^2 + v_y^2} \text{ and } \sigma_{v_r} = \sqrt{\sigma_{v_x}^2 + \sigma_{v_y}^2}.$$

Taking into account the complete information presented in Tables 4.4 and 4.5, a measurement campaign of 90 simulations was launched. Each variable taking five values with inclusion and exclusion of z_m (optimization of the gradiometer position with respect to the B-pulse coil). These 90 simulations are distributed as 45 simulations evaluating unoptimized phases (excluding z_m) and 45 simulations evaluating optimized phases (including z_m). Information about all the physical quantities associated with this simulation is listed in Tables 4.4 and 4.5. The results of all these simulations describe the phase stability when all the atomic cloud variables associated with the modified experimental sequence to carry out phase noise minimization are varied, reported in Figures 4.18 - 4.21.

4.11 Results from Monte Carlo simulation

All the results reported here are produced in the time span of about two and a half months considering the example of a 4 m tall atomic fountain tower, using a better computation machine at MAGIA-Advanced laboratory.

4.11.1 All variable behaviours associated with 3D scenario

Here, we present the results for phase variations corresponding to selected variations in all the participating variables (three - dimensional case) in the gradiometric sequence. Results are graphically shown in Figures 4.16 - 4.20.

The ranges of the error bars for all the variables in these plots are reported in Table 4.6. In Table 4.6, the labels $NOPE_{ERR}$ and OP_{ERR} indicate the error ranges in the absence and presence of z_m respectively, concisely defining the error bars for unoptimized and optimized phases. Also, Table 4.7 lists all calculated corresponding averaged uncertainties AC and AC_{ZM} when z_m is absent and present respectively. Here, averaged uncertainty is calculated by taking mean of the lower limit and the upper limit of error bars for each variable.

Variable (Units)	$NOPE_{ERR}(\mu\text{rad})$	$OP_{ERR}(\mu\text{rad})$
σ_r (mm)	55-57	41-44
σ_{v_z} (mm/s)	60-62	48-50
σ_{v_r} (mm/s)	56-73	47-67
σ_z (mm)	54-62	46-49
r (mm)	55-59	40-46
z_{DW} (m)	54-55	41-42
z_{UP} (m)	53-57	40-43
v_r (mm/s)	57-72	40-59
v_z (m/s)	53-55	40-42

Table 4.6: Reduction in lower and upper limits of the error bar ranges when z_m is included in the Monte Carlo phase noise minimization simulation. Here, $NOPE_{ERR}$ and OP_{ERR} indicate the error ranges in the absence and presence of z_m respectively.

Variable (Units)	AC	AC_{ZM}
σ_r (mm)	$5.60 \times 10^{-5} G$	$4.25 \times 10^{-5} G$
σ_{v_z} (mm/s)	$6.10 \times 10^{-5} G$	$4.90 \times 10^{-5} G$
σ_{v_r} (mm/s)	$6.45 \times 10^{-5} G$	$5.70 \times 10^{-5} G$
σ_z (mm)	$5.80 \times 10^{-5} G$	$4.75 \times 10^{-5} G$
r (mm)	$5.70 \times 10^{-5} G$	$4.30 \times 10^{-5} G$
z_{DW} (m)	$5.45 \times 10^{-5} G$	$4.15 \times 10^{-5} G$
z_{UP} (m)	$5.50 \times 10^{-5} G$	$4.15 \times 10^{-5} G$
v_r (mm/s)	$6.45 \times 10^{-5} G$	$4.95 \times 10^{-5} G$
v_z (m/s)	$5.40 \times 10^{-5} G$	$4.10 \times 10^{-5} G$

Table 4.7: Decrease in averaged uncertainties in the possible measurement of G (calculated from the information in Table 4.6) when z_m is included in the simulation dealing with minimizing the phase noise. AC and AC_{ZM} are measures of accuracies when z_m is absent and present respectively.

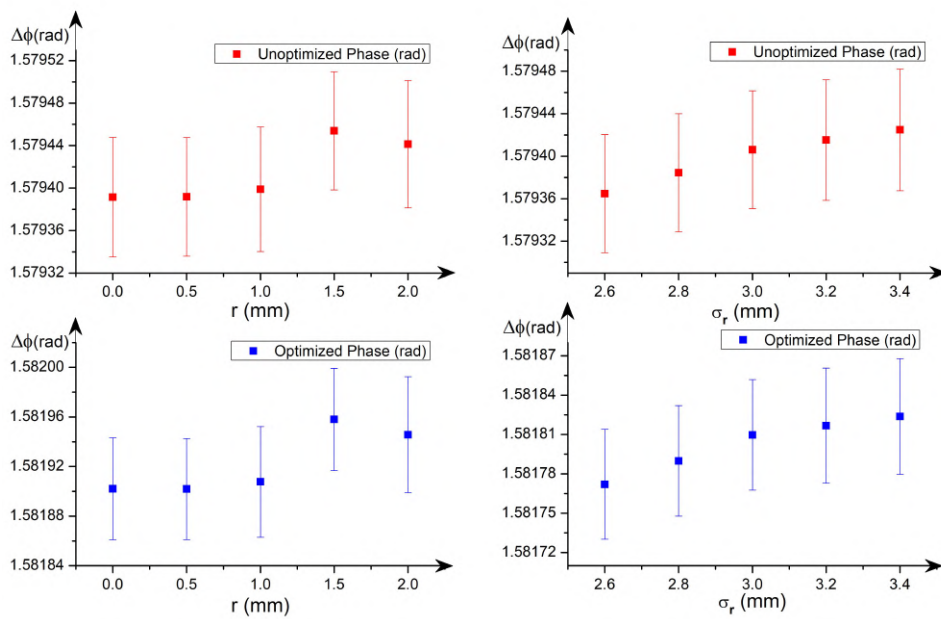


Figure 4.16: Phase variation with respect to change in the values of variables r and σ_r . Note that $r = 0$ and $\sigma_r = 0$ indicate a situation when most of the position of atoms (and their changes) are very close to the centre of the atomic cloud.

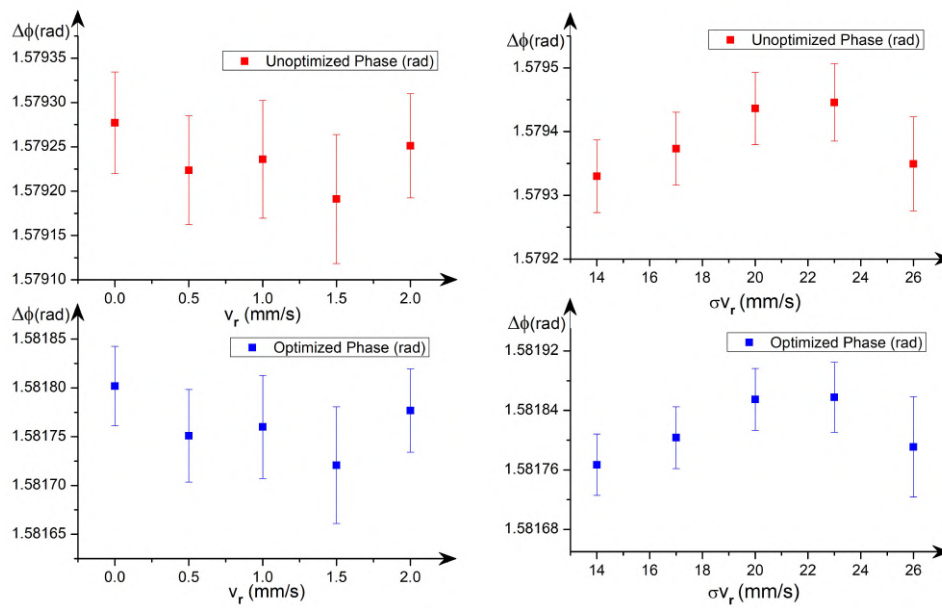


Figure 4.17: Phase variation with respect to change in the values of variables v_r and σ_{v_r} . Note that $v_r = 0$ and $\sigma_{v_r} = 0$ indicate a situation when velocities (and the change in velocities) of most of the atoms inside the atomic cloud are negligible.

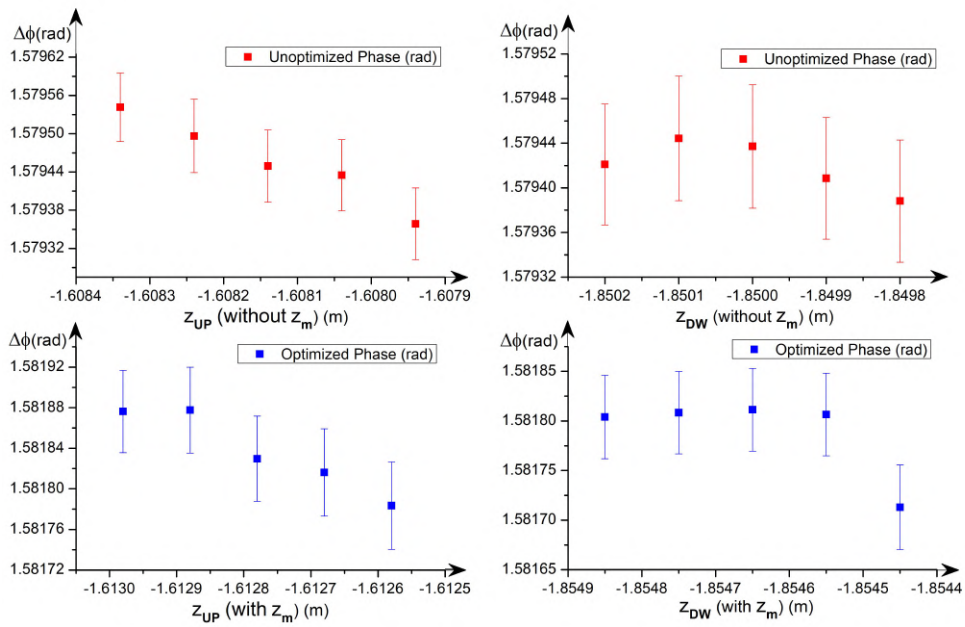


Figure 4.18: Phase variation with respect to change in the values of variables z_{UP} and z_{DW} .

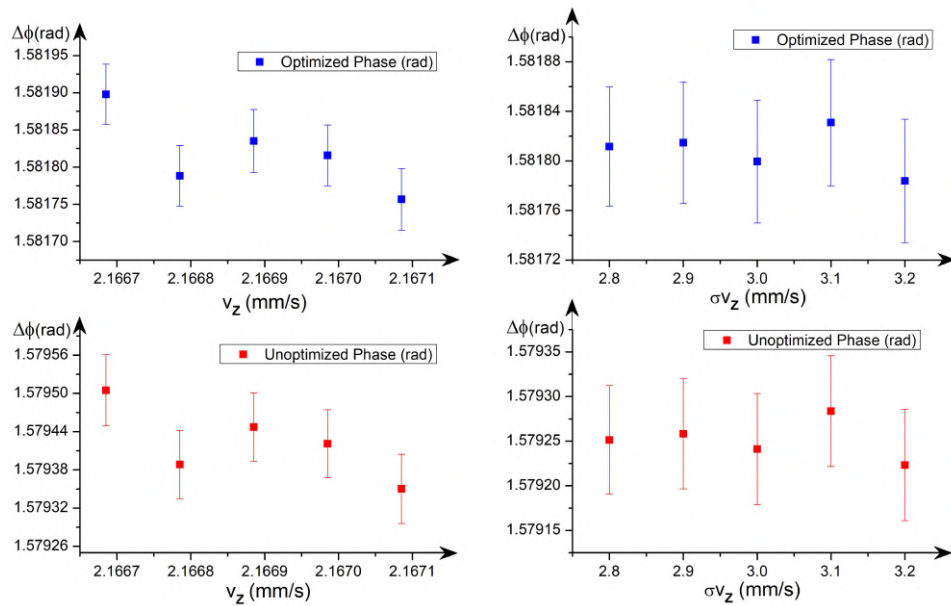


Figure 4.19: Phase variation with respect to change in the values of variables v_z and σ_{v_z} .

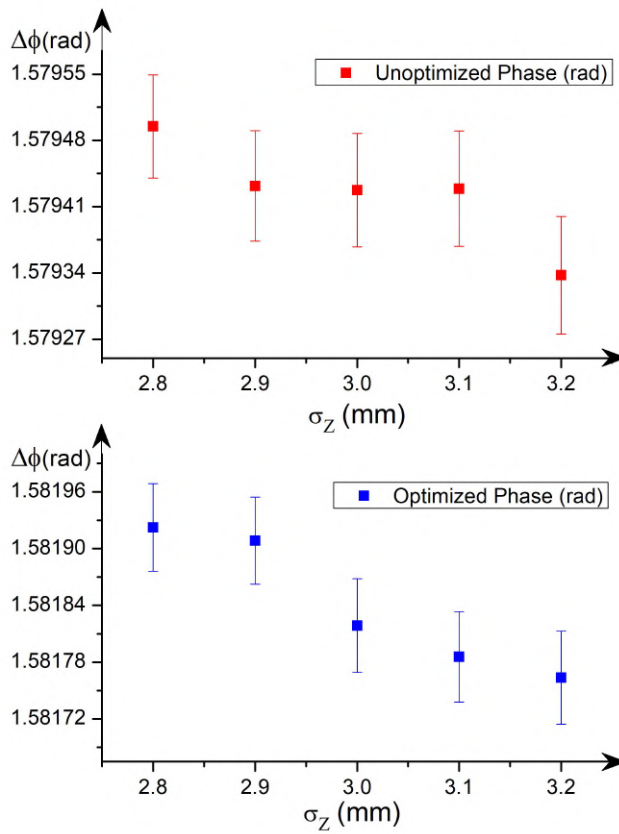


Figure 4.20: Phase variation with respect to change in the values of variable σ_z .

4.11.2 Comments about graphs

In this Chapter, we have scrutinized how the magnetic fields employed in the experimental sequence affect the stability of the gradiometric phase. Additionally, $\Delta\phi$ shows no clear trends with respect to any variable governing dynamics of the atomic clouds. But still, we carried out these simulations so as to check the stability in our results ($\Delta\phi$). In some graphs (like σ_r), it may seem like it exhibits a linear trend, but the reality is that all the graphs (Figures 4.16 - 4.20) happen to be random fluctuations rather than being a part of systematic variation. To summarize, if one carries out infinitely many simulations taking infinite number of variations across the X-axis (all the variables in Figures 4.16 - 4.20), then one would be able to observe that all the phase values (Y-axis of Figures 4.16 - 4.20) average to one particular value. The maximum relative variations are always within 10^{-4} G (for both cases of optimized and unoptimized phases). We conclude that, given the typical stability of an atomic fountain, the phase noise minimization setup of the experiment allows to integrate $\Delta\phi$ down to 10^{-4} resolution prior to shift the source mass position.

4.11.3 Peak-to-peak variations

Now, we present another effective way to describe simulation results. This is done by calculating peak-to-peak variations (denoted by $\Delta\phi_R^{P-P}$). Mathematically speaking, $\Delta\phi_R^{P-P}$ is the difference between maximum and minimum value in each atomic cloud parameter (in the simulation) for each uncertainty percent introduced in our simulation. These results are reported in Table 4.8.

4.12 Stability of fixed parameters

In this Section we present the sensitivities of our results due to slight variations in the possible *fixed parameters* stated in Tables 4.1, 4.2, 4.3 and 4.4.

4.12.1 Baseline stability

The baseline (d) is a parameter that defines the vertical separation distance between the centre of mass coordinates of the upper and lower clouds. Considering each cloud containing 1000 atoms, the standard deviation in baseline becomes 1.35×10^{-4} m, with its mean value being equal to 0.2299 m. Here, baseline is calculated using $d = (z_{UP} - z_{DW}) + T(v_z^{UP} - v_z^{DW})$, where the interrogation time T is kept fixed at 220 ms with position and velocity variables along the axis of gravity following a normal distribution.

Parameters (units)	$\Delta\phi_R^{N(P-P)}(\mu\text{rad})$	$\Delta\phi_R^{O(P-P)}(\mu\text{rad})$
σ_r (mm)	60.05	51.65
σ_{v_z} (mm/s)	34.85	31.38
σ_{v_r} (mm/s)	115.92	90.65
v_r (mm/s)	85.82	81.05
r (mm)	62.44	56.08
σ_z (mm)	157.21	158.72
z_{DW} (m)	56.16	98.33
v_z (mm/s)	154.58	141.27
z_{UP} (m)	182.76	94.27

Table 4.8: $\Delta\phi_R^{N(P-P)}$ and $\Delta\phi_R^{O(P-P)}$ represent unoptimized and optimized peak-to-peak variations respectively for each participating parameter in the simulation. The standard error is equal to $45 \mu\text{rad}$, equivalent to 31×10^{-6} G.

4.12.2 Phase sensitivity due to variation in bias coil current

The percentage errors in the phases produced by two parallel atom interferometers for three values of bias coil current are listed in Table 4.9.

The six values of relative sensitivities for unoptimized and optimized phases are reported below. This is done by comparing the single-atom phase values from simulations ϕ^{Ns} (unoptimized) and ϕ^{Os} (optimized) with theoretical phase values ϕ^{Nt} (unoptimized) and ϕ^{Ot} (optimized) for each value of bias coil current as follows:

$$\mathcal{S}_{9.8mA}^N = 1 - \frac{\phi_{9.8mA}^{Ns}}{\phi_{9.8mA}^{Nt}} = 1.85 \times 10^{-3}$$

$$\mathcal{S}_{9.8mA}^O = 1 - \frac{\phi_{9.8mA}^{Os}}{\phi_{9.8mA}^{Ot}} = 2.94 \times 10^{-4}$$

$$\mathcal{S}_{9.9mA}^N = 1 - \frac{\phi_{9.9mA}^{Ns}}{\phi_{9.9mA}^{Nt}} = 1.68 \times 10^{-3}$$

$$\mathcal{S}_{9.9mA}^O = 1 - \frac{\phi_{9.9mA}^{Os}}{\phi_{9.9mA}^{Ot}} = 4.95 \times 10^{-4}$$

$$\mathcal{S}_{10mA}^N = 1 - \frac{\phi_{10mA}^{Ns}}{\phi_{10mA}^{Nt}} = 2.67 \times 10^{-3}$$

I_{bias} (mA)	P_{ϕ^O}	P_{ϕ^N}
9.8	0.0294%	0.1855%
9.9	0.0495%	0.1685%
10.0	0.0393%	0.2674%

Table 4.9: P_{ϕ^O} and P_{ϕ^N} representing percentage errors in optimized and unoptimized phases with respect to a slight current variation of 0.1 mA in the bias coil.

$$\mathcal{S}_{10mA}^O = 1 - \frac{\phi_{10mA}^{OS}}{\phi_{10mA}^{OT}} = 3.92 \times 10^{-4}$$

Note that while obtaining the above calculated values, B-pulse coil was not turned off and its current value was fixed at 19 mA. All the phase values for three different current values are calculated here incorporating the experimental scheme explained in Chapter 3, but only for two single atoms (separated by a fixed baseline).

4.12.3 Phase sensitivity due to variation in B-pulse coil current

The percentage errors in the phases produced by two parallel atom interferometers for three values of B-pulse coil current are listed in Table 4.10.

The six values of relative sensitivities for unoptimized and optimized phases are reported below. This is done by comparing the single-atom phase values from simulations ϕ^{NS} (unoptimized) and ϕ^{OS} (optimized) with theoretical phase values ϕ^{NT} (unoptimized) and ϕ^{OT} (optimized) for each value of B-pulse coil current as follows:

$$\mathcal{S}_{19mA}^N = 1 - \frac{\phi_{19mA}^{NS}}{\phi_{19mA}^{NT}} = 2.67 \times 10^{-3}$$

$$\mathcal{S}_{19mA}^O = 1 - \frac{\phi_{19mA}^{OS}}{\phi_{19mA}^{OT}} = 3.93 \times 10^{-4}$$

$$\mathcal{S}_{18.9mA}^N = 1 - \frac{\phi_{18.9mA}^{NS}}{\phi_{18.9mA}^{NT}} = 8.14 \times 10^{-3}$$

$$\mathcal{S}_{18.9mA}^O = 1 - \frac{\phi_{18.9mA}^{OS}}{\phi_{18.9mA}^{OT}} = 8.44 \times 10^{-4}$$

$$\mathcal{S}_{18.8mA}^N = 1 - \frac{\phi_{18.8mA}^{NS}}{\phi_{18.8mA}^{NT}} = 1.49 \times 10^{-3}$$

$I_{B-pulse}$ (mA)	$P_{\phi O}$	$P_{\phi N}$
18.8	0.0051%	0.1487%
18.9	0.0844%	0.8139%
19.0	0.0393%	0.2674%

Table 4.10: $P_{\phi O}$ and $P_{\phi N}$ representing percentage errors in optimized and unoptimized phases with respect to a slight current variation of 0.1 mA in the B-pulse coil.

$$\mathcal{S}_{18.8mA}^O = 1 - \frac{\phi_{18.8mA}^{O_S}}{\phi_{18.8mA}^{O_T}} = 5.10 \times 10^{-5}$$

Note that while obtaining the above calculated sensitivity values, the bias coil was not turned off and its current value was fixed at 10 mA. All the phase values for three different B-pulse current values are calculated here as explained in Chapter 3, but only for two single atoms (separated by a fixed baseline). The phases evaluated when the current in the B-pulse coil was set to 18.8 mA and 18.9 mA satisfied the phase noise minimization condition of $\Delta\phi \approx \pi/2$ less precisely when being compared to the B-pulse coil current being set at 19 mA. So, all the main results reported in this Chapter are produced with B-pulse coil current being set to 19 mA.

4.12.4 Phase sensitivity due to z_m

It is clear from the calculated single-atom sensitivity values (in Sections 4.12.2 and 4.12.3), the importance of the parameter z_m governing the optimized position of gravity gradiometer with respect to the B-pulse coil. The calculations in the preceding sections reflect an increase in the relative sensitivity by one order of magnitude just for the case of single atoms. Whereas, the information reported in Tables 4.9 and 4.10 clearly show that the inclusion of z_m leads to reduction of percentage errors by one order of magnitude. This is justified when we compare both $P_{\phi O}$ and $P_{\phi N}$ (Tables 4.9 and 4.10) considering the current variation of 0.1 mA in both bias and B-pulse coils.

4.13 Designing new anti-helmholtz coil system

The idea of two-dimensional magneto-optical trap (2D-MOT) plays a vital role in realization of several methods, techniques or effects such as: Electromagnetically Induced Transparency (EIT) [80, 81], EIT based cold atomic

Quantum Memory [82, 83, 84, 85] with high storage efficiency [86, 87]. A decade ago, a pair of rectangular coils in the MOT for the production of cold atom clouds with large optical density was implemented [88] inspired by the 2D-MOT systems achieved in the past [89, 90, 91, 92, 93, 94, 95, 96, 97, 98].

In this thesis, the 2D-MOT system in the new design consists of two pairs of rectangular coils arranged in an anti-helmholtz configuration [99]. Instead of circular coils, the rectangular arrangement were preferred because in the case of rectangular coils, there exists a larger area in which the magnetic field remains uniform.

4.13.1 2D-MOT coil system with rectangular arrangement: Mathematical Analysis

As shown in Figure 4.21, we have two pairs of coils, one pair of rectangular coils parallel to each other in XZ plane and the other pair of rectangular coils parallel to each other in YZ plane arranged in an anti-helmholtz current flowing configuration. In Figure 4.21, the tiny red bubble indicates the coordinates of origin $(0, 0, 0)$ in a 3D cartesian system, where the essential condition $B(0, 0, 0) = 0$ was verified. At this point of origin, the magnetic field resulting from all the coils should sum to zero, which was clearly observed, as shown in Figure 4.22.

The length and breadth of the rectangular coil are $2a$ and $2b$ respectively. Here, we have calculated and plotted the total magnetic field of the system of two pairs of rectangular coils by first calculating vector potentials across each axis for all the coils for rectangular anti - helmholtz coils. The curl of the total vector potential will yield the magnetic fields along all the three axes. A theoretical derivation was done and all the relevant physical parameters were calculated (reported in this Section) using MATHEMATICA, the code evaluation time was ≈ 14 minutes on INTEL-i5 processor. The vector potentials for lower half part in the first pair of coils are:

$$A_z(x, y, z) = \frac{\mu_0 I}{4\pi} \left[\int_{-b}^b \frac{dz}{R_1} \right] + \frac{\mu_0 I}{4\pi} \left[\int_b^{-b} \frac{(-dz)}{R_3} \right] \quad (4.26)$$

$$A_x(x, y, z) = \frac{\mu_0 I}{4\pi} \left[\int_{-a}^a \frac{dz}{R_2} \right] + \frac{\mu_0 I}{4\pi} \left[\int_a^{-a} \frac{(-dz)}{R_4} \right] \quad (4.27)$$

$$A_y(x, y, z) = 0 \quad (4.28)$$

where,

$$R_1^2 = (z - s)^2 + (x + a)^2 + (y + d)^2 \quad (4.29)$$

$$R_2^2 = (x - s)^2 + (y + d)^2 + (z - b)^2 \quad (4.30)$$

$$R_3^2 = (z - s)^2 + (x - a)^2 + (y + d)^2 \quad (4.31)$$

$$R_4^2 = (x - s)^2 + (y + d)^2 + (z + b)^2 \quad (4.32)$$

The vector potentials for upper half part in the first pair of coils are:

$$A_z(x, y, z) = \frac{\mu_0 I}{4\pi} \left[\int_b^{-b} \frac{dz}{R_1'} \right] + \frac{\mu_0 I}{4\pi} \left[\int_{-b}^b \frac{(-dz)}{R_3'} \right] \quad (4.33)$$

$$A_x(x, y, z) = \frac{\mu_0 I}{4\pi} \left[\int_a^{-a} \frac{dz}{R_2'} \right] + \frac{\mu_0 I}{4\pi} \left[\int_{-a}^a \frac{(-dz)}{R_4'} \right] \quad (4.34)$$

$$A_y(x, y, z) = 0 \quad (4.35)$$

where,

$$R_1'^2 = (z - s)^2 + (x + a)^2 + (y - d)^2 \quad (4.36)$$

$$R_2'^2 = (x - s)^2 + (y - d)^2 + (z - b)^2 \quad (4.37)$$

$$R_3'^2 = (x - a)^2 + (y - d)^2 + (z - s)^2 \quad (4.38)$$

$$R_4'^2 = (x - s)^2 + (y - d)^2 + (z + b)^2 \quad (4.39)$$

The vector potentials for upper half part in the second pair of coils are:

$$A_y(x, y, z) = \frac{\mu_0 I}{4\pi} \left[\int_a^{-a} \frac{dy}{R_2} \right] + \frac{\mu_0 I}{4\pi} \left[\int_{-a}^a \frac{(-dy)}{R_4} \right] \quad (4.40)$$

$$A_z(x, y, z) = \frac{\mu_0 I}{4\pi} \left[\int_b^{-b} \frac{dz}{R_1} \right] + \frac{\mu_0 I}{4\pi} \left[\int_{-b}^b \frac{(-dz)}{R_3} \right] \quad (4.41)$$

$$A_x(x, y, z) = 0 \quad (4.42)$$

where,

$$R_1^2 = (x - d)^2 + (y + a)^2 + (z - s)^2 \quad (4.43)$$

$$R_3^2 = (x - d)^2 + (y - a)^2 + (z - s)^2 \quad (4.44)$$

$$R_2^2 = (x - d)^2 + (y - s)^2 + (z - b)^2 \quad (4.45)$$

$$R_4^2 = (x - d)^2 + (y - s)^2 + (z + b)^2 \quad (4.46)$$

The vector potentials for lower half part in the second pair of coils are:

$$A_z(x, y, z) = \frac{\mu_0 I}{4\pi} \left[\int_{-b}^b \frac{dz}{R_1'} \right] + \frac{\mu_0 I}{4\pi} \left[\int_b^{-b} \frac{(-dz)}{R_3'} \right] \quad (4.47)$$

$$A_y(x, y, z) = \frac{\mu_0 I}{4\pi} \left[\int_{-a}^a \frac{dy}{R_2} \right] + \frac{\mu_0 I}{4\pi} \left[\int_a^{-a} \frac{(-dy)}{R_4} \right] \quad (4.48)$$

$$A_x(x, y, z) = 0 \quad (4.49)$$

where,

$$R_1'^2 = (z - s)^2 + (x + d)^2 + (y + a)^2 \quad (4.50)$$

$$R_3'^2 = (x + d)^2 + (z - s)^2 + (y - a)^2 \quad (4.51)$$

$$R_2'^2 = (x + d)^2 + (y - s)^2 + (z - b)^2 \quad (4.52)$$

$$R_4'^2 = (y - s)^2 + (x + d)^2 + (z + b)^2 \quad (4.53)$$

These all vector potentials were derived analytically and computed from our simulation. After, it was written as a total vector in the following form:

$$\vec{A} = A_x \hat{i} + A_y \hat{j} + A_z \hat{k} \quad (4.54)$$

The squared magnitude of the curl of the above equation results as:

$$B^2(x, y, z) = (B_x)^2 + (B_y)^2 + (B_z)^2 \quad (4.55)$$

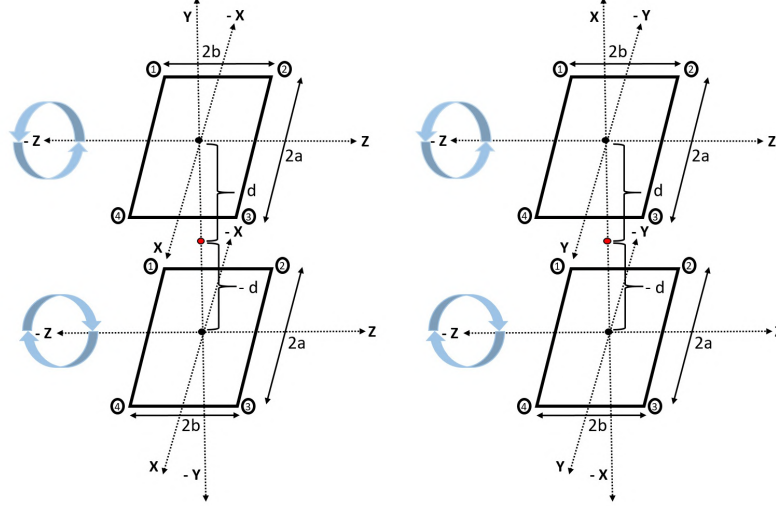


Figure 4.21: First and second pair of rectangular coils in the two-dimensional magneto-optical trap of the new design. The clockwise and anti-clockwise arrows indicate the direction of current flowing through the coils.

4.13.2 2D-MOT coil system - Calculation and Simulation: Coil parameters, magnetic field and magnetic field gradients

Magnetic fields and magnetic field gradients generated by all the coils along X, Y and Z axes are depicted in Figures 4.22 - 4.24. Other important parameters for the preparation and to ensure the functioning of 2D-MOT system - current, coil length, coil resistance, magnetic field gradients along all axes and power dissipation due to the coils, which are calculated as follows:

1. *Peak magnetic field gradients:* The peak value of magnetic field gradients across X, Y and Z axes were deduced from the value marking the peaks pointing along plots of Y-axis in Figure 4.23. The total magnetic field gradient of the system is expressed by the following equation:

$$\frac{dB_{\text{peak}}(x, y, z)}{dr(x, y, z)} = \sqrt{\left(\frac{dB_{\text{peak}}(x, y, z)}{dx}\right)^2 + \left(\frac{dB_{\text{peak}}(x, y, z)}{dy}\right)^2 + \left(\frac{dB_{\text{peak}}(x, y, z)}{dz}\right)^2} \quad (4.56)$$

As per our data, the values from Figure 4.23 are:

$$\frac{dB_{\text{peak}}}{dx} = \frac{dB_{\text{peak}}}{dy} = 14 \text{ G/cm} \quad (4.57)$$

$$\frac{dB_{\text{peak}}}{dz} = 10.5 \text{ G/cm} \quad (4.58)$$

2. *Coil Length*: The desired coil length L is evaluated as follows:

$$L = 2n_h n_v ((A + B) + 2d(n_v - 1)) \approx 27 \text{ m} \quad (4.59)$$

where n_h and n_v denote the number of turns in horizontal direction and number of turns in vertical direction respectively. They are taken as $n_h = 7$ and $n_v = 8$. In above equation, d denotes the cross-sectional diameter of the coil which is taken as $d = 0.0015 \text{ m}$, A and B denote the length and breadth of the rectangular coils including the cross-sectional diameter d .

3. *Coil Current*: The value of current in all the coils is the ratio of peak value of magnetic field gradient to the absolute value of the gradient for 1 A of current flowing through all the coils. Magnetic field gradients along X and Y axes when 1 A of current will be passed through the coils is 2.33 G/cm, provided that the magnetic field gradient of the system is 14 G/cm because we want to circulate a current magnitude $\approx 6 \text{ A}$ in our coils. With this information, we have:

$$I = \frac{dB_{\text{peak}}}{d(x, y)} / \frac{dB}{d(x, y)} \approx 6 \text{ A} \quad (4.60)$$

Figure 4.23 shows that the magnetic field gradient along Z - axis is 10.5 G/cm for 6 A of coil current, which implies the magnetic field gradient along Z - axis for 1 A of current is 1.75 G/cm, this reduced magnitude comes from the reason that all of our rectangular coils are spanned across XZ and YZ planes (Figure 4.23), all sharing Z as a common axis for magnetic field and magnetic field gradient contributions.

4. *Coil Resistance*: The correct magnitude of the coil resistance R_{coil} is calculated as follows:

$$R_{\text{coil}} = \frac{L\rho}{s} \approx 257 \text{ m}\Omega \quad (4.61)$$

where $L = 26.992 \text{ m}$, $\rho = 1.68 \times 10^{-8} \Omega\text{m}$ is the resistivity of the copper coils and $s = 1.76715 \times 10^{-6} \text{ m}^2$ is the cross - sectional area of the coil.

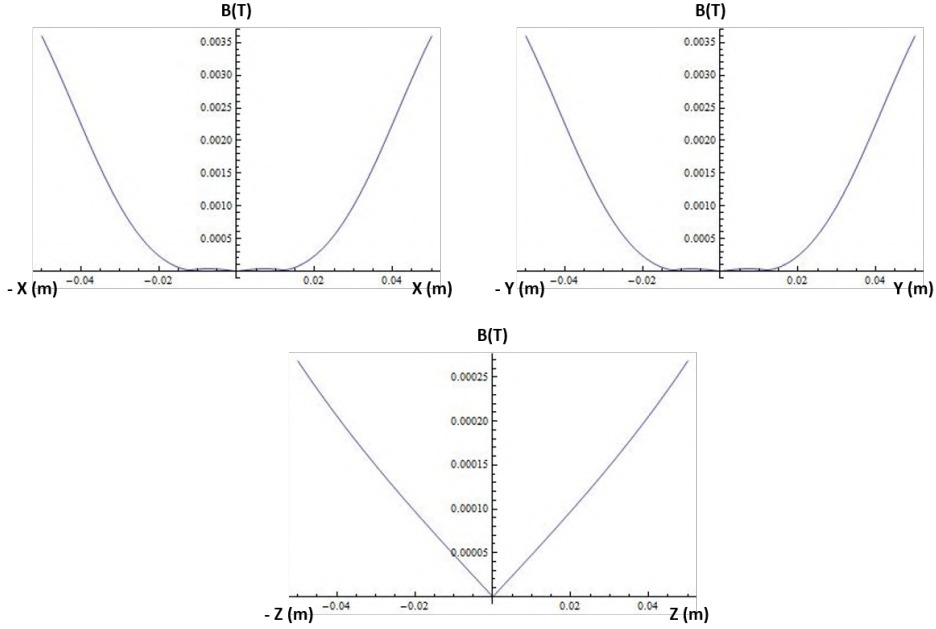


Figure 4.22: Plots of the magnetic fields versus axial along all three axes. An important condition $B(0,0,0) = 0$ was verified from this simulation leading to these plots.

5. *Power Dissipation*: Power dissipation is evaluated as follows:

$$P = RI^2 \approx 9.27 \text{ W} \quad (4.62)$$

Note that in our case, the half - value of the distance from the centre of the MOT to the internal face of the second pair of rectangular shaped coil is taken to be 37 mm. Hence the observation in graph 4.23 is in agreement that with this distance of 37 mm, one would expect trapping along X and Y axes while atoms being almost free across Z - axis. This expectation makes sense because in Figure 4.23, the magnetic field gradient along the Z - axis is negligible within the stretch of about 80 cm.

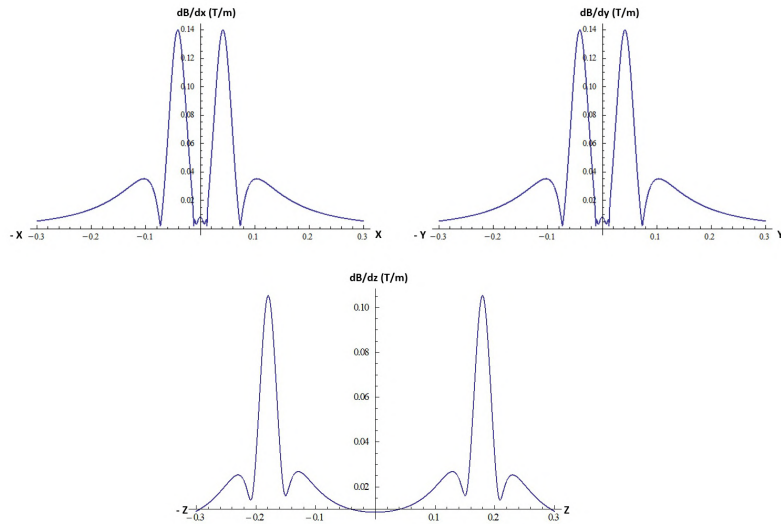


Figure 4.23: Plots of the peak magnetic field gradients versus axial distance for all three axes.

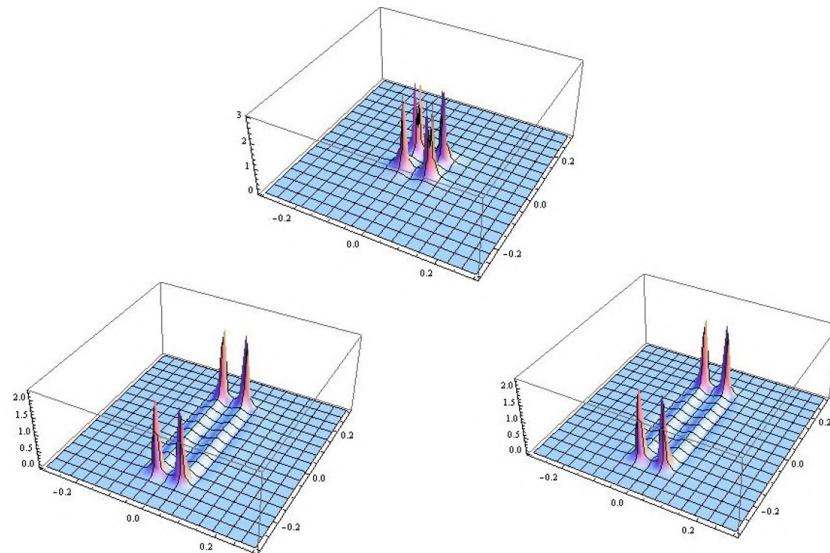


Figure 4.24: 3D-plots of the peak magnetic field gradients: The plot at the top shows the behavior of the magnetic field gradient in XY plane, the other two below 3D-plots show the behavior of magnetic field gradient in XZ and YZ planes.

4.14 Conclusions and Outlook

Taking into account all the results presented in this Chapter, we can conclude that the interferometric signal of the atomic clouds undergoing a Mach-Zehnder interferometric sequence can be maximized by employing the idea of second order Zeeman effect. Experimentally, this idea should be able to produce interferometric fringes with a good contrast and least possible noise. In the near future, higher relative accuracy than reported in this thesis can be achieved provided that experimentalists should be able to load more number of atoms in the MOT chamber as compared to the atomic population considered in our simulations. Other two parameters which will play a vital role in increasing the relative accuracy for high precision measurements in the experiments of gravity gradiometry are: height of atomic fountain tube and the interrogation time. Taller the atomic fountain tube, more is the interrogation time. For example, if we consider an atomic fountain tube which is 1 m tall with an interrogation time of 160 ms [66], then interrogation time for a 4 m tall atomic fountain becomes 220 ms (as accounted in this thesis). Effects of longer interrogation times in the gravity gradiometry experiments without the implementation of the phase noise minimization scheme is shown in Figure 4.25. Also, not to forget that the sensitivity to inertial effects increases as the square of interrogation time.

An important outlook concerning the phase noise minimization scheme described and implemented in this thesis is presented as follows. The atom interference fringes detected at the upper and lower interferometers have a fixed phase difference proportional to the gravity gradient experienced by the atomic clouds. Therefore, when plotted one as the function of the other, atom interference fringes trace an ellipse whose eccentricity and rotation angle provides a measurement of the differential phase shift. As presented in this work, it is crucial to open the ellipse to minimize the error with which the differential phase is extracted. In fact, implementing the phase noise minimization scheme (by introducing a controlled phase shift in the vicinity of $\pi/2$) helps the elliptic contour transform into a circle, and that circle degenerates into a straight line representing a zero phase shift, henceforth displaying the cancellation of gravity gradients.

A concluding outlook on the experimental scheme presented in this thesis is that this unique apparatus will serve as a foundation for independent measurements of Newtonian Gravitational constant and precision tests of gravity to reveal new scenarios in physics.

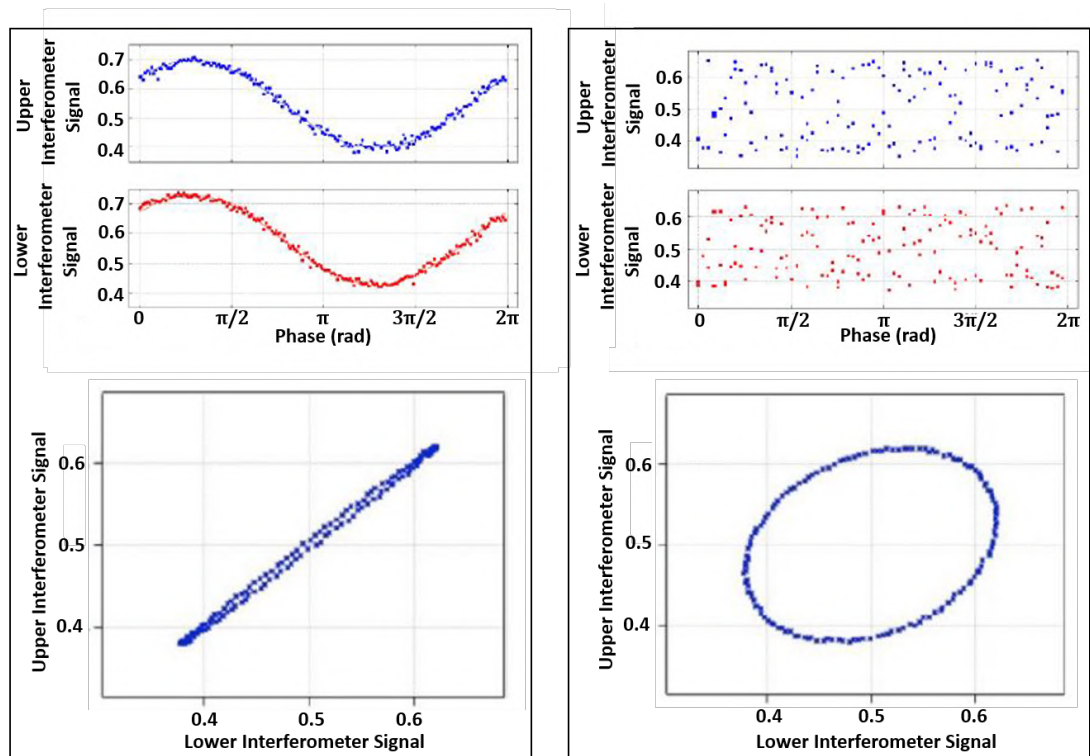


Figure 4.25: Effect of longer interrogation times on the interferometric signal in a gravity gradiometer: In the case presented at the left, a pair of clear sinusoidal interferometric signals are visible, but resulting in an ellipse which is not easily readable. In the case presented at the right, same pair of sinusoidal interferometric signals become very noisy, but yield a readable ellipse.

Chapter 5

Source Masses: Design, Calculation and Simulation

In this Chapter, we state the two possible source mass designs to produce a linear gravitational acceleration profile for the purpose of gravity gradient cancellation with a high relative accuracy using significantly lesser number of atoms in atomic cloud samples. These two favourable configurations are shown in Figure 5.1.

5.1 Source Mass Design: Geometrical Configuration - I

Source mass tower is arranged in the form of 16 individually (and closely) stacked identical - cylindrical tungsten source masses each with a height of 3.75 cm and radius of 10 cm. There are 12 identical source mass towers forming two hexagonal enclosure rings around the atomic fountain tube, as shown in the left side of Figure 5.1.

In order to include the hexagonal symmetry (only in configuration - I) and other effects from all the source mass towers, accurate knowledge of coordinates is necessary. All the coordinates in hexagonal configuration are defined in Figure 5.2.

5.1.1 Z - Coordinates

The sixteen cylindrical source masses stacked one above each other can be expressed by the following equation:

$$z_i^{(n)} = \mathcal{H}_T - \mathcal{H}n_i + D \quad (5.1)$$

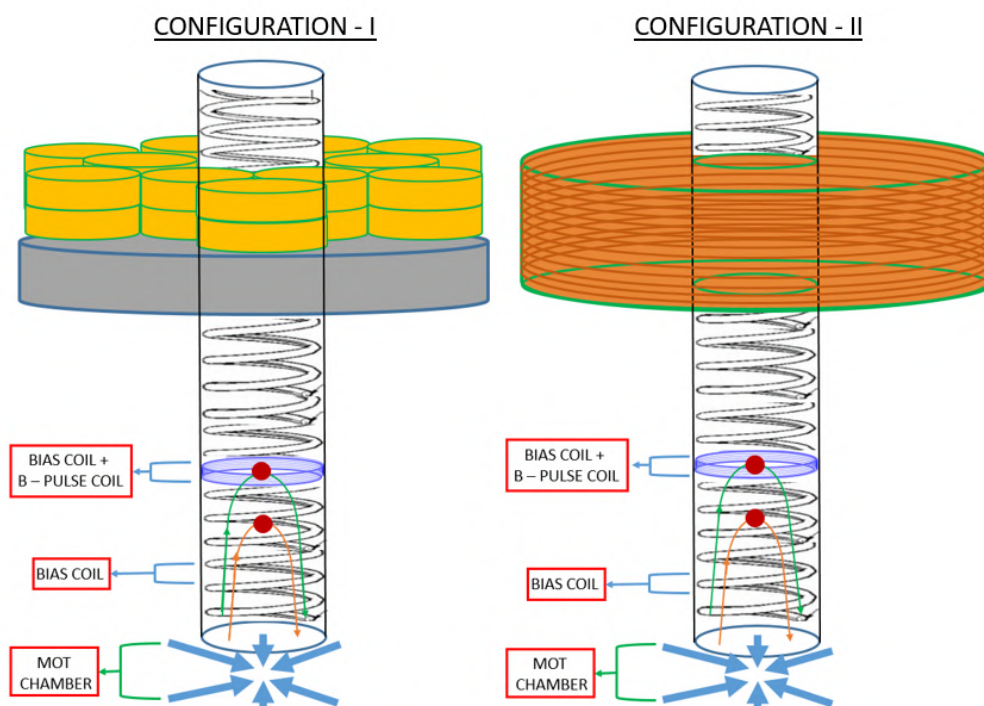


Figure 5.1: Two atomic clouds separated by a calibrated baseline \mathcal{D} producing phases due to the design of source masses ϕ_{SM} and from fictitious gravity gradient $\phi_{\Gamma_{zz}^*}$ arising due to two different geometrical configurations and choice of materials, LEFT: Geometrical arrangement comprising of stacked individual cylindrical tungsten source masses supported by aluminium torus platform, RIGHT: According to this geometrical construction, the source masses are prepared using 43 stacked copper rings, each of them possessing same torus geometry.

where \mathcal{H} is height of one cylindrical tungsten source mass, \mathcal{H}_T is the height of source mass tower, D is the distance of the lowest located source mass in the complete configuration of source mass tower with respect to the ground and $n_i = 1/2, 3/2, 5/2, 7/2, 9/2, \dots, 31/2$. Here, $n = 1$ gives the Z - coordinate of the cylindrical source mass located at the topmost position of the source mass tower. Similarly, $n = 2$ gives the Z - coordinate of the cylindrical source mass stacked exactly below the cylindrical source mass located at the topmost position of the cylindrical source mass tower.

5.1.2 X and Y - Coordinates

Let $x_i^{(0)}$ and $y_i^{(0)}$ be the X and Y coordinates of the cylindrical source mass in i th hexagonal ring, with $x_i^{(0)} = a/2 + R$ and $y_i^{(0)} = R$, where a is the radius of the atomic fountain tube and R is the radius of cylindrical source mass. Using the idea of 2×2 rotation matrix, other coordinates can be expressed as a linear combination of $x_i^{(0)}$ and $y_i^{(0)}$, as follows:

$$\begin{pmatrix} x_i^{(1)} \\ y_i^{(1)} \end{pmatrix} = \begin{bmatrix} \cos(\pi/3) & -\sin(\pi/3) \\ \sin(\pi/3) & \cos(\pi/3) \end{bmatrix} \begin{pmatrix} x_i^{(0)} \\ y_i^{(0)} \end{pmatrix} \quad (5.2)$$

$$\begin{pmatrix} x_i^{(2)} \\ y_i^{(2)} \end{pmatrix} = \begin{bmatrix} \cos(2\pi/3) & -\sin(2\pi/3) \\ \sin(2\pi/3) & \cos(2\pi/3) \end{bmatrix} \begin{pmatrix} x_i^{(0)} \\ y_i^{(0)} \end{pmatrix} \quad (5.3)$$

$$\begin{pmatrix} x_i^{(3)} \\ y_i^{(3)} \end{pmatrix} = \begin{bmatrix} \cos \pi & -\sin \pi \\ \sin \pi & \cos \pi \end{bmatrix} \begin{pmatrix} x_i^{(0)} \\ y_i^{(0)} \end{pmatrix} \quad (5.4)$$

$$\begin{pmatrix} x_i^{(4)} \\ y_i^{(4)} \end{pmatrix} = \begin{bmatrix} \cos(4\pi/3) & -\sin(4\pi/3) \\ \sin(4\pi/3) & \cos(4\pi/3) \end{bmatrix} \begin{pmatrix} x_i^{(0)} \\ y_i^{(0)} \end{pmatrix} \quad (5.5)$$

$$\begin{pmatrix} x_i^{(5)} \\ y_i^{(5)} \end{pmatrix} = \begin{bmatrix} \cos(5\pi/3) & -\sin(5\pi/3) \\ \sin(5\pi/3) & \cos(5\pi/3) \end{bmatrix} \begin{pmatrix} x_i^{(0)} \\ y_i^{(0)} \end{pmatrix} \quad (5.6)$$

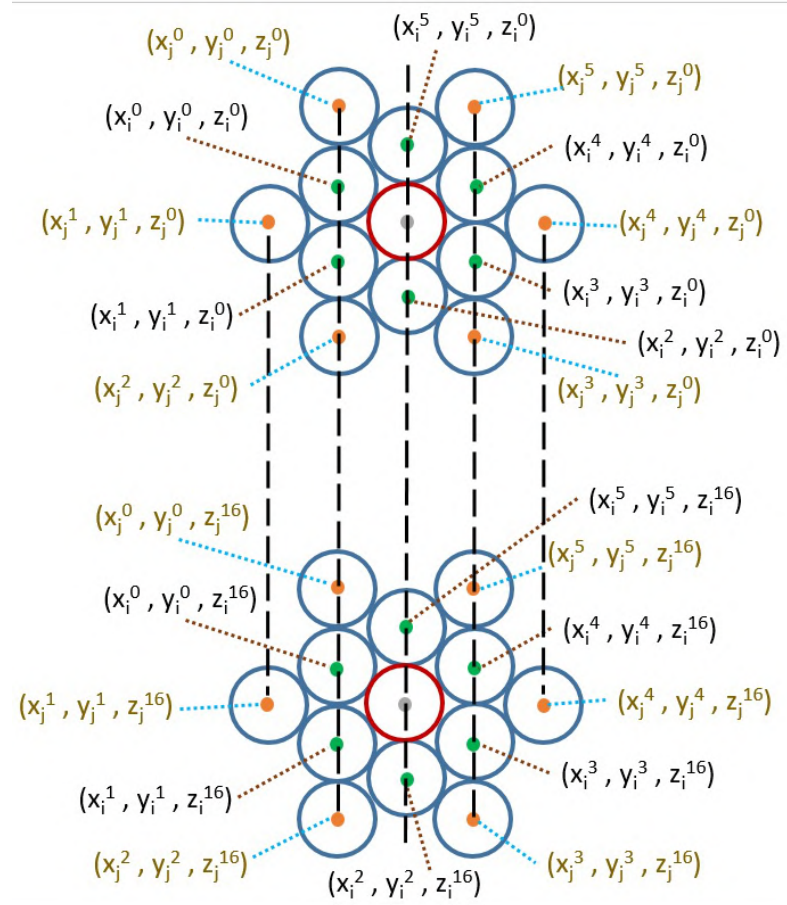


Figure 5.2: Cylindrical source masses (blue hollow circles) forming a hexagonal pattern starting from the individual cylindrical source masses located at the top of the six identical source mass towers, the other ones shown at the bottom of the figure denote the masses located at the bottom of the tower (closer to the ground). Calculation of all the coordinates is explained in Sections 5.1.1 and 5.1.2. Red hollow circle denotes the atomic fountain tube of the new design, and the pale grey colour-filled circles denote the atoms.

5.1.3 Gravitational Potentials and Accelerations

In this Section, we discuss about the comparison between the equations and nature of the gravitational potentials and accelerations deduced by two different mathematical approaches [17, 100]. This was crucial as it was necessary to determine the coinciding point between gravitational potential formulation of these two methods. One out of the two methods marks gravitational potential as a truncation of terms representing series governed by the value of azimuthal quantum number l [17], whereas the other represents an exact analytical solution [100]. The primary focus while deriving the exact analytical expression [100] was the calculation of standard deviation and the differential phase shift (see Figure 1.1 and Section 1.3) due to the uncertainties of the mean values of the initial coordinates and the velocities of atomic clouds, intended for a high precision measurement of G .

Comparison of Gravitational Potentials: Truncation v/s Analytic

Let R , ρ and h be the radius, density and height of cylindrical source mass respectively. Analytical formulation [100] provides the gravitational potential equation in terms of cylindrical coordinate system as follows:

$$\Phi(r, z) = -2G\rho \int_0^R dy \int_{r+\sqrt{R^2-y^2}}^{r-\sqrt{R^2-y^2}} d\xi \int_{z-h}^z \left(\frac{d\zeta}{\sqrt{y^2 + \xi^2 + \zeta^2}} \right) \quad (5.7)$$

Hence, to compare this potential with the gravitational potential from multipole expansion, this equation was first rewritten in the form of cylindrical coordinate system. Equation for potential generated by homogeneous cylindrical mass distribution [17] having mass M , height h and radius R in cylindrical coordinate system is:

$$U(r, z) = -\frac{GM}{R} \sum_{l=0}^{\infty} \beta^{2l+1} P_{2l} \left(\frac{z}{r} \right) \mathcal{Q}_l(\alpha^2) \quad (5.8)$$

where α and β are dimensionless coefficients:

$$\beta(r) = \frac{r}{R}$$

$$\alpha = \frac{h}{2R}$$

and

$$v' = \frac{r'}{R}$$

$r(\text{m})$	U_A	U_T
0.1	-1.48074×10^{-8}	-1.48074×10^{-8}
0.2	-7.27304×10^{-9}	-7.27304×10^{-9}
0.3	-4.77631×10^{-9}	-4.77630×10^{-9}
0.4	-3.56225×10^{-9}	-3.56222×10^{-9}
0.5	-2.84221×10^{-9}	-2.84228×10^{-9}
0.6	-2.36516×10^{-9}	-2.36515×10^{-9}
0.7	-2.02550×10^{-9}	-2.02551×10^{-9}
0.8	-1.77132×10^{-9}	-1.77132×10^{-9}
0.9	-1.57382×10^{-9}	-1.57389×10^{-9}
1.0	-1.41611×10^{-9}	-1.41611×10^{-9}

Table 5.1: Matching of gravitational potential from analytical and truncated approaches upto fourth decimal place.

$$u' = \frac{2z'}{h}$$

Values of r were incremented with 10 cm from 0 to 1 m, so as to compute the gravitational potentials using equations 5.7 and 5.8 for comparison of results. For $l = 3$ in equation 5.8, the gravitational potential was matched upto fourth decimal place as reported in the Table 5.1. Here, U_A is calculated from equation 5.7 and U_T is calculated from equation 5.8.

The Table 5.1 applies for truncation of terms upto $l = 3$ for column U_T . With $R = 0.1$ m, $h = 0.0375$ m, $\rho = 18000$ kg/m³, $M = 21.2058$ kg, $\alpha = 0.1875$ at $l = 3$, the coefficients and terms in equation 5.8 reduce as follows:

$$U(r, z)|_{l=3} = -1.41 \times 10^{-8} \left(\frac{0.1}{r} - \frac{\mathcal{I}_U}{r^5} + \frac{\mathcal{J}_U}{r^9} - \frac{\mathcal{S}_U}{r^{12}} \right) \quad (5.9)$$

where:

$$\mathcal{I}_U = -1.19 \times 10^{-4} (3z^2 - r^2)$$

$$\mathcal{J}_U = 1.34 \times 10^{-7} (3r^4 - 30r^2z^2 + 35z^4)$$

$$\mathcal{S}_U = 3.67 \times 10^{-10} (-5r^6 + 105r^4z^2 - 315r^2z^4 + 231z^6)$$

Truncation of series in equation 5.8 upto $l = 3$ resulted in the potential described by the equations above and are depicted as a 3D-plot in Figure 5.3. Likewise, the 3D - plot resulting from equation 5.7 is shown in Figure 5.4.

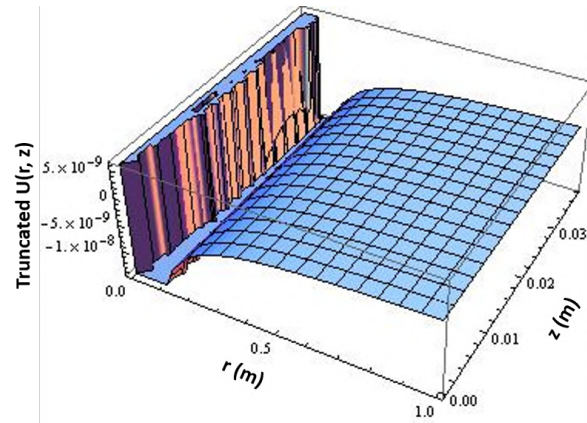


Figure 5.3: *Truncated Potential*: 3D-Plot using equation 5.9.

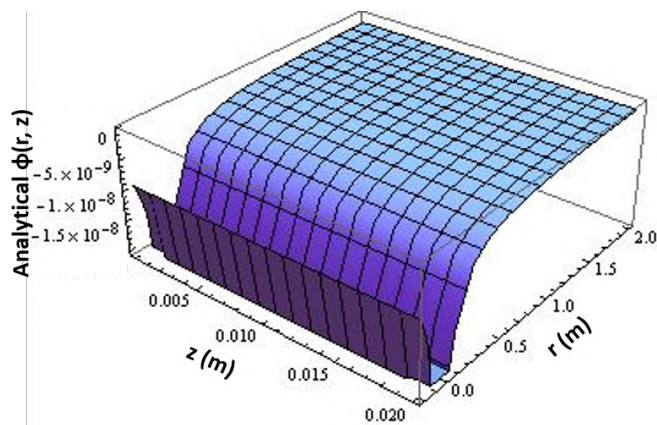


Figure 5.4: *Analytical Potential*: 3D-Plot using equation 5.7.

Comparison of Gravitational Accelerations: Truncation v/s Analytic

Gravitational acceleration arising from the gravitational potential (from series - truncation approach [17]) is deduced as follows:

$$\mathcal{A}_T = -\frac{\partial U(r, z)}{\partial r} \quad (5.10)$$

The above equation reduces for $R = 0.1$ m, $h = 0.0375$ m, $\rho = 18000$ kg/m³, $M = 21.2058$ kg, $\alpha = 0.1875$ at $l = 3$ as follows:

$$\mathcal{A}_T|_{l=3} = 1.41 \times 10^{-8} \left(\frac{2.38 \times 10^{-4}}{r^4} - \frac{0.1}{r^2} + \frac{\mathcal{I}_A}{r^6} + \frac{\mathcal{J}_A}{r^9} - \frac{\mathcal{S}_A}{r^{10}} - \frac{\mathcal{V}_A}{r^{13}} + \frac{\mathcal{Q}_A}{r^{14}} \right) \quad (5.11)$$

where:

$$\mathcal{I}_A = 5.95 \times 10^{-4} (3z^2 - r^2)$$

$$\mathcal{J}_A = 1.34 \times 10^{-7} (12r^3 - 60zr^2)$$

$$\mathcal{S}_A = 1.21 \times 10^{-6} (3r^4 - 30r^2z^2 + 35z^4)$$

$$\mathcal{V}_A = 3.56 \times 10^{-10} (420r^3z^2 - 30r^5 - 630rz^4)$$

$$\mathcal{Q}_A = 4.63 \times 10^{-9} (105r^4z^2 - 5r^6 - 315r^2z^4 + 231z^6)$$

Now, equation 5.11 needs to be compared to the analytical expression for gravitational acceleration [100]. Gravitational acceleration determined from analytical approach is stated as follows:

$$\mathcal{A}_A = 2G\rho(g_r(r, z) - g_r(r, z - h)) \quad (5.12)$$

where:

$$g_r(r, \zeta) = \left(\frac{\zeta}{2r\sqrt{\zeta^2 + (r+R)^2}} \right) [g_{\mathcal{K}}(r, \zeta) + g_{\mathcal{E}}(r, \zeta) + g_{\mathcal{E}_\pi}(r, \zeta)] \quad (5.13)$$

such that \mathcal{K} , \mathcal{E} and \mathcal{E}_π denote elliptic functions:

$$g_{\mathcal{K}}(r, \zeta) = -(\zeta^2 + 2r^2 + 2R^2)\mathcal{K}\left(\frac{4rR}{z^2 + (r+R)^2}\right)$$

$$g_{\mathcal{E}}(r, \zeta) = (\zeta^2 + (r+R)^2)\mathcal{E}\left(\frac{4rR}{z^2 + (r+R)^2}\right)$$

$r(\text{m})$	\mathcal{A}_A	\mathcal{A}_T
0.2	-3.82951×10^{-8}	-3.82140×10^{-8}
0.3	-1.62693×10^{-8}	-1.63236×10^{-8}
0.4	-9.01230×10^{-9}	-9.03528×10^{-9}
0.5	-5.72765×10^{-9}	-5.73803×10^{-9}
0.6	-3.96254×10^{-9}	-3.96779×10^{-9}
0.7	-2.90466×10^{-9}	-2.90757×10^{-9}
0.8	-2.22062×10^{-9}	-2.22235×10^{-9}
0.9	-1.75280×10^{-9}	-1.75389×10^{-9}
1.0	-1.41875×10^{-9}	-1.41947×10^{-9}

Table 5.2: Gravitational accelerations produced by set of dense tungsten source masses arranged as per configuration - I from analytical and truncated approaches.

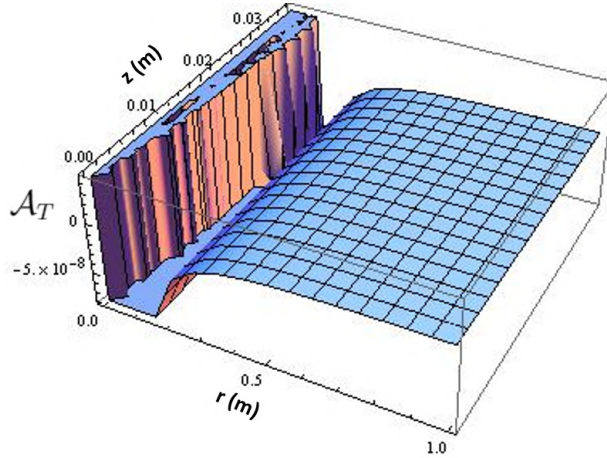


Figure 5.5: *Truncated Acceleration*: 3D-Plot using equation 5.11.

$$g_{\mathcal{E}_\pi}(r, \zeta) = \left(\frac{(r^2 - R^2)^2}{(r + R)^2} \right) (\zeta^2 + (r + R)^2) \mathcal{E}_\pi \left(\frac{4rR}{(r + R)^2} \middle| \frac{4rR}{\zeta^2 + (r + R)^2} \right)$$

Several values of r were chosen from 0 to 1m, so as to compute the gravitational accelerations using equations 5.11 and 5.12 for comparison of results presented in Table 5.2.

The gravitational acceleration profiles in both the cases are shown in Figures 5.5 and 5.6, with exact values provided in Table 5.2. Figure 5.7 shows the comparison of both gravitational acceleration and potential profiles calculated from both of these methods [17, 100].

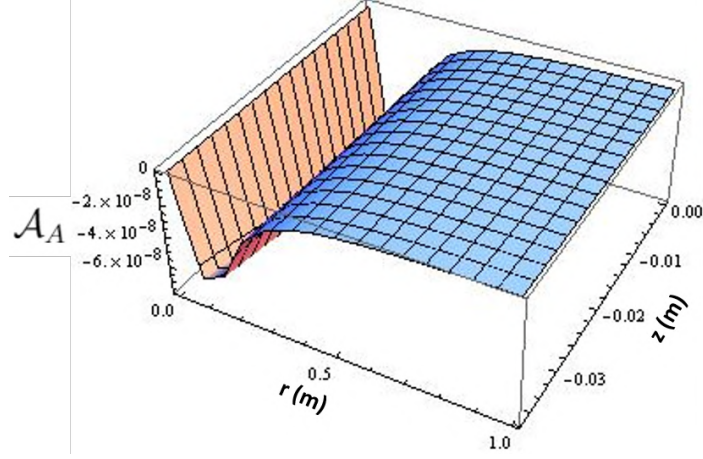


Figure 5.6: *Analytical Acceleration*: 3D-Plot using equation 5.12.

Source Masses: Total Gravitational Potential

Equation for potential generated by homogeneous cylindrical mass distribution in cylindrical coordinate system is:

$$U(r, z) = -\frac{GM}{R} \sum_{l=0}^3 \beta^{2l+1} Q_l(\alpha^2) P_{2l} \left(\frac{z}{r} \right) \quad (5.14)$$

with

$$Q_l(\alpha^2) = \int_{-1}^1 \int_0^1 v' P_{2l} \left(\frac{\alpha u'}{\sqrt{v'^2 + (\alpha u')^2}} \right) (v'^2 + (\alpha u')^2)^l dv' du' \quad (5.15)$$

where α and β are dimensionless coefficients:

$$\beta(r) = \frac{R}{r} \quad (5.16)$$

$$\alpha = \frac{h}{2R} = 0.1875 \quad (5.17)$$

Magnitude of the position vector r (between the coordinates of atom (x, y, z) and coordinates of source mass (x_i^k, y_i^k, z_i^k)) for the case of i th (in our case, the ring assumes a hexagonal form) ring of source masses modifies (in cartesian coordinate system) as follows:

$$r_i^k = \sqrt{(x - x_i^k)^2 + (y - y_i^k)^2} \quad (5.18)$$

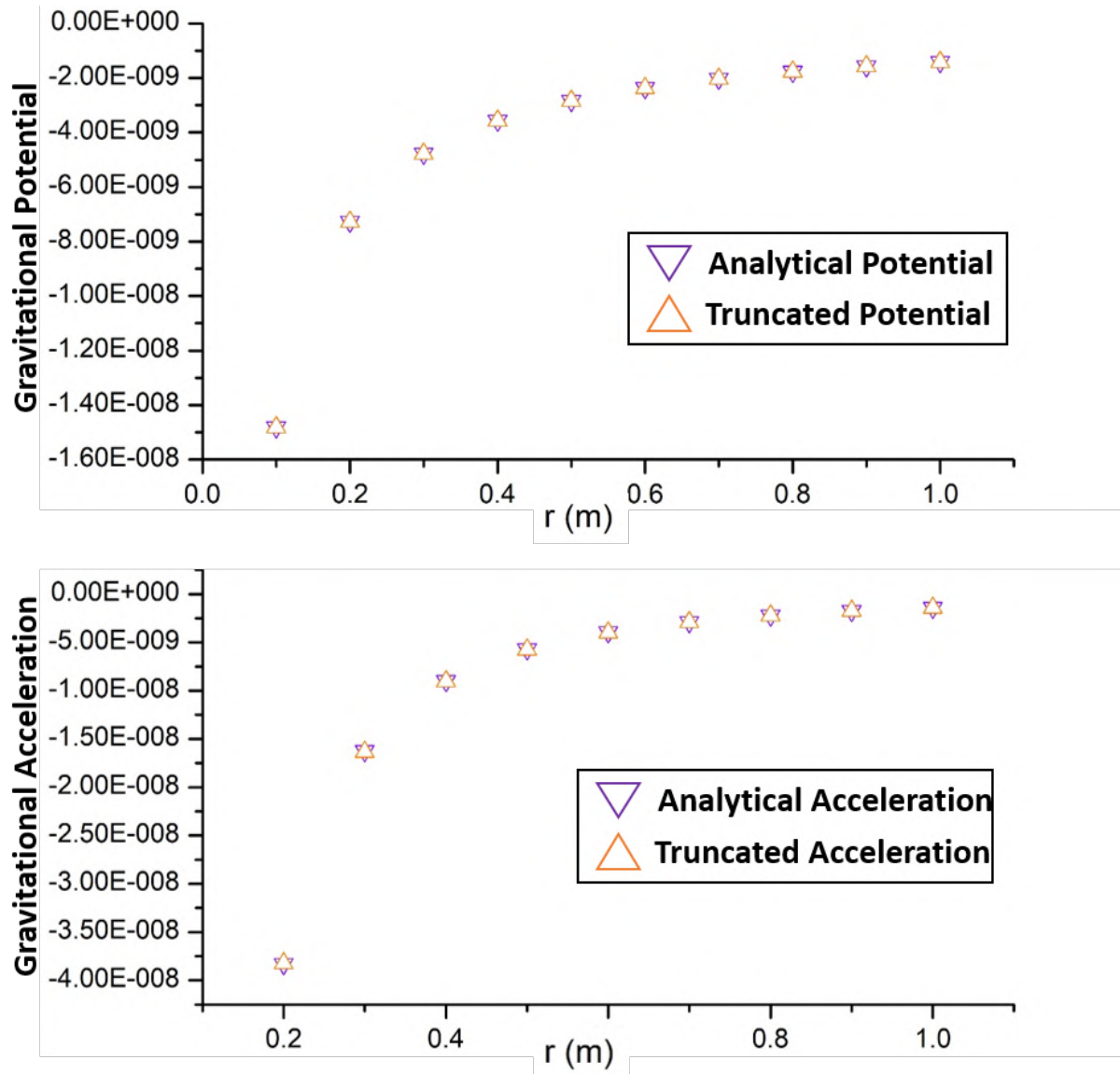


Figure 5.7: Comparison of values of gravitational accelerations and gravitational potentials (for different values of r), using multipole expansion from truncated approach [17] for $2l = 6$, as this was matched with exact analytical solution [100].

resulting in the modification of β :

$$\beta(r_i^k) = \frac{R}{r_i^k} = \frac{R}{\sqrt{(x - x_i^k)^2 + (y - y_i^k)^2}} \quad (5.19)$$

Gravitational potential experienced by single atom in one gravimeter due to i th ring of source masses is:

$$U(x - x_i^k, y - y_i^k, z - z_i^n) = -\frac{GM}{R} \sum_{l=0}^{\infty} \beta^{2l+1} \mathcal{Q}_l(\alpha^2) P_{2l} \left(\frac{z - z_i^n}{\sqrt{(x - x_i^k)^2 + (y - y_i^k)^2}} \right) \quad (5.20)$$

Total gravitational potential experienced by single atoms in each gravimeter due to all the source masses is expressed as:

$$U(x - x_i, y - y_i, z - z_i) = \sum_{i=0}^1 \sum_{n=1}^{16} \sum_{k=0}^5 U(x - x_i^k, y - y_i^k, z - z_i^n) \quad (5.21)$$

Gravitational potential difference (equation 5.21) experienced by two individual atoms (for example; if one atom is located at 1.54 m and the other atom is located at 1.77 m above the point of origin of the fountain tube) inside the atomic fountain tube surrounded by the two concentric hexagonal rings $i = 0$ and $i = 1$:

$$U|_{z=1.54} = U_{i=0}(x - x_0, y - y_0, 1.54 - z_0) + U_{i=1}(x - x_1, y - y_1, 1.54 - z_1) \quad (5.22)$$

$$U|_{z=1.77} = U_{i=0}(x - x_0, y - y_0, 1.77 - z_0) + U_{i=1}(x - x_1, y - y_1, 1.77 - z_1) \quad (5.23)$$

leading to gravitational potential difference U_{DIFF} experienced by two - single atoms forming a gravimeter:

$$U_{DIFF} = U|_{z=1.77} - U|_{z=1.54} \quad (5.24)$$

Extending all this knowledge to the case of atomic clouds, a Monte Carlo simulation was developed to produce the results shown in Section 5.6, of which the complete code is provided in Appendix B.

Torus-shaped Platform: Gravitational Potential

The purpose of the torus-shaped platform is to support the massive collection of the dense tungsten source masses (in configuration - I). When the platform is included in the system of source masses, platform will also play a role along with the existing system in impacting the atomic clouds with its gravitational potential.

For a torus-shaped platform, forming one external and one internal rings, their gravitational potential is expressed as a difference of gravitational potentials of two rings with unequal radii, resulting in the formation of internal and external rings of a torus. This is done because there is supposed to be a vacuum region created due to unequal radii of the two torus-shaped rings.

For the internal ring:

$$U_{Rin}(r, z) = -G\pi\rho_{Al}r_{i1}^2(V_1(z) + 0.5(\eta(r))^2V_2(z)) \quad (5.25)$$

where ρ_{Al} is density of aluminium platform, $V_1(z)$ and $V_2(z)$ are z-dependent gravitational potential terms expressed as:

$$\begin{aligned} V_1(z) &= V_1^1 + V_1^2 + V_1^3 + V_1^4 \\ V_1^1 &= a_1^2 \left(\left(\frac{y(z) + b_1}{a_1} \right) - \left(\frac{y(z) - b_1}{a_1} \right) \right) \\ V_1^2 &= -((y(z) + b_1) - (y(z) - b_1)) \\ V_1^3 &= (y(z) + b_1)(h_2(z) - h_4(z)) \\ V_1^4 &= -(y(z) - b_1)(h_1(z) - h_3(z)) \end{aligned}$$

and:

$$\begin{aligned} V_2(z) &= V_2^1 + V_2^2 + V_2^3 + V_2^4 \\ V_2^1 &= -\frac{y(z) + b_1}{h_2(z)} \\ V_2^2 &= \frac{y(z) - b_1}{h_1(z)} \\ V_2^3 &= \frac{y(z) + b_1}{h_4(z)} \\ V_2^4 &= -\frac{y(z) - b_1}{h_3(z)} \end{aligned}$$

such that for the internal ring:

$$h_1(z) = \sqrt{a_1^2 + (y(z) - b_1)^2}$$

$$h_2(z) = \sqrt{a_1^2 + (y(z) + b_1)^2}$$

$$h_3(z) = \sqrt{1 + (y(z) - b_1)^2}$$

$$h_4(z) = \sqrt{1 + (y(z) + b_1)^2}$$

where:

$$\eta(r) = \frac{r}{r_{i1}}$$

$$y(z) = \frac{z}{r_{i1}}$$

$$a_1 = \frac{r_{e1}}{r_{i1}}$$

$$b_1 = \frac{r_{i1}H_1}{2}$$

Similarly, for the external ring:

$$U_{R_{out}}(r, z) = -G\pi\rho_{Al}r_{i2}^2(V_{1e}(z) + 0.5(\eta_e(r))^2V_{2e}(z)) \quad (5.26)$$

where:

$$V_{1e}(z) = V_{1e}^1 + V_{1e}^2 + V_{1e}^3 + V_{1e}^4$$

$$V_{1e}^1 = a_2^2 \left(\left(\frac{y_e(z) + b_2}{a_2} \right) - \left(\frac{y_e(z) - b_2}{a_2} \right) \right)$$

$$V_{1e}^2 = -((y_e(z) + b_2) - (y_e(z) - b_2))$$

$$V_{1e}^3 = (y_e(z) + b_2)(h_{2e}(z) - h_{4e}(z))$$

$$V_{1e}^4 = -(y_e(z) - b_2)(h_{1e}(z) - h_{3e}(z))$$

and:

$$V_{2e}(z) = V_{2e}^1 + V_{2e}^2 + V_{2e}^3 + V_{2e}^4$$

$$V_{2e}^1 = -\frac{y_e(z) + b_2}{h_{2e}(z)}$$

$$V_{2e}^2 = \frac{y_e(z) - b_2}{h_{1e}(z)}$$

$$V_{2e}^3 = \frac{y_e(z) + b_2}{h_{4e}(z)}$$

$$V_{2e}^4 = -\frac{y_e(z) - b_2}{h_{3e}(z)}$$

such that for the external ring:

$$h_{1e}(z) = \sqrt{a_2^2 + (y_e(z) - b_2)^2}$$

$$h_{2e}(z) = \sqrt{a_2^2 + (y_e(z) + b_2)^2}$$

$$h_{3e}(z) = \sqrt{1 + (y_e(z) - b_2)^2}$$

$$h_{4e}(z) = \sqrt{1 + (y_e(z) + b_2)^2}$$

where:

$$\eta_e(r) = \frac{r}{r_{i2}}$$

$$y_e(z) = \frac{z}{r_{i2}}$$

$$a_2 = \frac{r_{e2}}{r_{i2}}$$

$$b_2 = \frac{r_{i2}H_2}{2}$$

Hence, the gravitational potential (in cylindrical coordinate system) of the torus-shaped platform becomes:

$$U_P(r, z) = U_{R_{out}}(r, z) - U_{R_{in}}(r, z) \quad (5.27)$$

Mathematical expression for phase due to source masses

In this Section, we theoretically state the phase calculation due to a set of stacked monolithic cylindrical source masses in both the presence and absence of an aluminium torus-shaped platform (described in preceding section). In the past, some theoretical methods to calculate exact phase shifts [101] and interferometric phase shift fluctuations [102] have been demonstrated.

Let U_{UP} and U_{DW} be the gravitational potentials experienced by atoms in the upper and lower arms of a single-atom interferometer respectively, where U is given by equation 5.21. The complete phase difference from time $t = 0$ to

$t = 2T$ due to the presence of new design of source masses is mathematically expressed as:

$$\begin{aligned}\phi_{SM} = & \frac{m_{Rb}}{\hbar} \oint U_{UP}(x - x_i, y - y_i, z - z_i) dt \\ & - \frac{m_{Rb}}{\hbar} \oint U_{DW}(x - x_i, y - y_i, z - z_i) dt\end{aligned}\quad (5.28)$$

The above equation is valid for the case when there is no platform present. To include the geometry of the platform, the gravitational potential of the platform U_P is also included:

$$\begin{aligned}\phi_{SM} = & \frac{m_{Rb}}{\hbar} \oint U_{UP}^{TOT}(x - x_i, y - y_i, z - z_i) dt \\ & - \frac{m_{Rb}}{\hbar} \oint U_{DW}^{TOT}(x - x_i, y - y_i, z - z_i) dt\end{aligned}\quad (5.29)$$

where,

$$U^{TOT} = U + U_P \quad (5.30)$$

5.1.4 Determination of radius of tungsten source mass cylindrical disks

Using the mathematical formulation [100] for gravitational accelerations for a dense cylinder in cylindrical coordinate system, we firstly estimate the region in which source mass (made out of material of user's choice) exhibits a linear trend of acceleration due to gravity. This estimation is performed using our result of $l = 3$ which comes from a thorough study on the comparison between the gravitational potentials and accelerations of a solid dense homogeneous cylinder (preceding section). The equations are rewritten labelling all the variables of interest here as follows:

$$\mathcal{A}(r, z, R, h) = 2G\rho \left(g_r \left(r, z + \frac{h}{2}, R \right) - g_r \left(r, z - \frac{h}{2}, R \right) \right) \quad (5.31)$$

where:

$$g_r(r, \zeta, R) = \left(\frac{\zeta}{2r\sqrt{\zeta^2 + (r+R)^2}} \right) [g_{\mathcal{K}}(r, \zeta, R) + g_{\mathcal{E}}(r, \zeta, R) + g_{\mathcal{E}_\pi}(r, \zeta, R)]$$

such that \mathcal{K} , \mathcal{E} and \mathcal{E}_π denote elliptic functions:

$$g_{\mathcal{K}}(r, \zeta, R) = -(\zeta^2 + 2r^2 + 2R^2)\mathcal{K} \left(\frac{4rR}{z^2 + (r+R)^2} \right)$$

$$g_{\mathcal{E}}(r, \zeta, R) = (\zeta^2 + (r + R)^2) \mathcal{E} \left(\frac{4rR}{z^2 + (r + R)^2} \right)$$

$$g_{\mathcal{E}_{\pi}}(r, \zeta, R) = \left(\frac{(r^2 - R^2)^2}{(r + R)^2} \right) (\zeta^2 + (r + R)^2) \mathcal{E}_{\pi} \left(\frac{4rR}{(r + R)^2} \middle| \frac{4rR}{\zeta^2 + (r + R)^2} \right)$$

Furthermore, using the same mathematical formulation, the acceleration experienced by a set of hexagonal arrangement of tungsten source masses can be represented as:

$$\mathcal{A}_z = 6\mathcal{A}(2R, z, R, h) + 6\mathcal{A}(2R\sqrt{3}, z, R, h) \quad (5.32)$$

and in the context of mathematical method following series truncation (the result with $l = 3$), the acceleration experienced is expressed as:

$$\mathcal{A}_z = -\frac{\partial U(r, z, R, h)}{\partial z} \quad (5.33)$$

Plotting equations 5.31, 5.32, 5.33 and first-order negative partial derivative of equation 5.9 provides a linear trend estimate for earth's acceleration due to gravity at $H = 3.75$ cm and $R = 10$ cm as shown in Figures 5.8 and 5.9. Figure 5.10 depicts a good level of compromise regarding the stability of gravity gradient magnitude (within a permissible baseline for the experiment) for chosen radius disk of 10 cm as compared to the other chosen radii magnitudes (8 cm and 12 cm).

5.2 Source Mass Design: Geometrical Configuration - II

In this configuration, the source mass design assumes the geometry analogous to that of the aluminium torus-shaped platform from former configuration (Figure 5.11). The gravitational potential is taken of the form presented extending equation 5.25 to 12 consecutively stacked copper rings:

$$U^{Cu}(r - r_m, z - z_m) = -G\pi\rho_{Cu}r_i^2 \sum_{m=1}^{12} (V_1(z - z_m) + 0.5(\eta(r - r_m))^2 V_2(z - z_m)) \quad (5.34)$$

where the summation index m denotes the number of cascaded torus-shaped rings. According to this design, the overall phase difference in the time circuit

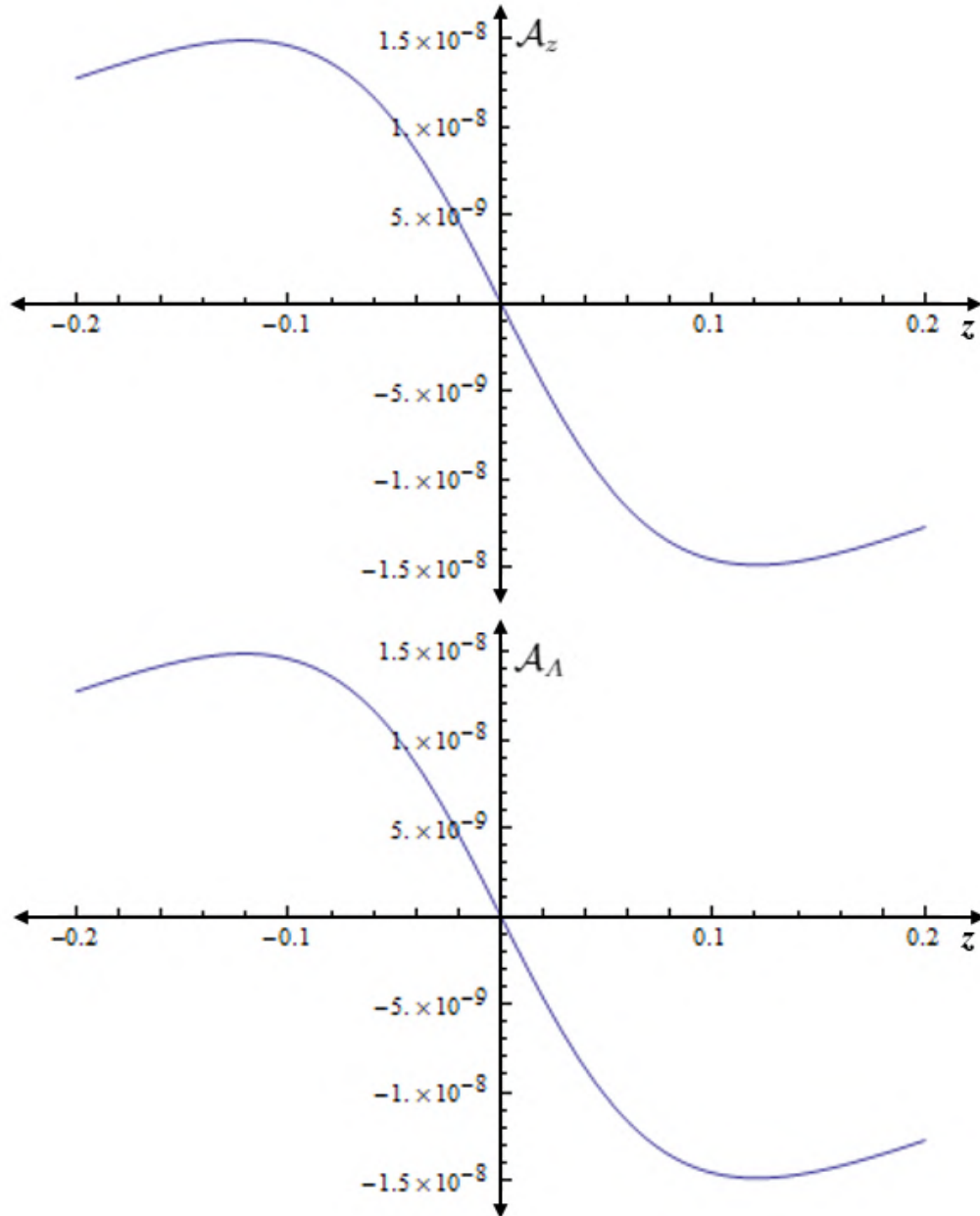


Figure 5.8: Plots representing variation in gravitational acceleration along the axis of gravity - *Upper Graph*: Plot from equation 5.33, *Lower Graph*: Plot from equation 5.31. Along with a display of linear trend, it is clearly visible that both of these plots coincide exactly when the radius and height of tungsten cylindrical disk are calculated to be 0.1 m and 0.0375 m respectively.

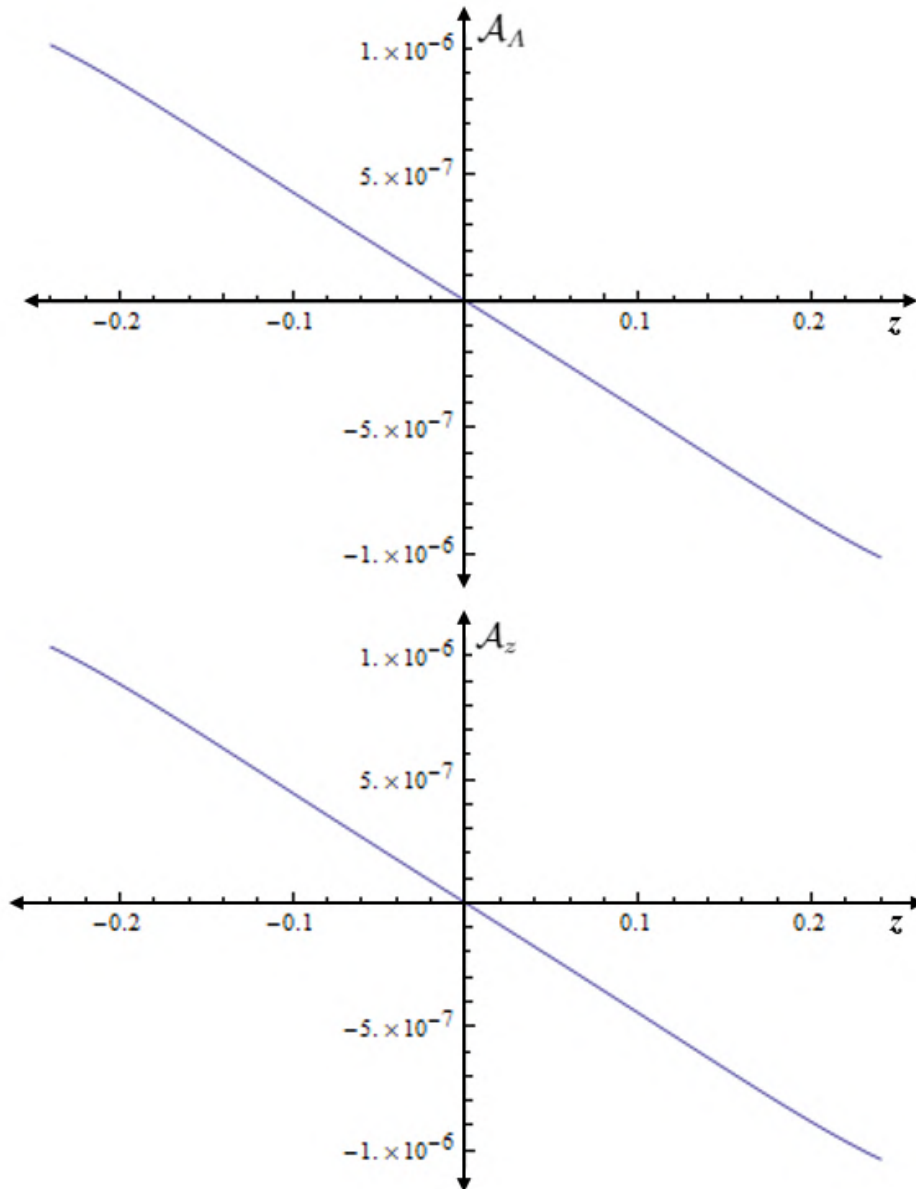


Figure 5.9: Plots representing constancy in gravity gradient Γ_{zz} along the fountain axis - *Upper Graph*: Plot from equation 5.32, *Lower Graph*: Plot from a negative first - order partial derivative (with respect to z) of equation 5.9 at $l = 3$. Along with a display of linear trend, it is clearly visible that both of these plots coincide exactly when the radius and height of tungsten cylindrical disk are calculated to be 0.1 m and 0.0375 m respectively.

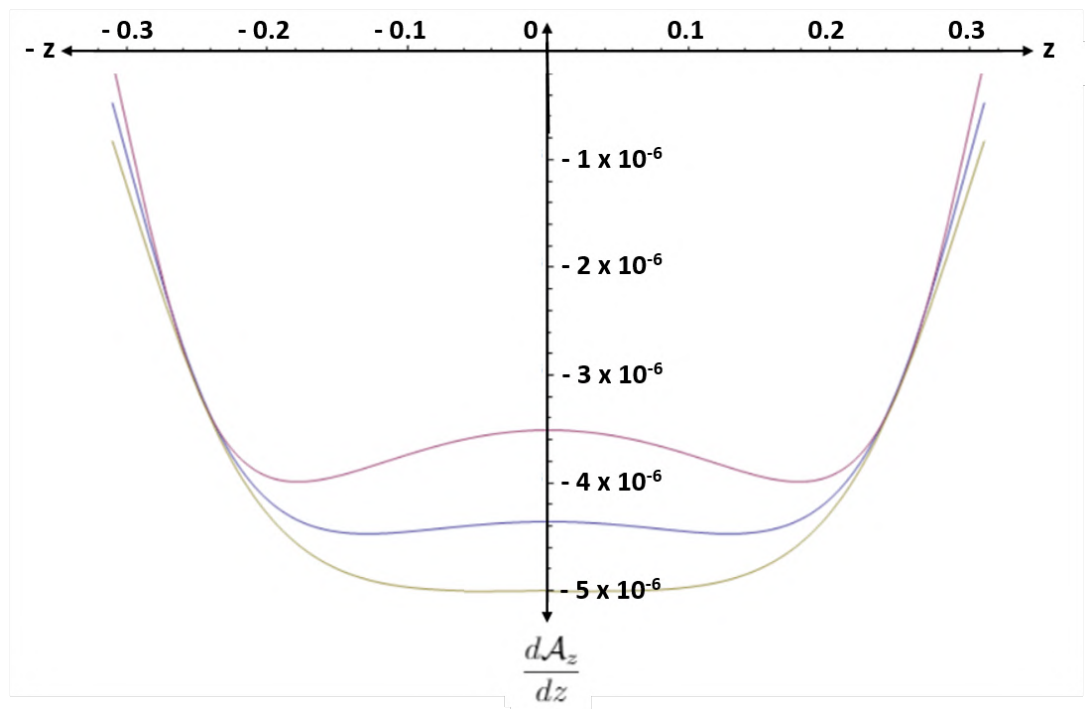


Figure 5.10: Plots created using first derivative of equation 5.34: Variation in gravity gradient Γ_{zz} with respect to slight variation in the radius of the tungsten cylindrical disk-shaped source masses. Here, the blue-coloured, magenta-coloured and dark-yellow coloured curves mark chosen radius disks as 10 cm, 8 cm and 12 cm respectively.

from $t = 0$ to $t = 2T$ becomes:

$$\begin{aligned} \phi_{SM}^{Cu} = & \frac{m_{Rb}}{\hbar} \oint U_{UP}^{Cu}(r - r_m, z - z_m) dt \\ & - \frac{m_{Rb}}{\hbar} \oint U_{DW}^{Cu}(r - r_m, z - z_m) dt \end{aligned}$$

such that subscripts UP and DW in U^{Cu} respectively indicate upper and lower trajectory arms of a single atom interferometer.

This configuration of source mass is carved out of copper simply because copper as a material is cheaper and in our case it possesses a simplified geometry along with it being homogeneous and pure. As shown in Figure 5.12, there are 12 identical copper rings stacked one above the other eventually forming as a single copper torus-shaped block. As presented in this thesis, we present two different geometrical source mass configurations in order to explore the physics arising from phase shifts arising due to gravitational potentials impacted on atoms by different materials. With our established design of configuration - I, we use an idea of a dimensionless parameter η . This ratio $\eta = \sqrt{\frac{\rho_W}{\rho_{Cu}}}$ is a relationship between the density of the materials used to build source masses, hence in our case it is tungsten(ρ_W) and copper(ρ_{Cu}). While in previous experimental schemes a high density value was instrumental to cancel the Earth's gravity gradient around trajectories apogee, here such condition is no longer required. However, when we use copper, the induced gravity gradient drops to half that of tungsten. Therefore, the overall source mass system size needs to be recalibrated in order to maintain the same gradiometric signal. With respect to this essential criteria, since the phase resulting from the real gravity gradient (i.e., due to the design of source masses) is proportional to the baseline and atoms dropping distance, a reduction in the average gravity gradient Γ_{zz} of a factor η is compensated by an increase in linear dimension (and therefore total mass) of $\sqrt{\eta}$. With this knowledge, this torus-shaped source mass geometry becomes applicable and useful for the other source mass models created using any suitable materials. Employing this dimensionless ratio η , it results in scaling of existing parameters of configuration - II with respect to configuration - I as shown vividly in Table 5.3.

5.3 Precise estimation of initial $\pi/2$ -pulse

In this Section, we precisely calculate the initial $\pi/2$ -pulse coordinates. In the vicinity of these coordinates, our cold rubidium atomic cloud samples will be launched when they are subjected under two different configurations of

Parameter(Units)	Configuration-I	Configuration-II
$\rho(\text{kg/m}^3)$	18300	8960
$H(\text{m})$	0.6	0.6η
$R^{EXT}(\text{m})$	0.362	0.362η
$R^{INT}(\text{m})$	0.105	0.105η
$z_0(\text{mm})$	-161.7,-170	-232.2
$T(\text{s})$	0.22	$0.22\sqrt{\eta}$
$d(\text{m})$	0.23	0.23η
$v_0(\text{m/s})$	$g(T+0.001)$	$g(T+0.001\eta)$

Table 5.3: Parameters impacted due to presence of η , as used in simulations regarding set of cylindrical tungsten source masses from configuration - I and cascaded copper rings in configuration - II. Here, ρ , H , R^{EXT} , R^{INT} , z_0 , T , d and v_0 respectively indicate the densities, complete source mass arrangement height, external radius (of aluminium platform), internal radius (of aluminium platform), initial $\pi/2$ -pulse Z-coordinate, interrogation time, baseline and atomic cloud launch velocity.

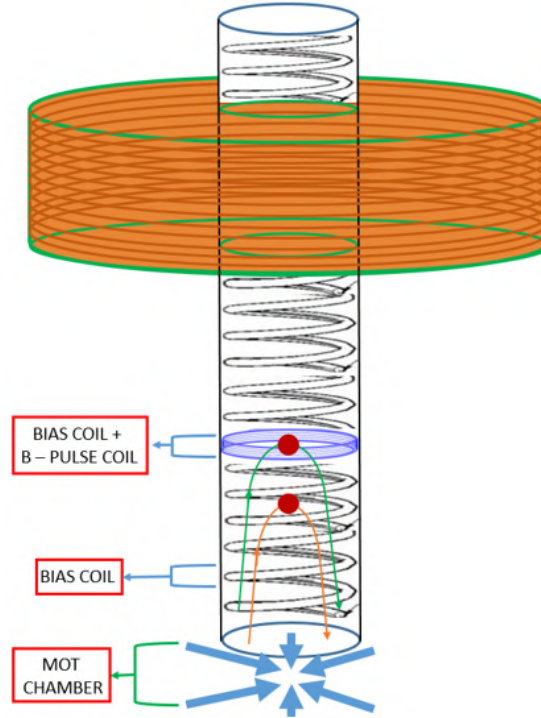


Figure 5.11: Cascaded torus - shaped source mass copper rings forming configuration - II.

source masses, configuration - I and configuration - II. This means that at this event, the atomic clouds should traverse first half of their parabolic launch from their modified Mach - Zehnder interferometric sequence as specified in Chapter 3.

Using classical trajectory equations of atoms (equations 4.12 - 4.19) and gravitational potential and gravitational acceleration equations from preceding section, the idea here is to equate the first derivative of the gradiometric phase (with respect to z) to zero which corresponds to determining locally a region where the value of gravity gradient can be made linear and equal both for upper and lower clouds. These first - order phase derivatives are marked as ϕ_A^P (for configuration - I with platform present), ϕ_A (for configuration - I with platform absent) and ϕ_A^{Cu} (for configuration - II).

Studying the impact of the source mass system concerning both the configurations, we estimated the initial $\pi/2$ -pulse coordinates (along Z-axis) of atomic clouds precisely by plotting variation in first order derivative of gradiometric phase versus a possible range of values that constitute the offset points marking as initial $\pi/2$ -pulse coordinates of our cold atomic cloud samples. Figures 5.12 and 5.13 show the Z-coordinates marking the initial $\pi/2$ -pulse coordinates, representing the variation of first derivative of gradiometric phase for configurations I and II respectively. For configuration - I, the initial firing point for $\pi/2$ -pulse is -161.7 mm and for configuration - II, the initial firing point of $\pi/2$ -pulse is -232.2 mm. The negative sign indicates the initial $\pi/2$ -pulse coordinates are below the origin of the atomic fountain, which lies at the midway of the complete atomic fountain tube.

These precisely estimated atomic cloud launch points were accounted in our simulations, as stated later in Section 5.6.

5.4 Linearity of gravitational acceleration

In principle, we have a limited region where the constant behavior of gravity gradients can be observed. For the sake of compactification of experimental apparatus, it is wise to stay within an altitude range corresponding to a few tons as per the total mass of desirable material to build the source masses. For example, if we choose the experimental configuration with the parameters listed in Section 5.2 for configuration - I, we have a region inside the atomic fountain of 0.5 m where gravity gradient can be made constant. This length of 0.5 m along the axis of gravity is 10 cm lesser than the total height of source mass configuration in configuration - I. At the centre, the gravity gradient is perfectly linear with visible nonlinearities at the edges. Strictly speaking, in this region of 0.5 m, linearity is better than elsewhere inside the

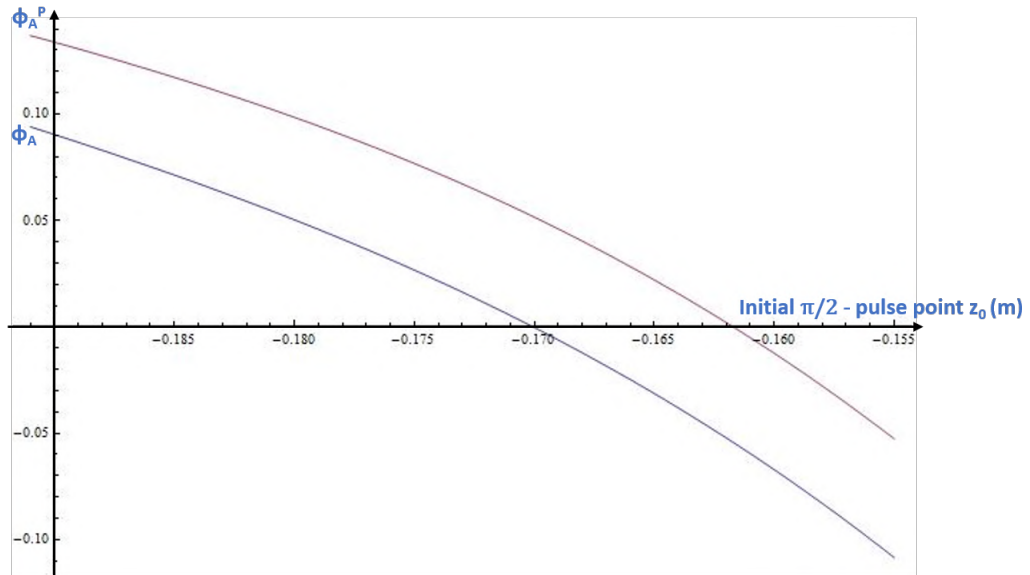


Figure 5.12: Variation of ϕ_A (blue curve) and ϕ_A^P (magenta curve): X-intercepts at -170 mm (ϕ_A -curve) and -161.70 mm (ϕ_A^P -curve) marking the cases of platform (in configuration - I) being absent and present respectively. This means that at these intercept values, the phase derivatives ϕ_A and ϕ_A^P take zero value concerning configuration - I.

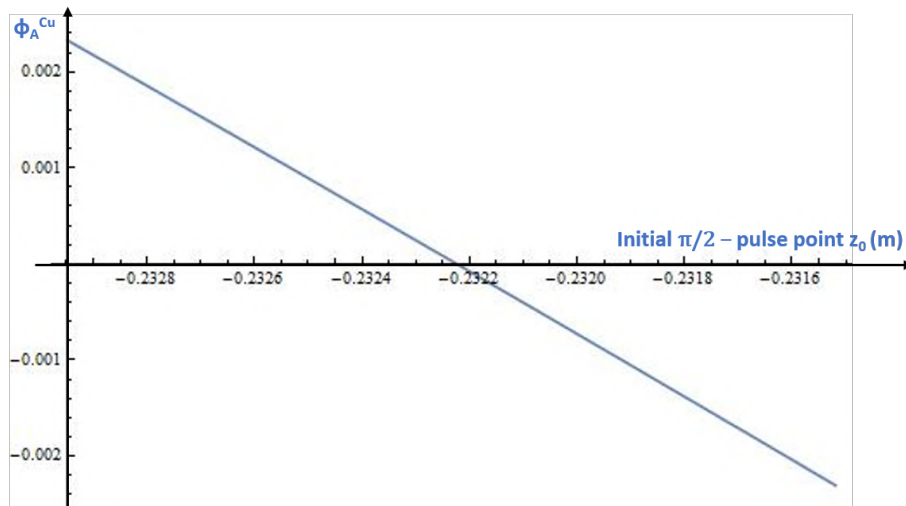


Figure 5.13: Variation of ϕ_A^{Cu} : The curve makes an intercept on X-axis at -232.22 mm, meaning that at this intercept value, the phase derivative ϕ_A^{Cu} is zero for configuration - II.

atomic fountain tube. Gradiometric phase ϕ_{GRD} is due to: $k_{\text{eff}}\gamma dT^2$, where d is baseline between the two cold atomic cloud samples, γ is the gravity gradient and T^2 is the square of the half time of the parabolic launch of atomic clouds, meaning that the atomic clouds acquire their apogees at the time T . So, the idea here is to balance these two parameters of interest: d and T . To achieve this, there exist two possibilities, one possibility is with small d and large T and the other possibility is large d and small T . In this case where d starts to be comparable with 0.5 m, our apogee is the place around where the atoms spend most of their time, quid pro quo most of the phase is accumulated around the apogee at time T . At this point, if we use this approach, apogee is in the region where gravity gradient is not constant, hence the choice of a larger d value is not good. In all, it is necessary to have apogee around the center but with maximizing also T^2 , henceforth arriving at a good compromise between d and T^2 . Note that with a shorter baseline between the atomic clouds, one cannot maximize the sensitivity. As a result, our compromise marks a trade-off between the two key parameters of interest d and T : $T \approx \sqrt{\frac{2d}{g}}$. To summarize, we achieve a maximized sensitivity without losing too much linearity (of gravitational acceleration) keeping in mind that the magnitudes of freely falling distance and baseline are nearly equal.

5.5 Simulation and Calculation: Phases due to fictitious gravity gradient

Readapting the effective wavevector Δk_{eff} of central π -pulse, a fictitious gravity gradient is generated which exactly compensates the effect of ambient gravity gradient. Here $k_{\text{eff}} = 4\pi/\lambda$ is wavevector for two - photon Raman transition. In our case, chosen wavelength is $\lambda = 421.5$ nm for the dipole-allowed transition ^{87}Rb : $5S_{1/2} \rightarrow 6P_{3/2}$. Detuning the laser frequency of the central π -pulse by $\Delta\nu$ imparting the momentum to atoms, the required change in magnitude in the effective wavevector to compensate the ambient gravity gradient:

$$\Delta k_{\text{eff}} = \frac{4\pi\Delta\nu}{c} \quad (5.35)$$

Simulated corresponding fictitious gravity gradient is expressed as:

$$\Gamma_{zz}^* = \frac{-2\Delta k_{\text{eff}}}{k_{\text{eff}}T^2} \quad (5.36)$$

The experimental matching condition to be achieved is:

$$\Phi = k_{\text{eff}}T^2(\Gamma_{zz} - \Gamma_{zz}^*)(d + \Delta v_z T) \quad (5.37)$$

where d is the baseline, Δv_z is the differential velocity between the two cold atomic cloud samples and T is the interrogation time. To find the crossing point(s) in the linear fit of gradiometric phase versus laser detuning frequency, the following expression gives the linear dependence of the gradiometric phase on the laser detuning frequency:

$$\Phi(\Delta\nu) = -\left(k_{\text{eff}}\Gamma_{zz}T^2 + \frac{8\pi}{c}\Delta\nu\right)(d + \Delta v_z T) \quad (5.38)$$

To summarize, at frequency value $\Delta\nu$ which nulls the differential phase, two gravimeters display the same phase magnitudes, independently of their positions.

This scheme generates a fictitious gravity gradient, expressed as a tensor Γ_{zz}^* and a corresponding differential phase which is equal to the phase from the real gravity gradient. Now, we will derive the mathematical expression of this phase as follows. The phase gradient over the fixed baseline between the centre of mass coordinates of the two clouds is:

$$\nabla\phi = \frac{\phi_{SM}(x_{UP}^{CM}, y_{UP}^{CM}, z_{UP}^{CM}) - \phi_{SM}(x_{DW}^{CM}, y_{DW}^{CM}, z_{DW}^{CM})}{d} \quad (5.39)$$

For our understanding to be more realistic, we include the translation of atoms along all the three axes, resulting in change in magnitude of the baseline, which is written as follows:

$$\mathcal{D} = (z_{UP} - z_{DW}) + (v_z^{UP} - v_z^{DW})T \quad (5.40)$$

In the above equation, v_z^{UP} and v_z^{DW} indicate the velocities of atoms inside the atomic clouds located at the upper and lower positions respectively, separated by the recalculated baseline \mathcal{D} . Hence, phase arising from fictitious gravity gradient becomes:

$$\phi_{\Gamma_{zz}^*} = \mathcal{D}\nabla\phi \quad (5.41)$$

Finally, to see this gravity gradient compensation scheme in action, the residual phase should be theoretically zero and experimentally negligible:

$$\phi_R = \phi_{SM} - \phi_{\Gamma_{zz}^*} \quad (5.42)$$

Here, ϕ_R is known as the residual phase which is the difference between the phase generated due to the gravitational potential of the source mass design and phase acquired due to the fictitious gravity gradient.

In order to precisely determine $\phi_{\Gamma_{zz}^*}$, it is necessary to calculate single - atom phase gradient, i.e., $\nabla\phi$. Hence, $\nabla\phi$ for each geometrical configuration: cylindrical tungsten source masses including and excluding torus-shaped aluminium platform, torus-shaped copper ring source masses, were precisely evaluated using equation 5.41 with results reported in Subsections 5.5.1 and 5.5.2.

5.5.1 Single - atom gradient calculation (Geometrical Configuration-I)

As per the new design of our experiment (Figure 5.1), our CLOSE and FAR configurations are defined as the system of source masses (with and without platform) lying closer to the ground and lying away from the ground respectively. The motivation here is to estimate the real gravity gradients for both CLOSE and FAR configurations compensating its effects using the recent technique [65, 66].

In order to precisely determine $\phi_{\Gamma_{zz}^*}$, it is necessary to calculate single - atom $\nabla\phi$ for both the cases of torus-shaped platform being present and absent in the experiment.

For the case of our complete set of tungsten source masses (arranged as described in Chapter 3), each source mass having a radius of 10 cm and a height of 3.75 cm, excluding the platform, the magnitude of single - atom gradient over a centre-of-mass baseline of 23 cm yields:

$$\nabla\phi = \frac{\phi_{SM}(x_{UP}^{CM}, y_{UP}^{CM}, z_{UP}^{CM}) - \phi_{SM}(x_{DW}^{CM}, y_{DW}^{CM}, z_{DW}^{CM})}{0.23} = 6.35$$

Incorporating the same radius and height parameters of source mass disks with presence of the platform and using equation 5.41, the magnitude of single - atom gradient over a centre-of-mass baseline of 23 cm yields:

$$\nabla\phi_{PLATFORM} = \frac{\phi_{SM}(x_{UP}^{CM}, y_{UP}^{CM}, z_{UP}^{CM}) - \phi_{SM}(x_{DW}^{CM}, y_{DW}^{CM}, z_{DW}^{CM})}{0.23} = 6.36$$

5.5.2 Single - atom gradient calculation (Geometrical Configuration-II)

Here ϕ_{SM} is calculated using gravitational potential from equation 5.36. Evaluation for single - atom $\nabla\phi$ for copper torus-shaped rings source mass configuration yields:

$$\nabla\phi = \frac{\phi_{SM}(x_{UP}^{CM}, y_{UP}^{CM}, z_{UP}^{CM}) - \phi_{SM}(x_{DW}^{CM}, y_{DW}^{CM}, z_{DW}^{CM})}{0.23\eta} = 4.80$$

where the dimensionless ratio $\eta = \sqrt{\frac{\rho_W}{\rho_{Cu}}}$ is used in the existing set of parameters (for geometrical configuration - I with torus-shaped aluminium platform) so as to invoke generalization of this torus-shaped geometry of source masses as explained earlier in the Section 5.2.

5.6 Residual Phases: Achieving the relative accuracy of 10^{-6}

We ran a virtual experiment by simulating the effects of real and fictitious gravity gradients. This simulation precisely calculates the magnitudes of the phases ϕ_{SM} , $\phi_{\Gamma_{zz}^*}$ and ϕ_R . In the next two subsections, we state the results obtained for different geometrical designs and configurations of source masses compensating the effects of ambient gravity gradient.

5.6.1 Results: Configuration - I

The results (plots: Figures 5.14 - 5.19) indicate the calculated ϕ_R with a relative accuracy of 10^{-6} . The 12 crucial variables to be set in this simulation are: x , y , z_{00} , z_{11} , σ_x , σ_y , σ_z , v_x , v_y , v_z , $\sigma_{v_{xy}}$ and σ_{v_z} . Here, the position and velocity variables respectively being x , y , z_{00} , z_{11} and v_x , v_y , v_z describe the motion of atoms in atomic clouds (z_{00} : upper cloud, z_{11} : lower cloud), σ_x , σ_y and σ_z represent the thickness of atomic clouds along each axis, $\sigma_{v_{xy}}$ and σ_{v_z} play the role of standard deviations in velocities of atoms along XY - plane and Z axis respectively. The initial velocities of two clouds are calculated to be: $v_0 = g(T + 0.001)$ m/s. At their launch, the clouds have offsets of 170 mm and 161.70 mm due to application of an initial $\pi/2$ -pulse (along axis of launch) respectively when platform is excluded and included (as shown previously in Section 5.3). This leads to a slight recalibration in the variables z_{00} and z_{11} , resulting in $z_{00}^{N,P} = z^{N,P} + z_{00}$ and $z_{11}^{N,P} = z^{N,P} + z_{11}$ (with $z^N = -170$ mm and $z^P = -161.70$ mm), where the labels N and P

Parameters	Variation (mm)
x	-1.0, -0.5, 0.0, 0.5, 1.0
y	-1.0, -0.5, 0.0, 0.5, 1.0
z_{11}	$z_{11}^{N,P} - 0.2, z_{11}^{N,P} - 0.1, z_{11}^{N,P}, z_{11}^{N,P} + 0.1, z_{11}^{N,P} + 0.2$
z_{00}	$z_{00}^{N,P} - 0.2, z_{00}^{N,P} - 0.1, z_{00}^{N,P}, z_{00}^{N,P} + 0.1, z_{00}^{N,P} + 0.2$
σ_x	2.6, 2.8, 3.0, 3.2, 3.4
σ_y	2.6, 2.8, 3.0, 3.2, 3.4
σ_z	2.8, 2.9, 3.0, 3.1, 3.2

Table 5.4: Selected variation of parameters (configuration - I) associated with the position of atoms spanned across each axis inside the atomic cloud.

Parameters	Variation (mm/s)
v_x	-1.0, -0.5, 0.0, 0.5, 1.0
v_y	-1.0, -0.5, 0.0, 0.5, 1.0
v_z	$v_0 - 0.2, v_0 - 0.1, v_0, v_0 + 0.1, v_0 + 0.2$
$\sigma_{v_{xy}}$	14, 17, 20, 23, 26
σ_{v_z}	2.8, 2.9, 3.0, 3.1, 3.2

Table 5.5: Selected variation of parameters (configuration - I) associated with the velocity of atoms spanned across each axis inside the atomic cloud.

stand for platform absence and platform presence respectively. The variations incorporated in our simulations associated with atomic positions and atomic velocities are listed in Tables 5.4 and 5.5 respectively.

Each atomic cloud variable stated in Tables 5.4 and 5.5 have 5 variations. This enabled us to visualize the stability of our phases produced by our cold atomic clouds due to the effect of our new design. Hence, in total, 120 simulations are executed with results shown in Figures 5.14 - 5.19 for relative uncertainties of 0.1%, 0.5% and 1.0% in $\nabla\phi$. The choice to introduce uncertainties as 0.1%, 0.5% and 1.0% in $\nabla\phi$ was made in our simulations because experimentally the values of gravity gradients cannot be cancelled exactly.

In Figures 5.14 - 5.19, the error bars indicate the error in calculation of ϕ_R with and without the platform in the units of μrad for the stated uncertainty percentages. From these figures, a linear trend of $\sigma_{v_{xy}}$ is clearly visible. The reason why $\sigma_{v_{xy}}$ is displaying a linear trend is explained in Subsection 5.6.3. The ranges of the error bars for all the variables are listed in Tables 5.6 and 5.7 designated as \mathcal{N} and \mathcal{P} , indicating the error bar ranges in the absence and presence of platform respectively. The last column in

Variable(Uncertainty)	$\mathcal{P}_{ERR}(\mu\text{rad})$	$\mathcal{N}_{ERR}(\mu\text{rad})$
$x(0.1\%)$	2.97-3.00	1.58-1.61
$x(0.5\%)$	3.11-3.14	1.72-1.75
$x(1.0\%)$	3.28-3.32	1.92-1.95
$y(0.1\%)$	2.96-3.00	1.56-1.60
$y(0.5\%)$	3.10-3.15	1.70-1.74
$y(1.0\%)$	3.20-3.33	1.90-1.94
$z_{00}(0.1\%)$	2.91-3.01	1.56-1.61
$z_{00}(0.5\%)$	3.05-3.15	1.70-1.76
$z_{00}(1.0\%)$	3.26-3.33	1.89-1.95
$z_{11}(0.1\%)$	2.95-2.99	1.56-1.61
$z_{11}(0.5\%)$	3.09-3.13	1.70-1.76
$z_{11}(1.0\%)$	3.27-3.31	1.89-1.95
$\sigma_x(0.1\%)$	2.95-3.01	1.55-1.58
$\sigma_x(0.5\%)$	3.08-3.16	1.70-1.72
$\sigma_x(1.0\%)$	3.26-3.34	1.89-1.92
$\sigma_y(0.1\%)$	2.94-2.98	1.57-1.62
$\sigma_y(0.5\%)$	3.07-3.12	1.73-1.76
$\sigma_y(1.0\%)$	3.25-3.31	1.90-1.95
$\sigma_z(0.1\%)$	2.82-3.15	1.49-1.64
$\sigma_z(0.5\%)$	2.95-3.30	1.63-1.80
$\sigma_z(1.0\%)$	3.12-3.50	1.80-2.00

Table 5.6: Error bar ranges due to atomic positions: Increase in lower and upper limits of error bar ranges with respect to increasing uncertainty in $\nabla\phi$ for configuration - I. \mathcal{P}_{ERR} and \mathcal{N}_{ERR} mark the error bar ranges produced by each participating variable in the simulation in the absence and presence of platform respectively.

Tables 5.6 and 5.7 clearly display the shortening of error bar magnitudes when the aluminium platform is not present. Furthermore, in Tables 5.8 and 5.9, the labels AC_P and AC_N indicate the averaged accuracy (in terms of Newtonian Gravitational Constant) when platform is included and excluded respectively. As reported in these two tables, the accuracy is higher when the uncertainty in $\nabla\phi$ is lesser and also when the aluminium platform is not included. This increased averaged accuracy marks reduction in uncertainty of these measurements from simulations, as it can be vividly seen that the error bars are shorter in the platform's absence concerning configuration - I.

Moreover, performing linear fits for the variable $\sigma_{v_{xy}}$ (as the trend of this variables depicts linear behaviour), the slope and its corresponding standard

Variable(Uncertainty)	$\mathcal{P}_{ERR}(\mu\text{rad})$	$\mathcal{N}_{ERR}(\mu\text{rad})$
$v_x(0.1\%)$	2.95-3.03	1.57-1.59
$v_x(0.5\%)$	3.09-3.17	1.71-1.74
$v_x(1.0\%)$	3.27-3.35	1.90-1.93
$v_y(0.1\%)$	2.91-2.98	1.55-1.90
$v_y(0.5\%)$	3.05-3.12	1.70-1.76
$v_y(1.0\%)$	3.22-3.30	1.89-1.95
$v_z(0.1\%)$	2.96-2.98	1.54-1.59
$v_z(0.5\%)$	3.10-3.12	1.69-1.74
$v_z(1.0\%)$	3.28-3.30	1.88-1.94
$\sigma_{v_{xy}}(0.1\%)$	2.84-3.28	1.54-1.63
$\sigma_{v_{xy}}(0.5\%)$	2.99-3.41	1.68-1.87
$\sigma_{v_{xy}}(1.0\%)$	3.18-3.57	1.88-2.05
$\sigma_{v_z}(0.1\%)$	2.92-3.01	1.57-1.59
$\sigma_{v_z}(0.5\%)$	3.06-3.15	1.72-1.73
$\sigma_{v_z}(1.0\%)$	3.24-3.33	1.91-1.93

Table 5.7: Error bar ranges due to atomic velocities: Increase in lower and upper limits of error bar ranges with respect to increasing uncertainty in $\nabla\phi$ for configuration - I. \mathcal{P}_{ERR} and \mathcal{N}_{ERR} have the same meaning (as Table 5.6).

error are shown below. The linear fit analysis for the $\sigma_{v_{xy}}$ taking into all the uncertainties in the absence and presence of platform is listed in Tables 5.10 and 5.11 respectively. Performing linear fits of z_{00} and z_{11} resulted in a high value of standard error which proves that just like all the other variables except $\sigma_{v_{xy}}$, these happen to be random fluctuations rather than being a part of systematic variation.

5.6.2 Results: Configuration - II

The results (Figures 5.20 - 5.24) indicate the calculated ϕ_R with a relative accuracy of 10^{-6} . Since the dense cylindrical tungsten source masses are absent in this source mass design and also for the sake of convenience, here we have incorporated cylindrical coordinate system, so that we have nine variables instead of twelve variables like in geometrical arrangement described in the preceding subsection. These nine crucial variables set in this simulation are: $r, \sigma_r, v_r, \sigma_{v_r}, z_{UP}, z_{DW}, \sigma_z, v_z$ and σ_{v_z} taking into account the initial $\pi/2$ -pulse coordinate as stated earlier in Section 5.3, an offset of -232.22 mm.

The variables (with their respective variations in Table 5.12) namely: r, σ_r, v_r and σ_{v_r} , reveal the collective information about the atomic motion

Variable(Uncertainty)	AC_P	AC_N
$x(0.1\%)$	$2.985 \times 10^{-6} G$	$1.595 \times 10^{-6} G$
$x(0.5\%)$	$3.125 \times 10^{-6} G$	$1.735 \times 10^{-6} G$
$x(1.0\%)$	$3.300 \times 10^{-6} G$	$1.935 \times 10^{-6} G$
$y(0.1\%)$	$2.980 \times 10^{-6} G$	$1.580 \times 10^{-6} G$
$y(0.5\%)$	$3.125 \times 10^{-6} G$	$1.720 \times 10^{-6} G$
$y(1.0\%)$	$3.265 \times 10^{-6} G$	$1.920 \times 10^{-6} G$
$z_{00}(0.1\%)$	$2.960 \times 10^{-6} G$	$1.585 \times 10^{-6} G$
$z_{00}(0.5\%)$	$3.100 \times 10^{-6} G$	$1.730 \times 10^{-6} G$
$z_{00}(1.0\%)$	$3.295 \times 10^{-6} G$	$1.920 \times 10^{-6} G$
$z_{11}(0.1\%)$	$2.970 \times 10^{-6} G$	$1.585 \times 10^{-6} G$
$z_{11}(0.5\%)$	$3.110 \times 10^{-6} G$	$1.730 \times 10^{-6} G$
$z_{11}(1.0\%)$	$3.290 \times 10^{-6} G$	$1.920 \times 10^{-6} G$
$\sigma_x(0.1\%)$	$2.980 \times 10^{-6} G$	$1.565 \times 10^{-6} G$
$\sigma_x(0.5\%)$	$3.120 \times 10^{-6} G$	$1.710 \times 10^{-6} G$
$\sigma_x(1.0\%)$	$3.300 \times 10^{-6} G$	$1.905 \times 10^{-6} G$
$\sigma_y(0.1\%)$	$2.960 \times 10^{-6} G$	$1.595 \times 10^{-6} G$
$\sigma_y(0.5\%)$	$3.095 \times 10^{-6} G$	$1.745 \times 10^{-6} G$
$\sigma_y(1.0\%)$	$3.280 \times 10^{-6} G$	$1.925 \times 10^{-6} G$
$\sigma_z(0.1\%)$	$2.985 \times 10^{-6} G$	$1.565 \times 10^{-6} G$
$\sigma_z(0.5\%)$	$3.125 \times 10^{-6} G$	$1.715 \times 10^{-6} G$
$\sigma_z(1.0\%)$	$3.310 \times 10^{-6} G$	$1.900 \times 10^{-6} G$

Table 5.8: Error bar ranges due relative accuracy occurring from atomic positions: Increase in relative accuracy with respect to decreasing uncertainty in $\nabla\phi$ and exclusion of aluminium platform from configuration - I. AC_P and AC_N are accuracies written in terms of measurement of G when the platform is present and absent respectively. These accuracies are written in terms of G so that these accuracies along with the error bar range information from Table 5.7 can be comparable with the actual experimental sequence.

Variable(Uncertainty)	AC_P	AC_N
$v_x(0.1\%)$	$2.990 \times 10^{-6} G$	$1.580 \times 10^{-6} G$
$v_x(0.5\%)$	$3.130 \times 10^{-6} G$	$1.725 \times 10^{-6} G$
$v_x(1.0\%)$	$3.310 \times 10^{-6} G$	$1.915 \times 10^{-6} G$
$v_y(0.1\%)$	$2.945 \times 10^{-6} G$	$1.725 \times 10^{-6} G$
$v_y(0.5\%)$	$3.085 \times 10^{-6} G$	$1.730 \times 10^{-6} G$
$v_y(1.0\%)$	$3.260 \times 10^{-6} G$	$1.920 \times 10^{-6} G$
$v_z(0.1\%)$	$2.970 \times 10^{-6} G$	$1.565 \times 10^{-6} G$
$v_z(0.5\%)$	$3.110 \times 10^{-6} G$	$1.715 \times 10^{-6} G$
$v_z(1.0\%)$	$3.290 \times 10^{-6} G$	$1.910 \times 10^{-6} G$
$\sigma_{v_{xy}}(0.1\%)$	$3.060 \times 10^{-6} G$	$1.585 \times 10^{-6} G$
$\sigma_{v_{xy}}(0.5\%)$	$3.200 \times 10^{-6} G$	$1.775 \times 10^{-6} G$
$\sigma_{v_{xy}}(1.0\%)$	$3.375 \times 10^{-6} G$	$1.965 \times 10^{-6} G$
$\sigma_{v_z}(0.1\%)$	$2.965 \times 10^{-6} G$	$1.580 \times 10^{-6} G$
$\sigma_{v_z}(0.5\%)$	$3.105 \times 10^{-6} G$	$1.725 \times 10^{-6} G$
$\sigma_{v_z}(1.0\%)$	$3.285 \times 10^{-6} G$	$1.920 \times 10^{-6} G$

Table 5.9: Error bar ranges due relative accuracy occurring from atomic velocities: Increase in relative accuracy with respect to decreasing uncertainty in $\nabla\phi$ and exclusion of aluminium platform from configuration - I. Here, AC_P and AC_N have exactly the same meaning as Table 5.8.

Variable(Uncertainty)	Slope	Standard Error
$\sigma_{v_{xy}}(0.1\%)$	$-6.319 \mu\text{rad}/\text{mm}/\text{s}$	0.44
$\sigma_{v_{xy}}(0.5\%)$	$-6.317 \mu\text{rad}/\text{mm}/\text{s}$	0.46
$\sigma_{v_{xy}}(1.0\%)$	$-6.312 \mu\text{rad}/\text{mm}/\text{s}$	0.49

Table 5.10: Slopes and corresponding standard errors calculated while performing linear fit analysis for $\sigma_{v_{xy}}$ in configuration - I (platform absent).

Variable(Uncertainty)	Slope	Standard Error
$\sigma_{v_{xy}}(0.1\%)$	$-7.066 \mu\text{rad}/\text{mm}/\text{s}$	0.35
$\sigma_{v_{xy}}(0.5\%)$	$-7.035 \mu\text{rad}/\text{mm}/\text{s}$	0.36
$\sigma_{v_{xy}}(1.0\%)$	$-6.997 \mu\text{rad}/\text{mm}/\text{s}$	0.37

Table 5.11: Slopes and corresponding standard errors calculated while performing linear fit analysis for $\sigma_{v_{xy}}$ in configuration - I (platform present).

Variables	Variations
r	{0.0, 0.5, 1.0, 1.5, 2.0} mm
z_{DW}	{ $z_{11} - 0.2, z_{11} - 0.1, z_{11}, z_{11} + 0.1, z_{11} + 0.2$ } mm
z_{UP}	{ $z_{00} - 0.2, z_{00} - 0.1, z_{00}, z_{00} + 0.1, z_{00} + 0.2$ } mm
σ_r	{2.6, 2.8, 3.0, 3.2, 3.4} mm
σ_z	{2.8, 2.9, 3.0, 3.1, 3.2} mm
v_r	{0.0, 0.5, 1.0, 1.5, 2.0} mm/s
v_z	{ $v_0 - 0.2, v_0 - 0.1, v_0, v_0 + 0.1, v_0 + 0.2$ } mm/s
σ_{v_r}	{14, 17, 20, 23, 26} mm/s
σ_{v_z}	{2.8, 2.9, 3.0, 3.1, 3.2} mm/s

Table 5.12: Variability of atomic cloud variables responsible for configuration - II associated with positions and velocities of atoms spanned across radial and gravity axes inside atomic cloud.

spanned across the XY-plane, such that: $r = \sqrt{x^2 + y^2}$, $\sigma_r = \sqrt{\sigma_x^2 + \sigma_y^2}$, $v_r = \sqrt{v_x^2 + v_y^2}$ and $\sigma_{v_r} = \sqrt{\sigma_{v_x}^2 + \sigma_{v_y}^2}$.

Employing the scaled parameters and variables with defined variability presented in Table 5.12, a measurement campaign of 45 simulations was launched. Each out of the 9 variables taking 5 values with an uncertainty of 0.1%, 0.5% and 1.0% in $\nabla\phi$, just like these uncertainty percentages were accounted in the preceding section. The results of all these simulations describe the stability of our phase values with respect to all the atomic cloud variables associated with the experiment, reported in Figures 5.20 - 5.24.

As per all the plots, the error bars indicate the error in calculation of ϕ_R in the units of μrad for uncertainty values of 0.1%, 0.5% and 1.0% in $\nabla\phi$. The range of the error bars - $ER_{U1.0\%}$, $ER_{U0.5\%}$, $ER_{U0.1\%}$ respectively for uncertainty percentages of 1.0%, 0.5% and 0.1% in $\nabla\phi$ for all the variables observed in these plots are reported in Table 5.13. Furthermore, the corresponding average accuracy (in terms of Newtonian Gravitational Constant) is calculated by taking the average of lower and upper limit of error bars stated in Table 5.13. Proceeding further, the three columns in Table 5.14, namely - $AC_{U0.1\%}$, $AC_{U0.5\%}$ and $AC_{U1.0\%}$ indicate the average accuracy respectively for the uncertainty percentages (in $\nabla\phi$) as 0.1%, 0.5% and 1.0%. Lastly, performing linear fit analysis for the variable σ_{v_r} (as the trend of this variable depicts a linear behaviour), the slopes and its corresponding standard errors taking into account all the values of uncertainties in $\nabla\phi$ are mentioned in Table 5.15.

Variable(Units)	$ER_{U1.0\%}(\mu\text{rad})$	$ER_{U0.5\%}(\mu\text{rad})$	$ER_{U0.1\%}(\mu\text{rad})$
$r(\text{mm})$	1.49-1.52	1.29-1.32	1.13-1.16
$\sigma_r(\text{mm})$	1.47-1.51	1.27-1.31	1.11-1.15
$\sigma_{v_r}(\text{mm/s})$	1.49-1.57	1.27-1.38	1.10-1.24
$\sigma_{v_z}(\text{mm/s})$	1.49-1.54	1.29-1.33	1.13-1.17
$\sigma_z(\text{mm})$	1.42-1.52	1.23-1.32	1.08-1.16
$v_r(\text{mm/s})$	1.48-1.52	1.28-1.31	1.12-1.15
$v_z(\text{m/s})$	1.48-1.52	1.28-1.32	1.13-1.15
$z_{DW}(\text{m})$	1.47-1.50	1.27-1.30	1.12-1.14
$z_{UP}(\text{m})$	1.48-1.54	1.27-1.33	1.11-1.16

Table 5.13: Decrease in lower and upper limits of error bar ranges with respect to decreasing uncertainty in $\nabla\phi$ for configuration - II. The columns with ER define the error bar ranges for all uncertainty percentages.

Variable(Units)	$AC_{U0.1\%}$	$AC_{U0.5\%}$	$AC_{U1.0\%}$
$r(\text{mm})$	$1.145 \times 10^{-6} G$	$1.305 \times 10^{-6} G$	$1.505 \times 10^{-6} G$
$\sigma_r(\text{mm})$	$1.130 \times 10^{-6} G$	$1.290 \times 10^{-6} G$	$1.490 \times 10^{-6} G$
$\sigma_{v_r}(\text{mm/s})$	$1.170 \times 10^{-6} G$	$1.325 \times 10^{-6} G$	$1.530 \times 10^{-6} G$
$\sigma_{v_z}(\text{mm/s})$	$1.150 \times 10^{-6} G$	$1.310 \times 10^{-6} G$	$1.515 \times 10^{-6} G$
$\sigma_z(\text{mm})$	$1.120 \times 10^{-6} G$	$1.275 \times 10^{-6} G$	$1.470 \times 10^{-6} G$
$v_r(\text{mm/s})$	$1.135 \times 10^{-6} G$	$1.295 \times 10^{-6} G$	$1.500 \times 10^{-6} G$
$v_z(\text{m/s})$	$1.140 \times 10^{-6} G$	$1.295 \times 10^{-6} G$	$1.500 \times 10^{-6} G$
$z_{DW}(\text{m})$	$1.135 \times 10^{-6} G$	$1.300 \times 10^{-6} G$	$1.510 \times 10^{-6} G$
$z_{UP}(\text{m})$	$1.130 \times 10^{-6} G$	$1.285 \times 10^{-6} G$	$1.485 \times 10^{-6} G$

Table 5.14: Decrease in relative accuracy with respect to increasing uncertainty in $\nabla\phi$ for configuration - II. The columns with AC define the accuracies in terms of G for all uncertainty percentages.

Variable(Uncertainty)	Slope	Standard Error
$\sigma_{v_r}(0.1\%)$	$-2.572 \mu\text{rad}/\text{mm/s}$	0.21
$\sigma_{v_r}(0.5\%)$	$-2.596 \mu\text{rad}/\text{mm/s}$	0.24
$\sigma_{v_r}(1.0\%)$	$-2.625 \mu\text{rad}/\text{mm/s}$	0.27

Table 5.15: Slopes and corresponding standard errors calculated while performing linear fit for σ_{v_r} in configuration - II.

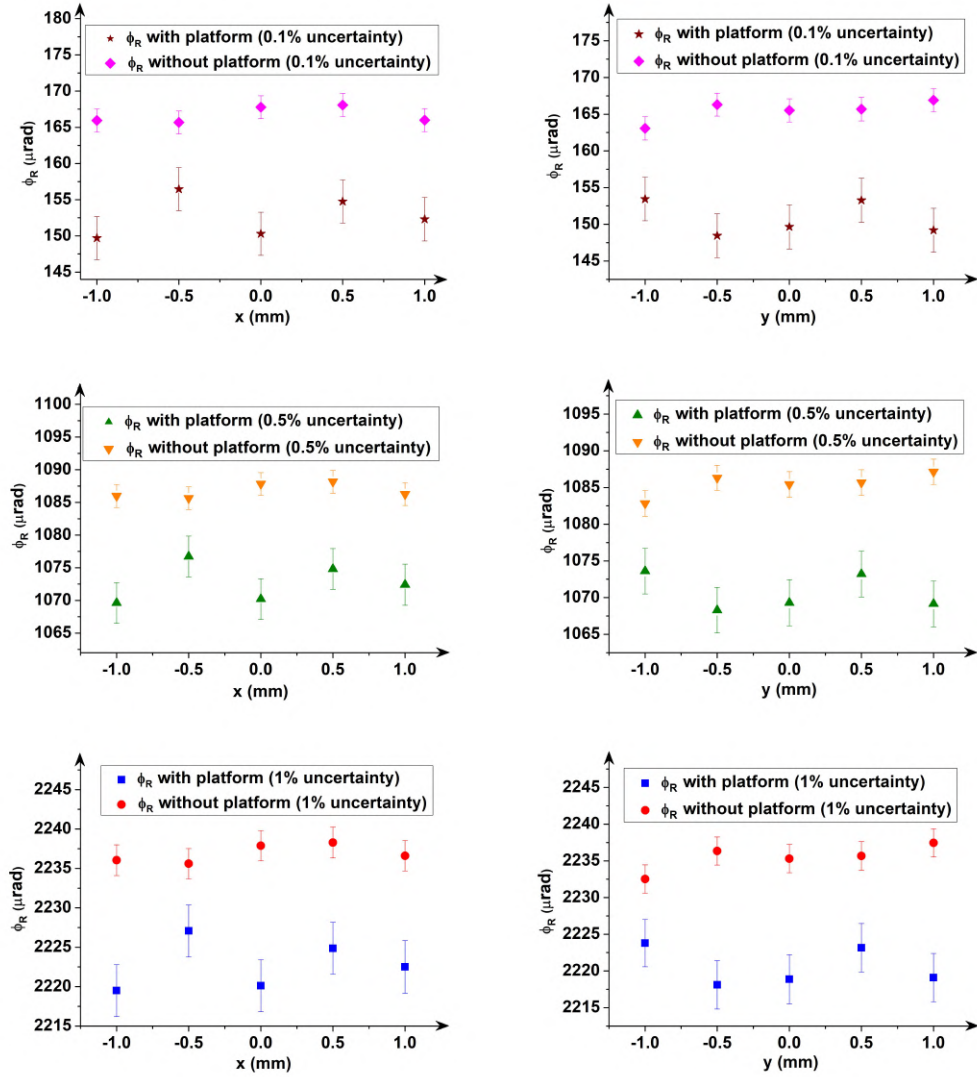


Figure 5.14: Variation in residual phase (ϕ_R from equation 5.42) in configuration - I versus the variations of x and y with relative uncertainties of 0.1%, 0.5% and 1.0% in $\nabla\phi$.

Development of a New Apparatus for Precision Gravity Measurements with Atom Interferometry

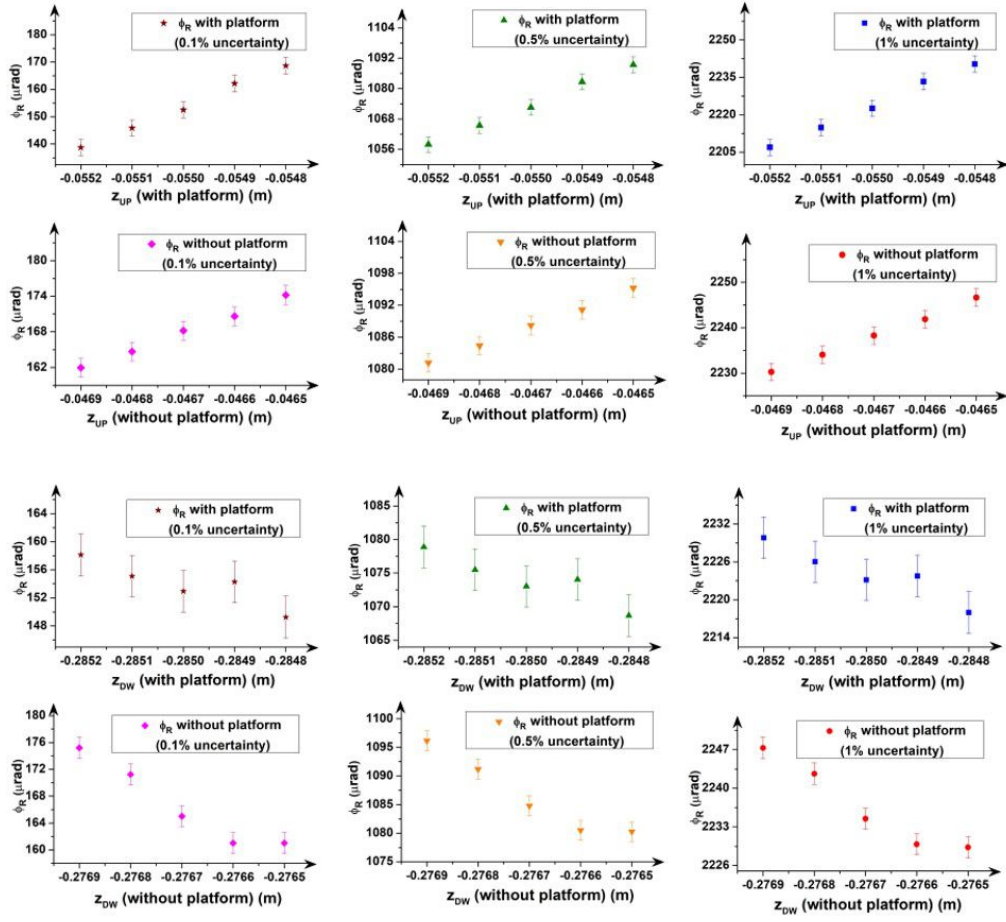


Figure 5.15: Variation in residual phase (ϕ_R from equation 5.42) in configuration - I versus the variations of z_{UP} (upper cloud Z-coordinate) and z_{DW} (lower cloud Z-coordinate) with relative uncertainties of 0.1%, 0.5% and 1.0% in $\nabla\phi$.

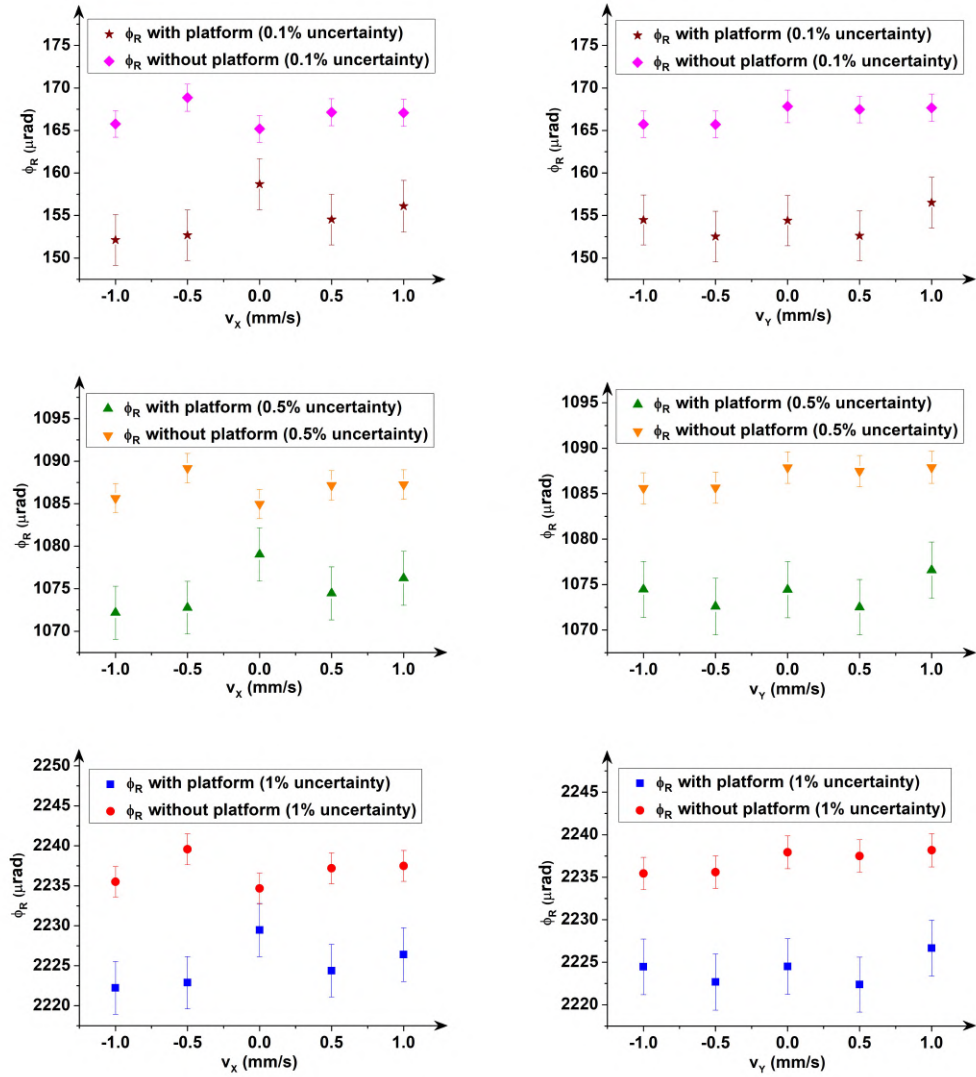


Figure 5.16: Variation in residual phase (ϕ_R from equation 5.42) in configuration - I versus the variations of v_x and v_y with relative uncertainties of 0.1%, 0.5% and 1.0% in $\nabla\phi$.

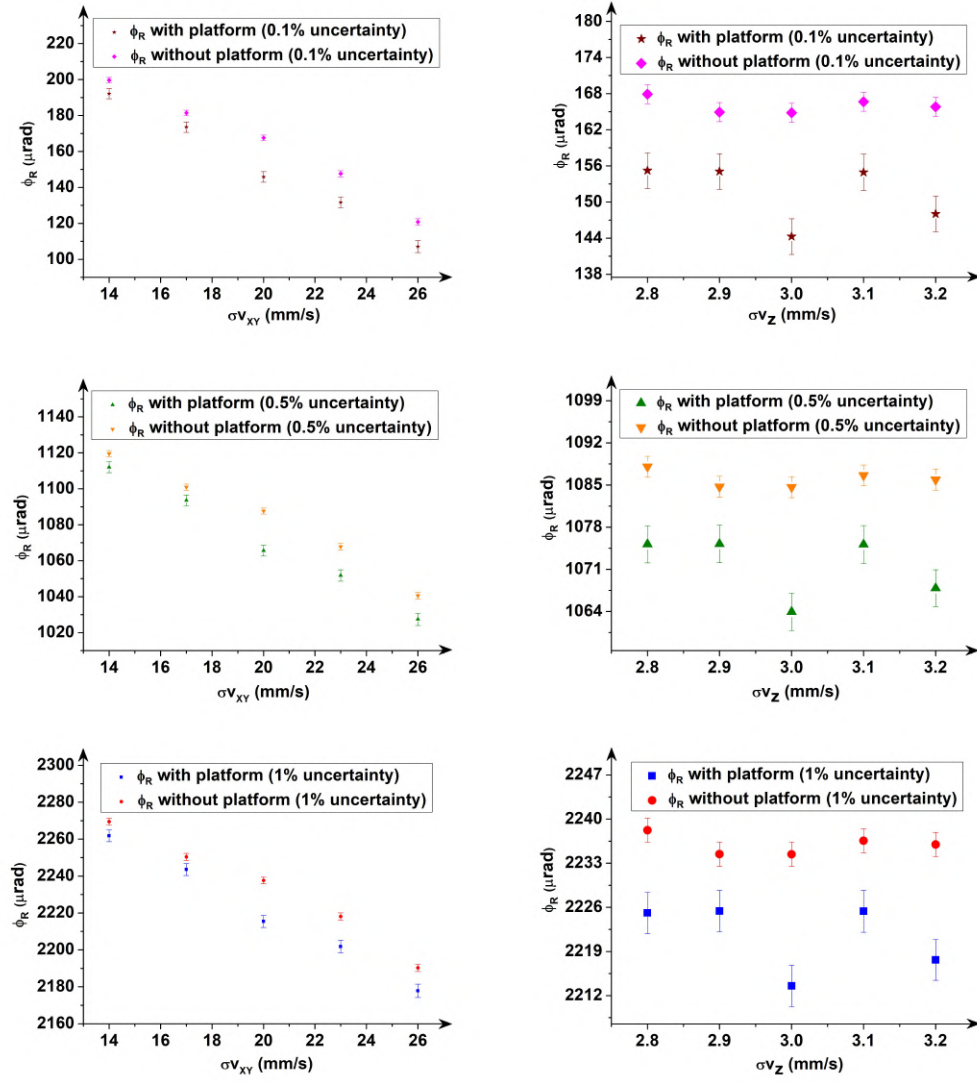


Figure 5.17: Variation in residual phase (ϕ_R from equation 5.42) in configuration - I versus the variations of $\sigma_{v_{xy}}$ and σ_{v_z} with relative uncertainties of 0.1%, 0.5% and 1.0% in $\nabla\phi$.

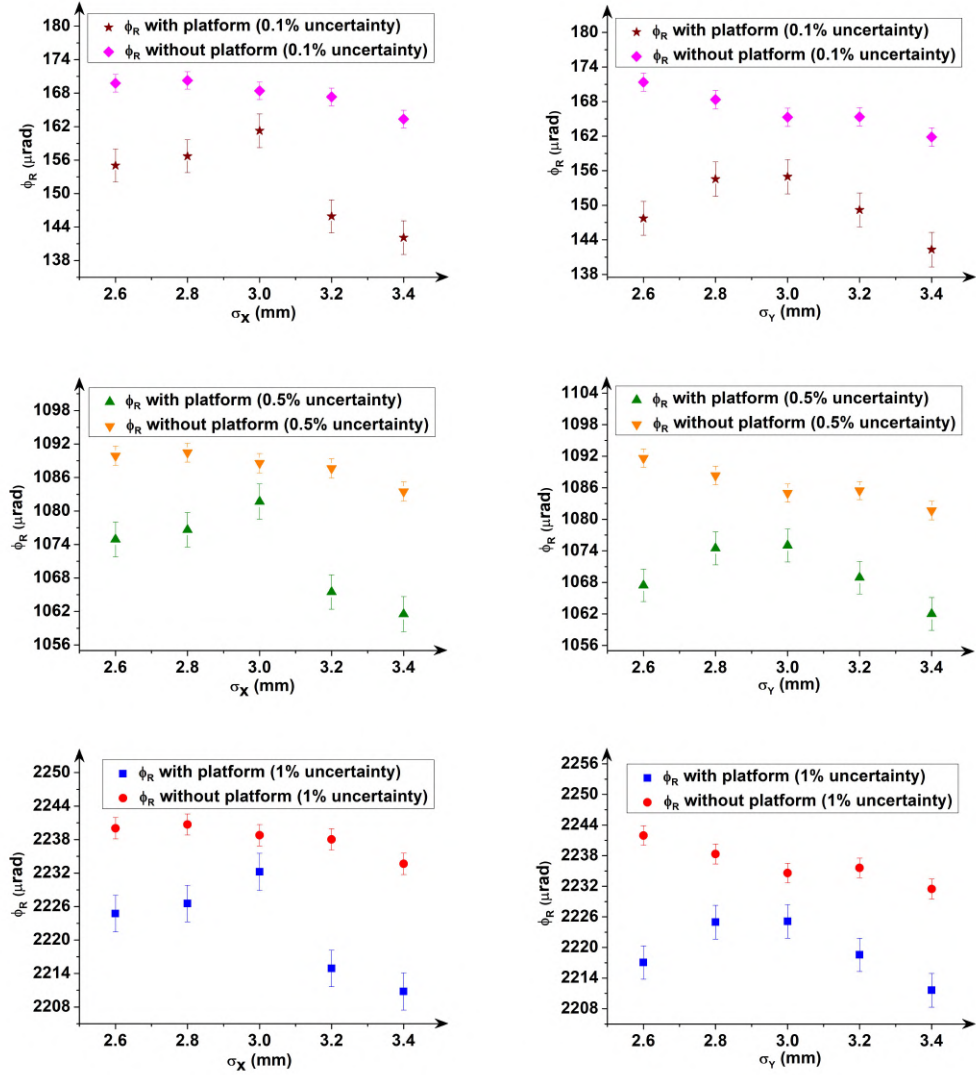


Figure 5.18: Variation in residual phase (ϕ_R from equation 5.42) from configuration - I versus the variations of σ_x and σ_y with relative uncertainties of 0.1%, 0.5% and 1.0% in $\nabla\phi$.

Development of a New Apparatus for Precision Gravity Measurements with Atom Interferometry

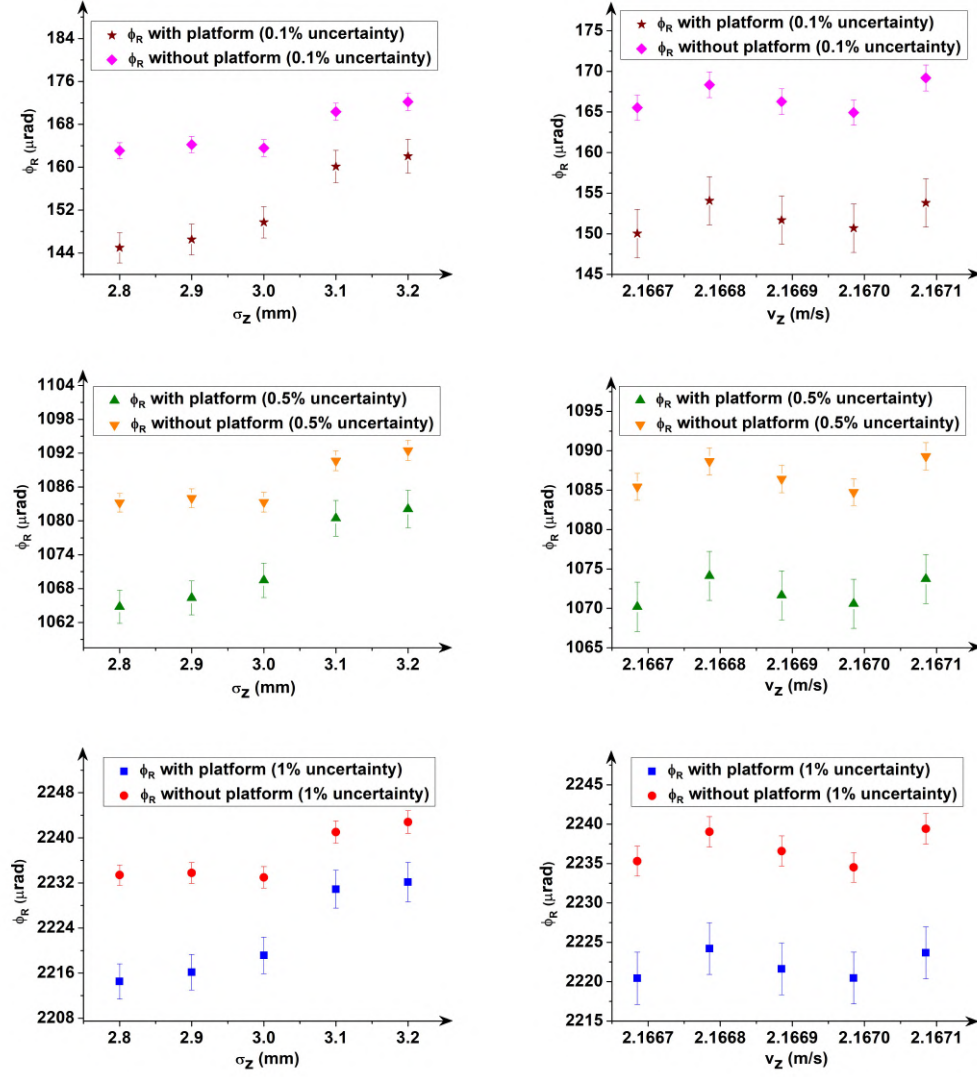


Figure 5.19: Variation in residual phase (ϕ_R from equation 5.42) from configuration - I versus the variations of σ_z and v_z with relative uncertainties of 0.1%, 0.5% and 1.0% in $\nabla\phi$.

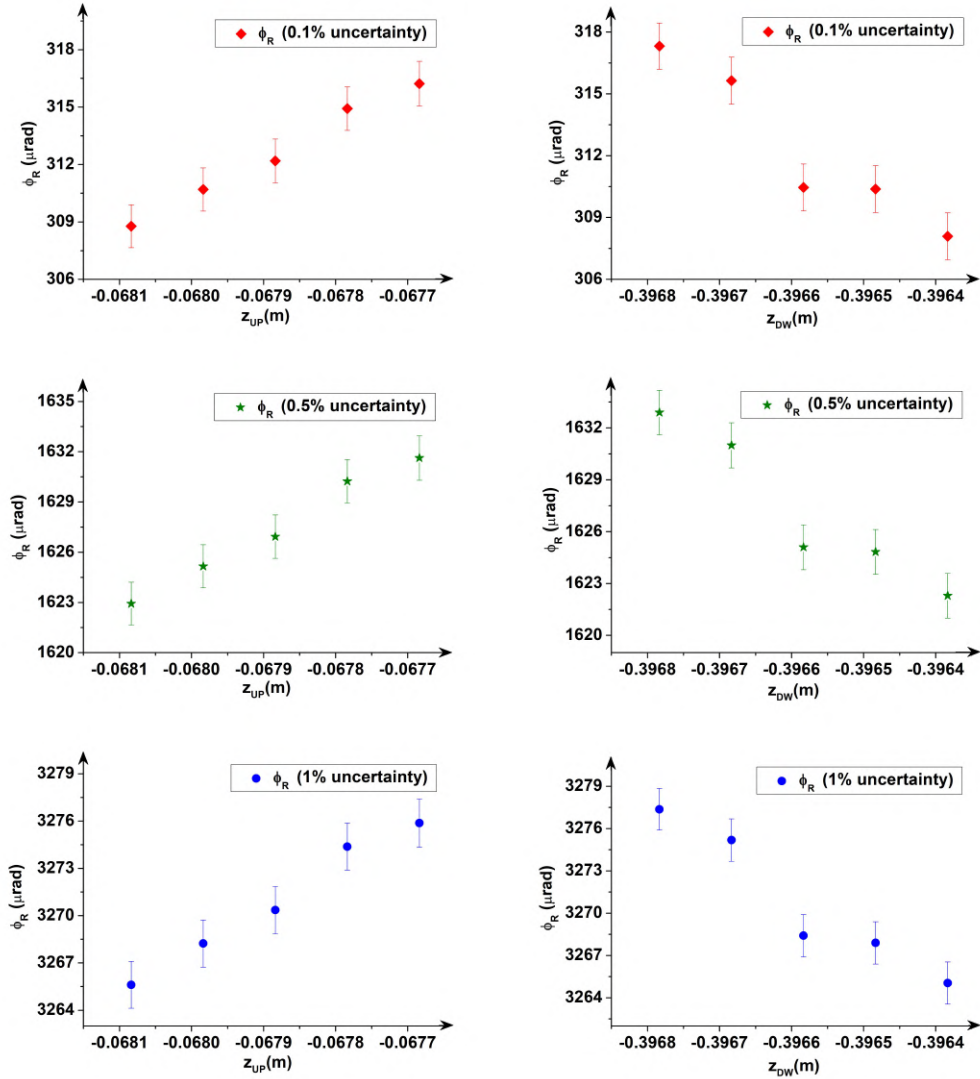


Figure 5.20: Variation in residual phase (ϕ_R from equation 5.42) with respect to the change in variables z_{UP} and z_{DW} with relative uncertainties of 0.1%, 0.5% and 1.0% in $\nabla\phi$ for source mass geometrical configuration - II.

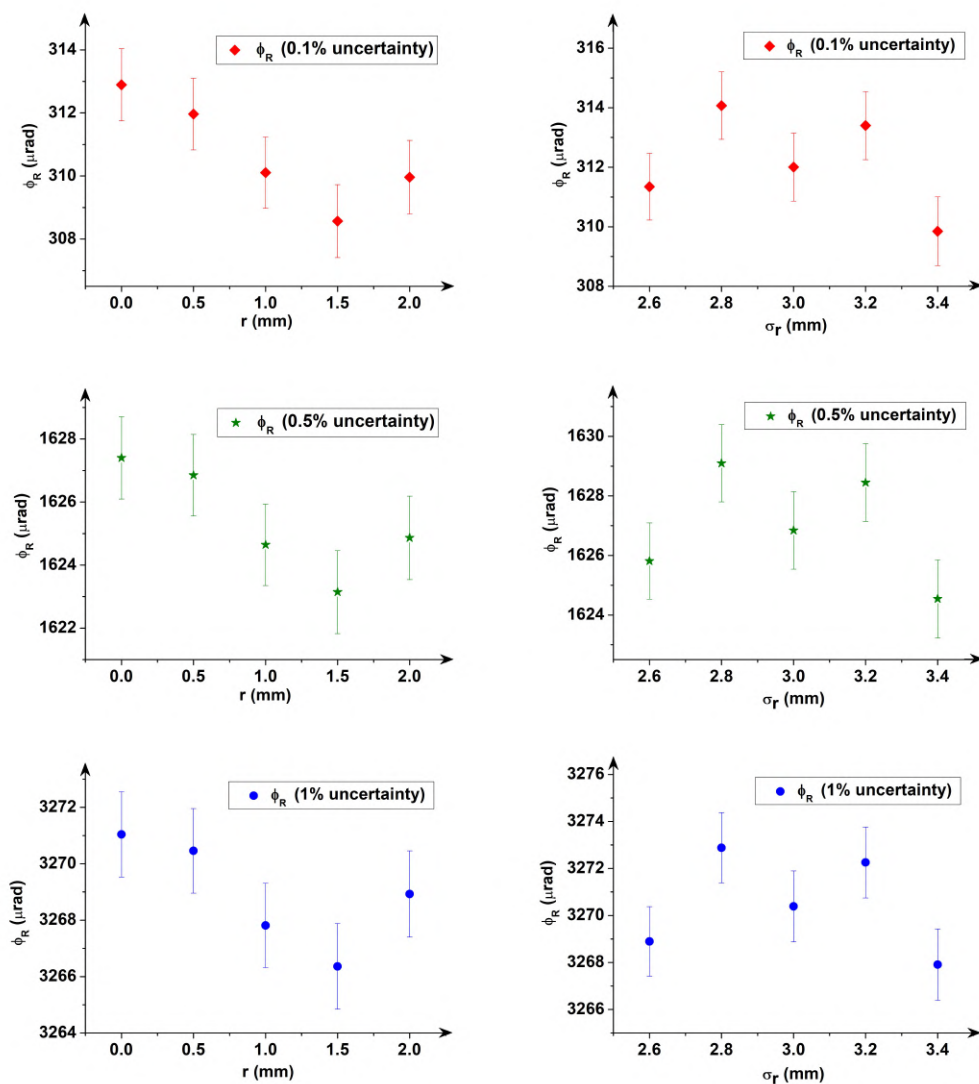


Figure 5.21: Variation in residual phase (ϕ_R from equation 5.42) with respect to the change in variables r and σ_r with relative uncertainties of 0.1%, 0.5% and 1.0% in $\nabla\phi$ for source mass geometrical configuration - II.

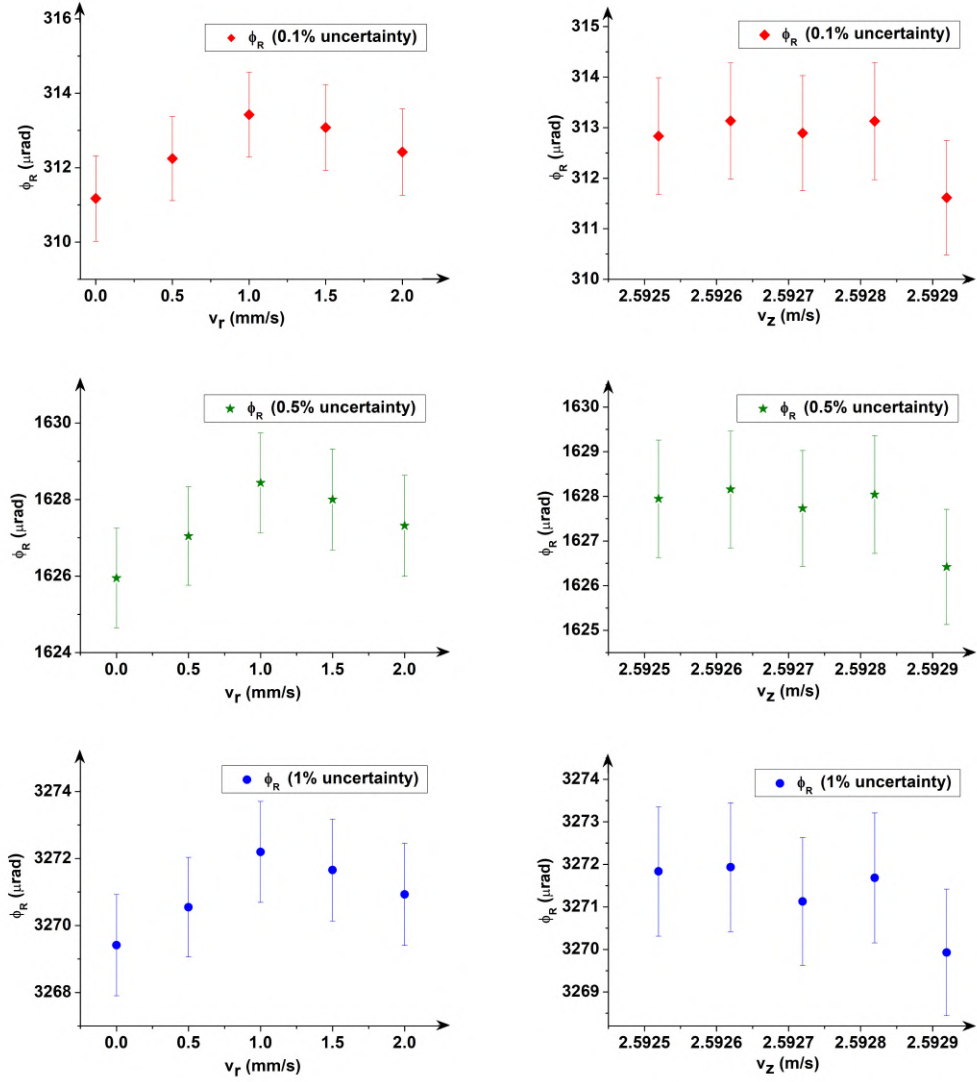


Figure 5.22: Variation in residual phase (ϕ_R from equation 5.42) with respect to the change in variables v_r and v_z with relative uncertainties of 0.1%, 0.5% and 1.0% in $\nabla\phi$ for source mass geometrical configuration - II.

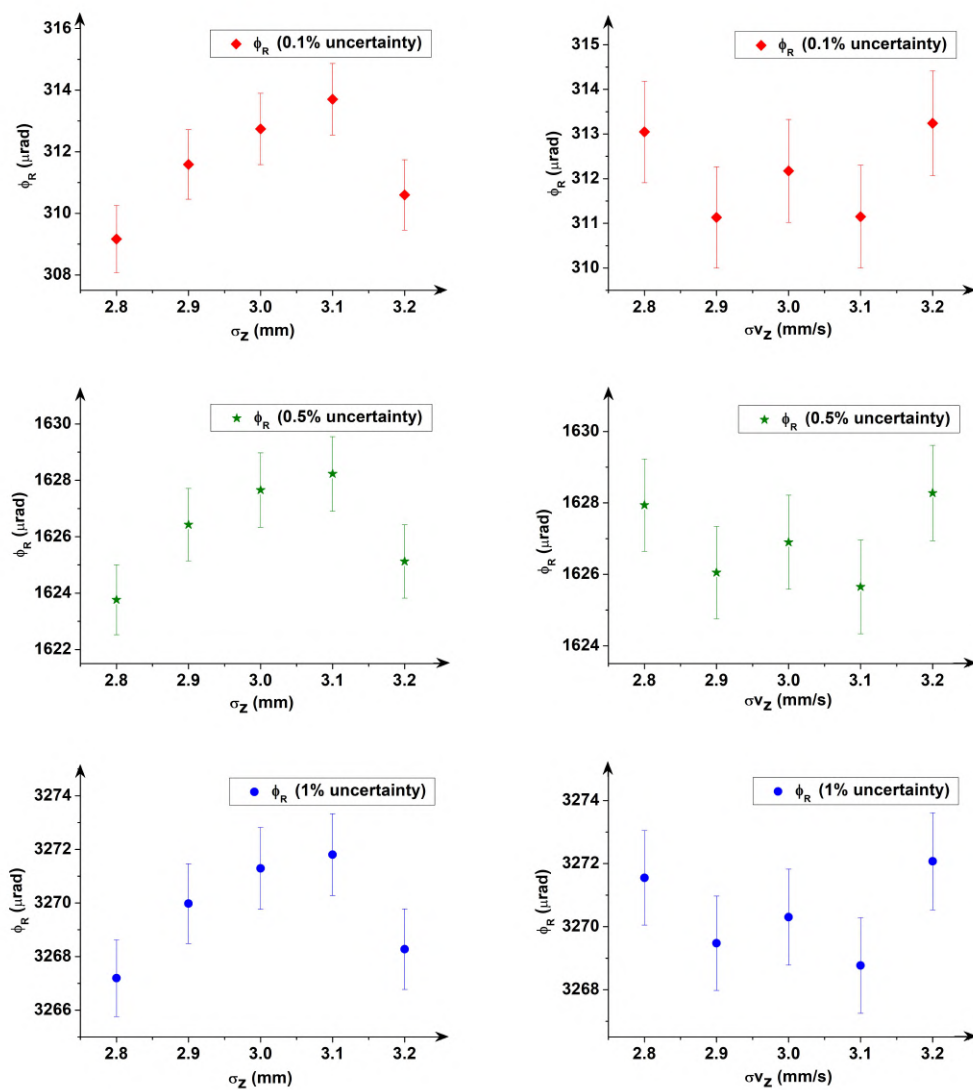


Figure 5.23: Variation in residual phase (ϕ_R from equation 5.42) with respect to the change in variables σ_z and σ_{v_z} with relative uncertainties of 0.1%, 0.5% and 1.0% in $\nabla\phi$ for source mass geometrical configuration - II.

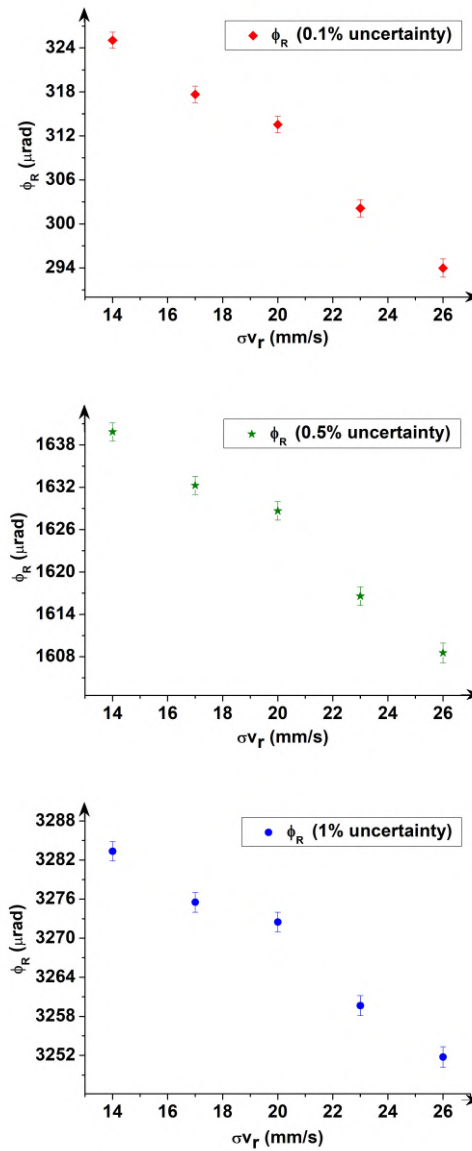


Figure 5.24: Variation in residual phase (ϕ_R from equation 5.42) with respect to the change in variable σ_{v_r} with relative uncertainties of 0.1%, 0.5% and 1.0% in $\nabla\phi$ for source mass geometrical configuration - II.

5.6.3 Comments about graphs

The residual phase behaviour is quite independent with respect to the accuracy of the gravity gradient compensation in both the source mass configurations. Consequently, a modest accuracy of 1% in the preliminary gravity gradient evaluation is already enough for our purposes. Also here we did not see clear trends of residual phase in function of any variables (that govern atomic cloud dynamics) with an exception of $\sigma_{v_{xy}}$ (and σ_{v_r}) representing the width of the radial velocity distribution (i.e. a correspondent of the radial temperature). We found linear slopes of approximately $7 \mu\text{rad}/\text{mm}/\text{s}$, $6.3 \mu\text{rad}/\text{mm}/\text{s}$ and $2.6 \mu\text{rad}/\text{mm}/\text{s}$ for configuration – I (platform present), configuration – I (platform absent) and configuration – II respectively. We can now say that from residual phases (ϕ_R) concerning both the source mass configurations, $\sigma_{v_{xy}}$ and σ_{v_r} show linear trends because they are associated with the radial temperature of the atoms and in our simulation (as described in this thesis), we have considered the gravitational potentials which lead to maximum atoms being located very close around the centre of the atomic cloud. So, as the values of $\sigma_{v_{xy}}$ (and σ_{v_r}) increase, the residual phase (ϕ_R) seems to drop linearly. Considering an uncertainty on $\sigma_{v_{xy}}$ (σ_{v_r} in the case of configuration – II) of $3 \text{ mm}/\text{s}$ [22] we obtained relative uncertainties on G of 13×10^{-6} and 5×10^{-6} respectively for configuration – I (platform present) and configuration – II (platform absent). In general and as expected the configuration – II presents the best result: the absence of a holding platform maximizes the linearity of the acceleration profile while the larger dimension mitigates the sensitivity versus the radial coordinates.

5.6.4 Peak-to-peak variations

To describe the physics of our simulated experiment in another effective way, we present the peak-to-peak variations for each participating variable in the simulation for each uncertainty percentage considered. Table 5.16 reports the peak-to-peak phase variations for configuration - I when the platform is absent and Table 5.17 reports the peak-to-peak phase variations for configuration - I when the platform is present. Similarly, Table 5.18 shows peak-to-peak phase variations for configuration - II. These peak-to-peak variations (denoted by $\Delta\phi_R^{P-P}$) are calculated by taking the difference between the maximum and the minimum values in each variable (which governs atomic cloud dynamics) for each uncertainty percentage. This helps us in realizing which variable is most suitable to be considered for the experimental measurement of G . Also, $\Delta\phi_R^{P-P}$ indicates how much the phase changes even when we consider the negligible motion of individual atoms in our atomic clouds.

Variables (Units)	$\Delta\phi_R^{P-P} _{0.1\%}(\mu\text{rad})$	$\Delta\phi_R^{P-P} _{0.5\%}(\mu\text{rad})$	$\Delta\phi_R^{P-P} _{1.0\%}(\mu\text{rad})$
$\sigma_{v_{xy}}$ (mm/s)	78.82	78.97	79.15
σ_z (mm)	9.14	9.25	9.81
σ_{v_z} (mm/s)	3.08	3.40	3.81
v_z (m/s)	4.27	4.54	4.89
σ_x (mm)	6.92	6.97	7.04
σ_y (mm)	9.53	9.54	10.48
x (mm)	2.39	2.52	2.68
y (mm)	3.82	4.31	4.92
v_x (mm/s)	3.66	4.21	4.91
v_y (mm/s)	2.12	2.28	2.73
z_{11} (mm)	14.19	15.89	18.03
z_{00} (mm)	12.22	14.06	16.35

Table 5.16: Peak-to-peak variations in phases for different uncertainties of gravity gradient compensation considering configuration - I with platform absent.

Variables (Units)	$\Delta\phi_R^{P-P} _{0.1\%}(\mu\text{rad})$	$\Delta\phi_R^{P-P} _{0.5\%}(\mu\text{rad})$	$\Delta\phi_R^{P-P} _{1.0\%}(\mu\text{rad})$
$\sigma_{v_{xy}}$ (mm/s)	85.05	84.61	84.04
σ_z (mm)	17.08	17.32	17.62
σ_{v_z} (mm/s)	10.94	11.27	11.87
v_z (m/s)	4.04	3.92	3.77
σ_x (mm)	19.17	20.18	21.45
σ_y (mm)	12.65	13.03	13.51
x (mm)	6.75	7.11	7.56
y (mm)	4.99	5.30	5.69
v_x (mm/s)	6.56	6.86	7.23
v_y (mm/s)	3.99	4.07	4.28
z_{11} (m)	8.86	10.19	11.86
z_{00} (m)	29.91	31.47	33.42

Table 5.17: Peak-to-peak variations in phases for different uncertainties of gravity gradient compensation considering configuration - I with platform present. The simulation standard error is equal to $3 \mu\text{rad}$ equivalent to 2×10^{-6} G.

Variables (Units)	$\Delta\phi_R^{P-P} _{0.1\%}(\mu\text{rad})$	$\Delta\phi_R^{P-P} _{0.5\%}(\mu\text{rad})$	$\Delta\phi_R^{P-P} _{1.0\%}(\mu\text{rad})$
v_r (mm/s)	2.25	2.48	2.78
v_z (m/s)	1.52	1.74	2.01
σ_{v_r} (mm/s)	31.07	31.29	31.59
σ_{v_z} (m/s)	2.11	2.63	3.30
r (m)	4.33	4.26	4.68
z_{UP} (m)	7.45	8.69	10.26
z_{DW} (m)	9.23	10.60	12.32
σ_r (mm)	4.97	4.55	4.22
σ_z (mm)	4.61	4.47	4.54

Table 5.18: Peak-to-peak variations in phases for different uncertainties of gravity gradient compensation considering configuration - II. The simulation standard error is equal to $1.5 \mu\text{rad}$ equivalent to 1×10^{-6} G.

5.7 Conclusions and Outlook

Considering all the results presented in this Chapter, we can conclude that the gravity gradients can be compensated with a higher accuracy in the near future when experimentalists will be able to load more number of atoms in the MOT chamber as compared to the atomic population considered in our simulations.

Experimentally speaking, the idea is to slightly vary the wavelength of the second laser pulse (resulting in wavevector change of the central π -pulse from k_{eff} to $k_{\text{eff}} + \Delta k_{\text{eff}}$), so that the momentum transfer in the two Mach - Zehnder interferometer branches becomes unbalanced. This implies that the total interferometer phase shift depends on the initial values of the central position and momentum of the atomic wave packets. As presented in this thesis, with a suitable selection of the laser detuning frequency (leading to the birth of fictitious gravity gradient), one can exactly cancel the analogous contribution caused by the ambient gravity gradient. Furthermore, this selection automatically leads to a closed interferometer (vanishing relative displacement between the interfering wave packets) with no loss of contrast.

An outlook concerning the gravity gradient cancellation scheme described and implemented in this thesis is that - small yet considerable differences in the central position and velocity of the initial wave packets for the two vertically separated atomic clouds can mimic the UFF (Universality of Free Fall) violation. In principle, preparing wave packets with a very well-defined central position and momentum does not suffer from limitations associated with Heisenberg's uncertainty principle, which only affects their position and

momentum widths. The work reported here employs a new scheme [65] that simultaneously overcomes the loss of contrast and the controlling of relative initial atomic cloud positions and velocities (also known as the *initial co-location problem*). As a result, this method circumvents the fundamental limitations due to Heisenberg's uncertainty principle. Due to this circumvention of Heisenberg's uncertainty principle, the stringent requirements on setting the relative initial positions and velocities for atomic clouds inside an atomic fountain tube are relaxed by several orders of magnitude.

Chapter 6

Conclusions

6.1 Results

This PhD work had as main goal the development of an atomic gravity gradiometer for compensation of gravity gradients with minimization of phase noise in the gravimetric signal, developing a clearer path towards an accurate determination of the gravitational constant G .

In the first two years, a simulation was developed for the design of 2D-MOT coils serving as the trapping chamber for the atoms to be launched into the atomic fountain tube. Another simulation was developed for the case of atomic clouds treated as fixed points inside a fountain tube producing phases from the second order Zeeman effect. Also, this simulation was generalized to three dimensions of the atomic clouds undergoing the modified Mach-Zehnder interferometric scheme for phase noise minimization when the atomic cloud samples prepared from cold atoms are subjected to a parabolic trajectory constituting a launch and a free-fall. The presence of elliptic functions in this python code resulted in the longer code evaluation times. So, we optimized the code evaluation time for the case of 1000 atoms in each atomic cloud sample by a factor of 8.

In the final year, we designed simulations for compensation of gravity gradients and to invoke the novel design and different geometrical configurations, which calculate the residual phases achieving a relative accuracy of 10^{-6} . Initially the proposed design [63] was supposed to be analogous to the MAGIA-Adv [16, 17, 48] experiment, but from the simulations it was realized that the configuration - II stated in this thesis (using torus-shaped copper ring as source mass design) produced better results yielding better accuracy along with a highly reduced code evaluation time. Not to forget that in our Monte Carlo simulations, we have only used 1000 and 10000 atoms

producing error bars in the range of μrad . This implies that when this experiment will be implemented in near future with a minimum atom loading rate of 10^5 atoms/s inside the MOT chamber, then the results will be far more accurate with error bars reducing down to nrad and prad. Enhancing the atom loading rate leading to increased atomic population contributing to the signal; an optimization of the launch sequence parameters to further cool the atoms and a more efficient method of selecting the state and the velocity after the launch could easily allow to exceed 10^6 atoms contributing to the signal. Thanks to the technique [65] and its recent demonstration in MAGIA-Adv experiment [66], concluding that an accurate knowledge of the atomic positions at the time of the interferometer pulses is not necessary.

Eventually, all of this will result in elimination of systematic error by one order of magnitude contributing to determination of gravitational constant G surpassing the relative accuracy of 10^{-4} , using the subject of cold atom interferometry.

6.2 Future Prospects

The computational work done in regard to the experiment described in this thesis is favorable for both the directions - applied and fundamental sciences. Programming the experiments before actual implementation gives an experimentalist an idea of what will be suitable both in aspects of producing good quality results with minimization of costs in purchasing the experimental apparatus. It gives theorist a validation of their concepts being applicable to the real world, henceforth encouraging experimentalists to witness the truth by their eyes by building the experiment, hoping a positive expectation of the desired outcome. The codes described in this thesis can be ran for any number of atoms at good computational facilities so as to witness the experimental side of physics virtually. Furthermore, the simulations described here are standardized and can be used by all the metrologists around the globe in order for them to build best experimental configuration (for gravity gradiometer with source masses with least noisy interferometric signal) suitable as per their requirements.

In the simulations presented in this thesis, the centre-of-mass Z-coordinates of the atomic clouds can be varied further and results can be reproduced in the zone of the atomic fountain tube where the gravitational acceleration profiles do not exhibit any nonlinearity. This set of simulations will help yield the results for either CLOSE or FAR configurations of source masses aiming at an accurate determination of G and eliminating systematics at a high precision with a simultaneous cancellation of gravity gradients.

When heading towards high accuracy and desired precision, one must also pay good attention to other parameters that did not constitute a limit in previous determinations of Newtonian Gravitational constant. The most troublesome one out of them especially for a cold atomic fountain is the *Coriolis shift*, which can bias the interferometer output if transverse velocity of the atomic samples and/or k_{eff} direction change on the displacement of the source mass. Compensation schemes based on counteracting the Earth's rotation rate by acting on the retroreflecting Raman mirror must be optimized towards the percent accuracy.

Lastly, the source mass movement system must be mechanically well isolated from the fountain holding structure, in order to avoid correlations between source mass position and launch direction of the atomic sample. In this way, such shift can be efficiently rejected, and thus an improvement by a factor of ten of the result appears feasible as reported earlier [16].

In general, the experiments in atom interferometry like the one presented in this thesis can be employed to realize transportable devices and implementation of atomic sensors to carry out precise measurements verifying laws in fundamental physics.

Bibliography

- [1] J. Williams, S. w. - Chiow, H. Mueller, and N. Yu, Quantum Test of the Equivalence Principle and Space – Time aboard the International Space Station, *New. J. Phys.* **18**, 025018 (2016), DOI: <https://doi.org/10.1088/1367-2630/18/2/025018>.
- [2] S. w. - Chiow, J. Williams, N. Yu, and H. Mueller, Gravity gradient suppression in spaceborne atomic tests of the equivalence principle, *Phys. Rev. A* **95**, 021603 (2017), DOI: <https://doi.org/10.1103/PhysRevA.95.021603>.
- [3] M. G. Tarallo, T. Mazzoni, N. Poli, D. V. Sutyryn, X. Zhang, and G. M. Tino, Test of Einstein Equivalence Principle for 0-Spin and Half-Integer-Spin Atoms: Search for Spin-Gravity Coupling Effects, *Phys. Rev. Lett.* **113**, 023005 (2014), DOI: <https://doi.org/10.1103/PhysRevLett.113.023005>.
- [4] D. Schlippert, J. Hartwig, H. Albers, L. L. Richardson, C. Schubert, A. Roura, W. P. Schleich, W. Ertmer, and E. M. Rasel, Quantum Test of the Universality of Free Fall, *Phys. Rev. Lett.* **112**, 203002 (2014), DOI: <https://doi.org/10.1103/PhysRevLett.112.203002>.
- [5] L. Zhou, S. Long, B. Tang, X. Chen, F. Gao, W. Peng, W. Duan, J. Zhong, Z. Xiong, J. Wang, Y. Zhang, and M. Zhan, Test of Equivalence Principle at 10^{-8} Level by a Dual-Species Double-Diffraction Raman Atom Interferometer *Phys. Rev. Lett.* **115**, 013004 (2015), DOI: <https://doi.org/10.1103/PhysRevLett.115.013004>.
- [6] X.-C. Duan, X.-B. Deng, M.-K. Zhou, K. Zhang, W.-J. Xu, F. Xiong, Y.-Y. Xu, C.-G. Shao, J. Luo, and Z.-K. Hu, Test of the Universality of Free Fall with Atoms in Different Spin Orientations, *Phys. Rev. Lett.* **117**, 023001 (2016), DOI: <https://doi.org/10.1103/PhysRevLett.117.023001>.

- [7] J. Rudolph, T. Wilkason, M. Nantel, H. Swan, C. M. Holland, Y. Jiang, B. E. Garber, S. P. Carman, and J. M. Hogan, Large Momentum Transfer Clock Atom Interferometry on the 689nm Intercombination Line of Strontium, *Phys. Rev. Lett.* **124**(8):083604 (2020), DOI: <https://doi.org/10.1103/physrevlett.124.083604>.
- [8] E. Fermi and L. Marshall, Interference Phenomena of slow neutrons, *Phys. Rev.* **71**, 666 (1947), DOI: <https://doi.org/10.1103/PhysRev.71.666>.
- [9] L. Marton, Electron interferometer, *Phys. Rev.* **85**, 1057 (1952), DOI: <https://doi.org/10.1103/PhysRev.85.1057>.
- [10] Moellenstedt and H. Dueker, Beobachtungen und Messungen an Biprisma-Interferenzen mit Elektronenwellen, *Zeitschrift für Physik* **145**, 377 (1956), DOI: <https://doi.org/10.1007/BF01326780>.
- [11] G. Moellenstedt and H. Dueker H, Fresnelscher Interferenzversuch mit einem Biprisma fuer Elektronenwellen , *Naturwiss* **42**, 41 (1954), DOI: <https://doi.org/10.1007/BF00621530>.
- [12] O. Carnal and J. Mlynek, Young's double-slit experiment with atoms: A simple atom interferometer, *Phys. Rev. Lett.* **66**, 2689 (1991), DOI: <https://doi.org/10.1103/PhysRevLett.66.2689>.
- [13] D. W. Keith, Ch. R. Ekstrom, Q. A. Turchette, and D. E. Pritchard, An interferometer for atoms, *Phys. Rev. Lett.* **66**, 2693 (1991), DOI: <https://doi.org/10.1103/PhysRevLett.66.2693>.
- [14] F. Riehle, Th. Kisters, A. Witte, J. Helmcke, and Ch. J. Bordé, Optical Ramsey spectroscopy in a rotating frame: Sagnac effect in a matter-wave interferometer, *Phys. Rev. Lett.* **67**, 177 (1991), DOI: <https://doi.org/10.1103/PhysRevLett.67.177>.
- [15] M. Kasevich and S. Chu, Atomic Interferometry using stimulated Raman transitions, *Phys. Rev. Lett.* **67**, 181 (1991), DOI: <https://doi.org/10.1103/PhysRevLett.67.181>.
- [16] G. Rosi, F. Sorrentino, L. Cacciapuoti, M. Prevedelli, and G. M. Tino, Precision measurement of the Newtonian gravitational constant using cold atoms, *Nature Comm.* **510**, 518 (2014), DOI: <https://doi.org/10.1038/nature13433>.

- [17] G. Lamporesi, *Determination of the gravitational constant by atom interferometry*, (**PhD thesis**), Università di Firenze (2006).
- [18] G. Lamporesi, A. Bertoldi, L. Cacciapuoti, M. Prevedelli, and G. M. Tino, Determination of the Newtonian Gravitational Constant Using Atom Interferometry, *Phys. Rev. Lett.* **100**, 050801 (2008), DOI: <https://doi.org/10.1103/PhysRevLett.100.050801>.
- [19] F. Sorrentino, Y. H. Lien, G. Rosi, L. Cacciapuoti, M. Prevedelli, and G. M. Tino, Sensitive gravity-gradiometry with atom interferometry: progress towards an improved determination of the gravitational constant, *New Journal Physics* **12**, 095009 1-17 (2010), DOI: <https://doi.org/10.1088/1367-2630/12/9/095009>.
- [20] G. Rosi, *Precision gravity measurements with atom interferometry*, (**PhD thesis**), Università di Firenze (2012).
- [21] T. Petelski, *Atom interferometers for precision gravity measurements* (**PhD thesis**), Università di Firenze - Université Paris 6 (2005).
- [22] M. Prevedelli, L. Cacciapuoti, G. Rosi, F. Sorrentino, and G. M. Tino, Measuring the Newtonian constant of gravitation G with an atomic interferometer, *Phil. Trans. R. Soc. A* **372**:20140030 (2014), DOI: <https://doi.org/10.1098/rsta.2014.0030>.
- [23] J. B. Fixler, G. T. Foster, J. M. McGuirk, M. A. Kasevich, Atom interferometer measurement of Newtonian Constant of Gravity, *Science* **315**, Issue 5808, 74 (2007), DOI: <https://doi.org/10.1126/science.1135459>.
- [24] Quinn, T. Measuring big G . *Nature* **408**, 919 (2000), DOI: <https://doi.org/10.1038/35050187>.
- [25] G. Lamporesi, A. Bertoldi, A. Cecchetti, B. Duhlach, M. Fattori, A. Malengo, S. Pettoruso, M. Prevedelli and G. M. Tino, Source mass and positioning system for an accurate measurement of G , *Rev. Sci. Inst.* **78**, 075109, (2007), DOI: <https://doi.org/10.1063/1.2751090>.
- [26] G. M. Tino, I. Ciufolini, D. Dominici, and L. Lusanna, editors: A relativistic spacetime odyssey - Johns Hopkins Workshop, 147 (Firenze 2001), *World Scientific 2003*.
- [27] A. Bertoldi, G. Lamporesi, L. Cacciapuoti, M. De Angelis, M. Fattori, T. Petelski, A. Peters, M. Prevedelli, J. Stuhler, and G. M. Tino, Atom

- interferometry gravity-gradiometer for the determination of the Newtonian gravitational constant G , *Eur. Phys. J. D* **40**:271 (2006), DOI: <https://doi.org/10.1140/epjd/e2006-00212-2>.
- [28] M. Fattori, G. Lamporesi, T. Petelski, J. Stuhler, and G. M. Tino, Towards an atom interferometric determination of the Newtonian gravitational constant, *Physics Letters A* **318**(3):184 (2003), DOI: <https://doi.org/10.1016/j.physleta.2003.07.011>.
- [29] M. Cadoret, E. De Mirandes, P. Cladé, F. Nez, L. Julien, F. Biraben, and S. Guellati-Khélifa, Atom interferometry based on light pulses : application to the high precision measurement of the ratio h/m and the determination of the fine structure constant, *The European Physical Journal Special Topics* **172**, 121 (2009), DOI: <https://doi.org/10.1140/epjst/e2009-01046-2>.
- [30] Pierre Cladé, François Biraben, Lucile Julien, François Nez and Saída Guellati-Khelifa, Precise determination of the ratio h/m_u : a way to link microscopic mass to the new kilogram, *Metrologia* **53** A75 (2016), DOI: <https://doi.org/10.1088/0026-1394/53/5/A75>.
- [31] Weiss, D. S., Young, B. C., and Chu S., Precision measurement of the photon recoil of an atom using atomic interferometry, *Phys. Rev. Lett.* **70**, 2706 (1993), DOI: <https://doi.org/10.1103/PhysRevLett.70.2706>.
- [32] S. Gupta, K. Dieckmann, Z. Hadzibabic, and D. E. Pritchard, Contrast interferometry using bose-einstein condensates to measure h/m and α , *Phys. Rev. Lett.* **89**, 140401, (2002), DOI: <https://doi.org/10.1103/PhysRevLett.89.140401>.
- [33] C. R. Ekstrom, J. Schmiedmayer, M. S. Chapman, T. D. Hammond, and D. E. Pritchard, Measurement of the electric polarizability of sodium with an atom interferometer, *Phys. Rev. A* **51**, 3883 (1995), DOI: <https://doi.org/10.1103/PhysRevA.51.3883>.
- [34] A. Miffre, M. Jacquy, M. Büchner, G. Tréneç, and J. Vigué, Measurement of the electric polarizability of lithium by atom interferometry, *Phys. Rev. A* **73**, 011603 (2006), DOI: <https://doi.org/10.1103/PhysRevA.73.011603>.
- [35] G. D'Amico, L. Cacciapuoti, M. Jain, S. Zhan, and G. Rosi, Measuring the gravitational acceleration with matter - wave velocimetry,

- Eur. Phys. J. D* **73**, 98 (2019), DOI: <https://doi.org/10.1140/epjd/e2019-90543-0>.
- [36] Peters, A., Chung, K. Y. and Chu, S. Measurement of gravitational acceleration by dropping atoms, *Nature* **400**, 849 (1999), DOI: <https://doi.org/10.1038/23655>.
- [37] M. Kasevich and S. Chu, Measurement of the gravitational acceleration of an atom with a lightpulse atom interferometer, *Applied Physics B* **54**, 321 (1992), DOI: <https://doi.org/10.1007/BF00325375>.
- [38] G. Rosi, L. Cacciapuoti, F. Sorrentino, M. Menchetti, M. Prevedelli, and G. M. Tino, Measurement of the Gravity-Field Curvature by Atom Interferometry, *Phys. Rev. Lett.* **114**, 013001 (2015), DOI: <https://doi.org/10.1103/PhysRevLett.114.013001>.
- [39] P. Asenbaum, C. Overstreet, T. Kovachy, D. D. Brown, J. M. Hogan, and M. A. Kasevich, Phase Shift in an Atom Interferometer due to Space-time Curvature across its Wave Function, *Phys. Rev. Lett.* **118**, 183602 (2017), DOI: <https://doi.org/10.1103/PhysRevLett.118.183602>.
- [40] M. J. Snadden, J. M. McGuirk, P. Bouyer, K. G. Haritos, and M. A. Kasevich, Measurement of the earth's gravity gradient with an atom interferometer based gravity gradiometer, *Phys. Rev. Lett.* **81**, 971 (1998), DOI: <https://doi.org/10.1103/PhysRevLett.81.971>.
- [41] J. M. McGuirk, G. T. Foster, J. B. Fixler, M. J. Snadden, and M. A. Kasevich, Sensitive absolute-gravity gradiometry using atom interferometry, *Physical Review A* **65**, 33 (2002), DOI: <https://doi.org/10.1103/PhysRevA.65.033608>.
- [42] R. H. Parker, C. Yu, W. Zhong, B. Estey, and H. Mueller, Measurement of the fine-structure constant as a test of the Standard Model, *Science* **360**, Issue 6385, 191 (2018), DOI: <https://doi.org/10.1126/science.aap7706>.
- [43] C. Yu, W. Zhong, B. Estey, J. Kwan, R. H. Parker and H. Mueller, Atom interferometry Measurement of the Fine Structure Constant, *Annalen der Physik* **531**, 1800346 (2019), DOI: <https://doi.org/10.1002/andp.201800346>.
- [44] T. L. Gustavson, A. Landragin, and M. A. Kasevich, Rotation sensing with a dual atom interferometer Sagnac gyroscope, *Class. Quantum*

- Grav.* **17**, 2385 (2000), DOI: <https://doi.org/10.1088/0264-9381/17/12/311>.
- [45] T. L. Gustavson, P. Bouyer, and M. A. Kasevich, Precision Rotation Measurements with an Atom Interferometer Gyroscope, *Phys. Rev. Lett.* **78**, 2046 (1997), DOI: <https://doi.org/10.1103/PhysRevLett.78.2046>.
- [46] B. Canuel, F. Leduc, D. Holleville, A. Gauguet, J. Fils, A. Virdis, A. Clairon, N. Dimarcq, C. J. Borde, A. Landragin, and P. Bouyer, Six-Axis Inertial Sensor Using Cold-Atom Interferometry, *Phys. Rev. Lett.* **97**, 010402 (2006), DOI: <https://doi.org/10.1103/PhysRevLett.97.010402>.
- [47] A. Gauguet, B. Canuel, T. Leveque, W. Chaibi, and A. Landragin, Characterization and limits of a cold-atom Sagnac interferometer, *Phys. Rev. A* **80**, 063604 (2009), DOI: <https://doi.org/10.1103/PhysRevA.80.063604>.
- [48] G. Rosi, G. D'Amico, L. Cacciapuoti, F. Sorrentino, M. Prevedelli, M. Zych, C. Brukner, and G. M. Tino, Quantum test of the equivalence principle for atoms in coherent superposition of internal energy states, *Nature Comm.* **8**, 15529 (2017), DOI: <https://doi.org/10.1038/ncomms15529>.
- [49] S. Fray, C. A. Diez, T.W. Hänsch, and M. Weitz, Atomic interferometer with amplitude gratings of light and its applications to atom based tests of the equivalence principle, *Phys. Rev. Lett.* **93**, 240404 (2004), DOI: <https://doi.org/10.1103/PhysRevLett.93.240404>.
- [50] Tino, G. M. and Kasevich, M. A. (eds.). *Atom Interferometry, Proceedings of the International School of Physics Enrico Fermi, Course CLXXXVIII, Varenna 2013* (Societa Italiana di Fisica and IOS Press).
- [51] M. de Angelis, A. Bertoldi, L. Cacciapuoti, A. Giorgini, G. Lamporesi, M. Prevedelli, G. Saccorotti, F. Sorrentino and G. M. Tino, Precision gravimetry with atomic sensors, *Meas. Sci. Technol.* **20**, 022001 (2009), DOI: <https://doi.org/10.1088/0957-0233/20/2/022001>.
- [52] G. D'Agostino, S. Desogus, A. Germak, C. Origlia, D. Quagliotti, G. Berrino, G. Corrado, V. D'Errico, and G. Ricciardi, The new IMGC-02 transportable absolute gravimeter: measurement apparatus and applications in geophysics and volcanology, *Annals of Geophysics* **51**, 1 (2008), DOI: <https://doi.org/10.4401/ag-3038>.

- [53] A. D. Cronin, J. Schmiedmayer, and D. E. Pritchard, Optics and interferometry with atoms and molecules, *Rev. Mod. Phys.* **81**, 1051 (2009), DOI: <https://doi.org/10.1103/RevModPhys.81.1051>
- [54] D. S. Durfee, Y. K. Shaham, and M. A. Kasevich, Long-Term Stability of an Area-Reversible Atom-Interferometer Sagnac Gyroscope, *Phys. Rev. Lett.* **97**, 240801 (2006), DOI; <https://doi.org/10.1103/PhysRevLett.97.240801>
- [55] A. Bresson, Y. Bidel, P. Bouyer, B. Leone, E. Murphy, and P. Silvestrin, Quantum mechanics for space applications, *Appl. Phys. B* **84**, 545 (2006), DOI: <https://doi.org/10.1007/s00340-006-2412-x>.
- [56] D. Aguilera et al., Test of the universality of free fall using cold atom interferometry, *Classical and Quantum Gravity* **31**, 15 (2014), DOI: <https://doi.org/10.1088/0264-9381/31/11/115010>.
- [57] J. Hartwig, S. Abend, C. Schubert, D. Schlippert, H. Ahlers, K. Posso-Trujillo, N. Gaaloul, W. Ertmer, and E. M. Rasel, Testing the universality of free fall with rubidium and ytterbium in a very large baseline atom interferometer, *New Journal of Physics* **17**, 035011 (2015), DOI: <https://doi.org/10.1088/1367-2630/17/3/035011>.
- [58] H. Müller, S.-W. Chiow, Q. Long, S. Herrmann, and S. Chu, Atom Interferometry with up to 24-Photon-Momentum-Transfer Beam Splitters, *Phys. Rev. Lett.* **100**, 180405 (2008), DOI: <https://doi.org/10.1103/PhysRevLett.100.180405>.
- [59] S. Dimopoulos, P. W. Graham, J. M. Hogan, and M. A. Kasevich, Testing General Relativity with Atom Interferometry, *Phys. Rev. Lett.* **98**, 111102 (2007), DOI: <https://doi.org/10.1103/PhysRevLett.98.111102>.
- [60] V. Ménoiret, P. Vermeulen, N. L. Moigne, S. Bonvalot, P. Bouyer, A. Landragin, and B. Desruelle, Gravity measurements below 10^{-9} g with a transportable absolute quantum gravimeter, *Sci. Rep.* **8**, 12300 (2018), DOI: <https://doi.org/10.1038/s41598-018-30608-1>.
- [61] Feng Yong-yuan, Zhang Guang-yuan, Li De-xi, Qiu Xiao-mei, Zhou Jing-hua, Gao Jing-Lung, Huang Da-lun, Huang Cheng-qing, and Guo You-Guang, A Transportable Absolute Gravimeter for Determining the Acceleration due to the Earth's Gravity, *Metrologia* **18**, 139 (1982), DOI: <https://doi.org/10.1088/0026-1394/18/3/005>.

- [62] M. Schmidt, M. Prevedelli, A. Giorgini, G. M. Tino, and A. Peters, A portable laser system for high-precision atom interferometry experiments, *Applied Physics B, Laser and optics* **102**, 11 (2011), DOI: <https://doi.org/10.1007/s00340-010-4263-8>.
- [63] G. Rosi, A proposed atom interferometry determination of G at 10^{-5} using a cold atomic fountain, *Metrologia* **55**, 1 (2017), DOI: <https://doi.org/10.1088/1681-7575/aa8fd8>.
- [64] A. Louchet-Chauvet, T. Farah, Q. Bodart, A. Clairon, A. Landragin, S. Merlet, and F. P. D. Santos, The influence of transverse motion within an atomic gravimeter, *New J. Phys.* **13**, 065025 (2011), DOI: <https://doi.org/10.1088/1367-2630/13/6/065025>.
- [65] A. Roura, Circumventing Heisenberg's Uncertainty Principle in Atom Interferometry Tests of the Equivalence Principle, *Phys. Rev. Lett.* **118**, 160401 (2017), DOI: <https://doi.org/10.1103/PhysRevLett.118.160401>.
- [66] G. D'Amico, G. Rosi, S. Zhan, L. Cacciapuoti, M. Fattori, and G. M. Tino, Canceling the Gravity Gradient Phase Shift in Atom Interferometry, *Phys. Rev. Lett.* **119**, 253201 (2017), DOI: <https://doi.org/10.1103/PhysRevLett.119.253201>.
- [67] P. Meystre and M. Sargent-III, eds., *Elements of Quantum Optics*, Springer Verlag, Berlin, 1999.
- [68] K. Moler, D. S. Weiss, M. Kasevich, and S. Chu, Theoretical analysis of velocity-selective Raman transitions, *Phys. Rev. A* **45**, 342 (1992), DOI: <https://doi.org/10.1103/PhysRevA.45.342>.
- [69] G. D'Amico, *Gravitational physics tests with a Rubidium atom interferometer*, (**PhD thesis**), Università di Firenze (2018).
- [70] R. J. Adler, Six easy roads to the Planck scale, *American Journal of Physics* **78**, 925 (2010), DOI: <https://doi.org/10.1119/1.3439650>
- [71] M. Zych and C. Brukner, Quantum formulation of the Einstein Equivalence Principle, **arXiv:1502.00971 [gr-qc]**, Available online: <https://arxiv.org/pdf/1502.00971.pdf>
- [72] T. Mazzoni, X. Zhang, R. D. Aguila, L. Salvi, N. Poli, and G. M. Tino, Large-momentum-transfer Bragg interferometer with strontium atoms, *Phys Rev. A.* **92**, 053619 (2015), DOI: <https://doi.org/10.1103/PhysRevA.92.053619>.

- [73] F. Sorrentino, Q. Bodart, L. Cacciapuoti, Y.-H. Lien, M. Prevedelli, G. Rosi, L. Salvi, and G. M. Tino, Sensitivity limits of a Raman atom interferometer as a gravity gradiometer, *Phys. Rev. A* **89**, 023607 (2014), DOI: <https://doi.org/10.1103/PhysRevA.89.023607>.
- [74] M. de Angelis, F. Greco, A. Pistorio, N. Poli, M. Prevedelli, G. Saccorotti, F. Sorrentino, and G. M. Tino, Absolute gravity acceleration measurement in atomic sensor laboratories, *Eur. Phys. J. Plus* **127**, 27 (2012), DOI: <https://doi.org/10.1140/epjp/i2012-12027-9>.
- [75] S.-w. Chiow, T. Kovachy, H.-C. Chien, and M. A. Kasevich, $102\hbar$ Large Area Atom Interferometers, *Phys. Rev. Lett.* **107**, 130403 (2011), DOI: <https://doi.org/10.1103/PhysRevLett.107.130403>.
- [76] M. Carey, M. Belal, M. Himsworth, J. Bateman, and T. Freegarde, Matterwave interferometric velocimetry of cold Rb atoms, *J. Mod. Opt.* **65**, 657 (2017), DOI: <https://doi.org/10.1080/09500340.2017.1397222>.
- [77] M. Carey, J. Saywell, D. Elcock, M. Belal, and T. Freegarde, Velocimetry of cold atoms by matterwave interferometry, *Phys. Rev. A* **99**, 023631 (2019), DOI: <https://doi.org/10.1103/PhysRevA.99.023631>.
- [78] https://en.wikipedia.org/wiki/Solenoid#Finite_continuous_solenoid
- [79] N. Derby and S. Olbert, Cylindrical magnets and ideal solenoids, *American Journal of Physics* **78**, 229 (2010), DOI: <https://doi.org/10.1119/1.3256157>.
- [80] S. E. Harris, J. E. Field, and A. Imamoglu, Nonlinear optical processes using electromagnetically induced transparency, *Phys. Rev. Lett.* **64**, 1107 (1990), DOI: <https://doi.org/10.1103/PhysRevLett.64.1107>.
- [81] M. Fleischhauer, A. Imamoglu, and J. P. Marangos, Electromagnetically induced transparency: Optics in coherent media, *Rev. Mod. Phys.* **77**, 633 (2005), DOI: <https://doi.org/10.1103/RevModPhys.77.633>.
- [82] M. Afzelius, N. Gisin, and H. de Riedmatten, Quantum Memory for photons, *Physics Today* **68**, 12, 42 (2015), DOI: <https://doi.org/10.1063/PT.3.3021>.
- [83] Y.-W. Cho, G. T. Campbell, J. L. Everett, J. Bernu, D. B. Higginbottom, M. T. Cao, J. Geng, N. P. Robins, P. K. Lam, and B. C.

- Buchler, Highly efficient optical quantum memory with long coherence time in cold atoms, *Optica* **3**, Issue 1, 100 (2016), DOI: <https://doi.org/10.1364/OPTICA.3.000100>.
- [84] Y.-H. Chen, M.-J. Lee, I.-C. Wang, S. Du, Y.-F. Chen, Y.-C. Chen, and I. A. Yu, Coherent Optical Memory with High Storage Efficiency and Large Fractional Delay, *Phys. Rev. Lett.* **110**, 083601 (2013), DOI: <https://doi.org/10.1103/PhysRevLett.110.083601>.
- [85] D. F. Phillips, A. Fleischhauer, A. Mair, R. L. Walsworth, and M. D. Lukin, Storage of Light in Atomic Vapor, *Phys. Rev. Lett.* **86**, 783 (2001), DOI: <https://doi.org/10.1103/PhysRevLett.86.783>.
- [86] S. Bhushan, V. S. Chauhan, and R. K. Easwaran, Ultracold Rydberg atoms for efficient storage of terahertz frequency signals using electromagnetically induced transparency, *Physics Letters A* **382**, 3500 (2018), DOI: <https://doi.org/10.1016/j.physleta.2018.10.006>.
- [87] S. Bhushan and R. K. Easwaran, Theoretical design for generation of slow light in a two-dimensional magneto optical trap using electromagnetically induced transparency, *Appl. Opt.* **56**, Issue 13, 3817 (2017), DOI: <https://doi.org/10.1364/AO.56.003817>.
- [88] Yen-Wei Lin, Hung-Chih Chou, Prashant P. Dwivedi, Ying-Cheng Chen, and Ite A. Yu, Using a pair of rectangular coils in the MOT for the production of cold atom clouds with large optical density, *Optics Express* **16**, Issue 6, 3753 (2008), DOI: <https://doi.org/10.1364/OE.16.003753>.
- [89] E. Riis, D. S. Weiss, K. A. Moler, and S. Chu, Atom Funnel for the Production of a slow, high-density atomic Beam, *Phys. Rev. Lett.* **64**, 1658 (1990), DOI: <https://doi.org/10.1103/PhysRevLett.64.1658>.
- [90] S. Weyers, E. Aucouturier, C. Valentin, and N. Dimarcq, A continuous beam of cold cesium atoms extracted from a two-dimensional magneto-optical trap, *Opt. Commun.* **143**, Issues 1-3, 30 (1997), DOI: [https://doi.org/10.1016/S0030-4018\(97\)00312-X](https://doi.org/10.1016/S0030-4018(97)00312-X).
- [91] P. Berthoud, A. Joyet, G. Dudle, N. Sagna and, P. Thomann, A continuous beam of slow, cold cesium atoms magnetically extracted from a 2D magneto-optical trap, *Europhys. Lett.* **41** (2), 141 (1998), DOI: <https://doi.org/10.1209/epl/i1998-00122-9>.

- [92] K. Dieckmann, R. J. C. Spreeuw, M. Weidemueller, and J. T. M. Walraven, Two-dimensional magneto-optical trap as a source of slow atoms, *Phys. Rev. A* **58**, 3891 (1998), DOI: <https://doi.org/10.1103/PhysRevA.58.3891>.
- [93] P. Cren, C. F. Roos, A. Aclan, J. Dalibard, D. Guery-Odelin, Loading of a cold atomic beam into a magnetic guide, *Eur. Phys. J. D* **20**, 107 (2002), DOI: <https://doi.org/10.1140/epjd/e2002-00106-3>.
- [94] J. Schoser, A. Bataer, R. Loew, V. Schweikhard, A. Grabowski, Yu. B. Ovchinnikov, and T. Pfau, Intense source of cold Rb atoms from a pure two-dimensional magneto-optical trap, *Phys. Rev. A* **66**, 023410 (2002), DOI: <https://doi.org/10.1103/PhysRevA.66.023410>.
- [95] M. Vengalattore, R. S. Conroy, and M. G. Prentiss, Enhancement of Phase Space Density by Increasing Trap Anisotropy in a Magneto-Optical Trap with a Large Number of Atoms, *Phys. Rev. Lett.* **92**, 183001 (2004), DOI: <https://doi.org/10.1103/PhysRevLett.92.183001>.
- [96] J. Ramirez-Serrano, N. Yu, J. M. Kohel, J. R. Kellogg, and L. Maleki, Multistage two-dimensional magneto-optical trap as a compact cold atom beam source, *Opt. Lett.* **31**, Issue 6, 682 (2006), DOI: <https://doi.org/10.1364/OL.31.000682>.
- [97] N. Castagnaa, J. Guenab, M.D. Plimmer, and P. Thomann, A novel simplified two-dimensional magneto-optical trap as an intense source of slow cesium atoms, *Eur. Phys. J. Appl. Phys.* **34**, Issue 1, 21 (2006), DOI: <https://doi.org/10.1051/epjap:2006037>.
- [98] S. Chaudhuri, S. Roy, and C. S. Unnikrishnan, Realization of an intense cold Rb atomic beam based on a two-dimensional magneto-optical trap: Experiments and comparison with simulations, *Phys. Rev. A* **74**, 023406 (2006), DOI: <https://doi.org/10.1103/PhysRevA.74.023406>.
- [99] Dejan M. Petković and Milica D. Radić, Generalization of Helmholtz Coil Problem, *Serbian Journal of Electrical Engineering* **12**, Issue 3, 375 (2012), DOI: <https://doi.org/10.2298/SJEE1503375P>.
- [100] B. Dubetsky, Optimization of the atom interferometer phase produced by the set of cylindrical source masses to measure the Newtonian gravity constant, **arXiv:1907.03352v5[physics.atom-ph]**, Available online: <https://arxiv.org/pdf/1907.03352.pdf>.

- [101] C. Antoine and C. J. Bordé, Exact phase shifts for atom interferometry, *Phys. Lett. A* **306**, Issues 5-6, 277 (2003), DOI: [https://doi.org/10.1016/S0375-9601\(02\)01625-0](https://doi.org/10.1016/S0375-9601(02)01625-0).
- [102] D. W. Allan, Statistics of atomic frequency standards, *Proceedings of the IEEE* **54**, Issue 2, 221 (1966), DOI: <https://doi.org/10.1109/PROC.1966.4634>.

Appendix A

Magnetic Fields: Exact solution

The origin coordinate for the B-pulse coil is taken to be $(0, 0, z_1)$ with $2b$ as length of the B-pulse/bias coil (Figure A.1), so that the following solution is generalized for all the possible coordinates along the altitude axis / Z - axis of the atomic fountain tower, hence this solution can be applied both for bias coil ($z_1 = 0$) and B-pulse coil ($z_1 \neq 0$). Using the knowledge from equations written for the case of finite solenoid in three dimensions [79], the components of the magnetic field for the case of the any finite solenoidal coil with its origin displaced along Z - axis in cartesian coordinate system are modified and rewritten as follows:

$$B_z(x, y, z) = \frac{\mu_0 n I}{\pi} \int_0^{\pi/2} \left[\frac{a((\cos \phi)^2 + \gamma(\sin \phi)^2)}{(\sqrt{x^2 + y^2 + a})(\cos \phi)^2 + \gamma^2(\sin \phi)^2} \right] [j_+ - j_-] d\phi \quad (\text{A.1})$$

$$B_x(x, y, z) = B_\rho \frac{x}{\sqrt{x^2 + y^2}} \quad (\text{A.2})$$

$$B_y(x, y, z) = B_\rho \frac{y}{\sqrt{x^2 + y^2}} \quad (\text{A.3})$$

such that

$$B_\rho(x, y, z) = \frac{\mu_0 n I}{\pi} \left[\alpha_+ \int_0^{\pi/2} \frac{\cos 2\phi}{\sqrt{(\cos \phi)^2 + k_+^2}} d\phi - \alpha_- \int_0^{\pi/2} \frac{\cos 2\phi}{\sqrt{(\cos \phi)^2 + k_-^2}} d\phi \right] \quad (\text{A.4})$$

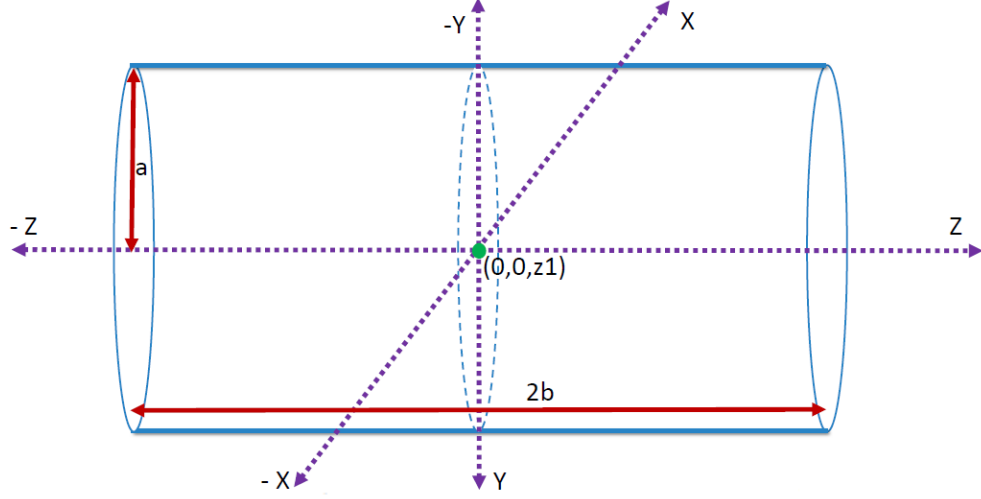


Figure A.1: Finite solenoidal coil centered at $(0, 0, z_1)$ with radius a : If $z_1 = 0$ the coil acts as a bias coil else ($z_1 \neq 0$) it is a B-pulse coil, considering different values of altitude magnitude $2b$ for both bias and B-pulse coils.

where

$$\gamma = \frac{a - \sqrt{x^2 + y^2}}{a + \sqrt{x^2 + y^2}} \quad (\text{A.5})$$

$$j_+ = \left[\frac{\beta_+}{\sqrt{(\cos \phi)^2 + k_+^2 (\sin \phi)^2}} \right] \quad (\text{A.6})$$

$$j_- = \left[\frac{\beta_-}{\sqrt{(\cos \phi)^2 + k_-^2 (\sin \phi)^2}} \right] \quad (\text{A.7})$$

$$\alpha_+ = \frac{a}{\sqrt{(z + b + z_1)^2 + (\sqrt{x^2 + y^2} + a)^2}} \quad (\text{A.8})$$

$$\alpha_- = \frac{a}{\sqrt{(z - b - z_1)^2 + (\sqrt{x^2 + y^2} + a)^2}} \quad (\text{A.9})$$

$$k_+ = \sqrt{\frac{(z + b + z_1)^2 + (a - \sqrt{x^2 + y^2})^2}{(z + b + z_1)^2 + (a + \sqrt{x^2 + y^2})^2}} \quad (\text{A.10})$$

$$k_- = \sqrt{\frac{(z - b - z_1)^2 + (a - \sqrt{x^2 + y^2})^2}{(z - b - z_1)^2 + (a + \sqrt{x^2 + y^2})^2}} \quad (\text{A.11})$$

$$\beta_+ = \frac{(z + b + z_1)}{\sqrt{(z + b + z_1)^2 + (\sqrt{x^2 + y^2} + a)^2}} \quad (\text{A.12})$$

$$\beta_- = \frac{(z - b - z_1)}{\sqrt{(z - b - z_1)^2 + (\sqrt{x^2 + y^2} + a)^2}} \quad (\text{A.13})$$

Here, a is the internal radius of the atomic fountain tower, L and $2b$ ($L = 2b$) represent the height of the atomic fountain tower, n is the ratio of number of turns to altitude, I is the current flowing through the bias coil. Using all the above equations, the modulus of the magnetic field was written using cartesian components. After this was done, equations of motion for a parabolic trajectory with a *kick* from the laser pulses were written to compute interferometric phases as explained and implemented in this thesis.

Approach towards generalized and exact solution: In both cylindrical and cartesian coordinate systems [79], Y - component is zero, X and Z components of the magnetic field are derived and reduced in terms of special functions as follows (solutions applicable to both cases : Bias coil ($z_1 = 0$) and B-pulse coil ($z_1 \neq 0$)). The following reduced expressions (in the terms of special functions) can be trusted well because a simulation was performed to check the values of magnetic fields at several coordinates for the cases of equations derived below, and for the ones stated in the preceding section. From the results of this particular simulation, the values of magnetic fields matched exactly, with this result it was clear that the equations derived in this Section and the ones stated in the previous Section are equivalent.

X - COMPONENT:

$$B_X = \frac{\mu_0 n I a}{2\pi} (B_{X1} + B_{X2}) \quad (\text{A.14})$$

where,

$$B_{X1} = \left[\int_0^\pi \frac{\cos \phi}{\sqrt{\rho^2 + a^2 + (z - z_1 - b_1)^2 - 2a\rho \cos \phi}} d\phi \right] \quad (\text{A.15})$$

$$B_{X2} = - \left[\int_0^\pi \frac{\cos \phi}{\sqrt{\rho^2 + a^2 + (z - z_1 + b_1)^2 - 2a\rho \cos \phi}} d\phi \right] \quad (\text{A.16})$$

Equations A.15 and A.16 are reduced in the terms of *elliptic functions* (elliptic-E(\mathcal{E}), elliptic-K(\mathcal{K}) and elliptic- π (\mathcal{E}_π)) as follows:

$$B_{X1} = \left(\frac{2A_+}{\mathcal{N}\sqrt{A_+ + \mathcal{N}}} \right) \mathcal{K} \left[\frac{2\mathcal{N}}{A_+ + \mathcal{N}} \right] - \left(\frac{2\sqrt{A_+ + \mathcal{N}}}{\mathcal{N}} \right) \mathcal{E} \left[\frac{2\mathcal{N}}{A_+ + \mathcal{N}} \right] \quad (\text{A.17})$$

and

$$B_{X2} = \left(\frac{2A_-}{\mathcal{N}\sqrt{A_- + \mathcal{N}}} \right) \mathcal{K} \left[\frac{2\mathcal{N}}{A_- + \mathcal{N}} \right] - \left(\frac{2\sqrt{A_- + \mathcal{N}}}{\mathcal{N}} \right) \mathcal{E} \left[\frac{2\mathcal{N}}{A_- + \mathcal{N}} \right] \quad (\text{A.18})$$

with

$$A_+ = \rho^2 + a^2 + (z - z_1 - b_1)^2 \quad (\text{A.19})$$

$$A_- = \rho^2 + a^2 + (z - z_1 + b_1)^2 \quad (\text{A.20})$$

$$\mathcal{N} = 2a\rho \quad (\text{A.21})$$

Z - COMPONENT:

$$B_Z = B_{Z1} + B_{Z2} \quad (\text{A.22})$$

where,

$$B_{Z1} = \int_0^\pi \frac{\mathcal{D}\mathcal{Z}_+}{(\mathcal{T} - \mathcal{N} \cos \phi) \sqrt{A_- - \mathcal{N} \cos \phi}} d\phi \quad (\text{A.23})$$

$$B_{Z2} = \int_0^\pi \frac{-\mathcal{D}\mathcal{Z}_-}{(\mathcal{T} - \mathcal{N} \cos \phi) \sqrt{A_+ - \mathcal{N} \cos \phi}} d\phi \quad (\text{A.24})$$

such that:

$$\mathcal{Z}_+ = z - z_1 + b_1 \quad (\text{A.25})$$

$$\mathcal{Z}_- = z - z_1 - b_1 \quad (\text{A.26})$$

$$\mathcal{T} = \rho^2 + a^2 \quad (\text{A.27})$$

$$\mathcal{D} = a - \rho \cos \phi \quad (\text{A.28})$$

Equations A.23 and A.24 are split in two parts:

$$B_{Z1} = B_{Z1}^a + B_{Z1}^\rho \quad (\text{A.29})$$

where,

$$B_{Z1}^a = \int_0^\pi \frac{a\mathcal{Z}_+}{(\mathcal{T} - \mathcal{N} \cos \phi)\sqrt{A_- - \mathcal{N} \cos \phi}} d\phi \quad (\text{A.30})$$

$$B_{Z1}^\rho = - \int_0^\pi \frac{\mathcal{Z}_+ \rho \cos \phi}{(\mathcal{T} - \mathcal{N} \cos \phi)\sqrt{A_- - \mathcal{N} \cos \phi}} d\phi \quad (\text{A.31})$$

B_{Z1}^a is reduced as follows:

$$B_{Z1}^a = \left(\frac{2a\mathcal{Z}_+}{(\mathcal{T} + \mathcal{N})(A_- + \mathcal{N})} \right) \mathcal{E}_\pi \left[\frac{2\mathcal{N}}{\mathcal{T} + \mathcal{N}}, \frac{2\mathcal{N}}{A_- + \mathcal{N}} \right] \quad (\text{A.32})$$

B_{Z1}^ρ is reduced as follows:

$$B_{Z1}^\rho = \left(\frac{-2\rho\mathcal{Z}_+ \sqrt{\frac{2A_-}{A_- + \mathcal{N}} - 1}}{\mathcal{N}(\mathcal{T} + \mathcal{N})\sqrt{A_- - \mathcal{N}}} \right) \left[(\mathcal{T} + \mathcal{N})\mathcal{K} \left[\frac{2\mathcal{N}}{A_- + \mathcal{N}} \right] - \mathcal{T}\mathcal{E}_\pi \left[\frac{2\mathcal{N}}{\mathcal{T} + \mathcal{N}}, \frac{2\mathcal{N}}{A_- + \mathcal{N}} \right] \right] \quad (\text{A.33})$$

Similarly, B_{Z2}^a and B_{Z2}^ρ are reduced as follows:

$$B_{Z2} = B_{Z2}^a + B_{Z2}^\rho \quad (\text{A.34})$$

where,

$$B_{Z2}^a = \int_0^\pi \frac{-a\mathcal{Z}_-}{(\mathcal{T} - \mathcal{N} \cos \phi)\sqrt{A_+ - \mathcal{N} \cos \phi}} d\phi \quad (\text{A.35})$$

$$B_{Z2}^{\rho} = \int_0^{\pi} \frac{Z_- \rho \cos \phi}{(\mathcal{T} - \mathcal{N} \cos \phi) \sqrt{A_+ - \mathcal{N} \cos \phi}} d\phi \quad (\text{A.36})$$

which gives:

$$B_{Z2}^a = \left(\frac{2aZ_-}{(\mathcal{T} + \mathcal{N})(A_+ + \mathcal{N})} \right) \mathcal{E}_{\pi} \left[\frac{2\mathcal{N}}{\mathcal{T} + \mathcal{N}}, \frac{2\mathcal{N}}{A_+ + \mathcal{N}} \right] \quad (\text{A.37})$$

$$B_{Z2}^{\rho} = \left(\frac{-2\rho Z_- \sqrt{\frac{2A_+}{A_+ + \mathcal{N}} - 1}}{\mathcal{N}(\mathcal{T} + \mathcal{N}) \sqrt{A_+ - \mathcal{N}}} \right) \left[(\mathcal{T} + \mathcal{N}) \mathcal{K} \left[\frac{2\mathcal{N}}{A_+ + \mathcal{N}} \right] - \mathcal{T} \mathcal{E}_{\pi} \left[\frac{2\mathcal{N}}{\mathcal{T} + \mathcal{N}}, \frac{2\mathcal{N}}{A_+ + \mathcal{N}} \right] \right] \quad (\text{A.38})$$

Hence, Z - COMPONENT:

$$B_Z = \frac{\mu_0 n I a}{2\pi} (B_{Z1}^a + B_{Z1}^{\rho} + B_{Z2}^a + B_{Z2}^{\rho}) \quad (\text{A.39})$$

Appendix B

List of Codes

Here, we present all the relevant codes used to produce results which are reported in this thesis. The simulations are arranged in this appendix as follows:

- Figure B.1 - Figure B.3: Simulation for calculation of optimized and unoptimized phases disregarding the radial motion of atomic clouds for $\Delta\phi \approx \pi/2$ (one - dimensional case).
- Figure B.4 - Figure B.10: Phase noise minimization simulation ($\Delta\phi \approx \pi/2$) accounting the motion of atomic clouds along X, Y and Z axes.
- Figure B.11 - Figure B.15: Code to evaluate the optimization point of gravity gradiometer and to estimate the relative sensitivity.
- Figure B.16 - Figure B.27: Simulation used to calculate ϕ_R for source mass configuration - I.
- Figure B.28 - Figure B.35: Simulation used to calculate ϕ_R for source mass configuration - II.

Development of a New Apparatus for Precision Gravity Measurements with Atom Interferometry

```

1  # -*- coding: utf-8 -*-
2  """
3  Created on Wed Feb 26 17:30:26 2020
4  RAW AND OPTIMIZED PHASE CALCULATION FOR 1-D SCENARIO
5  @author: Manan Jain
6  """
7
8  import numpy as np
9  import matplotlib.pyplot as plt
10 import scipy.integrate as integrate
11 import time
12 from scipy import stats
13 timestart = time.time()
14 G=6.67408*10**(-11)
15 keff = 4*np.pi/(421.5)*10**9
16 mRb = 1.443*10**(-25)
17 hbar = 1.055*10**(-34)
18 vr = (keff*hbar)/mRb #Recoil velocity of rubidium atom
19 g = 9.80491
20 T = 0.220 #Half-time of the interferometric sequence
21 v0 = (T + 0.001)*g #Initial velocity of atomic cloud along the fountain axis
22 d = 0.23
23 baseline = d
24 offset = 2.00-(baseline*0.5)-0.15
25 TmeansAp = ((0.221+0.22322)*0.5) #Average apogee time
26 DmeansAp = ((0.244236+0.239487)*0.5) #Average apogee distance
27 zm = -0.004645344727698374 #optimization of the gradiometer position with respect to
the B-pulse coil
28 z0s = (0.+(baseline*0.5)-offset)
29 z0ms = (zm+(baseline*0.5)-offset)
30 z00corr = -(baseline*0.5)-DmeansAp+offset)
31 zlls = (0.-(baseline*0.5)-offset)
32 zllms = (zm-(baseline*0.5)-offset)
33
34 def zdw(z0,vzz,t):
35     val = 0
36     if(t.all() < T):
37         val = z0 + vzz*t - 1/2*g*t**2 #ARM-4
38     else:
39         val = z0 + vzz*T - 1/2*g*T**2 + (vzz + vr - g*T)*(t - T) - 0.5*g*(t - T)**2
40         #ARM-3
41     return val
42
43 def zup(z0,vzz,t):
44     val = 0
45     if(t.all() < T):
46         val = z0 + (vzz + vr)*t - 1/2*g*t**2 #ARM-1
47     else:
48         val = z0 + (vzz + vr)*T - 1/2*g*T**2 + (vzz - g*T)*(t - T) - 0.5*g*(t -
49         T)**2 #ARM-2
50     return val
51
52 tvalss=np.linspace(0.221,0.22322,100)
53 yvalss=[]
54 for tvals in tvalss:
55     yvalss.append(zup(0,vz,tvals))
56 yvalssArray=np.array(yvalss)
57
58 yvalss=[]
59 for tvals in tvalss:
60     yvalss.append(zdw(0,vz,tvals))
61 yvalssArray=np.array(yvalss)
62
63 TmeansAp = (0.221 + 0.22322)/2
64 DmeansAp = (0.244236 + 0.239487)/2
65 u0 = 4*np.pi*10**(-7)
66 n = 1000
67 alfa = 575.33
68 R = 0.032
69
70 def B(z, I, L):
71     return u0*n*I*0.5*((z + L/2)/((z + L/2)**2 + R**2)**0.5 - (z - L/2)/((z -

```

Figure B.1: Simulation in PYTHON for 1D case: Calculation of unoptimized and optimized phases.

Development of a New Apparatus for Precision Gravity Measurements with Atom Interferometry

```

    L/2)**2 + R**2)**0.5)*10000
70
71 def Blongfixed(z):
72     return (0.0628319*(-((-2 + z)/(0.001024 + (-2 + z)**2)**0.5) + (2 + z)/(0.001024
    + (2 + z)**2)**0.5))
73
74 print("Blong[z_](mG):",B(0,0.01,4)*1000)
75 baseline = 0.23
76 offset = 2.00 - (baseline/2) - 0.15
77
78 def Bshort(z, I, L):
79     return B(z - baseline/2 - DmeansAp + offset, I, L)
80
81 def Bpulse(z, I, L):
82     return (Bshort(z, I, L) + (0.0628319*(-((-2 + z)/(0.001024 + (-2 + z)**2)**0.5)
    + (2 + z)/(0.001024 + (2 + z)**2)**0.5)))
83
84 Tpulse = 0.004
85 nn = 1000
86
87 def GetValAtDiffT(z,vz,tvals):
88     valList=[]
89     for tval in tvals:
90         valList.append(Blongfixed(zup(z,vz,tval))**2+Blongfixed(zdw(z,vz,tval))**2)
91     return np.array(valList)
92
93 def GetBPulseValAtDiffT(z,vz,tvals,I,L):
94     valList=[]
95     for tval in tvals:
96         valList.append((Bpulse(zup(z,vz,tval),I,L))**2+(Bpulse(zdw(z,vz,tval),I,L))**2
    )
97     return np.array(valList)
98
99 def phi(I,L,z,vzz):
100     tvall = np.linspace(0.0,T,nn)
101     vall = -1.0*np.pi*alfa*integrate.simps(GetValAtDiffT(z,vzz,tvall),tvall)
102     tval2 = np.linspace(T,TmeansAp-Tpulse*0.5,nn)
103     val2 = np.pi*alfa*integrate.simps(GetValAtDiffT(z,vzz,tval2),tval2)
104     tval3 = np.linspace(TmeansAp-Tpulse*0.5,TmeansAp + Tpulse*0.5,nn)
105     val3 = np.pi*alfa*integrate.simps(GetBPulseValAtDiffT(z,vzz,tval3,I,L),tval3)
106     tval4 = np.linspace(TmeansAp+Tpulse*0.5,2*T,nn)
107     val4 = np.pi*alfa*integrate.simps(GetValAtDiffT(z,vzz,tval4),tval4)
108     return (vall+val2+val3+val4)
109
110 def gradphi(I,L,z,vzz):
111     return (phi(I,L,z+baseline/2-offset,vzz)-phi(I,L,z-baseline/2-offset,vzz))
112
113 LS = 0.23
114 IB = 0.019
115 print("GRADPHI:",gradphi(IB,LS,0.,v0))
116
117 numOfParticles = 1000
118 particleIndexArray = np.linspace(0,numOfParticles,numOfParticles)
119 z00 = np.random.normal(0.+(baseline*0.5)-offset, 0.003, numOfParticles)
120 print("z00:",z00)
121 z00m = np.random.normal(zm+(baseline*0.5)-offset, 0.003, numOfParticles)
122 print("z00m:",z00m)
123 z11 = np.random.normal(0.-(baseline*0.5)-offset, 0.003, numOfParticles)
124 print("z11:",z11)
125 z11m = np.random.normal(zm-(baseline*0.5)-offset, 0.003, numOfParticles)
126 print("z11m:",z11m)
127 zsc = np.random.normal(z11s-(z00corr+z00s), 0.003, numOfParticles)
128 print("zsc:",zsc)
129 zscm = np.random.normal(z11ms-(z00corr+z00ms), 0.003, numOfParticles)
130 print("zscm:",zscm)
131 z00n = np.random.normal(-1.62, 0.003, numOfParticles)
132 z11n = np.random.normal(-1.85, 0.003, numOfParticles)
133 vz = np.random.normal(v0, 0.003, numOfParticles)
134
135 MAGPHASEList = []
136 MAGPHASEOPTMZList = []

```

Figure B.2: Simulation in PYTHON for 1D case: Calculation of unoptimized and optimized phases.

Development of a New Apparatus for Precision Gravity Measurements with Atom Interferometry

```

137
138 for particleIndex in range(numOfParticles):
139     print("##### Particle Num : "+str(particleIndex)+"
#####")
140     vzz = vz[particleIndex]
141     MAGPHASE =
phi(IB,LS,zsc[particleIndex],vz[particleIndex])-phi(IB,LS,zll[particleIndex],vz[pa
rticleIndex])
142     print("MAGPHASE for Particle : "+str(particleIndex)+" :: "+str(MAGPHASE))
143     MAGPHASEList.append(MAGPHASE)
144     MAGPHASEOPTMZ =
phi(IB,LS,zscm[particleIndex],vz[particleIndex])-phi(IB,LS,zllm[particleIndex],vz[
particleIndex])
145     print("Optimized MAGPHASE for Particle : "+str(particleIndex)+" ::
"+str(MAGPHASEOPTMZ))
146     MAGPHASEOPTMZList.append(MAGPHASEOPTMZ)
147
148     MAGPHASEArray = np.array(MAGPHASEList)
149     MEANMAGPHASE = np.mean(MAGPHASEArray)
150     print("#####")
151     print("mean : "+str(MEANMAGPHASE))
152     print("#####")
153     MAGPHASEOPTMZArray = np.array(MAGPHASEOPTMZList)
154     MEANMAGPHASEOPTMZ = np.mean(MAGPHASEOPTMZArray)
155     print("#####")
156     print("optimized mean : "+str(MEANMAGPHASEOPTMZ))
157     print("#####")
158
159     np.savetxt("PIBY2-1D-RAWVALUES.txt",MAGPHASEArray)
160     np.savetxt("PIBY2-1D-OPTIMIZEDVALUES.txt",MAGPHASEOPTMZArray)
161
162     serMAG = MAGPHASEArray
163     serMAGOPTMZ = MAGPHASEOPTMZArray
164     numarray = np.arange(numOfParticles)
165     plt.plot(numarray, serMAG, 'r^', numarray, serMAGOPTMZ, 'bs')
166     plt.ylabel('\u03C6 (radians)')
167     plt.show()
168
169     plt.hist(MAGPHASEArray, bins=50)
170     plt.hist(MAGPHASEOPTMZArray, bins=50)
171     plt.show()
172     plt.show()
173
174     plt.hist(serMAG, normed = True)
175     plt.hist(serMAGOPTMZ, normed = True)
176
177     xt = plt.xticks()[0]
178     xmin, xmax = min(xt), max(xt)
179     MAGN = np.linspace(xmin, xmax, len(serMAG))
180
181     xxt = plt.xticks()[0]
182     xxmin, xxmax = min(xxt), max(xxt)
183     MAGNOPTMZ = np.linspace(xxmin, xxmax, len(serMAGOPTMZ))
184
185     m, s = stats.norm.fit(serMAG)
186     print("m:",m)
187     print("s:",s/(np.sqrt(numOfParticles)))
188     pdf_gA = stats.norm.pdf(MAGN, m, s)
189     plt.plot(MAGN, pdf_gA, label = "NormA")
190     plt.show()
191
192     mo, so = stats.norm.fit(serMAGOPTMZ)
193     print("mo:",mo)
194     print("so:",so/(numOfParticles))
195     pdf_gB = stats.norm.pdf(MAGNOPTMZ, mo, so)
196     plt.plot(MAGNOPTMZ, pdf_gB, label = "NormB")
197     plt.show()
198
199     timeend = time.time()
200     diff = timeend-timestart
201     print("Execution time (s) : ",diff)

```

Figure B.3: Simulation in PYTHON for 1D case: Calculation of unoptimized and optimized phases.

Development of a New Apparatus for Precision Gravity Measurements with Atom Interferometry

```
# -*- coding: utf-8 -*-
"""
Created on Tue Jun  9 10:41:02 2020
@author: JAIN MANAN
sigma-r-radial XY-plane FILE
"""

import numpy as np
from mpmath import ellipk
from mpmath import ellippi
from mpmath import ellipe
from scipy.special import legendre
import matplotlib.pyplot as plt
from scipy import integrate
from scipy.integrate import quad
import time
import scipy.special as sc
from scipy import stats
import sys

timestart = time.time()

u0 = (4.*np.pi)/10**7
g = 9.80491
Nspireshort = 230
Nspire = 4000
R = 0.032
baseline = 0.23
DmeansAp = (0.244236 + 0.239487)/2
offset = 2.00 - (baseline/2) - 0.15
alfa = 575.15
TmeansAp = (0.221 + 0.22322)/2
Tpulse = 0.004
T = 0.220
keff = 10**9*((4.*np.pi)/(421.5))
hbar = 1.055/10**34
mRb = 1.443/10**25
zm = -0.00464534210
vr = (keff*hbar)/mRb
v0 = 2.16688511
nn = 1100
z00s = (0.+(baseline*0.5)-offset)
z00ms = (zm+(baseline*0.5)-offset)
z00corr = (-(baseline*0.5)-DmeansAp+offset)
z11s = (0.-(baseline*0.5)-offset)
z11ms = (zm-(baseline*0.5)-offset)
vz = np.random.normal(v0, 0.003, 1000)

def zdw(z0,vzz,t):
    val = 0
    if(t.all() < T):
        val = z0 + vzz*t - 1/2*g*t**2
    else:
        val = z0 + vzz*T - 1/2*g*T**2 + (vzz + vr - g*T)*(t - T) - 0.5*g*(t - T)**2
    return val

def zup(z0,vzz,t):
    val = 0
```

Figure B.4: Simulation in PYTHON for 3D case: Phase calculation as per $\Delta\phi \approx \pi/2$ (both bias and B-pulse coils included).

```

if(t.all() < T):
    val = z0 + (vzz+vr)*t - 1/2*g*t**2
else:
    val = z0 + (vzz+vr)*T - 1/2*g*T**2 + (vzz - g*T)*(t - T) - 0.5*g*(t - T)**2

return val

tvalss = np.linspace(0.221,0.22322,100)
yvalss = []
for tvals in tvalss:
    yvalss.append(zup(0,vz,tvals))
yvalssArray = np.array(yvalss)

yvalss = []
for tvals in tvalss:
    yvalss.append(zdw(0,vz,tvals))
yvalssArray = np.array(yvalss)

def etaplus(z,L):
    return z + L/2

def etaminus(z,L):
    return z - L/2

def h(r):
    numerator = 4.*R*r
    denominator = (r + R)*(r + R)
    return (numerator/denominator)**(1/2)

def kplus(z,r,L):
    numerator = 4.*r*R
    denominator = ((r + R)**2 + (etaplus(z,L))**2)
    return (numerator/denominator)**(1/2)

def kminus(z,r,L):
    numerator = 4.*r*R
    denominator = ((r + R)**2 + (etaminus(z,L))**2)
    return (numerator/denominator)**(1/2)

def Kplus(z,r,L):
    #print("==== Raman : "+str(kplus(z,r,L))+" =====")
    return ellipk(kplus(z,r,L)**2)

def Kminus(z,r,L):
    return ellipk(kminus(z,r,L)**2)

def Eplus(z,r,L):
    return ellipse(kplus(z,r,L)**2)

def Eminus(z,r,L):
    return ellipse(kminus(z,r,L)**2)

def Pplus(z,r,L):
    return ellippi(h(r)**2,kplus(z,r,L)**2)

def Pminus(z,r,L):
    return ellippi(h(r)**2,kminus(z,r,L)**2)

def BR(z,r,J,L):

```

Figure B.5: Simulation in PYTHON for 3D case: Phase calculation as per $\Delta\phi \approx \pi/2$ (both bias and B-pulse coils included).

Development of a New Apparatus for Precision Gravity Measurements with Atom Interferometry

```

    c0 = (0.002*J/L*np.sqrt(R/r))
    retVal = c0*((kplus(z,r,L)**2-2)/kplus(z,r,L)*Kplus(z,r,L)
+2/kplus(z,r,L)*Eplus(z,r,L)-(kminus(z,r,L)**2-2)/kminus(z,r,L)*Kminus(z,r,L)-
2/kminus(z,r,L)*Eminus(z,r,L))
    return retVal

print("BR:",BR(0.5,4,0.0000001,0.23))

def BZ(z,r,J,L):
    coeff = (0.001*J/L*np.sqrt(r*R))
    term1 = etaplus(z,L)*kplus(z,r,L)*(Kplus(z,r,L)+(R-r)/(R+r)*Pplus(z,r,L))
    term2 = etaminus(z,L)*kminus(z,r,L)*(Kminus(z,r,L)+(R-r)/(R+r)*Pminus(z,r,L))
    Val = coeff*(term1-term2)
    return Val

print("BZ:",BZ(0.5,4,0.0000001,0.23))

def BRLong(z,r):
    #print("==== Inside BRLong function =====")
    #print("=== Printing varuiso shapes ===")
    #print("Z shape :"+str(z.shape))
    #print("r shape :"+str(r.shape))
    return (Nspire*BR(z,r,0.01,4))

def BZLong(z,r):
    return (Nspire*BZ(z,r,0.01,4))

def BRshort(z,r):
    return (Nspireshort*(BR(z-baseline/2-DmeansAp+offset,r,0.019,0.23)))

def BZshort(z,r):
    return (Nspireshort*(BZ(z-baseline/2-DmeansAp+offset,r,0.019,0.23)))

def BRpulse(z,r):
    return (BRshort(z,r)+BRLong(z,r))

def BZpulse(z,r):
    return (BZshort(z,r)+BZLong(z,r))

def BabsPulse(z,r):
    return (BRpulse(z,r)**2+BZpulse(z,r)**2)**(1/2)

def Babslong(z,r):
    brlongVal= BRLong(z,r)
    #print("===== Returned from BRLONG can calc value : "+str(brlongVal)+
=====)
    #return (BRLong(z,r)**2+BZLong(z,r)**2)**(1/2)
    return (brlongVal**2+BZLong(z,r)**2)**(1/2)

def ra(r,v,t):
    return r+v*t

def GetValAtDiffT(z,vz,r,v,tvals,val=1):
    valList=[]
    if(val==1):
        for tval in tvals:
            valList.append(Babslong(zup(z,vz,tval),ra(r,v,tval))**2+Babslong(zdw(z,vz,tval),ra(
r,v,tval))**2)

```

Figure B.6: Simulation in PYTHON for 3D case: Phase calculation as per $\Delta\phi \approx \pi/2$ (both bias and B-pulse coils included).

Development of a New Apparatus for Precision Gravity Measurements with Atom Interferometry

```

    if(val==2):
        for tval in tvals:
            vallList.append(BabsPulse(zup(z,vz,tval),ra(r,v,tval))**2 +
BabsPulse(zdw(z,vz,tval),ra(r,v,tval))**2)
        return np.array(vallList)

def newPhi(z,vzz,r,v):
    tval1 = np.linspace(0,0,T,nn)
    tval2 = np.linspace(T,TmeansAp-(Tpulse/2),nn)
    tval3 = np.linspace(TmeansAp-(Tpulse/2),TmeansAp+(Tpulse/2),nn)
    tval4 = np.linspace(TmeansAp+(Tpulse/2),2.*T,nn)
    val1 = -np.pi*alfa*integrate.simps(GetValAtDiffT(z,vzz,r,v,tval1,1),tval1)
    val2 = np.pi*alfa*integrate.simps(GetValAtDiffT(z,vzz,r,v,tval2,1),tval2)
    val3 = np.pi*alfa*integrate.simps(GetValAtDiffT(z,vzz,r,v,tval3,2),tval3)
    val4 = np.pi*alfa*integrate.simps(GetValAtDiffT(z,vzz,r,v,tval4,1),tval4)
    return (val1+val2+val3+val4)

#def GradPhiMag(Z,r,v):
#    return newPhi(z+baseline/2-offset,r,v)-newPhi(z-baseline/2-offset,r,v)

#print("==== Checking dummy Results ====")
#finalVal=GradPhiMag(-0.00464534210,0.000000001,0.0)
#print(finalVal)
#print("==== Starting Particle Loop ====")

startpoint=int(sys.argv[1]) #start event number
numOfParticleForOneJob=int(sys.argv[2]) #number of particles per job
#Creating file name to store the result
filename="Output"+str(startpoint)+"-"+str(startpoint+numOfParticleForOneJob)

numOfParticles=numOfParticleForOneJob
particleIndexArray=np.linspace(0,numOfParticles,numOfParticles)
vz = np.random.normal(v0, 0.003, numOfParticles)
z00 = np.random.normal(0.+(baseline*0.5)-offset, 0.003, numOfParticles)
z11 = np.random.normal(0.-(baseline*0.5)-offset, 0.003, numOfParticles)
print("z11:",z11)
z00m = np.random.normal(zm+(baseline*0.5)-offset, 0.003, numOfParticles)
z11m = np.random.normal(zm-(baseline*0.5)-offset, 0.003, numOfParticles)
print("z11m:",z11m)
zsc = np.random.normal(z11s-(z00corr+z00s), 0.003, numOfParticles)
print("zsc:",zsc)
zscm = np.random.normal(zm+z11s-(z00corr+z00s), 0.003, numOfParticles)
print("zscm:",zscm)
vArr=np.absolute(np.random.normal(0.,0.020,numOfParticles))
rArr=np.absolute(np.random.normal(0.,0.0026,numOfParticles))
rArrp=np.absolute(np.random.normal(0.,0.0028,numOfParticles))
rArrpp=np.absolute(np.random.normal(0.,0.0030,numOfParticles))
rArrppp=np.absolute(np.random.normal(0.,0.0032,numOfParticles))
rArrpppp=np.absolute(np.random.normal(0.,0.0034,numOfParticles))

MAGPHASELIST=[]
MAGPHASEOPTMZLIST=[]
MAGPHASELISTrp=[]
MAGPHASEOPTMZLISTrp=[]
MAGPHASELISTrpp=[]
MAGPHASEOPTMZLISTrpp=[]
MAGPHASELISTrppp=[]
MAGPHASEOPTMZLISTrppp=[]
MAGPHASELISTrpppp=[]
MAGPHASEOPTMZLISTrpppp=[]

```

Figure B.7: Simulation in PYTHON for 3D case: Phase calculation as per $\Delta\phi \approx \pi/2$ (both bias and B-pulse coils included).

Development of a New Apparatus for Precision Gravity Measurements with Atom Interferometry

```

MAGPHASEOPTMZLISTrpppp=[]

for particleIndex in range(numOfParticles):
    print("@@@@@@@@@@@@@@@@@@@@ Particle Num : "+str(startpoint+particleIndex)+"
@@@@@@@@@@@@@@@@@@@@")
    vzz = vz[particleIndex]

    MAGPHASE =
newPhi(zsc[particleIndex],vz[particleIndex],rArr[particleIndex],vArr[particleIndex]
)-
newPhi(z11[particleIndex],vz[particleIndex],rArr[particleIndex],vArr[particleIndex]
)
    print("MAGPHASE for Particle : "+str(particleIndex)+" :: "+str(MAGPHASE))
    MAGPHASELIST.append(MAGPHASE)
    MAGPHASEOPTMZ =
newPhi(zscm[particleIndex],vz[particleIndex],rArr[particleIndex],vArr[particleIndex]
])-
newPhi(z11m[particleIndex],vz[particleIndex],rArr[particleIndex],vArr[particleIndex]
)
    print("MAGPHASEOPTMZ for Particle : "+str(particleIndex)+" ::
"+str(MAGPHASEOPTMZ))
    MAGPHASEOPTMZLIST.append(MAGPHASEOPTMZ)

    MAGPHASERp =
newPhi(zsc[particleIndex],vz[particleIndex],rArr[particleIndex],vArr[particleIndex]
])-
newPhi(z11[particleIndex],vz[particleIndex],rArr[particleIndex],vArr[particleIndex]
)
    print("MAGPHASERp for Particle : "+str(particleIndex)+" :: "+str(MAGPHASERp))
    MAGPHASELISTrp.append(MAGPHASERp)
    MAGPHASEOPTMZrp =
newPhi(zscm[particleIndex],vz[particleIndex],rArr[particleIndex],vArr[particleIndex]
x])-
newPhi(z11m[particleIndex],vz[particleIndex],rArr[particleIndex],vArr[particleIndex]
x)
    print("MAGPHASEOPTMZrp for Particle : "+str(particleIndex)+" ::
"+str(MAGPHASEOPTMZrp))
    MAGPHASEOPTMZLISTrp.append(MAGPHASEOPTMZrp)

    MAGPHASERpp =
newPhi(zsc[particleIndex],vz[particleIndex],rArrpp[particleIndex],vArr[particleIndex]
x])-
newPhi(z11[particleIndex],vz[particleIndex],rArrpp[particleIndex],vArr[particleIndex]
x)
    print("MAGPHASERpp for Particle : "+str(particleIndex)+" :: "+str(MAGPHASERpp))
    MAGPHASELISTrpp.append(MAGPHASERpp)
    MAGPHASEOPTMZrpp =
newPhi(zscm[particleIndex],vz[particleIndex],rArrpp[particleIndex],vArr[particleIndex]
ex])-
newPhi(z11m[particleIndex],vz[particleIndex],rArrpp[particleIndex],vArr[particleIndex]
ex)
    print("MAGPHASEOPTMZrpp for Particle : "+str(particleIndex)+" ::
"+str(MAGPHASEOPTMZrpp))
    MAGPHASEOPTMZLISTrpp.append(MAGPHASEOPTMZrpp)

    MAGPHASERppp =
newPhi(zsc[particleIndex],vz[particleIndex],rArrppp[particleIndex],vArr[particleIndex]
ex])-
newPhi(z11[particleIndex],vz[particleIndex],rArrppp[particleIndex],vArr[particleIndex]

```

Figure B.8: Simulation in PYTHON for 3D case: Phase calculation as per $\Delta\phi \approx \pi/2$ (both bias and B-pulse coils included).

```

ex])
    print("MAGPHASERppp for Particle : "+str(particleIndex)+" ::
"+str(MAGPHASERppp))
    MAGPHASELISTrppp.append(MAGPHASERppp)
    MAGPHASEOPTMZrppp =
newPhi(zscm[particleIndex],vz[particleIndex],rArrppp[particleIndex],vArr[particleIn
dex])-
newPhi(z11m[particleIndex],vz[particleIndex],rArrppp[particleIndex],vArr[particleIn
dex])
    print("MAGPHASEOPTMZrppp for Particle : "+str(particleIndex)+" ::
"+str(MAGPHASEOPTMZrppp))
    MAGPHASEOPTMZLISTrppp.append(MAGPHASEOPTMZrppp)

    MAGPHASERppppp =
newPhi(zsc[particleIndex],vz[particleIndex],rArrpppp[particleIndex],vArr[particleIn
dex])-
newPhi(z11[particleIndex],vz[particleIndex],rArrpppp[particleIndex],vArr[particleIn
dex])
    print("MAGPHASERppppp for Particle : "+str(particleIndex)+" ::
"+str(MAGPHASERppppp))
    MAGPHASELISTrpppp.append(MAGPHASERppppp)
    MAGPHASEOPTMZrpppp =
newPhi(zscm[particleIndex],vz[particleIndex],rArrpppp[particleIndex],vArr[particleI
ndex])-
newPhi(z11m[particleIndex],vz[particleIndex],rArrpppp[particleIndex],vArr[particleI
ndex])
    print("MAGPHASEOPTMZrpppp for Particle : "+str(particleIndex)+" ::
"+str(MAGPHASEOPTMZrpppp))
    MAGPHASEOPTMZLISTrpppp.append(MAGPHASEOPTMZrpppp)

MAGPHASEArray = np.array(MAGPHASELIST)
MEANMAGPHASE = np.mean(MAGPHASEArray)
print("+++++")
print("mean : "+str(MEANMAGPHASE))
print("+++++")
MAGPHASEOPTMZArray = np.array(MAGPHASEOPTMZLIST)
MEANMAGPHASEOPTMZ = np.mean(MAGPHASEOPTMZArray)
print("+++++")
print("optimized mean : "+str(MEANMAGPHASEOPTMZ))
print("+++++")
MAGPHASERpArray = np.array(MAGPHASELISTrp)
MEANMAGPHASERp = np.mean(MAGPHASERpArray)
print("+++++")
print("meanrp : "+str(MEANMAGPHASERp))
print("+++++")
MAGPHASEOPTMZrpArray = np.array(MAGPHASEOPTMZLISTrp)
MEANMAGPHASEOPTMZrp = np.mean(MAGPHASEOPTMZrpArray)
print("+++++")
print("optimized meanrp : "+str(MEANMAGPHASEOPTMZrp))
print("+++++")
MAGPHASERppArray = np.array(MAGPHASELISTrpp)
MEANMAGPHASERpp = np.mean(MAGPHASERppArray)
print("+++++")
print("meanrpp : "+str(MEANMAGPHASERpp))
print("+++++")
MAGPHASEOPTMZrppArray = np.array(MAGPHASEOPTMZLISTrpp)
MEANMAGPHASEOPTMZrpp = np.mean(MAGPHASEOPTMZrppArray)
print("+++++")

```

Figure B.9: Simulation in PYTHON for 3D case: Phase calculation as per $\Delta\phi \approx \pi/2$ (both bias and B-pulse coils included).

Development of a New Apparatus for Precision Gravity Measurements with Atom Interferometry

```
print("optimized meanrpp : "+str(MEANMAGPHASEOPTMzrpp))
print("+++++")
MAGPHASERpppArray = np.array(MAGPHASELISTrppp)
MEANMAGPHASERppp = np.mean(MAGPHASERpppArray)
print("+++++")
print("meanrppp : "+str(MEANMAGPHASERppp))
print("+++++")
MAGPHASEOPTMzrpppArray = np.array(MAGPHASEOPTMZLISTrppp)
MEANMAGPHASEOPTMzrppp = np.mean(MAGPHASEOPTMzrpppArray)
print("+++++")
print("optimized meanrppp : "+str(MEANMAGPHASEOPTMzrppp))
print("+++++")
MAGPHASERppppArray = np.array(MAGPHASELISTrpppp)
MEANMAGPHASERpppp = np.mean(MAGPHASERppppArray)
print("+++++")
print("meanrpppp : "+str(MEANMAGPHASERpppp))
print("+++++")
MAGPHASEOPTMzrppppArray = np.array(MAGPHASEOPTMZLISTrpppp)
MEANMAGPHASEOPTMzrpppp = np.mean(MAGPHASEOPTMzrppppArray)
print("+++++")
print("optimized meanrpppp : "+str(MEANMAGPHASEOPTMzrpppp))
print("+++++")

np.savetxt(filename+"MAGPHASE.txt",MAGPHASEArray)
np.savetxt(filename+"MAGPHASEOPTMZ.txt",MAGPHASEOPTMZArray)
np.savetxt(filename+"MAGPHASERp.txt",MAGPHASERpArray)
np.savetxt(filename+"MAGPHASEOPTMzrp.txt",MAGPHASEOPTMzrpArray)
np.savetxt(filename+"MAGPHASERpp.txt",MAGPHASERppArray)
np.savetxt(filename+"MAGPHASEOPTMzrpp.txt",MAGPHASEOPTMzrppArray)
np.savetxt(filename+"MAGPHASERppp.txt",MAGPHASERpppArray)
np.savetxt(filename+"MAGPHASEOPTMzrppp.txt",MAGPHASEOPTMzrpppArray)
np.savetxt(filename+"MAGPHASERpppp.txt",MAGPHASERppppArray)
np.savetxt(filename+"MAGPHASEOPTMzrpppp.txt",MAGPHASEOPTMzrppppArray)

timeend = time.time()
diff = timeend - timestart
print("Execution time (s)",diff)
```

Figure B.10: Simulation in PYTHON for 3D case: Phase calculation as per $\Delta\phi \approx \pi/2$ (both bias and B-pulse coils included).

Development of a New Apparatus for Precision Gravity Measurements with Atom Interferometry

```

In[331]:= Clear["Global`*"];
In[332]:= keff = 4 * Pi / (421.5) * 10^9
Out[332]:= 2.98135 * 10^7

In[333]:= mRb = 1.443 * 10^(-25)
Out[333]:= 1.443 * 10^-25

In[334]:= hbar = 1.055 * 10^(-34)
Out[334]:= 1.055 * 10^-34

In[335]:= vr = keff * hbar / mRb
Out[335]:= 0.0217971

In[336]:= g = 9.80491
Out[336]:= 9.80491

In[337]:= T = 0.220
Out[337]:= 0.22

In[338]:= v0 = (T + 0.001) * g
Out[338]:= 2.16689

In[339]:= zdw[z0_, t_] = If[t < T, z0 + v0 * t - 1 / 2 * g * t^2,
    z0 + v0 * T - 1 / 2 * g * T^2 + (v0 + vr - g * T) * (t - T) - 0.5 * g * (t - T)^2]
Out[339]:= If[t < 0.22, z0 + v0 t - (g t^2) / 2, z0 + v0 T - (g T^2) / 2 + (v0 + vr - g T) (t - T) - 0.5 g (t - T)^2]

In[340]:= zup[z0_, t_] = If[t < T, z0 + (v0 + vr) * t - 1 / 2 * g * t^2,
    z0 + (v0 + vr) * T - 1 / 2 * g * T^2 + (v0 - g * T) * (t - T) - 0.5 * g * (t - T)^2]
Out[340]:= If[t < 0.22, z0 + (v0 + vr) t - (g t^2) / 2,
    z0 + (v0 + vr) T - (g T^2) / 2 + (v0 - g T) (t - T) - 0.5 g (t - T)^2]

In[341]:= Plot[{zup[0, t]}, {t, 0.221, 0.22322}]
Out[341]:=

```

Figure B.11: Code in MATHEMATICA: Determination of optimization point of gravity gradiometer z_m and relative sensitivity estimation.

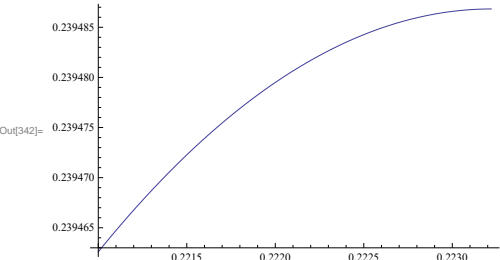
Development of a New Apparatus for Precision Gravity Measurements with Atom Interferometry

2 | Bias+Bpulse_coils.nb

```

In[342]:= Plot[{zdw[0, t]}, {t, 0.221, 0.22322}]

```



```

Out[342]:= 0.239475
0.239470
0.239465
0.2215 0.2220 0.2225 0.2230

```

```

In[343]:= TmeansAp = (0.221 + 0.22322) / 2 (*average apogee time*)
Out[343]:= 0.22211

In[344]:= DmeansAp = (0.244236 + 0.239487) / 2 (*average apogee distance*)
Out[344]:= 0.241862

In[345]:= u0 = 4 * Pi * 10 ^ (-7)
Out[345]:=  $\frac{\pi}{2500000}$ 

In[346]:= n = 1000
Out[346]:= 1000

In[347]:= alfa = 575.33
Out[347]:= 575.33

In[348]:= R = 0.032
Out[348]:= 0.032

In[349]:= B[x_, i_, L_] = u0 * n * i / 2 *
((x + L / 2) / ((x + L / 2) ^ 2 + R ^ 2) ^ 0.5 - (x - L / 2) / ((x - L / 2) ^ 2 + R ^ 2) ^ 0.5) *
10000 (*finite solenoid, B axial*)
Out[349]:=  $2 i \pi \left( -\frac{-\frac{L}{2} + x}{\left(0.001024 + \left(-\frac{L}{2} + x\right)^2\right)^{0.5}} + \frac{\frac{L}{2} + x}{\left(0.001024 + \left(\frac{L}{2} + x\right)^2\right)^{0.5}} \right)$ 

In[350]:= Blong[z_] = B[z, 0.01, 4]
(*Long coil (4 m). z=0 => center of the long coil. Offset current: 10 mA*)
Out[350]:=  $0.0628319 \left( -\frac{-2 + z}{\left(0.001024 + (-2 + z)^2\right)^{0.5}} + \frac{2 + z}{\left(0.001024 + (2 + z)^2\right)^{0.5}} \right)$ 

In[351]:= Blong[0]
Out[351]:= 0.125648

```

Figure B.12: Code in MATHEMATICA: Determination of optimization point of gravity gradiometer z_m and relative sensitivity estimation.

Development of a New Apparatus for Precision Gravity Measurements with Atom Interferometry

Bias+Bpulse_coils.nb | 3

```

In[352]:= baseline = 0.23
Out[352]:= 0.23

In[353]:= offset = 2 - baseline / 2 - 0.15
(*Position of the gradiometer. Starting point of the lower
interferometer (first pi/2) 15 cm above the lower end of the long tube*)
Out[353]:= 1.735

In[354]:=
In[355]:=
In[356]:= Bshort[z_, i_, l_] = B[z - baseline / 2 - DmeansAp + offset, i, l] (*Short coil. Its
center is placed at the apogee point of the upper interferometer*)
Out[356]:= 2 i π  $\left( -\frac{1.37814 - \frac{1}{2} + z}{\left(0.001024 + \left(1.37814 - \frac{1}{2} + z\right)^2\right)^{0.5}} + \frac{1.37814 + \frac{1}{2} + z}{\left(0.001024 + \left(1.37814 + \frac{1}{2} + z\right)^2\right)^{0.5}} \right)$ 

In[357]:= Bpulse[z_, i_, l_] = Bshort[z, i, l] + Blong[z]
Out[357]:= 0.0628319  $\left( -\frac{-2 + z}{\left(0.001024 + (-2 + z)^2\right)^{0.5}} + \frac{2 + z}{\left(0.001024 + (2 + z)^2\right)^{0.5}} \right) +$ 
 $2 i \pi \left( -\frac{1.37814 - \frac{1}{2} + z}{\left(0.001024 + \left(1.37814 - \frac{1}{2} + z\right)^2\right)^{0.5}} + \frac{1.37814 + \frac{1}{2} + z}{\left(0.001024 + \left(1.37814 + \frac{1}{2} + z\right)^2\right)^{0.5}} \right)$ 

In[358]:= Tpulse = 0.004 (*B pulse duration*)
Out[358]:= 0.004

In[359]:= TmeansAp - Tpulse / 2
Out[359]:= 0.22011

In[360]:= TmeansAp + Tpulse / 2
Out[360]:= 0.22411

In[361]:= phi[z_, i_, l_] =
(NIntegrate[-Pi * alfa * ((Blong[zup[z, t]]) ^ 2 + (Blong[zdw[z, t]]) ^ 2),
{t, 0, T}, Method -> {Automatic, "SymbolicProcessing" -> 0}]) +
(NIntegrate[Pi * alfa * ((Blong[zup[z, t]]) ^ 2 + (Blong[zdw[z, t]]) ^ 2),
{t, T, TmeansAp - Tpulse / 2},
Method -> {Automatic, "SymbolicProcessing" -> 0}]) + (NIntegrate[
Pi * alfa * ((Bpulse[zup[z, t], i, l]) ^ 2 + (Bpulse[zdw[z, t], i, l]) ^ 2),
{t, TmeansAp - Tpulse / 2, TmeansAp + Tpulse / 2},
Method -> {Automatic, "SymbolicProcessing" -> 0}]) +
(NIntegrate[Pi * alfa * ((Blong[zup[z, t]]) ^ 2 + (Blong[zdw[z, t]]) ^ 2),
{t, TmeansAp + Tpulse / 2, 2 * T},
Method -> {Automatic, "SymbolicProcessing" -> 0}]);
(*phase of a single interferometer*)

```

Figure B.13: Code in MATHEMATICA: Determination of optimization point of gravity gradiometer z_m and relative sensitivity estimation.

Development of a New Apparatus for Precision Gravity Measurements with Atom Interferometry

4 | Bias+Bpulse_coils.nb

```
In[362]:= GradphiMag[z_, i_, l_] =  
  phi[z + baseline / 2 - offset, i, l] - phi[z - baseline / 2 - offset, i, l];  
  (*phase of the gradiometer*)  
  
In[363]:= IB = 0.019 (*current short coil*)  
Out[363]:= 0.019  
  
In[364]:= GradphiMag[0, IB, 0.230]  
Out[364]:= 1.5824  
  
In[365]:= lshort = 0.23 (*length of the short coil*)  
Out[365]:= 0.23  
  
In[366]:= zm = z /. Last[FindMaximum[GradphiMag[z, IB, lshort], {z, -0.02}]]  
  (*optimization of the gradiometer position with respect to the short coil*)  
Out[366]:= -0.00464534  
  
In[367]:=  
  
In[368]:= GradphiMag[zm, IB, lshort]  
Out[368]:= 1.58287  
  
In[369]:= dist = 0.230 - zm - lshort / 2 (*distance of the average apogee of the  
  lower interferometer from the lower edge of the B-pulse coil*)  
Out[369]:= 0.119645  
  
In[370]:= Plot [1 - GradphiMag[z, IB, lshort] / GradphiMag[zm, IB, lshort],  
  {z, -0.001 + zm, 0.001 + zm}] (*Relative sensitivity of  
  the gradiometer phase to the gradiometer position*)
```

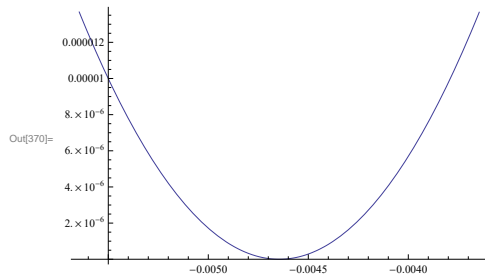


Figure B.14: Code in MATHEMATICA: Determination of optimization point of gravity gradiometer z_m and relative sensitivity estimation.

```
In[371]:= Plot [1 - (phi[zm + z / 2 + baseline / 2 - offset, IB, lshort] -  
phi[zm - z / 2 - baseline / 2 - offset, IB, lshort]) / GradphiMag[zm, IB, lshort],  
{z, -0.001, 0.001}] (*Relative sensitivity of the gradiometer  
phase to the baseline value*)
```

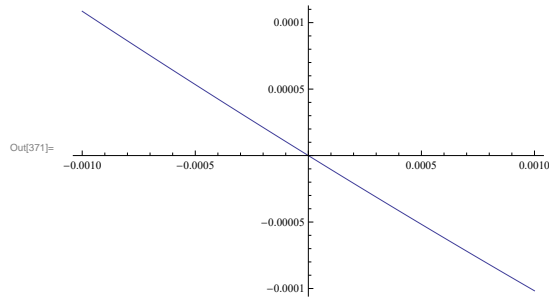


Figure B.15: Code in MATHEMATICA: Determination of optimization point of gravity gradiometer z_m and relative sensitivity estimation.

Development of a New Apparatus for Precision Gravity Measurements with Atom Interferometry

```
# -*- coding: utf-8 -*-
"""
Created on Sat Jul 25 13:10:11 2020
@author: Manan Jain
KONSOLE 5/A
"""

import numpy as np
from scipy.special import legendre
import matplotlib.pyplot as plt
from scipy import integrate
import time
import scipy.special as sc
from scipy import stats
timestart = time.time()
#defining required constants-----
G=6.67408*10**(-11)
rho = 18300
keff = 4*np.pi/(421.5)*10**9
mRb = 1.443*10**(-25)
hbar = 1.055*10**(-34)
vr = keff*hbar/mRb
g = 9.80491
T = 0.220
v0 = (T + 0.001)*g
z1 = -0.15
z0 = -0.1535
d = 0.23
dinv = 1/d
vxx = 0
vyy = 0
SINGLEATOMGRAD = 6.354549077676691+0.005
SINGLEATOMGRADPLTF = 6.360881600213782+0.005
SINGLEATOMGRADONEPERCENTUNC = 6.354549077676691+0.01
SINGLEATOMGRADPLTFONEPERCENTUNC = 6.360881600213782+0.01
SINGLEATOMGRADPOINTONEPERCENTUNC = 6.354549077676691+0.001
SINGLEATOMGRADPLTFPOINTONEPERCENTUNC = 6.360881600213782+0.001
rhoAl = 2700
zplatform = -0.1617

def Q(l,x):
    val = 0
    if(l==0):
        val = 1
    elif(l==1):
        val = (1/3)*x - (1/4)
    elif(l==2):
        val = 0.2*x*x - 0.5*x + 0.125
    elif(l==3):
        val = (1/7)*x**3 - (0.75)*x**2 + (5/8)*x - (5/64)
    elif(l==4):
        val = (1/9)*x**4 - x**3 + (7/4)*x*x - (35/48)*x + (7/128)
    return val

def V(r, z, R, H):
    firstVal=-G*rho*np.pi*R*H
    secondVal = 0
    for l in range(0,4):
        Pn = legendre(2*l)
        secondVal += (R/(r**2 + z**2)**0.5)**(2*l + 1)*Q(l,(H/(2*R)))**2* Pn(z/(r**2 + z**2)**0.5)
    retVal = firstVal*secondVal
    return retVal

def V22(x, y, z, R, H):
    val=0
    for n in range(0,6):
        val += V(((x + 2*R*np.sin(n*np.pi/3 + np.pi/6))**2 + (y - 2*R*np.cos(n*np.pi/3 + np.pi/6))**2)**0.5, z, R, H) + V(((x +
```

Figure B.16: Simulation in PYTHON for 3D case: Residual phase calculation for configuration - I.

Development of a New Apparatus for Precision Gravity Measurements with Atom Interferometry

```
2*3**0.5*R*np.sin(n*np.pi/3)**2 + (y - 2*3**0.5*R*np.cos(n*np.pi/3))**2)**0.5, z, R, H)
    return val

def Vtot(x, y, z, R, H):
    val = 0
    for n in range(-7,9):
        val += V22(x, y, (z - H/2 + n*H), R, H)
    return val

def xxu(x0, t):
    val = x0+vxxup*t
    return val

def yyu(y0, t):
    val = y0+vyyup*t
    return val

def xxd(x0, t):
    val = x0+vxxdw*t
    return val

def yyd(y0, t):
    val = y0+vyydw*t
    return val

def xxuplft(x0, t):
    val = x0+vxx0uplft*t
    return val

def yyuplft(y0, t):
    val = y0+vyy0uplft*t
    return val

def xxdwplft(x0, t):
    val = x0+vxx0dwplft*t
    return val

def yydwplft(y0, t):
    val = y0+vyy0dwplft*t
    return val

def zdwcloudup(z0, t):
    val = 0
    if(t.all() < T):
        val = z0 + v0up*t - 1/2*g*t**2
    else:
        val = z0 + v0up*T - 1/2*g*T**2 + (v0up + vr - g*T)*(t - T) - 0.5*g*(t - T)**2
    return val

def zupcloudup(z0, t):
    val = 0
    if(t.all() < T):
        val = z0 + (v0up + vr)*t - 1/2*g*t**2
    else:
        val = z0 + (v0up + vr)*T - 1/2*g*T**2 + (v0up - g*T)*(t - T) - 0.5*g*(t - T)**2
    return val

def zdwclouddw(z0, t):
    val = 0
    if(t.all() < T):
        val = z0 + v0dw*t - 1/2*g*t**2
    else:
        val = z0 + v0dw*T - 1/2*g*T**2 + (v0dw + vr - g*T)*(t - T) - 0.5*g*(t - T)**2
    return val
```

Figure B.17: Simulation in PYTHON for 3D case: Residual phase calculation for configuration - I.

Development of a New Apparatus for Precision Gravity Measurements with Atom Interferometry

```
def zupclouddw(z0, t):
    val = 0
    if(t.all() < T):
        val = z0 + (v0dw + vr)*t - 1/2*g*t**2
    else:
        val = z0 + (v0dw + vr)*T - 1/2*g*T**2 + (v0dw - g*T)*(t - T) - 0.5*g*(t - T)**2
    return val

def zdwcloudupPLTFUP(z0, t):
    val = 0
    if(t.all() < T):
        val = z0 + v0upPLTFUP*t - 1/2*g*t**2
    else:
        val = z0 + v0upPLTFUP*T - 1/2*g*T**2 + (v0upPLTFUP + vr - g*T)*(t - T) - 0.5*g*(t - T)**2
    return val

def zupcloudupPLTFUP(z0, t):
    val = 0
    if(t.all() < T):
        val = z0 + (v0upPLTFUP + vr)*t - 1/2*g*t**2
    else:
        val = z0 + (v0upPLTFUP + vr)*T - 1/2*g*T**2 + (v0upPLTFUP - g*T)*(t - T) - 0.5*g*(t - T)**2
    return val

def zdwclouddwPLTFDW(z0, t):
    val = 0
    if(t.all() < T):
        val = z0 + v0dwPLTFDW*t - 1/2*g*t**2
    else:
        val = z0 + v0dwPLTFDW*T - 1/2*g*T**2 + (v0dwPLTFDW + vr - g*T)*(t - T) - 0.5*g*(t - T)**2
    return val

def zupclouddwPLTFDW(z0, t):
    val = 0
    if(t.all() < T):
        val = z0 + (v0dwPLTFDW + vr)*t - 1/2*g*t**2
    else:
        val = z0 + (v0dwPLTFDW + vr)*T - 1/2*g*T**2 + (v0dwPLTFDW - g*T)*(t - T) - 0.5*g*(t - T)**2
    return val

def BASELINE(zu, zd, vzu, vzd, tall):
    return ((zu - zd) + (vzu - vzd)*tall)

def phicloudup(x, y, z, R, H):
    tval1 = np.linspace(0.0, T, 1000)
    tval2 = np.linspace(T, 2*T, 1000)
    val1 = integrate.simps(Vtot(xxu(x, tval1), yyu(y, tval1), zupcloudup(z, tval1), R, H)-Vtot(xxu(x, tval1), yyu(y, tval1), zdwcloudup(z, tval1), R, H), tval1)/hbar*mRb
    val2 = integrate.simps(Vtot(xxu(x, tval2), yyu(y, tval2), zupcloudup(z, tval2), R, H)-Vtot(xxu(x, tval2), yyu(y, tval2), zdwcloudup(z, tval2), R, H), tval2)/hbar*mRb
    return val1+val2

def phicloudw(x, y, z, R, H):
    tval1 = np.linspace(0.0, T, 1000)
    tval2 = np.linspace(T, 2*T, 1000)
    val1 = integrate.simps(Vtot(xxd(x, tval1), yyd(y, tval1), zupclouddw(z, tval1), R, H)-Vtot(xxd(x, tval1), yyd(y, tval1), zdwclouddw(z, tval1), R, H), tval1)/hbar*mRb
    val2 = integrate.simps(Vtot(xxd(x, tval2), yyd(y, tval2), zupclouddw(z, tval2), R, H)-Vtot(xxd(x, tval2), yyd(y, tval2), zdwclouddw(z, tval2), R, H), tval2)/hbar*mRb
    return val1+val2

rint2 = 0.15
H2 = 0.12
bm2 = H2/2/rint2
rext2 = 0.45
```

Figure B.18: Simulation in PYTHON for 3D case: Residual phase calculation for configuration - I.

```

a2 = rext2/rint2
rint1 = 0.1
H1 = 0.2
bm1 = H1/2/rint1
rext1 = 0.5
a1 = rext1/rint1
z0p = -0.1535

def y(z):
    val = z/rint1
    return val

print("y:",y(z0p))

def h1(z):
    val = (a1**2 + (y(z) - bm1)**2)**0.5
    return val

print("h1:",h1(z0p))

def h2(z):
    val = (a1**2 + (y(z) + bm1)**2)**0.5
    return val

print("h2:",h2(z0p))

def h3(z):
    val = (1 + (y(z) - bm1)**2)**0.5
    return val

print("h3:",h3(z0p))

def h4(z):
    val = (1 + (y(z) + bm1)**2)**0.5
    return val

print("h4:",h4(z0p))

def plus(z):
    val = (z/rint1)+bm1
    return val

def minus(z):
    val = (z/rint1)-bm1
    return val

def V1(z):
    val1 = a1*a1*(np.arcsinh(plus(z)/a1)-np.arcsinh(minus(z)/a1))
    val2 = (np.arcsinh(plus(z))-np.arcsinh(minus(z)))
    val3 = plus(z)*(h2(z)-h4(z))
    val4 = minus(z)*(h1(z)-h3(z))
    val = (val1-val2+val3-val4)
    return val

print("V1(z0p):",V1(z0p))

def V2(z):
    plus = y(z)+bm1
    minus = y(z)-bm1
    val1 = -plus/h2(z)
    val2 = minus/h1(z)
    val3 = plus/h4(z)
    val4 = -minus/h3(z)
    val = (val1+val2+val3+val4)
    return val

```

Figure B.19: Simulation in PYTHON for 3D case: Residual phase calculation for configuration - I.

Development of a New Apparatus for Precision Gravity Measurements with Atom Interferometry

```
print("V2(z0p):",V2(z0p))

def yout(z):
    val = z/rint2
    return val

print("yout:",yout(z0p))

def h1out(z):
    val = (a2**2 + (yout(z) - bm2)**2)**0.5
    return val

print("h1out:",h1out(z0p))

def h2out(z):
    val = (a2**2 + (yout(z) + bm2)**2)**0.5
    return val

print("h2out:",h2out(z0p))

def h3out(z):
    val = (1 + (yout(z) - bm2)**2)**0.5
    return val

print("h3out:",h3out(z0p))

def h4out(z):
    val = (1 + (yout(z) + bm2)**2)**0.5
    return val

print("h4out:",h4out(z0p))

def plusout(z):
    val = (z/rint2)+bm2
    return val

def minusout(z):
    val = (z/rint2)-bm2
    return val

def V1out(z):
    val1 = a2*a2*(np.arcsinh(plusout(z)/a2)-np.arcsinh(minusout(z)/a2))
    val2 = (np.arcsinh(plusout(z))-np.arcsinh(minusout(z)))
    val3 = plusout(z)*(h2out(z)-h4out(z))
    val4 = minusout(z)*(h1out(z)-h3out(z))
    val = (val1-val2+val3-val4)
    return val

print("V1out(z0p):",V1out(z0p))

def V2out(z):
    plusout = yout(z)+bm2
    minusout = yout(z)-bm2
    val1 = -plusout/h2out(z)
    val2 = minusout/h1out(z)
    val3 = plusout/h4out(z)
    val4 = -minusout/h3out(z)
    val = (val1+val2+val3+val4)
    return val

print("V2out(z0p):",V2out(z0p))

def Vfinzring1(x,y,z):
    r = np.sqrt(x**2 + y**2)
    fn = -G*rhoA*rint1*rint1*np.pi*(0.5*(r/rint1)*(r/rint1)*V2(z)+V1(z))
```

Figure B.20: Simulation in PYTHON for 3D case: Residual phase calculation for configuration - I.

Development of a New Apparatus for Precision Gravity Measurements with Atom Interferometry

```

return fn

print("Vfinzring1(z0p):",Vfinzring1(0,0,z0p))

def Vfinzring2(x,y,z):
    r = np.sqrt(x**2 + y**2)
    fn = -G*rhoA*rint2*rint2*np.pi*(0.5*(r/rint2)*(r/rint2)*V2out(z)+V1out(z))
    return fn

print("Vfinzring2(z0p):",Vfinzring2(0,0,z0p))

def Vfinal(x,y,z,R,H):
    val = Vtot(x, y, z, R, H)
    fn = Vfinzring2(x,y,z+0.2*8+0.1)-Vfinzring1(x,y,z+0.2*8+0.1)
    return fn+val

print("Vfinal(0,0,-0.1617+0.115,0.1,0.0375):",Vfinal(0,0,-0.1617+0.115,0.1,0.0375))

def phiwithplatformcloudup(x, y, z, R, H):
    tval3 = np.linspace(0.0,T,1000)
    tval4 = np.linspace(T,2*T,1000)
    val3 = integrate.simps(Vfinal(xxuppltf(x,tval3), yyuppltf(y,tval3), zupcloudupPLTFUP(z, tval3), R, H) - Vfinal(xxuppltf(x,tval3),
yyuppltf(y,tval3), zdwcloudupPLTFUP(z, tval3), R, H),tval3)/hbar*mRb
    val4 = integrate.simps(Vfinal(xxuppltf(x,tval4), yyuppltf(y,tval4), zupcloudupPLTFUP(z, tval4), R, H) - Vfinal(xxuppltf(x,tval4),
yyuppltf(y,tval4), zdwcloudupPLTFUP(z, tval4), R, H),tval4)/hbar*mRb
    return val3+val4

def phiwithplatformclouddw(x, y, z, R, H):
    tval3 = np.linspace(0.0,T,1000)
    tval4 = np.linspace(T,2*T,1000)
    val3 = integrate.simps(Vfinal(xxdwpltf(x,tval3), yydwpltf(y,tval3), zupclouddwPLTFDW(z, tval3), R, H) - Vfinal(xxdwpltf(x,tval3),
yydwpltf(y,tval3), zdwclouddwPLTFDW(z, tval3), R, H),tval3)/hbar*mRb
    val4 = integrate.simps(Vfinal(xxdwpltf(x,tval4), yydwpltf(y,tval4), zupclouddwPLTFDW(z, tval4), R, H) - Vfinal(xxdwpltf(x,tval4),
yydwpltf(y,tval4), zdwclouddwPLTFDW(z, tval4), R, H),tval4)/hbar*mRb
    return val3+val4

numOfParticles=10000
particleIndexArray=np.linspace(0,numOfParticles,numOfParticles)
x00up = np.random.normal(0., 0.003, numOfParticles)
y00up = np.random.normal(0., 0.003, numOfParticles)
x00uppltf = np.random.normal(0., 0.003, numOfParticles)
y00uppltf = np.random.normal(0., 0.003, numOfParticles)
z00 = np.random.normal(-0.17+0.115, 0.003, numOfParticles)
z00pltf = np.random.normal(zplatform+0.115, 0.003, numOfParticles)
vxup=np.random.normal(0.0000, 0.02, numOfParticles)
vyup=np.random.normal(0.0000, 0.02, numOfParticles)
vzup=np.random.normal(2.16688511, 0.003, numOfParticles)
vxuppltf=np.random.normal(0.0000, 0.02, numOfParticles)
vyuppltf=np.random.normal(0.0000, 0.02, numOfParticles)
vzuppltf=np.random.normal(2.16688511, 0.003, numOfParticles)
print("vzup:",vzup)
x00dw = np.random.normal(0., 0.003, numOfParticles)
y00dw = np.random.normal(0., 0.003, numOfParticles)
x00dwpltf = np.random.normal(0., 0.003, numOfParticles)
y00dwpltf = np.random.normal(0., 0.003, numOfParticles)
z11 = np.random.normal(-0.17-0.115, 0.003, numOfParticles)
z11pltf = np.random.normal(zplatform-0.115, 0.003, numOfParticles)
vxdw=np.random.normal(0.0000, 0.02, numOfParticles)
vydw=np.random.normal(0.0000, 0.02, numOfParticles)
vzdwnp.random.normal(2.16688511, 0.003, numOfParticles)
vxdwpltf=np.random.normal(0.0000, 0.02, numOfParticles)
vydwpltf=np.random.normal(0.0000, 0.02, numOfParticles)
vzdwpltf=np.random.normal(2.16688511, 0.003, numOfParticles)
print("vzdw:",vzdw)

valList=[]

```

Figure B.21: Simulation in PYTHON for 3D case: Residual phase calculation for configuration - I.

Development of a New Apparatus for Precision Gravity Measurements with Atom Interferometry

```

PHIWITHPLATFORMList=[]
BASEList=[]
BASEPLTFList=[]
#-----0.5%-----
PHIOURAList=[]
PHIOURAPLTFList=[]
PHIRESList=[]
PHIRESPLATFORMList=[]
#-----1.0%-----
PHIOURAONEPERCENTList=[]
PHIRESONEPERCENTList=[]
PHIOURAPLTFONEPERCENTList=[]
PHIRESPLATFORMONEPERCENTList=[]
#-----0.1%-----
PHIOURAPOINTONEPERCENTList=[]
PHIRESPOINTONEPERCENTList=[]
PHIOURAPLTFPOINTONEPERCENTList=[]
PHIRESPLATFORMPOINTONEPERCENTList=[]

for particleIndex in range(numOfParticles):

    print("##### Particle Num : "+str(particleIndex)+"#####")
    v0upPLTFUP=vzuppltf[particleIndex]
    v0dwPLTFDW=vzdwpltf[particleIndex]
    vxx0uppltf=vxuppltf[particleIndex]
    vyy0uppltf=vxuppltf[particleIndex]
    vxx0dwpltf=vxdwpltf[particleIndex]
    vyy0dwpltf=vxdwpltf[particleIndex]
    v0up=vzup[particleIndex]
    v0dw=vzd[particleIndex]
    vxxup=vxup[particleIndex]
    vyyup=vyup[particleIndex]
    vxxdw=vxdw[particleIndex]
    vyydw=vydw[particleIndex]
    val = (phicloudup(x00up[particleIndex], y00up[particleIndex], z00[particleIndex], 0.10, 0.0375) -
    phicloudw(x00dw[particleIndex], y00dw[particleIndex], z11[particleIndex], 0.10, 0.0375))
    valList.append(val)
    phiplusplatform = (phiwithplatformcloudup(x00uppltf[particleIndex], y00uppltf[particleIndex], z00pltf[particleIndex], 0.10,
    0.0375) - phiwithplatformcloudw(x00dwpltf[particleIndex], y00dwpltf[particleIndex], z11pltf[particleIndex], 0.10, 0.0375))
    PHIWITHPLATFORMList.append(phiplusplatform)
    base = (BASELINE(z00[particleIndex], z11[particleIndex], vzup[particleIndex], vzdw[particleIndex], T))
    BASEList.append(base)
    basepltf = (BASELINE(z00pltf[particleIndex], z11pltf[particleIndex], vzuppltf[particleIndex], vzdwpltf[particleIndex], T))
    BASEPLTFList.append(basepltf)
    #-----COMMANDS FOLLOWING FOR DELTAPHI UNCERTAINTY = 0.5%-----#
    phiro = base*SINGLEATOMGRAD
    PHIOURAList.append(phiro)
    phires = phiro - val
    PHIRESList.append(phires)
    phiropltf = SINGLEATOMGRADPLTF*basepltf
    PHIOURAPLTFList.append(phiropltf)
    phiresplatform = phiropltf-phiplusplatform
    PHIRESPLATFORMList.append(phiresplatform)
    #-----COMMANDS FOLLOWING FOR DELTAPHI UNCERTAINTY = 1.0%-----#
    phiroONEPERCENT = base*SINGLEATOMGRADONEPERCENTUNC
    PHIOURAONEPERCENTList.append(phiroONEPERCENT)
    phiresONEPERCENT = phiroONEPERCENT - val
    PHIRESONEPERCENTList.append(phiresONEPERCENT)
    phiropltfONEPERCENT = SINGLEATOMGRADPLTFONEPERCENTUNC*basepltf
    PHIOURAPLTFONEPERCENTList.append(phiropltfONEPERCENT)
    phiresplatformONEPERCENT = phiropltfONEPERCENT - phiplusplatform
    PHIRESPLATFORMONEPERCENTList.append(phiresplatformONEPERCENT)
    #-----SIMILAR COMMANDS FOLLOW FOR DELTAPHI UNCERTAINTY = 0.1%-----#
    phiroPOINTONEPERCENT = base*SINGLEATOMGRADPOINTONEPERCENTUNC
    PHIOURAPOINTONEPERCENTList.append(phiroPOINTONEPERCENT)
    phiresPOINTONEPERCENT = phiroPOINTONEPERCENT - val

```

Figure B.22: Simulation in PYTHON for 3D case: Residual phase calculation for configuration - I.

Development of a New Apparatus for Precision Gravity Measurements with Atom Interferometry

```

PHIRESPOINTONEPERCENTList.append(phiresPOINTONEPERCENT)
phiropltfPOINTONEPERCENT = SINGLEATOMGRADPLTFPOINTONEPERCENTUNC*basepltf
PHIROURAPLTFPOINTONEPERCENTList.append(phiropltfPOINTONEPERCENT)
phiresplatformPOINTONEPERCENT = phiropltfPOINTONEPERCENT - phiplusplatform
PHIRESPLATFORMPOINTONEPERCENTList.append(phiresplatformPOINTONEPERCENT)

valArray=np.array(valList)
mean=np.mean(valArray)
phiwithplattArray=np.array(PHIWITHPLATFORMList)
meanphipltf=np.mean(phiwithplattArray)
print("Mean : "+str(mean))
print("Meanphipltf : "+str(meanphipltf))
np.savetxt("sigmavxy20mmpersec-sm-design-phases-at-center-phi-val.txt",valArray)
np.savetxt("sigmavxy20mmpersec-sm-design-phases-at-center-phiplusplatform-val.txt",phiwithplattArray)
ser = valArray
serPLATFORM = phiwithplattArray
#-----RECORDING RESULTS FOR DELTAPHI UNCERTAINTY = 0.5%-----#
PHIROURAAArray=np.array(PHIROURAList)
meanroua=np.mean(PHIROURAAArray)
phiresArray=np.array(PHIRESList)
phiresmean=np.mean(phiresArray)
phiropltfArray=np.array(PHIROURAPLTFList)
meanrouapltf=np.mean(phiropltfArray)
PHIRESPLATFORMArray=np.array(PHIRESPLATFORMList)
phiresplatformmean=np.mean(PHIRESPLATFORMArray)
print("PHIROURAMEAN : "+str(meanroua))
print("PHIROURAPLATFORMMEAN : "+str(meanrouapltf))
print("PHIRESMEAN : "+str(phiresmean))
print("PHIRESWITHPLATFORMMEAN : "+str(phiresplatformmean))

np.savetxt("sigmavxy20mmpersec-point5percent-unc-all-at-center-roua-val.txt",PHIROURAAArray)
np.savetxt("sigmavxy20mmpersec-point5percent-unc-all-at-center-res-val.txt",phiresArray)
np.savetxt("sigmavxy20mmpersec-point5percent-unc-all-at-center-roua-pltf-val.txt",phiropltfArray)
np.savetxt("sigmavxy20mmpersec-point5percent-unc-all-at-center-res-phiplusplatform-val.txt",PHIRESPLATFORMArray)

serROURA = PHIROURAAArray
serROURAPLTF = phiropltfArray
serRES = phiresArray
serRESPLATFORM = PHIRESPLATFORMArray

plt.hist(valArray,bins=50)
plt.hist(PHIROURAAArray,bins=50)
plt.show()
plt.show()

plt.hist(ser, normed=True)
plt.hist(serROURA, normed=True)

xt = plt.xticks()[0]
xmin, xmax = min(xt), max(xt)
lnspc = np.linspace(xmin, xmax, len(ser))

xxt = plt.xticks()[0]
xxmin, xxmax = min(xxt), max(xxt)
lnspcROURA = np.linspace(xxmin, xxmax, len(serROURA))

#Trying normal distribution first
m, s = stats.norm.fit(ser) # get mean and standard deviation
print("m:",m)
print("s/numOfParticles**0.5:.",s/numOfParticles**0.5)
pdf_gA = stats.norm.pdf(lnspc, m, s/numOfParticles**0.5) # now get theoretical values in our interval
plt.plot(lnspc, pdf_gA, label="NormA") # plot it

mROURA, sROURA = stats.norm.fit(serROURA) # get mean and standard deviation
print("mROURA:.",mROURA)
print("sROURA:.",sROURA)

```

Figure B.23: Simulation in PYTHON for 3D case: Residual phase calculation for configuration - I.

Development of a New Apparatus for Precision Gravity Measurements with Atom Interferometry

```
pdf_gB = stats.norm.pdf(lnspcROURA, mROURA, sROURA) # now get theoretical values in our interval
plt.plot(lnspcROURA, pdf_gB, label="NormB") # plot it

plt.show()
plt.show()

plt.hist(phiresArray,bins=45)
plt.hist(PHIRESPLATFORMArray,bins=45)
plt.show()
plt.show()

plt.hist(serRES, normed=True)

xxxxt = plt.xticks()[0]
xxxxmin, xxxxmax = min(xxxt), max(xxxt)
lnspcRES = np.linspace(xxxmin, xxxmax, len(serRES))

mRES, sRES = stats.norm.fit(serRES) # get mean and standard deviation
print("mRES:",mRES)
print("sRES/numOfParticles**0.5:",sRES/numOfParticles**0.5)
pdf_gC = stats.norm.pdf(lnspcRES, mRES, sRES/numOfParticles**0.5) # now get theoretical values in our interval
plt.plot(lnspcRES, pdf_gC, label="NormC") # plot it

plt.show()

plt.hist(serPLATFORM, normed=True)
xxxxt = plt.xticks()[0]
xxxxmin, xxxxmax = min(xxxx), max(xxxx)
lnspcPLATFORM = np.linspace(xxxxmin, xxxxmax, len(serPLATFORM))

mPLATFORM, sPLATFORM = stats.norm.fit(serPLATFORM) # get mean and standard deviation
print("mPLATFORM:",mPLATFORM)
print("sPLATFORM/numOfParticles**0.5:",sPLATFORM/numOfParticles**0.5)
pdf_gD = stats.norm.pdf(lnspcPLATFORM, mPLATFORM, sPLATFORM/numOfParticles**0.5) # now get theoretical values in
our interval
plt.plot(lnspcPLATFORM, pdf_gD, label="NormD") # plot it

plt.show()

plt.hist(serRESPLATFORM, normed=True)

xxxxxt = plt.xticks()[0]
xxxxxmin, xxxxxmax = min(xxxxxt), max(xxxxxt)
lnspcRESPLATFORM = np.linspace(xxxxmin, xxxxmax, len(serRESPLATFORM))

mRESPLATFORM, sRESPLATFORM = stats.norm.fit(serRESPLATFORM) # get mean and standard deviation
print("mRESPLATFORM:",mRESPLATFORM)
print("sRESPLATFORM/numOfParticles**0.5:",sRESPLATFORM/numOfParticles**0.5)
pdf_gE = stats.norm.pdf(lnspcRESPLATFORM, mRESPLATFORM, sRESPLATFORM/numOfParticles**0.5) # now get
theoretical values in our interval
plt.plot(lnspcRESPLATFORM, pdf_gE, label="NormE") # plot it

plt.show()

plt.hist(serROURAPLTF, normed=True)

xxxxxt = plt.xticks()[0]
xxxxxmin, xxxxxmax = min(xxxxxt), max(xxxxxt)
lnspcROURAPLTF = np.linspace(xxxxmin, xxxxmax, len(serROURAPLTF))

mROURAPLTF, sROURAPLTF = stats.norm.fit(serROURAPLTF) # get mean and standard deviation
print("mROURAPLTF:",mROURAPLTF)
print("sROURAPLTF/numOfParticles**0.5:",sROURAPLTF/numOfParticles**0.5)
pdf_gF = stats.norm.pdf(lnspcROURAPLTF, mROURAPLTF, sROURAPLTF/numOfParticles**0.5) # now get theoretical values
in our interval
plt.plot(lnspcROURAPLTF, pdf_gF, label="NormF") # plot it
```

Figure B.24: Simulation in PYTHON for 3D case: Residual phase calculation for configuration - I.

Development of a New Apparatus for Precision Gravity Measurements with Atom Interferometry

```

plt.show()

#-----RECORDING RESULTS FOR DELTAPHI UNCERTAINTY = 1.0%-----#
PHIROURAONEPERCENTArray=np.array(PHIROURAONEPERCENTList)
PHIROURAPLTFONEPERCENTArray=np.array(PHIROURAPLTFONEPERCENTList)
PHIRESONEPERCENTArray=np.array(PHIRESONEPERCENTList)
PHIRESPLATFORMONEPERCENTArray=np.array(PHIRESPLATFORMONEPERCENTList)
serROURAONEPERCENT = PHIROURAONEPERCENTArray
serROURAPLTFONEPERCENT = PHIROURAPLTFONEPERCENTArray
serRESONEPERCENT = PHIRESONEPERCENTArray
serRESPLATFORMONEPERCENT = PHIRESPLATFORMONEPERCENTArray
meanrouraONEPERCENT=np.mean(PHIROURAONEPERCENTArray)
meanrourapltfONEPERCENT=np.mean(PHIROURAPLTFONEPERCENTArray)
phiresmeanONEPERCENT=np.mean(PHIRESONEPERCENTArray)
phiresplatformmeanONEPERCENT=np.mean(PHIRESPLATFORMONEPERCENTArray)

np.savetxt("sigmaxy20mmpersec-ONEpercent-unc-all-at-center-roura-val.txt",PHIROURAONEPERCENTArray)
np.savetxt("sigmaxy20mmpersec-ONEpercent-unc-all-at-center-res-val.txt",PHIRESONEPERCENTArray)
np.savetxt("sigmaxy20mmpersec-ONEpercent-unc-all-at-center-roura-pltf-val.txt",PHIROURAPLTFONEPERCENTArray)
np.savetxt("sigmaxy20mmpersec-ONEpercent-unc-all-at-center-res-phiplusplatform-
val.txt",PHIRESPLATFORMONEPERCENTArray)

plt.hist(serROURAONEPERCENT, normed=True)

xt = plt.xticks()[0]
xmin, xmax = min(xt), max(xt)
lnspcROURAONEPERCENT = np.linspace(xmin, xmax, len(serROURAONEPERCENT))

mROURA1PERC, sROURA1PERC = stats.norm.fit(serROURAONEPERCENT) # get mean and standard deviation
print("mROURA1PERC:",mROURA1PERC)
print("sROURA1PERC/numOfParticles**0.5:",sROURA1PERC/numOfParticles**0.5)
pdf_gG = stats.norm.pdf(lnspcROURAONEPERCENT, mROURA1PERC, sROURA1PERC/numOfParticles**0.5) # now get
theoretical values in our interval
plt.plot(lnspcROURAONEPERCENT, pdf_gG, label="NormG") # plot it

plt.show()

plt.hist(serRESONEPERCENT, normed=True)

xt = plt.xticks()[0]
xmin, xmax = min(xt), max(xt)
lnspcRESONEPERCENT = np.linspace(xmin, xmax, len(serRESONEPERCENT))

m1RESPERC, s1RESPERC = stats.norm.fit(serRESONEPERCENT) # get mean and standard deviation
print("m1RESPERC:",m1RESPERC)
print("s1RESPERC/numOfParticles**0.5:",s1RESPERC/numOfParticles**0.5)
pdf_gH = stats.norm.pdf(lnspcRESONEPERCENT, m1RESPERC, s1RESPERC/numOfParticles**0.5) # now get theoretical
values in our interval
plt.plot(lnspcRESONEPERCENT, pdf_gH, label="NormH") # plot it

plt.show()

plt.hist(serROURAPLTFONEPERCENT, normed=True)

xt = plt.xticks()[0]
xmin, xmax = min(xt), max(xt)
lnspcROURAPLTFONEPERCENT = np.linspace(xmin, xmax, len(serROURAPLTFONEPERCENT))

mROURAPLTF1PERC, sROURAPLTF1PERC = stats.norm.fit(serROURAPLTFONEPERCENT) # get mean and standard
deviation
print("mROURAPLTF1PERC:",mROURAPLTF1PERC)
print("sROURAPLTF1PERC/numOfParticles**0.5:",sROURAPLTF1PERC/numOfParticles**0.5)
pdf_gI = stats.norm.pdf(lnspcROURAPLTFONEPERCENT, mROURAPLTF1PERC, sROURAPLTF1PERC/numOfParticles**0.5)
# now get theoretical values in our interval
plt.plot(lnspcROURAPLTFONEPERCENT, pdf_gI, label="NormI") # plot it

plt.show()

```

Figure B.25: Simulation in PYTHON for 3D case: Residual phase calculation for configuration - I.

Development of a New Apparatus for Precision Gravity Measurements with Atom Interferometry

```
plt.hist(serRESPLATFORMONEPERCENT, normed=True)

xt = plt.xticks()[0]
xmin, xmax = min(xt), max(xt)
lnspcRESPLTFONEPERCENT = np.linspace(xmin, xmax, len(serRESPLATFORMONEPERCENT))

mRESPLTF1PERC, sRESPLTF1PERC = stats.norm.fit(serRESPLATFORMONEPERCENT) # get mean and standard deviation
print("mRESPLTF1PERC:", mRESPLTF1PERC)
print("sRESPLTF1PERC/numOfParticles**0.5:", sRESPLTF1PERC/numOfParticles**0.5)
pdf_gJ = stats.norm.pdf(lnspcRESPLTFONEPERCENT, mRESPLTF1PERC, sRESPLTF1PERC/numOfParticles**0.5) # now
get theoretical values in our interval
plt.plot(lnspcRESPLTFONEPERCENT, pdf_gJ, label="NormJ") # plot it

plt.show()

#-----RECORDING RESULTS FOR DELTAPHI UNCERTAINTY = 0.1%-----#
PHIROURAPOINTONEPERCENTArray=np.array(PHIROURAPOINTONEPERCENTList)
PHIROURAPLTFPOINTONEPERCENTArray=np.array(PHIROURAPLTFPOINTONEPERCENTList)
PHIRESPOINTONEPERCENTArray=np.array(PHIRESPOINTONEPERCENTList)
PHIRESPLATFORMPOINTONEPERCENTArray=np.array(PHIRESPLATFORMPOINTONEPERCENTList)
serROURAPOINTONEPERCENT = PHIROURAPOINTONEPERCENTArray

serROURAPLTFPOINTONEPERCENT = PHIROURAPLTFPOINTONEPERCENTArray
serRESPOINTONEPERCENT = PHIRESPOINTONEPERCENTArray
serRESPLATFORMPOINTONEPERCENT = PHIRESPLATFORMPOINTONEPERCENTArray
meanrouaPOINTONEPERCENT=np.mean(PHIROURAPOINTONEPERCENTArray)
meanrouaplTFPOINTONEPERCENT=np.mean(PHIROURAPLTFPOINTONEPERCENTArray)
phiresmeanPOINTONEPERCENT=np.mean(PHIRESPOINTONEPERCENTArray)
phiresplatformmeanPOINTONEPERCENT=np.mean(PHIRESPLATFORMPOINTONEPERCENTArray)

np.savetxt("sigmaxy20mmpersec-POINTONEpercent-unc-all-at-center-roua-val.txt",PHIROURAPOINTONEPERCENTArray)
np.savetxt("sigmaxy20mmpersec-POINTONEpercent-unc-all-at-center-res-val.txt",PHIRESPOINTONEPERCENTArray)
np.savetxt("sigmaxy20mmpersec-POINTONEpercent-unc-all-at-center-roua-pltf-
val.txt",PHIROURAPLTFPOINTONEPERCENTArray)
np.savetxt("sigmaxy20mmpersec-POINTONEpercent-unc-all-at-center-res-phiplusplatform-
val.txt",PHIRESPLATFORMPOINTONEPERCENTArray)

plt.hist(serROURAPOINTONEPERCENT, normed=True)

xt = plt.xticks()[0]
xmin, xmax = min(xt), max(xt)
lnspcROURAPOINTONEPERCENT = np.linspace(xmin, xmax, len(serROURAPOINTONEPERCENT))

mROURAP1PERC, sROURAP1PERC = stats.norm.fit(serROURAPOINTONEPERCENT) # get mean and standard deviation
print("mROURAP1PERC:", mROURAP1PERC)
print("sROURAP1PERC/numOfParticles**0.5:", sROURAP1PERC/numOfParticles**0.5)
pdf_gK = stats.norm.pdf(lnspcROURAPOINTONEPERCENT, mROURAP1PERC, sROURAP1PERC/numOfParticles**0.5) #
now get theoretical values in our interval
plt.plot(lnspcROURAPOINTONEPERCENT, pdf_gK, label="NormK") # plot it

plt.show()

plt.hist(serRESPOINTONEPERCENT, normed=True)

xt = plt.xticks()[0]
xmin, xmax = min(xt), max(xt)
lnspcRESPOINTONEPERCENT = np.linspace(xmin, xmax, len(serRESPOINTONEPERCENT))

mP1RESPERC, sP1RESPERC = stats.norm.fit(serRESPOINTONEPERCENT) # get mean and standard deviation
print("mP1RESPERC:", mP1RESPERC)
print("sP1RESPERC/numOfParticles**0.5:", sP1RESPERC/numOfParticles**0.5)
pdf_gL = stats.norm.pdf(lnspcRESPOINTONEPERCENT, mP1RESPERC, sP1RESPERC/numOfParticles**0.5) # now get
theoretical values in our interval
plt.plot(lnspcRESPOINTONEPERCENT, pdf_gL, label="NormL") # plot it

plt.show()
```

Figure B.26: Simulation in PYTHON for 3D case: Residual phase calculation for configuration - I.

Development of a New Apparatus for Precision Gravity Measurements with Atom Interferometry

```
plt.hist(serROURAPLTFPOINTONEPERCENT, normed=True)

xt = plt.xticks()[0]
xmin, xmax = min(xt), max(xt)
lnspcROURAPLTFPOINTONEPERCENT = np.linspace(xmin, xmax, len(serROURAPLTFPOINTONEPERCENT))

mROURAPLTFP1PERC, sROURAPLTFP1PERC = stats.norm.fit(serROURAPLTFPOINTONEPERCENT) # get mean and
standard deviation
print("mROURAPLTFP1PERC:",mROURAPLTFP1PERC)
print("sROURAPLTFP1PERC/numOfParticles**0.5:",sROURAPLTFP1PERC/numOfParticles**0.5)
pdf_gM = stats.norm.pdf(lnspcROURAPLTFPOINTONEPERCENT, mROURAPLTFP1PERC,
sROURAPLTFP1PERC/numOfParticles**0.5) # now get theoretical values in our interval
plt.plot(lnspcROURAPLTFPOINTONEPERCENT, pdf_gM, label="NormM") # plot it

plt.show()

plt.hist(serRESPLATFORMPOINTONEPERCENT, normed=True)

xt = plt.xticks()[0]
xmin, xmax = min(xt), max(xt)
lnspcRESPLTFPOINTONEPERCENT = np.linspace(xmin, xmax, len(serRESPLATFORMPOINTONEPERCENT))

mRESPLTFP1PERC, sRESPLTFP1PERC = stats.norm.fit(serRESPLATFORMPOINTONEPERCENT) # get mean and standard
deviation
print("mRESPLTFP1PERC:",mRESPLTFP1PERC)
print("sRESPLTFP1PERC/numOfParticles**0.5:",sRESPLTFP1PERC/numOfParticles**0.5)
pdf_gN = stats.norm.pdf(lnspcRESPLTFPOINTONEPERCENT, mRESPLTFP1PERC,
sRESPLTFP1PERC/numOfParticles**0.5) # now get theoretical values in our interval
plt.plot(lnspcRESPLTFPOINTONEPERCENT, pdf_gN, label="NormN") # plot it

plt.show()

timeend = time.time()
diff=timeend-timestart
print("Time taken : ",diff)
```

Figure B.27: Simulation in PYTHON for 3D case: Residual phase calculation for configuration - I.

Development of a New Apparatus for Precision Gravity Measurements with Atom Interferometry

```
# -*- coding: utf-8 -*-
"""
Created on Sat Jul 25 13:10:11 2020
@author: Manan Jain
KONSOLE 36/A
"""
import numpy as np
from scipy.special import legendre
import matplotlib.pyplot as plt
from scipy import integrate
from scipy.integrate import quad
import time
import scipy.special as sc
from scipy import stats
import sys
timestart = time.time()

#defining required constants-----
G=6.67408*10**(-11)
rho = 8960
eta = (18300/8960)**0.5
keff = 4*np.pi/(421.5)*10**9
mRb = 1.443*10**(-25)
hbar = 1.055*10**(-34)
vr = keff*hbar/mRb
g = 9.80491
T = 0.220*np.sqrt(eta)
v0 = (T + (0.001*eta))*g
z0 = -0.23223352024224914
d = 0.23*eta
dinv = 1/d
H = 0.6*eta
print("eta:", eta)
print("keff:", keff)
rext = eta*0.362
rint = eta*0.105
a = rext/rint
bm = H/2/rint
print("bm:", bm)
GRADPHIEXACT = 4.803185609115827
GRAPHIPOINTONEPERCENT = 4.803185609115827+0.001
GRAPHIPOINTFIVEPERCENT = 4.803185609115827+0.005
GRAPHIONEPERCENT = 4.803185609115827+0.01

def etaa(r):
    #r = np.sqrt(x**2 + y**2)
    val = r/rint
    return val

def y(z):
    val = z/rint
    return val

print("y:", y(z0))

def h1(z):
    val = (a**2 + (y(z) - bm)**2)**0.5
    return val
```

Figure B.28: Simulation in PYTHON for 3D case: Residual phase calculation for configuration - II.

```

print("h1:",h1(z0))

def h2(z):
    val = (a**2 + (y(z) + bm)**2)**0.5
    return val

print("h2:",h2(z0))

def h3(z):
    val = (1 + (y(z) - bm)**2)**0.5
    return val

print("h3:",h3(z0))

def h4(z):
    val = (1 + (y(z) + bm)**2)**0.5
    return val

print("h4:",h4(z0))

def plus(z):
    val = (z/rint)+bm
    return val

def minus(z):
    val = (z/rint)-bm
    return val

def v1(z):
    val1 = a*a*(np.arcsinh(plus(z)/a)-np.arcsinh(minus(z)/a))
    val2 = (np.arcsinh(plus(z))-np.arcsinh(minus(z)))
    val3 = plus(z)*(h2(z)-h4(z))
    val4 = minus(z)*(h1(z)-h3(z))
    val = (val1-val2+val3-val4)
    return val

print("v1(z0):",v1(z0))

def v2(z):
    plus = y(z)+bm
    minus = y(z)-bm
    val1 = -plus/h2(z)
    val2 = minus/h1(z)
    val3 = plus/h4(z)
    val4 = -minus/h3(z)
    val = (val1+val2+val3+val4)
    return val

print("v2(z0):",v2(z0))

def Vfin(z,r):
    fn = -G*rho*rint*rint*np.pi*(0.5*(r/rint)*(r/rint)*v2(z)+v1(z))
    return fn

print("Vfin(0,0):",Vfin(0,0))

def zdw(z0,vz,t):
    val = 0
    if(t.all() < T):

```

Figure B.29: Simulation in PYTHON for 3D case: Residual phase calculation for configuration - II.

Development of a New Apparatus for Precision Gravity Measurements with Atom Interferometry

```

        val = z0 + vz*t - 1/2*g*t**2
    else:
        val = z0 + vz*T - 1/2*g*T**2 + (vz + vr - g*T)*(t - T) - 0.5*g*(t - T)**2

    return val

def zup(z0,vz,t):
    val = 0
    if(t.all() < T):
        val = z0 + (vz + vr)*t - 1/2*g*t**2
    else:
        val = z0 + (vz + vr)*T - 1/2*g*T**2 + (vz - g*T)*(t - T) - 0.5*g*(t - T)**2

    return val

def ra(r,v,t):
    return r+v*t

def phi(z,vz,r,v):
    tval1 = np.linspace(0.0,T,1000)
    tval2 = np.linspace(T,2.*T,1000)
    val1 = (mRb/hbar)*(integrate.simps((Vfin(zup(z,vz,tval1),ra(r,v,tval1))-
Vfin(zdw(z,vz,tval1),ra(r,v,tval1))),tval1))
    val2 = (mRb/hbar)*(integrate.simps((Vfin(zup(z,vz,tval2),ra(r,v,tval2))-
Vfin(zdw(z,vz,tval2),ra(r,v,tval2))),tval2))
    val = val1+val2
    return val

print("PHI:",phi(z0+0.115*eta,v0,0,0)-phi(z0-0.115*eta,v0,0,0))

def BASELINE(zu, zd, vzu, vzd, tall):
    return ((zu - zd) + (vzu - vzd)*tall)

numOfParticles=10000
#-----UPPER-CLOUD-----#
particleIndexArray=np.linspace(0,numOfParticles,numOfParticles)
r00up = np.random.normal(0., 0.003, numOfParticles)
z00 = np.random.normal(z0+0.115*eta, 0.003, numOfParticles)
vzup = np.random.normal(v0, 0.003, numOfParticles)
vrup = np.random.normal(0., 0.020, numOfParticles)
#-----LOWER-CLOUD-----#
r00dw = np.random.normal(0., 0.003, numOfParticles)
z11 = np.random.normal(z0-0.115*eta, 0.003, numOfParticles)
vzdw = np.random.normal(v0, 0.003, numOfParticles)
vrdw = np.random.normal(0., 0.020, numOfParticles)

baseList=[]
#-----0.1% UNCERTAINTY-----#
phivalList=[]
phirovalList=[]
phiresList=[]
#-----0.5% UNCERTAINTY-----#
phivalPOINTFIVEList=[]
phirovalPOINTFIVEList=[]
phiresPOINTFIVEList=[]
#-----1.0% UNCERTAINTY-----#
phivalONEList=[]
phirovalONEList=[]
phiresONEList=[]

```

Figure B.30: Simulation in PYTHON for 3D case: Residual phase calculation for configuration - II.

Development of a New Apparatus for Precision Gravity Measurements with Atom Interferometry

```

for particleIndex in range(numOfParticles):
    print("@@@@@@@@@@@@@@@@@@@@@@ Particle Num : "+str(particleIndex)+"
@@@@@@@@@@@@@@@@@@@@@@@@@@@@")
    base =
(BASELINE(z00[particleIndex], z11[particleIndex], vzup[particleIndex], vzw[particleIndex], T))
    baseList.append(base)
    #-----0.1% UNCERTAINTY-----#
    phival =
(phi(z00[particleIndex], vzup[particleIndex], r00up[particleIndex], vrup[particleIndex]
) -
phi(z11[particleIndex], vzw[particleIndex], r00dw[particleIndex], vrdw[particleIndex]
))
    phivalList.append(phival)

    phiroval = base*GRAPHIPPOINTONEPERCENT
    phirovalList.append(phiroval)

    phires = phiroval - phival
    phiresList.append(phires)
    #-----0.5% UNCERTAINTY-----#
    phivalPOINTFIVE = phival
    phivalPOINTFIVEList.append(phivalPOINTFIVE)

    phirovalPOINTFIVE = base*GRAPHIPPOINTFIVEPERCENT
    phirovalPOINTFIVEList.append(phirovalPOINTFIVE)

    phiresPOINTFIVE = phirovalPOINTFIVE - phivalPOINTFIVE
    phiresPOINTFIVEList.append(phiresPOINTFIVE)
    #-----1.0% UNCERTAINTY-----#
    phivalONE = phival
    phivalONEList.append(phivalONE)

    phirovalONE = base*GRAPHIPONEPERCENT
    phirovalONEList.append(phirovalONE)

    phiresONE = phirovalONE - phivalONE
    phiresONEList.append(phiresONE)

#-----0.1% UNCERTAINTY-----#
phivalArray=np.array(phivalList)
phimean=np.mean(phivalArray)
print("Mean : "+str(phimean))
phirovalArray=np.array(phirovalList)
phiromean=np.mean(phirovalArray)
print("Meanro : "+str(phiromean))
phiresArray=np.array(phiresList)
phiresmean=np.mean(phiresArray)
print("Meanres : "+str(phiresmean))

np.savetxt("POINTONEPERCENTunc-phi-at-z11center.txt", phivalArray)
np.savetxt("POINTONEPERCENTunc-phiroval-at-z11center.txt", phirovalArray)
np.savetxt("POINTONEPERCENTunc-phiresval-at-z11center.txt", phiresArray)

#-----0.5% UNCERTAINTY-----#
phivalPOINTFIVEArray=np.array(phivalPOINTFIVEList)

```

Figure B.31: Simulation in PYTHON for 3D case: Residual phase calculation for configuration - II.

Development of a New Apparatus for Precision Gravity Measurements with Atom Interferometry

```
phiPOINTFIVEmean=np.mean(phivalPOINTFIVEArray)
print("Mean0.5unc : "+str(phiPOINTFIVEmean))
phirovalPOINTFIVEArray=np.array(phirovalPOINTFIVEList)
phiroPOINTFIVEmean=np.mean(phirovalPOINTFIVEArray)
print("Meanro0.5unc : "+str(phiroPOINTFIVEmean))
phiresPOINTFIVEArray=np.array(phiresPOINTFIVEList)
phiresPOINTFIVEmean=np.mean(phiresPOINTFIVEArray)
print("Meanres0.5unc : "+str(phiresPOINTFIVEmean))

np.savetxt("FIVEPERCENTunc-phi-at-z11center.txt",phivalPOINTFIVEArray)
np.savetxt("FIVEPERCENTunc-phiroval-at-z11center.txt",phirovalPOINTFIVEArray)
np.savetxt("FIVEPERCENTunc-phiresval-at-z11center.txt",phiresPOINTFIVEArray)

#-----1.0% UNCERTAINTY-----#
phivalONEArray=np.array(phivalONEList)
phiONEmean=np.mean(phivalONEArray)
print("Mean1unc : "+str(phiONEmean))
phirovalONEArray=np.array(phirovalONEList)
phiroONEmean=np.mean(phirovalONEArray)
print("Meanro1unc : "+str(phiroONEmean))
phiresONEArray=np.array(phiresONEList)
phiresONEmean=np.mean(phiresONEArray)
print("Meanres1unc : "+str(phiresONEmean))

np.savetxt("ONEPERCENTunc-phi-at-z11center.txt",phivalONEArray)
np.savetxt("ONEPERCENTunc-phiroval-at-z11center.txt",phirovalONEArray)
np.savetxt("ONEPERCENTunc-phiresval-at-z11center.txt",phiresONEArray)

#-----0.1% UNCERTAINTY-----#
ser = phivalArray
serROURA = phirovalArray
serRES = phiresArray

plt.hist(ser,bins=50)
plt.hist(serROURA,bins=50)
plt.show()
plt.show()

plt.hist(ser, normed=True)
plt.hist(serROURA, normed=True)

xt = plt.xticks()[0]
xmin, xmax = min(xt), max(xt)
lnspc = np.linspace(xmin, xmax, len(ser))

xxt = plt.xticks()[0]
xxmin, xxmax = min(xxt), max(xxt)
lnspcROURA = np.linspace(xxmin, xxmax, len(serROURA))

#Trying normal distribution first
m, s = stats.norm.fit(ser) # get mean and standard deviation
print("m:",m)
print("s/numOfParticles**0.5:",s/numOfParticles**0.5)
pdf_gA = stats.norm.pdf(lnspc, m, s/numOfParticles**0.5) # now get theoretical
values in our interval
plt.plot(lnspc, pdf_gA, label="NormA") # plot it

mROURA, sROURA = stats.norm.fit(serROURA) # get mean and standard deviation
print("mROURA:",mROURA)
```

Figure B.32: Simulation in PYTHON for 3D case: Residual phase calculation for configuration - II.

```

print("sROURA:", sROURA)
pdf_gB = stats.norm.pdf(lnspcROURA, mROURA, sROURA) # now get theoretical values in
our interval
plt.plot(lnspcROURA, pdf_gB, label="NormB") # plot it

plt.show()
plt.show()

plt.hist(serRES, bins=45)
plt.show()

plt.hist(serRES, normed=True)

xxx1 = plt.xticks()[0]
xxxmin, xxxmax = min(xxx1), max(xxx1)
lnspcRES = np.linspace(xxxmin, xxxmax, len(serRES))

mRES, sRES = stats.norm.fit(serRES) # get mean and standard deviation
print("mRES:", mRES)
print("sRES/numOfParticles**0.5:", sRES/numOfParticles**0.5)
pdf_gC = stats.norm.pdf(lnspcRES, mRES, sRES/numOfParticles**0.5) # now get
theoretical values in our interval
plt.plot(lnspcRES, pdf_gC, label="NormC") # plot it

plt.show()

#-----0.5% UNCERTAINTY-----#
serF = phivalPOINTFIVEArray
serFROURA = phirovalPOINTFIVEArray
serFRES = phiresPOINTFIVEArray

plt.hist(serF, bins=50)
plt.hist(serFROURA, bins=50)
plt.show()
plt.show()

plt.hist(serF, normed=True)
plt.hist(serFROURA, normed=True)

xt = plt.xticks()[0]
xmin, xmax = min(xt), max(xt)
lnspcF = np.linspace(xmin, xmax, len(serF))

xxt = plt.xticks()[0]
xxmin, xxmax = min(xxt), max(xxt)
lnspcFROURA = np.linspace(xxmin, xxmax, len(serFROURA))

#Trying normal distribution first
mF, sF = stats.norm.fit(serF) # get mean and standard deviation
print("mPOINTFIVEUNC:", mF)
print("sPOINTFIVEUNC/numOfParticles**0.5:", sF/numOfParticles**0.5)
pdf_gD = stats.norm.pdf(lnspcF, mF, sF/numOfParticles**0.5) # now get theoretical
values in our interval
plt.plot(lnspcF, pdf_gD, label="NormD") # plot it

mFROURA, sFROURA = stats.norm.fit(serFROURA) # get mean and standard deviation
print("mROURAPOINTFIVEUNC:", mFROURA)
print("sROURAPOINTFIVEUNC:", sFROURA)
pdf_gE = stats.norm.pdf(lnspcFROURA, mFROURA, sFROURA) # now get theoretical values

```

Figure B.33: Simulation in PYTHON for 3D case: Residual phase calculation for configuration - II.

Development of a New Apparatus for Precision Gravity Measurements with Atom Interferometry

```
in our interval
plt.plot(lnspcFROURA, pdf_gE, label="NormE") # plot it

plt.show()
plt.show()

plt.hist(serFRES, bins=45)
plt.show()

plt.hist(serFRES, normed=True)

xxxxt = plt.xticks()[0]
xxxmin, xxxmax = min(xxxxt), max(xxxxt)
lnspcFRES = np.linspace(xxxmin, xxxmax, len(serFRES))

mFRES, sFRES = stats.norm.fit(serFRES) # get mean and standard deviation
print("mRESPOINTFIVEUNC:", mFRES)
print("sRESPOINTFIVEUNC/numOfParticles**0.5:", sFRES/numOfParticles**0.5)
pdf_gF = stats.norm.pdf(lnspcFRES, mFRES, sFRES/numOfParticles**0.5) # now get
theoretical values in our interval
plt.plot(lnspcFRES, pdf_gF, label="NormF") # plot it

plt.show()

#-----1.0% UNCERTAINTY-----#
ser0 = phivalONEArray
serOROURA = phirovalONEArray
serORES = phiresONEArray

plt.hist(ser0, bins=50)
plt.hist(serOROURA, bins=50)
plt.show()
plt.show()

plt.hist(ser0, normed=True)
plt.hist(serOROURA, normed=True)

xt = plt.xticks()[0]
xmin, xmax = min(xt), max(xt)
lnspc0 = np.linspace(xmin, xmax, len(ser0))

xxxxt = plt.xticks()[0]
xxmin, xxmax = min(xxxxt), max(xxxxt)
lnspcOROURA = np.linspace(xxmin, xxmax, len(serOROURA))

#Trying normal distribution first
m0, s0 = stats.norm.fit(ser0) # get mean and standard deviation
print("mONEUNC:", m0)
print("sONEUNC/numOfParticles**0.5:", s0/numOfParticles**0.5)
pdf_gG = stats.norm.pdf(lnspc0, m0, s0/numOfParticles**0.5) # now get theoretical
values in our interval
plt.plot(lnspc0, pdf_gG, label="NormG") # plot it

mOROURA, sOROURA = stats.norm.fit(serOROURA) # get mean and standard deviation
print("mROURAONEUNC:", mOROURA)
print("sROURAONEUNC:", sOROURA)
pdf_gH = stats.norm.pdf(lnspcOROURA, mOROURA, sOROURA) # now get theoretical values
in our interval
plt.plot(lnspcOROURA, pdf_gH, label="NormH") # plot it
```

Figure B.34: Simulation in PYTHON for 3D case: Residual phase calculation for configuration - II.

```
plt.show()
plt.show()

plt.hist(serORES, bins=45)
plt.show()

plt.hist(serORES, normed=True)

xxxxt = plt.xticks()[0]
xxxmin, xxxmax = min(xxxxt), max(xxxxt)
lnspcORES = np.linspace(xxxmin, xxxmax, len(serORES))

mORES, sORES = stats.norm.fit(serORES) # get mean and standard deviation
print("mRESONEUNC:", mORES)
print("sRESONEUNC/numOfParticles**0.5:", sORES/numOfParticles**0.5)
pdf_gI = stats.norm.pdf(lnspcORES, mORES, sORES/numOfParticles**0.5) # now get
theoretical values in our interval
plt.plot(lnspcORES, pdf_gI, label="NormI") # plot it

plt.show()

timeend = time.time()
diff=timeend-timestart
print("Time taken : ", diff)
```

Figure B.35: Simulation in PYTHON for 3D case: Residual phase calculation for configuration - II.

Appendix C

List of Publications

This Appendix summarizes a collection of research contributions made during the doctoral candidature.

C.1 Publications in International Journals

- “*New apparatus design for high - precision measurement of G with atom interferometry*”, **M. Jain**, G. M. Tino, L. Cacciapuoti and G. Rosi, (submitted).
- “*Measuring the gravitational acceleration with matter - wave velocimetry*”, G.D’Amico, L. Cacciapuoti, **M. Jain**, S. Zhan and G. Rosi, *Eur. Phys. J. D.*, **73**:98 (2019), DOI: <https://doi.org/10.1140/epjd/e2019-90543-0>.

C.2 Conference Proceedings

- “*Detecting gravitational waves with atomic sensors*”, G. Rosi, A. Vicere, L. Cacciapuoti, G. D’Amico, L. Hu, **M. Jain**, N. Poli, L. Salvi, E. Wang and G. M. Tino, AIIPS conference proceedings, *IL NUOVO CIMENTO 41 C* **130** (2018), DOI: <https://doi.org/10.1393/ncc/i2018-18130-8>.
- “*Testing gravity with atomic quantum sensors on ground and in space*”, Leonardo Salvi, Luigi Cacciapuoti, Giulio D’Amico, Liang Hu, **Manan Jain**, Nicola Poli, Gabriele Rosi, Enlong Wang and Guglielmo. M. Tino, *SPIE Proceedings Volume 10674, Quantum Technologies 2018*; **1067409** (2018), DOI: <https://doi.org/10.1117/12.2317923>.

अभिस्वीकृति

इस थीसिस के बहुत शुरुआत में, सबसे पहले मैं अपने डॉक्टरेट पर्यवेक्षक प्रो. गुग्लिल्लो टिनो और मेरे शोध संरक्षक डॉ. गैब्रियल रोजी के प्रति हार्दिक धन्यवाद व्यक्त करना चाहूँगा। मैं प्रो. टिनो के निरंतर समर्थन, प्रोत्साहन और मार्गदर्शन के लिए ऋणी हूँ। मैं खुद को बहुत भाग्यशाली मानता हूँ कि मुझे डॉ. रोजी के साथ काम करने का अवसर मिला। मैं प्रो. टिनो का शुक्रगुजार हूँ कि उन्होंने मुझे यह मौका दिया क्योंकि यह अवसर ही मेरे लिए सब कुछ था। यह वास्तव में एक विशेषाधिकार है कि प्रो. टिनो और डॉ. रोजी को मुझ पर विश्वास था, बावजूद इसके कि मैंने अपने डॉक्टरेट अनुसंधान के दौरान कई तुच्छ त्रुटियाँ की हैं। व्यक्तिगत रूप से, मैंने अपने वर्षों के दौरान अपने शोध गुरु गैब्रियल रोजी जैसे युवक को कभी नहीं देखा है, जो बेहद चतुर, मददगार और विचारशील होते हुए भी मैंने गलतियाँ कीं, जिस पर देखकर कोई भी प्रोफेसर या सलाहकार अपना विश्वास खो सकता है। मुझे यह घोषणा करते हुए खुशी हो रही है कि इन तीन वर्षों में, मैं न केवल एक बेहतर शोधकर्ता बन गया, बल्कि एक अच्छा स्तर का धैर्य और विचार रखने वाला व्यक्ति भी बन गया।

मैं अपनी बहन का शुक्रगुजार हूँ क्योंकि उसने मुझे थीसिस लिखने के लिए प्रोत्साहित किया। मैं अपने माता-पिता और मासी को धन्यवाद देता हूँ कि उन्होंने मेरे जैसे जिद्दी और आवेगी बच्चे की परवरिश की और मुझे एक महत्वाकांक्षी भौतिक विज्ञानी के रूप में और एक अच्छे स्वभाव वाले व्यक्ति के रूप में खुद का सर्वश्रेष्ठ संस्करण प्राप्त करने में मदद की।

मैं भौतिक विज्ञान में अपने सभी सर्वोत्तम आकाओं और वरिष्ठों का बहुत आभारी हूँ जिन्होंने मुझे सार्थक और उत्तेजक चर्चाओं के लिए अपना बहुमूल्य समय दिया, जिनके नाम हैं - रमन सहगल, सुशील शर्मा, पुलकित राय, जुलियो द'अमीको, कन्हैया पांडे। यह शुद्ध भाग्य था कि मुझे रमन सहगल जैसे वैज्ञानिक से सीखने का अवसर मिला, जिन्होंने मुझे स्क्रैच से पाइथन प्रोग्रामिंग सिखाई, अंततः इस थीसिस में एक रिकॉर्ड समय में बताए गए परिणामों की उपज हो सकी। मेरे मास्टर डिग्री के पहले दिन से लेकर अब तक, मैंने पुलकित राय जैसे एक वरिष्ठ युवक की प्रशंसा की है, जिनके भौतिक विज्ञान और जीवन के ज्ञान में कई पहलू अनुकरणीय और दोषरहित हैं, उनको देखकर निरंतर पीछे न हटने और परिणाम तक पहुँचने के लिए हृदय में एक आसमान छूने वाला उत्साह और हौसला उत्पन्न होता है। उनसे सीखना एक बड़ा सम्मान था क्योंकि वह एक ऐसे व्यक्ति है जो लगातार मुस्कुराते हैं चाहे वह कितनी भी कठोर परिस्थितियों और चुनौतियों से जूझ रहे हों। मैं डॉ. सुशील शर्मा का भी हार्दिक धन्यवाद करता हूँ, जिन्होंने अपना बहुमूल्य समय मुझे अपने डॉक्टरेट के काम के बारे में अनौपचारिक बात करने और अपने सहयोगियों के सामने भौतिक शास्त्रों पर चर्चा करने के लिए मुझे प्रोत्साहन दिया। डॉ. सुशील शर्मा और उनके सहयोगियों की प्रतिक्रिया ने संगोष्ठी देते हुए मेरा आत्मविश्वास बढ़ाया, जो एक अच्छा शैक्षणिक करियर बनाने के लिए एक कदम के रूप में चिह्नित करता है। मुझे याद है कि जब मैं अपनी पीएचडी उम्मीदवारी के पहले वर्ष में था, तो मैंने जुलियो द'अमीको को बड़ी प्रेरणा के साथ लैब में एक अथक रूप से परिश्रम करते देखा है, मेरे पास उनके प्रति आभार व्यक्त करने के लिए पर्याप्त शब्द नहीं हैं। मैं सौभाग्यशाली था कि उनके साथ परमाणु भौतिकी की उत्तेजक चर्चाएँ करने का अवसर मुझे प्राप्त हुआ। उन्होंने अपने व्यस्त कार्यक्रम के बावजूद लैब छोड़ने के बाद भी मेरे विज्ञान-संबन्धि प्रश्नों का उत्तर देकर मेरी मदद की, जो कि मेरे डॉक्टरेट की उम्मीदवारी में एक महत्वपूर्ण कदम था। इस महत्वपूर्ण चौकी ने एक पोस्टडॉक्टरल स्थिति को सुरक्षित करने में मेरी अर्थपूर्ण भूमिका निभाई। अंत में, मेरे जीवन में, पहला व्यक्ति जिसने परमाणु प्रयोगशाला में प्रायोगिक तंत्रों का इस्तेमाल करना सिखाया, वह थे डॉ. कन्हैया पांडे। मैं डॉ. पांडे से फिर से मिलने

की उम्मीद करता हूँ यदि मैं उन जैसे कुशल और शानदार व्यक्ति के साथ भौतिकी या परमाणु प्रयोगों पर चर्चा करने में सक्षम हो जाऊँ।

जिन्दगी में जब नरेंद्र राठौड़ जैसा आनंदपूर्वक और होशियार मित्र हो, तो उनको देखकर बड़े भाई का क्या कर्तव्य होता है उसका एहसास होता है। जब मेरे पीएचडी के समय मैं बिलकुल भी वक्त नहीं बचा था, तो मेरे परम मित्र नरेंद्र राठौड़ ने मेरे कुछ सिमुलेशन उनके कंप्यूटर में भी चलाएँ, जिससे मेरे पीएचडी के परिणाम सही समय पर आ गए, इस प्रकार का योगदान देना अपने आप में ही एक बहुत ही बहुमूल्य कार्य है।

मैं अवनी सराफ का शुक्रगुजार हूँ कि उन्होंने मुझे यह सिखाया कि गंभीर चुनौतियों का सामना करते हुए भी जिंदगी को कैसे खुशी से जीना है। एक सच्ची साथी वास्तव में, वह मेरी अनिद्र-दिनचर्या के बावजूद मेरे साथ रही, जब मैं अपनी पीएचडी उम्मीदवारी के दौरान घंटों और दिनों तक उससे बात नहीं कर पाया। मेरे पेशेवर और व्यक्तिगत जीवन की बेहतरी के लिए उनका नैतिक समर्थन हमेशा महत्वपूर्ण रहा है। एक महत्वाकांक्षी भौतिक वैज्ञानिक, अजेय और जिद्दी शोध छात्र के रूप में, मेरे लिए शुरू में यह स्वीकार करना मुश्किल हो गया कि मुझे अपने परिवार और मित्रों के अलावा किसी और के नैतिक समर्थन और अपने मन की शांति के लिए आवश्यकता हो सकती है, लेकिन फिर, मेरे जीवन का प्यार अवनी ने मेरे जीवन में प्रवेश करके मेरे सभी प्रश्नों के उत्तर दिए। उसकी उपस्थिति सीधे मेरे जीवन को प्रभावित करती है जैसे सूखे खेतों में फूल खिल रहे हों। उसके साथ होने कारणवश, जीवन ने मुझे परिवर्तनों का स्वागत करना और उन्हें गले लगाना भी सिखाया।

मेरी डॉक्टरेट की डिग्री मेरे जीवनकाल के सबसे चुनौतीपूर्ण दिन थे, क्योंकि यह वास्तव में एक रोलर-कोस्टर की सवारी थी। दो साल तक कंप्यूटर पर काम करने वाली एक परिष्कृत प्रयोगशाला में मौजूद होने के कारण मुझे एक स्वतंत्र शोधकर्ता होने की दिशा में प्रगति करने में मदद मिली। इसी वजह से मैं अपनी छिपी क्षमता को विपाश करने में सक्षम हुआ जो कि मैं अपने पीएचडी पर्यवेक्षक और मेरे शोध संरक्षक के मार्गदर्शन और टिप्पणियों के बिना कभी पूरा नहीं कर सकता। मेरा जीवन कम तनावपूर्ण हो गया जब मुझे यहाँ ऐसे लोग मिले जिनकी सभी उपस्थिति बहुत महत्व रखती थी। मैं फ्लोरेंस के इन लोगों का शुक्रगुजार हूँ, जिन्होंने मुझे पुनर्मिलन, घर की पार्टियों, इनडोर / आउटडोर गेम्स खेलने और यात्रा अन्वेषणों के शानदार तरीकों से नैतिक समर्थन प्रदान करते हुए मेरे साथ अच्छा व्यवहार रखा। इन सभी लोगों के नाम हैं: हर्षल, श्वेता, अविषेक, मैत्रेयी, मुर्तजा, शमैला, निहार, दीप्ती, गुंजन, आतिफ, तस्सदिक, प्रसन्ना, अकांदा, प्रोसेनजीत, राघव, सुहास, नजीब, फहाद, शाहनवाज़, प्येतर, लोरेंजो, एलेसांद्रो, फ्रांसेस्को, जुलिओ, लियोनार्डो।

मैं अपने दिल के करीब सभी भारतीय लोगों को धन्यवाद देना चाहता हूँ। इन अनमोल लोगों के नाम जो समान रूप से मानते थे कि मैं इस प्रयास को आगे बढ़ा सकता हूँ और फलदायी परिणाम दे सकता हूँ: अभिनीत परेलकर, आदित्य खांडेकर, अजिंक्य भावसार, आमिर अहमद, अंकित जैन, अरुण यादव, अविनाश राजेंद्रन, अवनी सराफ, इयान फॉसेका, मुस्तफा बोहरा, नरेंद्र राठौड़, निश्चल द्विवेदी, प्रसाद दामले, प्रतीक भानुसे, पुलकित राय, राजेश्वरी शेकर, ऋषभ जगलपुरे, ऋषि जैन, साहिल उपाध्याय, तथा अहमद, ज़ीशान सिद्दीकी।